SCUOLA
NORMALE
SUPERIORE

Classe di Scienze

Corso di perfezionamento in
Fisica

XXXIV ciclo

Probing high redshift massive black hole coalescence through gravitational waves and electromagnetic signals

Settore Scientifico Disciplinare **FIS/05**

Candidata
dr.ssa Srija CHAKRABORTY

SCUOLA
NORMALE
SUPERIORE

Anno accademico 2024/2025

SCUOLA NORMALE SUPERIORE

Classe di Scienze

Tesi di perfezionamento in Fisica

Probing high redshift massive black hole coalescence through gravitational waves and electromagnetic signals

Candidate:

Srija Chakraborty

Supervisor:

Prof.ssa Simona Gallerani

2024

"I have a naive trust in the Universe – that at some level it all makes sense, and we can get glimpses of that sense if we try."

- Mihaly Csikszentmihalyi

Contents

Abstract

The existence of supermassive black holes (SMBHs) with masses exceeding billions of solar masses at early cosmic epochs (less than one Gyr after the Big Bang) poses an intriguing challenge in astrophysics. Despite ongoing investigations, the origin and evolution of such SMBHs are still riddled with many uncertainties related to their formation and growth mechanisms and remain intriguing and actively debated topics of research in astrophysics.

In this thesis we study the formation and evolution of SMBHs with the use of gravitational waves (GWs) arising from the coalescence of the progenitor massive black holes (MBHs).

We investigate the coalescence of massive black hole ($M_{\rm BH} \gtrsim 10^6$ $\rm M_\odot$) binaries (MBHBs) at $6 < z < 10$ by adopting a suite of cosmological hydrodynamical simulations of galaxy formation, zoomed-in on biased ($> 3\sigma$) overdense regions ($M_h \sim 10^{12}$ $\rm M_\odot$ dark matter halos at $z = 6$) of the Universe. We first analyse the impact of different resolutions and active galactic nucleus (AGN) feedback prescriptions on the merger rate of MBHs, assuming instantaneous mergers. Then, we compute the halo bias correction factor due to the overdense simulated region.

We then select our fiducial model, for which we further study the effect of delay in the MBHB coalescence due to dynamical friction. Next, we compute the expected properties of the GW signals and find the fraction of MBHB mergers to be detected by the Laser Interferometer Space Antenna (LISA) and calculate the angular resolution of LISA detectable events (LDEs) to estimate the sky-localization limits of the detectable MBHB mergers.

For the LDEs with known GW properties, we further investigate the intrinsic and observational properties of $z \gtrsim 6$ galaxies that host the coalescing MBHBs. We associate the LDEs to

their host galaxies and select those that, based on their intrinsic properties ($\dot{M}$, SFR, gas metallicity, and dust mass), are expected to be bright in one or more electromagnetic (EM) bands, e.g. rest-frame X-ray, ultra-violet (UV) and far-infrared (FIR). We further restrict our selection to those LDEs that, after considering the effect of delay due to dynamical friction in the MBH coalescence, are still occurring at $z \gtrsim 6$. We find that $\sim$20-30% of the LDEs and their host galaxies are also detectable with EM telescopes. We post-process these events with dust radiative transfer calculations to make accurate predictions about their spectral energy distributions (SEDs) and continuum maps in the JWST to ALMA wavelength range. We compare the spectra arising from galaxies hosting the merging MBHs with those arising from AGN powered by single accreting BHs. We find that it will be impossible to identify an LDE from the continuum SEDs because of the absence of specific imprints from the merging MBHs. Finally, we compute the profile of the H_α line arising from LDEs, taking into account both the contribution from their star-forming regions and the accreting MBHs. We conclude that the combined detection of GW and EM signals from $z \gtrsim 6$ MBHs is challenging (if not impossible) not only because of the poor sky-localization ($\sim$10 deg^2) provided by LISA, but also because the loudest GW emitters ($M_{\mathrm{BH}} \sim 10^{5-6}\,\mathrm{M}_\odot$) are not massive enough to leave significant signatures (e.g. extended wings) in the emission lines arising from the broad line region.

This thesis is composed of four parts: theoretical background, numerical background, analysis and results and finally discussions and summary. Each part is composed of several chapters, the overview of which we highlight below:

- We begin with Chapter 1 to give a general introduction to the readers about the cosmological framework this work is based on, timeline of the various epochs of our Universe, theoretical modelling of AGN and different possible pathways of the origin and evolution of SMBHs.

- We then describe in Chapter 2 the theory of gravitational waves and its relevance to the formation and evolution of massive black hole binaries (MBHBs). We begin with a brief overview of the general theory of relativity, then describe the different timescales related to the coalescence of MBHs. We then describe some key aspects of GWs from binary systems and a basic concept of GW detectors. We end this chapter with a synopsis of

electomagnetic (EM) signals from merging MBHs and the expected detections till date.

- Next, in Chapter 3 we outline the key components of a cosmological simulation and provide an overview of modern simulations. Thereafter, we describe the hydrodynamical simulations (HDS) used in this work and highlight the comparison of the two simulations we used as well as the differences within each for varying feedback effects.

- Chapter 4 gives a rundown on the principle of radiative transfer (RT), different approaches to solve the RT problem and finally the numerical aspect of the code SKIRT used in this work to model dust surrounding the AGNs in our model.

- In Chapter 5 we derive the merger rate of MBHBs in different simulation runs and also compute the effect of considering overdense halos as MBHB hosting sites and the bias produced from such assumptions. Correcting for this bias, we then compare out results with contemporary merger rates derived from various semi-analytical models (SAMs) and HDS.

- We begin Chapter 6 with the technique we used to associate MBHBs in our simulations to the galaxy hosting them. We then compute the time delays that can be induced in MBHB coalescence due to dynamical friction against the stars surrounding the MBHB in post-processing.

- In Chapter 7 we study the GW properties arising from the coalescence of MBHBs. We compute the signal-to-noise ratio of the binaries for LISA and the angular resolution of the mergers which leads to GW emission. We also discuss about the mass ratio and different time, frequqency and spatial scales of interest for the GW events.

- Finally, in Chapter 8 we delve into the possible EM signals from GW events discussed preciously. We first select the LDEs associated with a host galaxy and compute various intrinsic and observable properties of the hosts. We then produce synthetic spectra and simulated maps of the events in different EM bands and discuss the possibility of detecting EM signals from LDEs before, during or after the coalescence. We also analyze the H_α line

profile from LDEs that we calculate considering the contributions from both star-forming regions and accreting MBHs.

- We conclude this thesis with Chapter 9 where we summarise our work and results and discuss the caveats involved in this work and future prospects.

Part I

Theoretical background

General introduction 1

1.1 Introduction

This chapter is aimed at providing a concise theoretical background on the basic principles of cosmology and astrophysics, on which this thesis is based on. We first begin with the cosmological framework (1.2) and discuss a brief history and chronology of structure formation in our Universe (1.3). We then provide a brief overview of AGNs (1.4) and Super Massive Black Hole (1.5) seeding scenarios. Finally, we conclude this introductory chapter with a synopsis of gravitational waves (2.1) outlining the theory and observations related to this topic.

1.2 Cosmological framework

One of the first questions that crosses our minds when we start thinking about the Universe is - how are the structures we see today in the Universe formed? What is their origin, how did these evolve and what will happen to these in the future?

Several observations and theoretical models exist to give us a reliable and scientific basis for these open questions. If we assume our Universe began with "Big Bang" - an initial singularity with infinitely hot and dense state, we can slowly build up our concept of the present Universe.

Before considering the various astrophysical objects, we should first provide a stable framework for the structures to exist. The ΛCDM (Lambda Cold Dark Matter) model is the prevailing cosmological model which is widely accepted as the standard framework for our Universe and is based on :

- The cosmological principle: According to this principle, the Universe is homogeneous and isotropic at adequately large scales ($\sim$ 100 Mpc, Hogg et al. 2005). In other words, at any time, on large scales, any given region of the Universe is indistinguishable from other regions (homogeneity, Maartens 2011) irrespectively of the direction assumed (isotropy, Saadeh et al. 2016).

- General relativity: At cosmological scales, we assume that the dynamics are governed by the theory of general relativity (Einstein, 1916).

The basis of the ΛCDM model are supported by several observational evidences, as collected in the last few decades. For example, the COBE [1], WMAP [2] and Planck satellites [3] have provided data of the cosmic microwave background (CMB) supporting the isotropy and homogeneity of the Universe on large scales. The CMB is a faint, pervasive glow of microwave radiation that extends through the entire universe. Measured at approximately 2.72 K (Fixsen, 2009), the CMB represents the thermal afterglow of the hot, ionized plasma that filled the early universe (see Sec.1.3 for more details). Also, surveys of galaxies such as the Sloan digital sky survey (SDSS, Doroshkevich et al. 2004; Skibba & Sheth 2009), 2-degree field galaxy redshift survey (2dfGRS, Colless et al. 2001) show a large-scale structure (LSS) that is consistent with a universe that is fairly uniform on large scales.

One of the results of the CMB experiment is the definition of the Universe composition:

- Dark energy (68%): The force driving the accelerated expansion of the universe, dark energy exerts negative pressure, causing the universe's expansion to accelerate. In Einstein's field equations (which we will see in Sec.1.6), this shows up as the cosmological constant, Λ. Though its origin is not fully understood, observations of distant supernovae (Peebles & Ratra, 2003; Goldhaber & Cline, 2009) and the CMB support its presence.

- Dark Matter (27%): The cold dark matter (CDM) influences the gravitational scaffolding of cosmic structures. Its existence can be inferred from the structural formation of galaxies, galaxy clusters, and the large-scale cosmic web (Peebles, 1982; Blumenthal et al., 1984).

[1] https://lambda.gsfc.nasa.gov/product/cobe/spacecraft_description.html
[2] https://lambda.gsfc.nasa.gov/product/wmap/current/
[3] https://www.esa.int/Enabling_Support/Operations/Planck

- Baryonic matter (5%): Ordinary matter (baryons), makes up for the smallest fraction of the three and is the building block of galaxies, stars, and interstellar gas, imprinting its signature on the CMB and LSS.

Apart from supporting the observational evidences of CMB and LSS, the ΛCDM model is also supported by the existing abundance of chemical elements such as hydrogen (including deuterium and tritium), helium and trace amount of other elements such as lithium and beryllium (Alpher et al., 1948).

Now that we have our basic model and the ingredients of the Universe, we define below some key expressions that are frequently used in the context of ΛCDM:

1.2.1 Scale factor and redshift

The scale factor, a, is a dimensionless quantity that characterizes the relative size of the Universe at a given time compared to its size at some reference time. It is a fundamental parameter in cosmology, particularly in the Friedmann-Lemaître-Robertson-Walker (FLRW) metric. The scale factor can be written in terms of redshift as:

$$a(t_{em}) = \frac{1}{1+z} \tag{1.1}$$

where t_{em} is the time at which the source emitted light initially and redshift (z), is a measure of how much the light from a distant object has shifted towards longer wavelengths due to the expansion of the universe (Doppler, 1846). Redshift can be defined as the fractional change in the wavelength of light:

$$z = \frac{\lambda_{\text{obs}} - \lambda_{\text{em}}}{\lambda_{\text{em}}}. \tag{1.2}$$

where λ_{obs} and λ_{em} are the observed and emitted wavelengths, respectively.

Eq.1.1 shows the reciprocal relationship between the scale factor and redshift: as the scale factor increases due to the expansion of the universe, the redshift becomes more pronounced for distant objects.

1.2.2 Hubble's law

Hubble's law describes the relationship between the recessional velocity of a galaxy and its distance from an observer. Mathematically, Hubble's law is expressed as (Hubble & Humason, 1931):

$$v = H_0\, r. \tag{1.3}$$

where v is the recessional velocity of the galaxy (measured in km/s) and r is the distance to the galaxy from the observer (measured in Mpc). H_0 is the Hubble parameter (expressed in km Mpc^{-1} s^{-1}), which is a proportionality constant. At present, that is for t_0, the Hubble constant H_0 assumes a value ~ 70 km Mpc^{-1} s^{-1}.

1.2.3 FLRW metric

Metric defines the notion of distance in curved spacetime (see Sec. 2.2 for a more detailed discussion). The Friedmann-Lemaître-Robertson-Walker metric describes the homogeneous and isotropic spacetime of our expanding universe in the context of general relativity (Robertson, 1935). The metric is written as follows:

$$-ds^2 = -cdt^2 + a^2(t)\left[\frac{dr^2}{1-Kr^2} + S_k^2(r)(d\theta^2 + \sin^2\theta d\phi^2)\right], \tag{1.4}$$

where r(θ, ϕ) denotes the comoving spatial coordinates in spherical polar system, dt is cosmic time interval and K is the curvature parameter representing the spatial curvature of the universe (1 for positive curvature, -1 for negative curvature, and 0 for flat spatial sections). $S_k(r)$ is expressed as :

$$S_{\mathrm{k}}(r) = \begin{cases} \sin(\sqrt{\mathrm{K}}\mathrm{r})/\sqrt{\mathrm{K}}, & \text{for K>0} \\ r, & \text{for K=0} \\ \sinh(\sqrt{\mathrm{K}}\mathrm{r})/\sqrt{-\mathrm{K}}, & \text{for K<0.} \end{cases} \tag{1.5}$$

1.2.4 Einstein's field equations

Einstein's field equations relates the geometry of spacetime to the distribution of matter and energy within it (Einstein, 1916; Maggiore, 2007). In the context of a flat, homogeneous, and isotropic universe described by the ΛCDM model, the field equations can be written as:

$$G_{\mu\nu} \equiv R_{\mu\nu} - \frac{1}{2} g_{\mu\nu} R = \frac{8\pi G}{c^4} T_{\mu\nu} + \Lambda g_{\mu\nu}, \tag{1.6}$$

where $G_{\mu\nu}$ is the Einstein tensor, $R_{\mu\nu}$ is the Ricci tensor that describes the local curvature of spacetime. It basically measures the distortment of a shape along a geodesic. $g_{\mu\nu}$ is the metric tensor which defines the geometry of spacetime.R is the Ricci scalar and it provides a scalar measure of the overall curvature of spacetime at a given point. It is related to the Ricci tensor as $R = g^{\mu\nu} R_{\mu\nu}$ where $g^{\mu\nu}$ represents the components of the inverse metric tensor. G is the Newtonian gravitational constant and finally, $T_{\mu\nu}$ is the energy-momentum tensor which accounts for the distribution of matter and energy within spacetime. Λ is the cosmological constant which was later introduced in the equation by Einstein to account for the "static-Universe" model back then. Λ is now re-evaluated to account for the dark energy that fuels the expansion of the Universe.

We delve more into this in Sec. 2.1.

1.2.5 Friedmann's equations

Friedmann's equations describe the dynamics of a homogeneous and isotropic universe within the framework of general relativity (Friedmann, 1922). For an ideal fluid, using FLRW metric

1.4 and field equation 1.6, we can typically derive the Friedmann equations as:

$$H^2 = \frac{8\pi G}{3}\rho - \frac{K}{a^2} \tag{1.7}$$

$$\dot{H} = \frac{\ddot{a}}{a} = -\frac{4\pi G}{3}(\rho + 3P). \tag{1.8}$$

In the above equations, ρ is the total energy density of the Universe which can be expressed as $\rho = \rho_m + \rho_r + \rho_\Lambda$ where ρ_m is the energy density of matter (including both dark matter and baryonic matter), ρ_r is the energy density of radiation and ρ_Λ is the energy density associated with the cosmological constant. Also, $\ddot{a}$ stands for the second derivative of the scale factor with respect to time and P is the total pressure of the Universe, which is a combination of the pressure of matter (P_m), the pressure of dark energy (P_Λ), and the radiation pressure (P_r). We can relate P and ρ as $P = \omega\rho$, where

$$\omega = \begin{cases} = 0, & \text{for non-relativistic matter} \\ = 1/3, & \text{for radiation} \\ = -1, & \text{for } \Lambda. \end{cases} \tag{1.9}$$

These equations describe how the expansion rate of the Universe (H) and the scale factor (a) evolve over time based on the energy content of the Universe, including matter, radiation, and dark energy. The curvature parameter (K) influences the spatial geometry of the Universe.

1.2.6 Density parameters

The density parameters in the context of the Friedmann equations describe the fractional contribution of different components (such as matter, radiation, and dark energy) to the total energy density of the Universe. The parameters (Lahav & Liddle, 2019) are given by:

$$\Omega_m = \frac{\rho_m}{\rho_c} = \frac{\rho_m}{3H^2/8\pi G} \tag{1.10}$$

$$\Omega_r = \frac{\rho_r}{\rho_c} = \frac{\rho_r}{3H^2/8\pi G} \tag{1.11}$$

$$\Omega_\Lambda = \frac{\rho_\Lambda}{\rho_c} = \frac{\rho_\Lambda}{3H^2/8\pi G} \tag{1.12}$$

The critical density ρ_c is defined as $3H^2/8\pi G$ where H is the Hubble parameter. The sum of these density parameters is expected to equal 1 in a flat Universe, i.e. $\Omega_m + \Omega_r + \Omega_\Lambda = 1$.

1.3 Epochs in the Universe

In this section we outline the chronology of our Universe as we know today (Bartelmann, 2010). To understand the timeline of the Universe, we must define a few time-scales.

If we assume the Universe began with a Big Bang at $a = 0$ (1.1), we can calculate the present age of the Universe using 1.7 and 1.8 as:

$$t_0 = \int_0^{a(t_0)=1} \frac{1}{aH}\, da = \frac{1}{H_0} \int_0^1 \frac{1}{a} \frac{1}{\sqrt{\Omega_\Lambda + \Omega_\mathrm{m} a^{-3} + \Omega_r a^{-4}}}\, da \simeq 13.7 \text{ Gyr} , \tag{1.13}$$

Now, from 1.3, we can define the expansion time-scale of the Universe as $t_\mathrm{H} = H^{-1}$.

The next time-scale is related to the temperature of the Universe. If we assume a density of particles in the Universe as n with relative velocity between interacting particles v , then the rate of interaction between any two particles can be written as $\Gamma = nv\sigma$ where σ is the interaction cross-section. The velocity of the particles is dependent on the temperature (T), hence we get a temperature related timescale Γ^{-1}. For a Universe in thermal equilibrium, $H^{-1} >> \Gamma^{-1}$.

With the above in mind, we now describe the subsequent timeline (Knobel, 2013) of the Universe:

- The very early Universe: This constitutes of the first picoseconds ($\sim 10^{-12}$ s) of the Universe. During this time, the Universe experienced extreme temperatures and energies.

Processes such as inflation occurred (Guth, 2007), fundamental forces were unified, and conventional physics broke down in this era.

- Early Universe: Between $10^{-5} - 1$ s, the Universe continued to expand and cool. Cosmic inflation rapidly expanded the Universe (Linde, 2007).Quarks and gluons to create protons and neutrons. Initially, thermal equilibrium was maintained between the elementary particles (like photons, electrons, neutrinos etc.). When $H^{-1} < \Gamma^{-1}$, the equilibrium was disrupted and the corresponding particles 'froze out' and by the time the temperature of 0.5 MeV/k_B was reached, only electrons, photons, protons and neutrons survived.

- Nucleosynthesis: During nucleosynthesis, protons and neutrons underwent nuclear fusion due to high temperatures ($\sim 10^7 - 10^9$ K) and densities to produce the nuclei of hydrogen, helium, and a small amount of light elements (such as deuterium, and lithium). This epoch occurred within the first few minutes and is consistent with observational data (Coc & Vangioni, 2017).

- Matter-Radiation-Equality: Around $t_{\rm mre}$= 60,000 years after the Big Bang as the Universe cooled, matter and radiation densities became comparable [$\Omega_{\rm r}(t_{\rm mre}) = \Omega_{\rm m}(t_{\rm mre})$]. The gravitational force of matter became equal to the pressure of radiation. Before this regime, the Universe was dominated by radiation and subsequently it was dominated by matter (Bahr-Kalus et al., 2023).

- Recombination: Recombination (Sunyaev & Chluba, 2009) is the process of electrons recombining with protons and neutrons to form neutral atoms. This happened about 380,000 years after the Big Bang, when the Universe had cooled to a temperature of about 3000 K. Recombination allowed photons to travel freely through the Universe, making it transparent to light. CMB radiation was created at this time (Bennett et al., 2003). The CMB anisotropies (Fig.1.1) marked the seeding of the structures in our Universe today. Hierarchical structure formation was driven by the growth of tiny fluctuations ($\sim 10^{-5}$) in the matter density that existed in the early homogeneous and isotropic Universe. These fluctuations (known as density perturbations) were imprinted by quantum fluctuations during the Big Bang, and sunbsequently they were amplified by the universal inflation. These

fluctuations can be treated as perturbations around the smooth, homogeneous background in the linear regime, where only terms of first order in perturbation quantities are considered. This model of evolution of linear perturbations in the early Universe uses Newtonian dynamics and Friedmann equations to describe the early stages of structure formation and evolution. However, below a certain scale, typically around 10 h^{-1}Mpc, the perturbations start to deviate from the linear regime and evolve in a non-linear fashion. In the early stages of the Universe, the gravitational force was not strong enough to overcome the expansion, so density perturbations grew slowly. But as more time passed, the gravitational force became stronger, and the density perturbations grew more swiftly. They continued to grow over time as gravity pulled matter together to form stars, galaxies, clusters of galaxies, and larger structures that we see today.

- Dark Ages: Recombination ended at $z \sim 1100$. After this, the so-called "dark ages" (Miralda-Escudé, 2003) begun which lasted till $z \sim 20$–30 when the first stars and galaxies were formed. During this time, the Universe was filled with a hot, dense soup of neutral hydrogen and helium atoms. These atoms were so tightly packed together that they were constantly colliding and absorbing any photons that were emitted. This meant that there was no light in the Universe, and the Universe was dark.

- Cosmic Dawn: Between $z \sim 20$–30, cosmic dawn occured. During this time, the early stars and galaxies were formed. These stars and galaxies released photons into the Universe, which started to ionize the hydrogen and helium atoms. This allowed the photons to travel through the Universe without being absorbed, and the Universe begins to transit to the reionization phase (Cooray et al., 2019).

- Reionization: The Reionization Era followed the Cosmic Dawn occuring between $z \sim 20$–6 (Natarajan & Yoshida, 2014). During this time, the remaining neutral hydrogen atoms in the Universe were ionized by the photons from the luminous sources such as stars, galaxies, and quasars. This completion of reionization marked the end of the dark ages and the beginning of the modern Universe (Barkana & Loeb, 2001; Oesch et al., 2016).

Between 0.1 Gyr to present time, i.e. 13.7 Gyr, the Universe's matter continued evolving

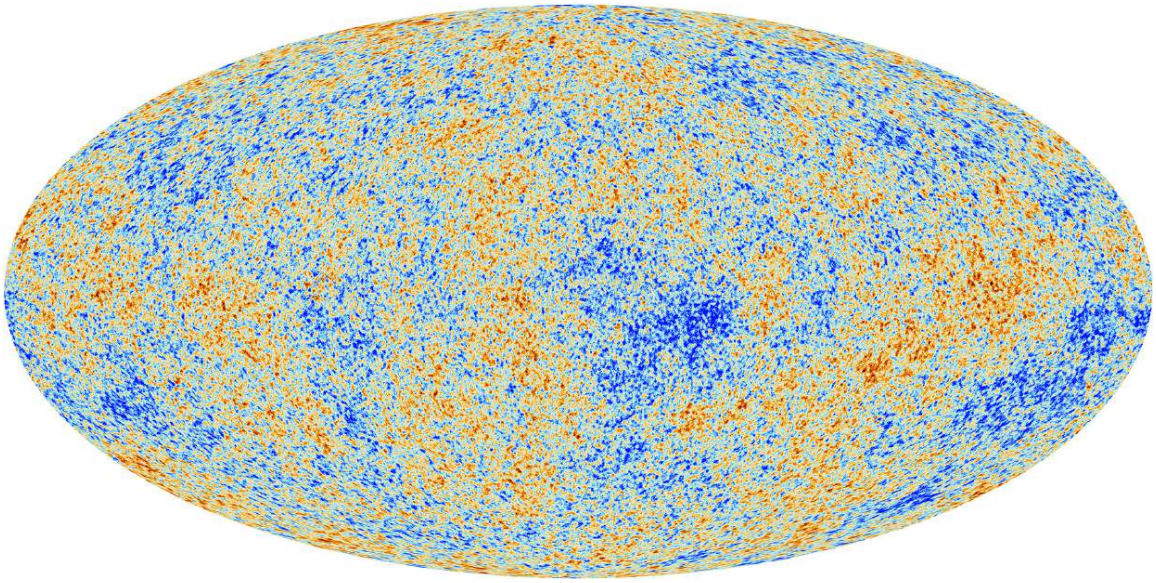

Figure 1.1: The CMB anisotropy represented as tiny temperature fluctuations as detected by the Planck satellite. Credit : Planck ESA collaboration (https://www.esa.int/ESA_Multimedia/Images/2013/03/Planck_CMB).

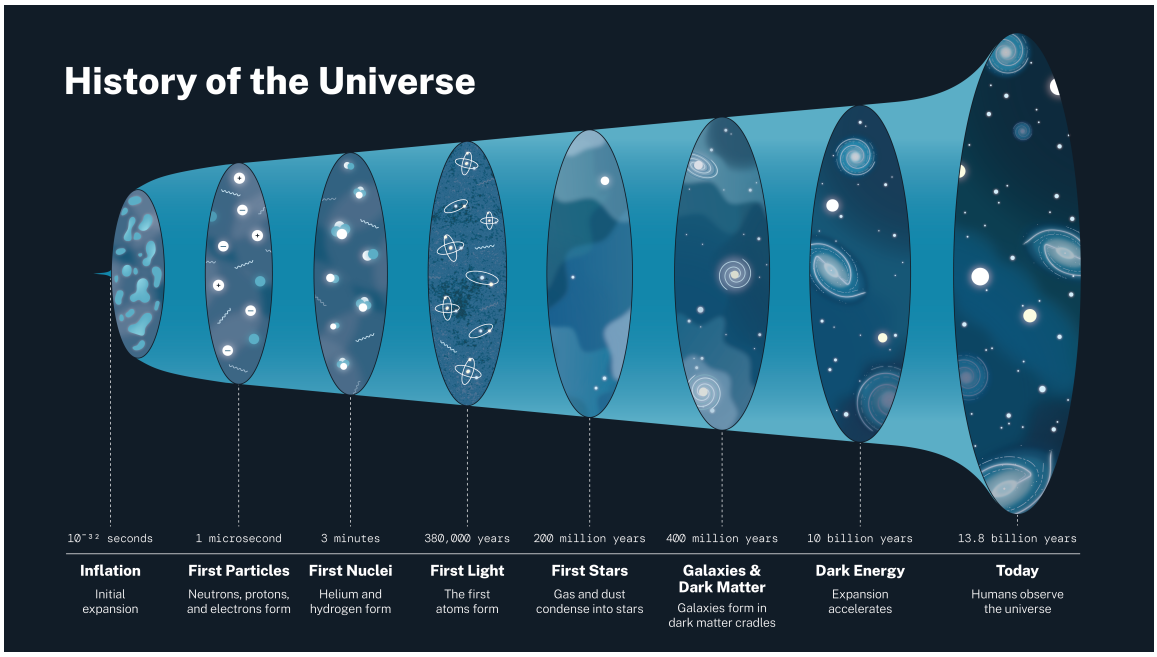

Figure 1.2: Brief history of our Universe showing different timesteps. Image credit: NASA, 2022

under gravity. At a redshift of $z \sim 0.3$, the Universe entered the dark energy era, a period of accelerated expansion driven by dark energy. This transition marked a significant shift in the evolution of the Universe, as it accelerated the expansion rate and altered the fate of the Universe.

All these epochs overlap with each other with no strict boundary. A concise representation of this timeline is schematised in Fig.1.2.

1.4 AGNs : How do they work

It is now widely agreed that that the centres of nearby galaxies host supermassive black holes (Kormendy, 2001; Magorrian et al., 1998). Observational evidence also indicate the existence of quasars at high redshifts (z>=6) (e.g. Fan et al. 2006; Jiang et al. 2010) indicating the presence of MBHs in the past and their host galaxies are expected to participate in multiple mergers according to the hierarchical structure formation in cold dark matter cosmology theory (e.g.White & Rees 1978; Blumenthal et al. 1984; Peebles 1980).

The AGN is a compact and energetically dynamic region at the center of certain galaxies. AGNs exhibit a distinctive and intense emission across the EM spectrum, powered by the accretion of surrounding material onto the central black hole (BH). This accretion process releases vast amounts of energy, resulting in phenomena such as powerful jets, X-ray emissions, and the

formation of obscuring tori composed of dust and gas. The study of AGNs is pivotal for understanding the co-evolution of galaxies and their central black holes, as AGN activity plays a crucial role in shaping galactic structures and regulating star formation. Investigating the mechanisms governing AGN variability, the impact of accretion processes, and the influence of surrounding galactic environments contributes to a comprehensive understanding of the intricate interplay between SMBHs and their host galaxies.

In this section, we provide a brief overview of AGNs and the unified model of AGN.

1.4.1 The unified model of AGNs

We follow (Netzer, 2015) and define an AGN as an accreting MBH ($M_{\rm BH} > 10^5 {\rm M}_\odot$) in the center of a galaxy with an accretion rate limited by $L_{\rm AGN}/L_{\rm Edd} > 10^{-5}$. Here $L_{\rm AGN}$ is the bolometric luminosity of the AGN and $L_{\rm Edd}$ is the Eddington luminosity [4]. We also expect most AGNs to be composed of Antonucci (1993); Ho (2008); Heckman & Best (2014):

- Accretion disk : Structures composed of gas and dust that orbit around the central MBH. As gas and dust from the galaxy's central region are drawn towards the MBH, angular momentum causes the matter to assume a flattened, rotating configuration, forming the accretion disk. The gas-dust matter in the disk experiences strong gravitational forces, leading to high temperatures and intense radiation from radio waves to X-rays, with the most significant contributions often occurring in the ultraviolet and optical wavelengths (see Abramowicz & Fragile (2013) for a comprehensive review).

- Broad line region (BLR) : The region near the central MBH (0.01-1 pc) where emission lines, particularly hydrogen Balmer lines[5], exhibit broadening due to high-velocity gas motions. The Doppler effect broadens the spectral lines, providing insights into the kinematics, ionization state, and physical conditions of the gas. The BLR is essential for understanding AGN dynamics, reflecting ionized gas clouds orbiting the BH and serv-

[4]The Eddington luminosity provides a critical limit to the luminosity that can be sustained by a gravitationally bound object without being disrupted by the radiation pressure. It can be expressed as $L_{\rm Edd} = \frac{4\pi G M m_p c}{\sigma_{\rm T}}$ where G is the gravitational constant, M is the mass of the object, m_p is the mass of a proton, c is the speed of light, and $\sigma_{\rm T}$is the Thomson scattering cross-section.

[5]Hydrogen Balmer lines are a series of spectral lines corresponding to transitions in the hydrogen atom's electron orbit from an energy level higher than n = 3 back down to n = 2

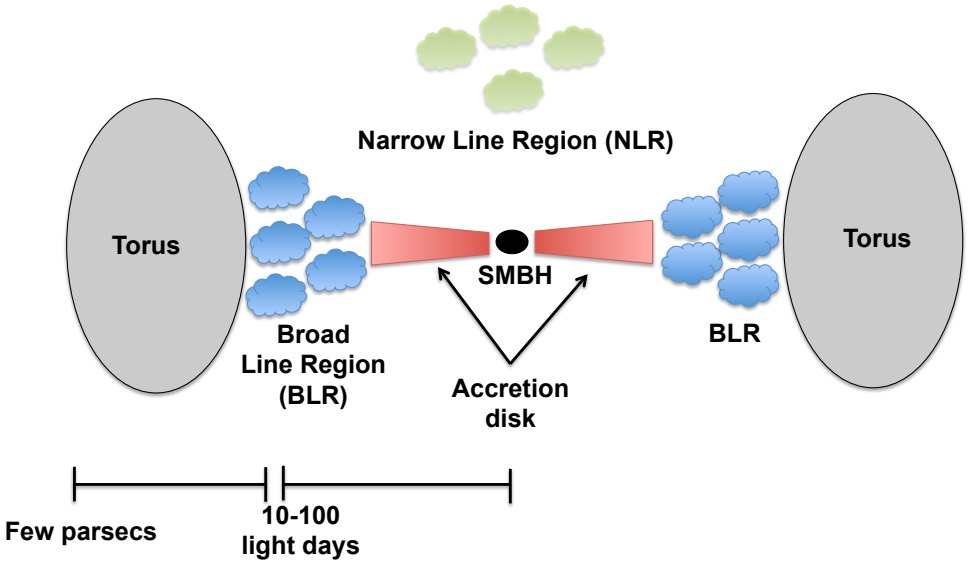

Figure 1.3: Schematic diagram of a typical AGN structure showing the central BH, accretion disk, dusty torus, BLR and NLR. Image credit: Claudio Ricci (https://www.isdc.unige.ch/~ricci/Website/Active_Galactic_Nuclei.html).

ing as a tool for investigating properties such as BH mass and accretion rate (Czerny & Hryniewicz, 2010; Mandal et al., 2021).

- Torus : A structure composed of dust and gas that surrounds the MBH. It plays a crucial role in obscuring and regulating the flow of matter towards the central regions, impacting the observed characteristics of AGN emissions (Zhao et al., 2021).

- Narrow line region (NLR) : It consists of ionized gas clouds with lower velocity and density as compared to the BLR. NLR spans from the end of the torus opening till upto $\sim$ 1000 pc in that direction. It emits narrow spectral lines and serves as a valuable probe for understanding the ionization mechanisms and feedback processes in AGN environments.

- Other components : Such as central radio jets, hot corona and maser disks.

A schematic diagram of an AGN composition is shown in Fig.1.3

The Unified Model of AGN is a theoretical framework aimed at explaining the diverse properties observed in AGNs through a unified perspective. According to this model, the intrinsic

properties of AGNs remain constant, with the observed differences arising primarily from the orientation of the observer relative to the central engine (Urry & Padovani, 1995; Urry, 2003). This simply arises from the fact that the source emission from AGN can be scattered, absorbed or reflected while passing through the dusty and gaseous environments leading to observations in different wavelength bands depending on the line of sight (LOS). For example, when the LOS is perpendicular to the torus, the observer views the unobscured central regions (face-on) that allows a direct view to the central BH. AGNs with such orientation are known as Type I AGNs and they exhibit broad emission lines ($\geq$1000 km/s) in their spectra in the optical or UV wavelengths. This emission arises typically from high density gas ($\sim 10^9 \mathrm{cm}^{-3}$) in the BLR. On the other hand, if the observer's LOS intersects the dusty torus, obscuring the central region (edge-on), we call that a Type II AGN. Type II AGNs typically display only narrow emission lines ($\sim$ 300–1000 km/s) associated with low density ($\sim 10^2 - 10^6 \mathrm{cm}^{-3}$) ionized gas in the NLR since the torus or other obscuring structures prevent direct observation of the broad emission lines.

The Unified Model has successfully explained the similarities and differences observed in AGNs, providing a coherent framework for understanding their varied manifestations. While the model has been widely accepted, challenges remain, particularly in understanding the detailed structure and dynamics of the torus and the exact mechanisms responsible for the orientation-dependent observables.

An important characteristic of AGN to consider is the feedback. AGN feedback plays a significant role in regulating the growth and evolution of galaxies. It is now widely known that there is a correlation between a BH mass and the properties of the galaxies that hosts the BH in its center (Richstone et al., 1998; Magorrian et al., 1998; Ferrarese & Merritt, 2000; Gebhardt et al., 2000). BHs interact with their host galaxies by driving a fraction of their accreted energy and/or momentum back to its environment in the form of feedback (see e.g. Kormendy, 2001, for a comprehensive review).

More recently, according to Heckman & Best (2014), AGNs can be differentiated into "radiative mode" and "jet-mode". In the radiative mode, the AGN primarily affects its surroundings through the emission of radiation. The intense radiation generated by the accretion of material onto the central BH can influence the surrounding gas and dust, regulating star formation in the

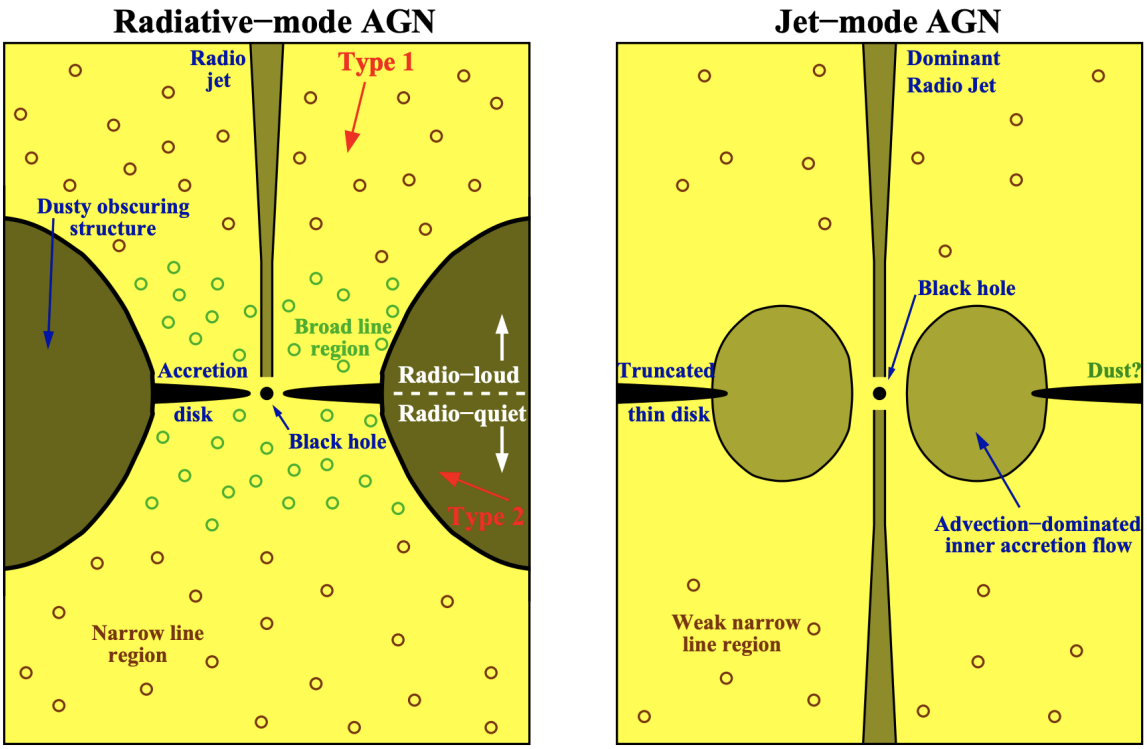

Figure 1.4: Schematic representations of the central power source of radiative-mode (left panel) and jet-mode AGN (right panel). Image taken from Heckman & Best (2014).

host galaxy. This group is commonly known as Seyfert galaxies or QSOs. The radiative mode of feedback is characterized by the radiative energy released during accretion processes, impacting the interstellar medium and influencing the galaxy's evolution. In the jet mode, the AGN's bulk kinetic energy is exerted through the launching of relativistic jets. These jets are powerful outflows of particles and magnetic fields accelerated near the central BH and arises from the accretion of matter or from the spin energy of the BH. The interaction of these jets with the surrounding medium can have profound effects, such as heating and energizing the interstellar gas, suppressing star formation, and even influencing the larger-scale structures of the host galaxy. Jet mode feedback is particularly relevant in galaxies where the AGN's activity is characterized by the presence of prominent radio jets and such AGN is commonly known as (low-excitation) radio galaxies. Fig. 1.4 shows the two modes of AGN for a general overview of the AGNs and further details can be also found in contemporary literature such as Krolik (1999); Osterbrock & Ferland (2006); Peterson (1997).

1.4.2 AGN spectra

According to Sanders et al. (1989), the SED of AGNs are composed of the following components:

- Big Blue Bump (BBB): The Big Blue Bump refers to the thermal emission from the accretion disk surrounding the MBH. This component dominates the optical to ultraviolet part of the spectrum (10 nm-0.3 μm) and is associated with the high temperatures of the accretion disk.

- X-ray Emission: The X-ray emission is thought to be primarily arising from the hot corona through inverse Compton scattering of optical/UV photons in the accretion disk. These high energy photons are typically associated with energies between 0.5–2 keV (Galeev et al., 1979).

- Infrared Emission: The infrared emission (2–300 μm) arises from the re-radiation of absorbed optical and ultraviolet radiation by dust in the vicinity of the central BH. This component is responsible for the infrared excess observed in AGN SEDs and is indicative of the presence of obscuring dust.

- BLR lines: The BLR is characterized by broad emission lines which result from the high-velocity motion of gas clouds in close proximity to the central BH (Peterson et al., 2004). These broad lines are broadened due to the Doppler effect, reflecting the intense gravitational forces near the black hole. Occasionally, absorption lines can be observed in the BLR spectra when intervening material absorbs specific wavelengths. These absorption features provide information about the composition and physical properties of the absorbing gas within the BLR.

- NLR lines: The NLR is characterized by narrow emission lines, including forbidden lines [6] such as O [III] and N [II]. These lines originate from lower-density, more extended gas

[6] "Forbidden lines" refer to spectral lines that arise from transitions between energy levels in atoms or ions that are typically not allowed by quantum mechanics. However, in certain astrophysical environments with high temperatures and densities, collisional and radiative processes can lead to the excitation and de-excitation of atoms or ions, resulting in the emission of these lines.

clouds farther from the central black hole. The narrow lines are typically associated with photoionization by the AGN's radiation (Dasyra et al., 2011). Absorption lines in the NLR are less commonly observed compared to emission lines. However, they can occur when intervening material absorbs specific wavelengths, providing information about the characteristics of the absorbing gas within the NLR (Ludwig et al., 2012).

- Radio emission: A significant component of the AGN spectra, radio emission originates from non-thermal processes associated with relativistic particles and magnetic fields. The primary mechanisms leading to radio emission in AGNs include synchrotron radiation and sometimes, in the case of powerful jets, inverse Compton scattering. Based on their strength of their radio emission relative to their overall energy output, AGNs can be categorised into radio-loud and radio-quiet AGNs Netzer (2013). Radio-loud AGNs are characterized by a significant and detectable radio emission compared to other types of electromagnetic radiation. These AGNs often exhibit powerful radio jets and lobes, indicating the presence of relativistic particles and strong magnetic fields. Radio-quiet AGNs, on the other hand, have relatively weak or undetectable radio emission compared to their overall energy output. The majority of AGNs fall into this category.

The BH nestled in the nuclei of the quasars can have masses of the order of $10^9 M_\odot$ (Mortlock et al., 2011; Bañados et al., 2018) and it is a theoretical challenge to explain such massive black hole growth in less than 10^9 years of cosmic time.

1.5 SMBH seeding

At $z \geq 6$, observations of quasars with BH masses of the order of $10^8 - 10^{10} M_\odot$ indicate that SMBHs must have been formed within the first Gyr of the Universe (Mortlock et al., 2011; Bañados et al., 2018). We can estimate the timescale of SMBH formation as following:

The bolometric luminosity of an accreting BH can be expressed in terms of the gas mass,

M_{gas} and the radiative efficiency ϵ_r[7] as:

$$L_{bol} = \epsilon_r c^2 \dot{M_{gas}} \tag{1.14}$$

A fraction of the accreted mass is radiated away. The remaining fraction can be written as:

$$\dot{M}_{BH} = \dot{M}_{gas}(1 - \epsilon_r). \tag{1.15}$$

From the above two equations, we can express the accretion rate as:

$$\dot{M_{BH}} = \left(\frac{1-\epsilon_r}{\epsilon_r}\right) \frac{L_{bol}}{c^2} \tag{1.16}$$

If we assume the mass accretion rate is limited by the Eddington luminosity, then we can substitute $L_{\rm bol}$ with the Eddington luminosity $L_{\rm Edd} = \frac{4\pi G c m_p M_{BH}}{\sigma_t}$ to get

$$\dot{M_{BH}} = \left(\frac{1-\epsilon_r}{\epsilon_r}\right) \left(\frac{4\pi G m_p}{c\sigma_t}\right) M_{BH}, \tag{1.17}$$

where G is the Newtonian gravitational constant, m_p is the mass of proton, c is the speed of light in vacuum and σ_t Thomson scattering cross section for electrons. Integrating the above equation with respect to time, we can show

$$M_{BH}(t) = M_{BH}(0) exp\left(\frac{1-\epsilon_r}{\epsilon_r}\right) \frac{t}{t_{Edd}} \tag{1.18}$$

where we can define t_{Edd} as:

$$t_{Edd} = \frac{4\pi G m_p}{c\sigma_t} = 0.45 Gyr \tag{1.19}$$

Using this estimation of BH formation timescale, we can check the feasibility of various progenitor masses of SMBHs.

It is assumed that SMBH grows through merging and gas accretion onto seeds whose masses are still uncertain. There are at least three scenarios that try to explain the formation of SMBH

[7]Radiative efficiency gives an estimate on the amount of matter converted to radiation.

progenitors (Sassano et al., 2021; Spinoso et al., 2022): (i) light seeds ($M_{\rm seed} \leq 10^2$ M$_\odot$) (ii) intermediate seeds (10^2 M$_\odot$ $< M_{\rm seed} \leq 10^4$ M$_\odot$) , and (iii) heavy seeds ($M_{\rm seed} > 10^4$ M$_\odot$). Below we describe in more details each of the aforementioned scenarios:

• Light seeds: Stellar mass black hole seeds, similar in mass to those detected by GW150914 (Abbott et al., 2016a,b), could possibly form as the remnants of the earliest Population III (Pop III) stars (Heger et al., 2003) at $z > 20$. Pop III stars are considered the first generation of stars in the Universe, formed from pristine, nearly primordial gas that lacked heavy elements. The conditions in the early universe, with a lack of metals could be conducive to the formation of massive stars that could potentially collapse directly into light seed BHs in mini DM halos (10^5 M$_\odot$ $\leq M_{\rm DM} \leq 10^7$ M$_\odot$) (see e.g Schaerer, 2002; Schneider, 2006). However, if we calculate the timescale of formation using Eq.1.18 with a typical light seed mass of ~ 100 M$_\odot$ and $\epsilon_r = 0.1$, we find it takes ~ 700 Myr to reach the mass of 10^9 M$_\odot$. This would mean in order for SMBHs to be formed from light seeds, a constant mass inflow at the highest possible rate will be required from the very beginning of the Universe, which would mean accretion rates higher than the Eddington limited accretion will be required. Super-Eddington or hyper-Eddington accretion rates are shown to be feasible by different semi-analytical models (Madau et al., 2014a; Pezzulli et al., 2016, 2017). However, it should be noted that for these models, continuous accretion at rates higher than the Eddington limit is not possible, especially for MBHs with masses less than 10^4 M$_\odot$ (Pacucci et al., 2015; Pacucci & Ferrara, 2015; Orofino et al., 2018). While the initial gas collapse is relatively well-understood, the subsequent evolution of fragmented disks, the interplay of competing accretion and outflow processes, mass loss through stellar winds and the long-term effects of stellar radiation on the surrounding environment are challenging to model resulting in significant uncertainties in the post-collapse phase (see e.g Omukai & Palla, 2003; Hosokawa et al., 2012). A more feasible situation could arise from considering SMBH seeds with higher mass. However, higher seed masses require specific sets of physical conditions to form (Agarwal et al., 2016; Latif et al., 2018) as we describe below.

• Intermediate seeds: An alternative scenario consists of very massive stars ($10^2 - 10^3$ $M_\odot$) which form in compact stellar clusters at $z \sim 10$ as a consequence of runaway stellar mergers (Ebisuzaki et al., 2001; Devecchi et al., 2012; Mapelli, 2016; Reinoso et al., 2018). In dense,

nuclear stellar clusters, the high stellar density and relative velocities increase the probability of stellar collisions. This in turn leads to the formation of a singular massive compact object that can later evolve to 10^8 $M_\odot$ SMBHs at $z \sim 7$ if Eddington-limited accretion is assumed.Intermediate seeds could also form in runaway GW driven stellar black hole coalescences in dense clusters with the condition of major gas inflows in the centre at z$\sim$10 (Davies et al., 2011; Lupi et al., 2014). The typical conditions for such intermediate seed formation include cooling of gas due to atomic hydrogen cooling, low metallicity of the gas ensuring stellar formation in the inner core of the halo, and an UV field to ensure dissociation of molecular hydrogen (Devecchi & Volonteri, 2009). The dynamics associated with infalling gas in this scenario could also have a significant effect (see e.g Chon & Omukai, 2020). Intermediate seeds are an important bridge between stellar mass BHs and BHs formed directly from collapse of dense gas. These seeds can trace the BH-bulge mass for dwarf galaxies and model the origins of Ultra Luminous X-ray sources (Greene et al., 2010; Reines & Volonteri, 2015; Mezcua et al., 2018; Barrows et al., 2019).

• Heavy seeds: Another proposed form of SMBH progenitor is the heavy seed model with typical mass $10^4 M_\odot \gtrsim M_{seed} \gtrsim 10^6 M_\odot$. These seeds are postulated to form directly from the collapse of primordial gas in a metal-free environment (Haehnelt, 1994; Loeb & Rasio, 1994; Eisenstein & Loeb, 1995; Silk & Rees, 1998; Shang et al., 2010; Johnson et al., 2012; Yue et al., 2013; Ferrara et al., 2014). The idea behind these seeds formation is that if the gas clouds at high redshifts contract such that no fragmentation occurs, then the direct collapse of these unfragmented gas clouds would give rise to the "heavy" seeds. Fragmentation can be avoided by the absence of metals in the gas clouds and suppression of molecular hydrogen formation which facilitates cooling. We expect low metallicities at such high redshifts of BH seed formation, however H_2 can easily form in high density gas clumps which could potentially be the birthplace of heavy seeds. There several proposed mechanisms that can delay the H_2 cooling and consequently, fragmentation and formation of stars in such environments. For example, the residual relative motion between gas and dark matter after cosmological recombination, known as baryonic streaming, offers a potential pathway to create an environment suitable for such Direct Collapse Black Hole (DCBH) formation. Streaming velocities exceeding twice the root-

mean-square velocity can significantly delay the initial star formation in dark matter halos. This delay, effectively hindering gas infall, allows halo virial temperatures to climb above 8000 K (Tanaka & Li, 2014). In rapidly growing halos, dynamical heating from accretion and mergers of protogalaxies can also counteract the limited cooling efficiency of molecular hydrogen postponing the formation of star-forming clouds (Yoshida et al., 2003; Lodato & Natarajan, 2006; Inayoshi & Omukai, 2012). H_2 can also be dissociated effectively through collisions which can be caused by high density shocks from cold inflow of accretion (Fernandez et al., 2014). Another major way for dissociation H_2 molecules is through the Lyman Werner (LW) UV photons[8]. LW radiation breaks down molecular hydrogen by exciting electrons to higher energy levels. At $z > 10$, the cosmic ionizing background is too low to be the source of the photodissociating photons. For local sources, active star formation could provide the required LW radiation, but star formation would also make the gas metal enriched, which must be avoided. So external local sources of UV radiation such as nearby star-forming galaxy companions are more probable causes of the LW background.

The critical value of the LW flux ,J_{21} required for DCBH formation is an active field of research (Habouzit et al., 2016; Agarwal et al., 2019). However, it is important to keep in mind that the minimum LW radiation required to account for all the seeds of SMBHs ubiquitously residing in galaxies in the present-day universe is too high (Shang et al., 2010; Wolcott-Green et al., 2011; Sugimura et al., 2014). But, this DCBH formation mechanism may be able to explain the existence of SMBHs at high redshifts and rarer in occurence. In the absence of metal and H_2 induced cooling, atomic cooling Halos (ACHs) [9] with a virial temperature $T_{vir} \geq 10^4 K$ with no molecular hydrogen are optimal candidates for producing DCBH seeds.

Other models on environments for DCBH formation have also been postulated. For example, another instance of heavy seed formation begins in low mass halos in the over-dense regions at high redshifts as a result of dynamic heating during fast mass growth of the low mass haloes (Wise et al., 2019; Regan et al., 2020). Alternatively, heavy nuclear inflows in galaxies which are gas-rich at lower redshift could also pose a plausible channel for formation of heavy seeds (Mayer et al., 2015). All these models show the possible effect of structural dynamics affecting

[8]LW radiation is typically associated with photons with energy between 11.2 eV and 13.6 eV
[9]In ACHs, gas cools down through atomic-hydrogen line cooling

SMBH formation rather than simply a critical LW flux.

The main difference in the formation of intermediate and heavy seeds is that for intermediate seeds, trace amounts of metals can facilitate fregmentation and stellar formation in the center of the halos where the stars then coalesce through runaway stellar mergers to form a very massive star (VMS). However for heavy seeds, condensation of the primordial gas with strictly no fragmentation is required to form to result in a DCBH.

Although many uncertainties remain associated to each of the scenarios discussed above (e.g. Volonteri et al., 2003; Koushiappas et al., 2004; Begelman et al., 2006; Lodato & Natarajan, 2006), the different nature of the black hole seeding should leave signatures in terms of merger rates, mass distribution, coalescence time, etc. These parameters can be determined by GW observations of merging black hole binaries.

1.6 SMBH merging and timescales

As discussed in Sec. 1.3, hierarchical structure formation is followed in the Universe with larger structures gradually forming from its smaller counterparts over time. When DM halos with central MBHs merge to form a larger halo, it may eventually lead to the coalescence of the central MBHs of the parent halos. However a limit in the mass-ratio of the parent halos exist for halo coalescence to take place. Numerical simulations show that below a critical mass ratio of DM halos (1:10), inefficient dynamical friction will result in the less massive halo to inspiral around the more massive halo for longer than the Hubble time or simply dissolve before the merger is effective (Taffoni et al., 2003).

A concise timeline of the evolution of MBHB merger would include the following steps:

- Mergers of galaxies containing MBH: Hierarchical structure formation dictates the formation of larger structures from the coalescence of smaller objects. As two galaxies containing MBHs merge, the MBHs may form a MBHB which may eventually merge depending on several factors.

- Pairing of MBHs due to dynamical friction and stellar hardening: when the galactic cores containing the MBHs, get close ($\sim$ hundreds of pc) to each other, the orbits of the MBHs

evolve due to dynamical friction against the surrounding gas and stars in the potential of the merged galaxy.

- Interaction of the MBHB with circumbinary gas disk and stellar scattering: At a distance of few pc, the MBHB evolves due to interaction with the circumbinary disk and/or stellar scattering. Once the final parsec limit is reached, the MBHB enters the GW regime.

- Coalescence due to GW emission: At this stage, the MBHB orbit shrinks due to emission of GWs. The intensity of the emitted GW increases as the MBHs get closer to each other. Finally, the MBHs merge to a single BH and settle down in the core of the newly formed galaxy.

When two galaxies collide, the bulges of the progenitor galaxies containing the MBHs interact dynamically to sink into the overall star-gas system of the resulting newly-formed galaxy. As the cores get closer to each other ($\sim$ few100 pc), the MBHs interact with their surroundings and gradually lose their stars. In the potential of the new galaxy, the separately spiraling MBHs then undergo orbital evolution due to loss of energy and momentum against the surrounding stars and gas by dynamical friction. At a distance of few parsecs between the MBHs, the orbital evolution of the holes slow down due to ejection of most of the interacting gas and stars from their surroundings which in turn shinks the orbit. At a certain stage, with most matter being ejected by the MBHB, further orbital shrinking stalls before the system reaches the scale of GW emission. The MBHB needs to jump this gap (known as the final parsec problem) from few pc to $\sim 10^{-2}$pc to eventually merge through gravitational radiation within the Hubble time. In the GW regime, the MBHs then evolve through the inspiral, merger and ringdown phases. For a concise review of this timeline we refer to Bogdanović et al. (2022).

We will now describe in the context of MBHs, the role of dynamical friction (DF) in gaseous and stellar environments.

Dynamical friction is a gravitational drag force experienced by a massive object moving through a field of lighter particles such as stars or gas. As the massive object moves through this field, it gravitationally interacts with the surrounding particles, causing a transfer of momentum and kinetic energy. This interaction leads to a deceleration of the massive object's motion, like

a frictional force acting in the opposite direction. If we consider the motion of a MBH in an isotropic field of stars, then the drag on the MBH can be expressed as (Binney & Tremaine, 2008):

$$\frac{d\mathbf{v}}{dt} = -\frac{4\pi \ \ln\Lambda \ G^2 \ M \ \rho}{\nu^3} \left[\mathrm{erf}(X) - \frac{2X}{\pi^{1/2}} exp(-X^2) \right] \mathbf{v} \tag{1.20}$$

where $M$is the mass of the MBH and **v** is the relative velocity with respect to the background stars, σ is the stellar velocity dispersion and ρ is the mass density of the stellar field. Here, X $\equiv \ \nu/\sqrt{2\sigma}$ and $ln\Lambda \ = \ ln(b_{max}/b_{min})$ is the Coulomb logarithm where b_{min} and b_{max} are the smallest and largest effective impact parameter, respectively. Due to multiple interactions with the stars, the MBH decelerates and this timescale can be written as:

$$t_{\mathrm{df}} = \frac{\nu}{d\nu/dt} \sim \frac{\nu^3}{4\pi G^2 M \rho}. \tag{1.21}$$

This means more massive MBH surrounded by more number of stars will sink in the potential of the merged galaxy faster as compared to MBHs of lower mass. The precise timescale of orbital decay in the stellar bulge depends on several characteristics such as the mass and velocity distribution of stars. We discuss this further in Sec. 6.3 where we define the dynamical friction timescales in the context of our simulations.

Along with the surrounding stars, gas also interacts with the MBHs which leads to their eventual pairing. According to Ostriker (1999), a massive perturber moving on a linear trajectory in a field of uniformly distributed gas experiences a drag force which can be expressed as a function of Mach number $\mathcal{M}\dashv \equiv \nu/c_s$ where ν is the relative speed of the perturber with respect to gas. If $\mathcal{M}\dashv$ » 1, then the drag force due to gas is effectively the same as a collisionless background with same density and velocity dispersion. If $\mathcal{M}\dashv$ < 1, then the drag force is lesser in gaseous medium as compared to a collisionless medium. And finally for $\mathcal{M}\dashv \sim 1$, drag force due to gas can be four times the drag force due to a collisionless medium.

Due to the effectiveness of gaseous drag as compared to a collisionless medium in pairing MBHs more efficiently, mergers in gas-rich environments have been studied extensively (see for eg. Mayer et al., 2015, for a review). Pairing helped by dynamical friction due to gas can be often faster than DF due stars (Berczik et al., 2006; Preto et al., 2011; Pfister et al., 2017) and

can bring the MBHs from the scale of galactic radii to a few hundred pc (Escala et al., 2004, 2005; Van Wassenhove et al., 2014). This efficiency of gaseous DF as compared to stellar DF is due to the capacity of gas to radiate energy as well as mutliple interactions with the MBH pair unlike the stars.

Due to the efficient stellar and gaseous dynamical interactions described above, the MBHs then form a gravitationally bound binary. MBHB formation is typically achieved when the mass of the stars and gas inside the orbit of MBHs are comparable to the total mass of the MBHB. At this stage, we can assume the MBHB to evolve through interactions with stars and gas in a spherically symmetric potential.

MBHBs can gradually harden through three-body interactions caused by nearby stars with the binary. If we assume an infinite supply of stars close to the MBHB and the MBHB mass is much larger than that of the interacting stars, then the binary hardening rate can be expressed as (Quinlan, 1996):

$$H = \frac{\sigma}{g\rho}\frac{d}{dt}\left(\frac{1}{a}\right) \tag{1.22}$$

This hardening rate usually ranges between 10 – 20 when the stellar speed at infinity can be assumed to be much less than the orbital speed of the MBHB. We later use this dimensionless parameter in Eq. 6.9.

We discuss further about the stellar hardening of the binary, particularly related to our simulations in Sec. 6.4.

Stellar hardening of the MBHBs due to three-body interactions with nearby stars is an efficient pathway of orbital evolution of MBHBs leading to the coalescence. We note, for the estimation of hardening rate, we assume an unlimited supply of nearby stars to interact with the binary. This assumption can be reasoned when the velocity dispersion of stars become comparable to the orbital speed of the MBHB, since under such condition, the stars are not completely ejected from the orbit and can come back for a subsequent interaction with the MBHB. When the orbital speed of the binary becomes quite larger than the velocity dispersion σ, in that case the stars, once they interact with MBHB, are promptly ejected from the orbit and the stellar population in the vicinity of the MBHB decreases. A continuous replenishment of the lost stars can

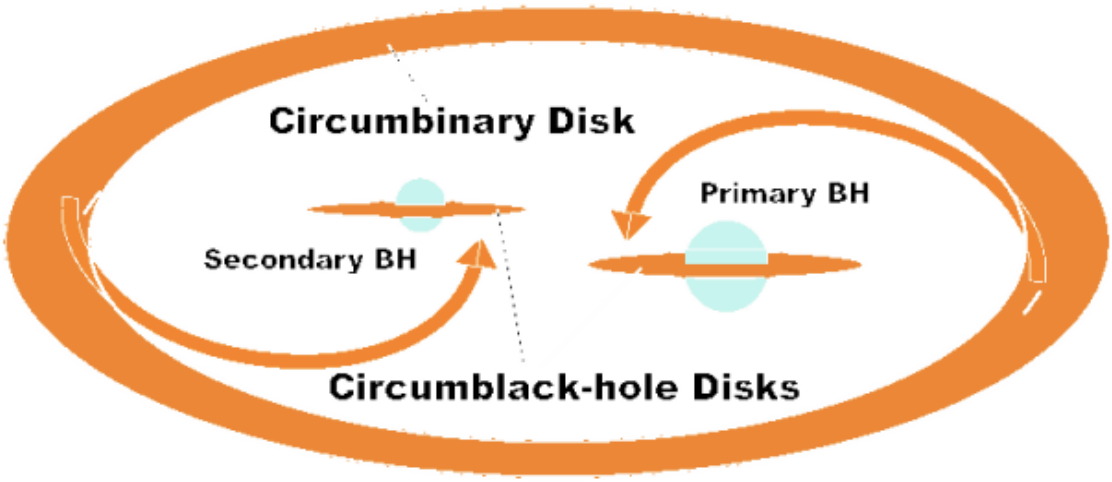

Figure 1.5: Schematic representation of a MBHB embedded in a circumbinary disk from which the gas is accreted into the binary around the circumblack-hole (mini) disks. Image taken from Hayasaki et al. (2007).

ensure the evolution of the MBHB (Bogdanović et al., 2022).

Numerous studies have been made about the evolution of MBHBs in gaseous environments at sub-parsec scales (see for eg. Armitage & Natarajan, 2005; Cuadra et al., 2009; Roedig et al., 2012; Tang et al., 2017, ,etc.). It is common to assume a scenario in which the MBHB is embedded in an optically thick and geometrically thin gas disk. These gas disks, similar to the accretion disks of AGN are radiatively efficient as a result of which could be a possible source of EM emission from inspiraling MBHBs (see also Sec. 2.6). The torque induced in a sufficiently cold circumbinary disk (CBD) by the MBHB during the gravitational pairing phase can result in an inner cavity which is less dense than the parent CBD (D'Orazio et al., 2016). Simulations show that around each MBH, a mini disk forms which accrete gas from the inner rim of the CBD (Bogdanović, 2014). A schematic representation of the circumbinary and circumblack-hole (mini) disks is shown in Fig. 1.5.

Due to accretion torques the orbit of the MBHB slowly decays and the inner edge of the circumbinary disk tracks the MBHB inward until the timescale for orbital decay due to gravitational radiation becomes shorter than the timescale on which angular momentum is transported outward through the disk (viscous timescale of the disk) (Milosavljević & Phinney, 2005; Armitage & Natarajan, 2005). In that case,the gravitational radiation causes the MBHB to rapidly lose energy and momentum and eventually coalesce.

Once the MBHB is close enough to each other through a combination of the processes dis-

cussed above, then GW emission primarily drives the binary to coalescence. The evolution in GW regime can be divided into three stages:

- **Inspiral :** This is the initial stage which is characterized by a gradual reduction of the orbital separation between the black holes. Initially, in the inspiral phase weak GW emission occurs due to large distance between the MBHs as a result of which, the orbital shrinking is very slow. At this stage, additional angular momentum loss can occur due to interactions with surrounding matter, such as other stars. As the MBHs come closer, the orbit decays more rapidly and GW emission gets more intense. The last stable complete orbit, or innermost stable circular orbit (ISCO), marks the boundary between the inspiral and the subsequent merger phase.

- **Merger :** Once the MBHs reach ISCO, the two BHs rapidly plunge into each other to merge into a new, single MBH. At this stage, the GW emission peaks.

- **Ringdown :** Right after the merger, the resulting single MBH undergoes a "ringing" phenomenon which is damped in the ringdown stage. This stage starts as the MBHs approach each other within the photon sphere, where most GWs head toward the event horizon of the MBHs and the GWs which can manage to escape have significantly lower amplitudes. Remotely detected GWs exhibit oscillations with rapidly diminishing amplitudes during the ringdown, reflecting the aftermath of the merger event.

The need to classify the GW regime in the above stages is mainly due to the different approaches needed to study each evolutionary phase. For example, semi-analytical models involving post-Newtonian technique and perturbation method can be used to analyse the inspiral and ringdown phases. However, the merger phase is extremely complicated and can only be effectively modelled through numerical models.

We have shown the three stages of MBHB evolution in the GW regime in Fig. 1.6.

Various scenarios at different scales of MBHB formation and evolution exist and a complete picture can be derived through GW detections as well as EM signatures associated with MBHB mergers.

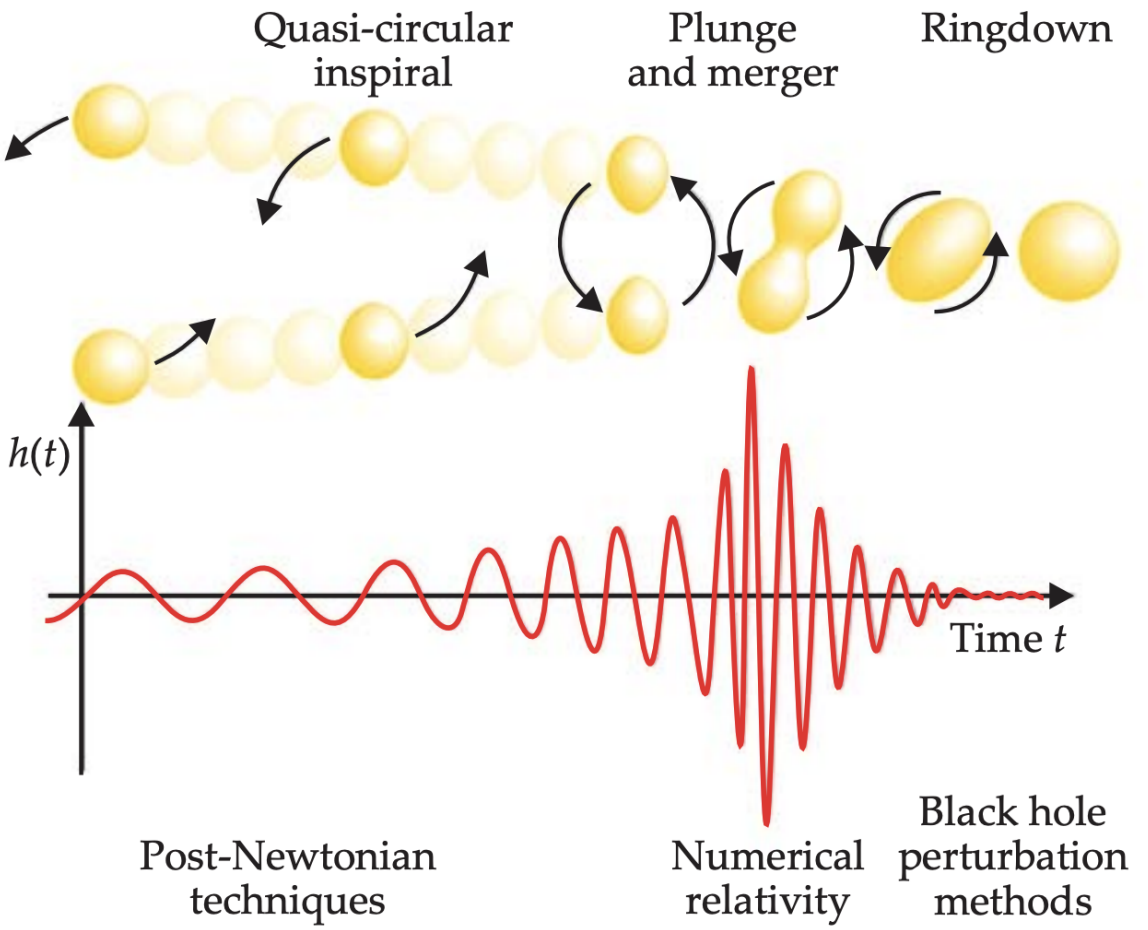

Figure 1.6: GW emission at different stages of MBHB evolution : inspiral, merger and ringdown. Image taken from Baumgarte & Shapiro (2011).

Gravitational waves 2

2.1 Introduction

The discovery of GWs (Abbott et al., 2016a,c) marked a new milestone in observational astrophysics. GWs arising from the acceleration of massive objects, carry information about various astrophysical objects such as black holes (stellar, supermassive), neutron stars, white dwarves.

In this chapter, we provide a brief overview of the gravitational wave astronomy particularly, in the context of MBHBs. We begin with a short synopsis of general theory of relativity in Sec. 2.2 and then describe some useful expressions for GW emission from MBHB systems in Sec. 2.3 and Sec. 2.4. After this we discuss the general principles behind different GW detectors in Sec. 2.5 and conclude this chapter in Sec. 2.6 with a discussion on the possibility of detecting EM signals from merging MBHs.

2.2 General theory of relativity overview

General Relativity (GR) is a geometrical theory of gravitation (see also the previous brief introduction in Sec. 1.2.4). Unlike Newton's classical theory, GR does not treat gravitation as a force, but as a manifestation of the curvature of the spacetime. This curvature determines the trajectory that free-falling bodies follow and it is directly related to the distribution of energy and momentum within the spacetime. This relation is described by Einstein's field equations (also

see Eq. 1.6, but with the cosmological constant Λ, which can be omitted in this context):

$$G_{\mu\nu} = \frac{8\pi G}{c^4} T_{\mu\nu} \ . \tag{2.1}$$

where $G_{\mu\nu}$ is the Einstein tensor and $T_{\mu\nu}$ is the stress-energy tensor [1]. The former describes the curvature, while the latter represents the energy and momentum content of the spacetime. In the following paragraphs, we discuss Einstein's field equations in more detail to unveil the most important and relevant aspects of this theory.

First, let us consider the right-hand side of equation 2.1, which essentially encapsulates information about the geometry of the spacetime. In GR, spacetime is represented by four-dimensional manifolds. The notion of distance for manifolds (typically referred to as *interval* in case of four-dimensional spacetime) is defined by the metric. The spacetime interval can be expressed from the line element, which can be given for a specific manifold as:

$$ds^2 = g_{\mu\nu} dx^\mu dx^\nu \tag{2.2}$$

where $g_{\mu\nu}$ is the metric, represented by a (4,4) tensor and dx^μ is the infinitesimal coordinate displacement. Integrating equation 2.2 yields the spacetime interval between any two events[2]. To derive such an expression, let us consider a timelike spacetime worldline $z^\rho(\tau)$, parameterised with proper time τ, which is the time measured by a clock carried along the given trajectory. The vector $u^\rho \equiv dz^\rho/d\tau$ is the tangent to the spacetime trajectory. If the timelike worldline extends from event A to event B, then the total spacetime interval between these events can be expressed as:

$$s = \int_{\mathrm{A}}^{\mathrm{B}} d\tau \sqrt{g_{\mu\nu} u^\mu u^\nu} \ . \tag{2.3}$$

Applying the principle of least action on Equation 2.3, that is, taking the extremal value of of s

[1] In this chapter, we use tensor notation, in which the different components of tensors and vectors are noted by Greek letters in the sub- and superscript. Each index can take integer values between 0 and 3. The zeroth index is for the time, while the rest is for the spatial components. We also assume Einstein's summation convention for repeated indices. For example, $v_\mu v^\mu = \sum_{\mu=0}^{3} v_\mu$ (see e.g. Carroll, 2004; M. P. Hobson, 2006). We also use the abbreviated partial derivative, $\partial_\mu \equiv \frac{\partial}{\partial x^\mu}$.

[2] In the context of GR, an event refers to a point in the spacetime.

(i.e. $\delta s = 0$), yields:

$$\frac{du^\mu}{d\tau} + \Gamma^\mu{}_{\nu\gamma} u^\nu u^\gamma = 0 \ . \tag{2.4}$$

where $\Gamma^\mu{}_{\nu\gamma}$ are the Christoffel symbols and they can be expressed in terms of the metric:

$$\Gamma^\mu{}_{\nu\gamma} = \frac{1}{2} g^{\mu\rho} \left(\partial_\gamma g_{\rho\nu} + \partial_\nu g_{\gamma\rho} - \partial_\rho g_{\nu\gamma} \right) \ . \tag{2.5}$$

Equation 2.4 is the so-called geodesic equation and it describes the path of free-falling bodies in a spacetime with a given metric. Its solution is a worldline, commonly referred to as a *geodesic*, which can be regarded as the generalisation of a straight line in a curved spacetime. Indeed, in case of a flat spacetime, the Christoffel symbols vanish, and therefore equation 2.4 reduces to $d^2x^\mu/d\tau = 0$, which represents an equation for a straight line, as expected.

When spacetime is curved, closeby geodesics diverge from each other. If ξ^μ is the displacement between the geodesics due to curved spacetime, then the divergence rate can be written as:

$$\frac{D^2 \xi^\mu}{d\tau^2} = R^\mu{}_{\nu\gamma\delta} u^\nu u^\gamma \xi^\delta \ , \tag{2.6}$$

where, $R^\mu{}_{\nu\gamma\delta}$ is the Riemann curvature tensor. $R^\mu{}_{\nu\gamma\delta}$ determines the change in a vector when parallel transported in an infinitesimal loop, and thereby it essentially quantifies the curvature of the spacetime. It can be expressed as:

$$R^\mu{}_{\nu\gamma\delta} = \partial_\gamma \Gamma^\mu{}_{\nu\delta} - \partial_\delta \Gamma^\mu{}_{\nu\gamma} + \Gamma^\mu{}_{\rho\gamma} \Gamma^\rho{}_{\nu\delta} - \Gamma^\mu{}_{\rho\delta} \Gamma^\rho{}_{\nu\gamma} \ . \tag{2.7}$$

The Einstein tensor is related to the Riemant curvature tensor as:

$$G_{\mu\nu} = R_{\mu\nu} - \frac{1}{2} g_{\mu\nu} R \ , \tag{2.8}$$

where $R_{\mu\nu} = R^\rho{}_{\mu\rho\nu}$ is the so-called Ricci tensor, and $R = R^\rho{}_\rho$ is the Ricci scalar. An important property of the Einstein tensor is: $\nabla^\mu G_{\mu\nu} = 0$. This can be shown from contracting the so-called Bianchi identity, which states $\nabla_\gamma R_{\mu\nu\rho\sigma} + \nabla_\nu R_{\gamma\mu\rho\sigma} + \nabla_\mu R_{\nu\gamma\rho\sigma} = 0$.

Now, let us consider the right-hand side of Einstein's field equations. The stress-energy

tensor has the following components:

$$T^{00} \equiv \text{Local energy density} \tag{2.9}$$

$$T^{0i} \equiv \text{Local energy flux (times } c\text{)} \tag{2.10}$$

$$T^{i0} \equiv \text{Local momentum density (times } c\text{)} \ ^{3} \tag{2.11}$$

$$T^{ij} \equiv \text{Local momentum flux (times } c^2\text{); } T^{ii} \text{ acts as pressure.} \tag{2.12}$$

Here, the indices with Latin letters (i.e. i and j) refer only to the spatial components. The local conservation of energy and momentum takes the following form:

$$\nabla_\rho T^{\rho\sigma} = 0 \ . \tag{2.13}$$

To show that $G_{\mu\nu}$ equals to $8\pi G/c^4 T_{\mu\nu}$ or in other words to derive Eq. 2.1, one could apply the principle of least action (see e.g. Chapter 4 in Carroll, 2004, for more details). We omit the derivation here, but we highlight a few important aspects of the Einstein field equations. First, as shown by Eq. 2.5 and 2.7, the field equations can be considered as a second-order, non-linear partial differential equations for the metric tensor field $g_{\mu\nu}$. Secondly, the field equations represent 6 independent equations. This is because both sides of Eq. 2.1 consist of symmetric two-index tensors, which decrease the degree of freedom from 16 to 10. Furthermore, Bianchi's identity introduce four additional constraints. Finally, in the weak field, low velocity, time-independent metric limit, Einstein's equations reduce to the Newton's law of gravitation:

$$\nabla^2 \Phi = 4\pi G\rho, \tag{2.14}$$

where $\Phi = -GM/r$, i.e the gravitational potential according to Newton's law of gravitation. This can be shown by considering the two following simplifications. First, in the weak field, the metric can be written as:

$$g_{\mu\nu} = \eta_{\mu\nu} + h_{\mu\nu} \ , \tag{2.15}$$

where $\eta_{\mu\nu}$ is the Minkowskian metric of flat spacetime (i.e. diag(-1,1,1,1)) and $h_{\mu\nu}$ is a weak

pertrubation to the flat spacetime (i.e. $|h_{\mu\nu}| \ll 1$). Therefore, any term that is second or higher order in $h_{\mu\nu}$ can be negelected. The second simplification is to only consider the (0,0) component of the field equations, as in the low velocity limit T_{00} is much larger than any of the other components of the stress-energy tensor. In this case, the (0,0) component of Einstein's field equation can be re-expressed as:

$$R_{00} = -\frac{4\pi G}{c^4} T_{00}. \tag{2.16}$$

Furthermore, R_{00} can be directly determined from the metric (i.e. $g_{00} = 1 + h_{00}$) via Eq 2.7, which gives:

$$\nabla^2 h_{00} = -4\pi G T_{00}. \tag{2.17}$$

Since T_{00} in the weak-field limit is simply the mass density ρ, Eq. 2.17 is equivalent to 2.14, as long as $h_{00} = -2\Phi$.

2.3 Linearised General Relativity and Gravitational Waves

Einstein's equations are non-linear, and therefore, it is notoriously hard to find their exact, analytical solutions. However, GWs typically induce very small changes to the background spacetime. Consequently, GWs far away from the source can be described as small perturbations to the flat, Minkowskian spacetime metric. This scenario can therefore be accurately described by the linearised version of Einstein's field equations (Eq. 2.1), which we are going to introduce below.

Let us consider a metric, which only slightly deviates from the flat spacetime due to the weak perturbations induced by GWs (see also Eq. 2.15):

$$g_{\mu\nu} = \eta_{\mu\nu} + h_{\mu\nu} \ , \tag{2.18}$$

where $h_{\mu\nu}$ are typically referred to as metric perturbation (Flanagan & Hughes, 2005) and $|h_{\mu\nu}| \ll 1$. Similarly to the treatment of the weak-field in section 2.3, we neglect any terms

that are second or higher order in $h_{\mu\nu}$. With this simplification, it can be shown that:

$$g^{\mu\nu} = \eta^{\mu\nu} - h^{\mu\nu}, \tag{2.19}$$

where $h^{\mu\nu} = \eta^{\mu\sigma}\eta^{\nu\rho}h_{\sigma\rho}$. The linearised Einstein tensor becomes:

$$G_{\mu\nu} = \frac{1}{2}\left(\partial_\mu\partial^\rho\bar{h}_{\rho\nu} + \partial_\nu\partial^\rho\bar{h}_{\rho\mu} - \Box\bar{h}_{\mu\nu} - \eta_{\mu\nu}\partial^\rho\partial^\sigma h_{\rho\sigma}\right) , \tag{2.20}$$

where we introduced the trace-reversed metric perturbation: $\bar{h}_{\mu\nu} \equiv h_{\mu\nu} - 1/2\eta_{\mu\nu}h$ (see e.g. Carroll, 2004; Maggiore, 2007). Furthermore, $h \equiv \eta^{\mu\nu}h_{\mu\nu}$ is the trace of $h_{\mu\nu}$, and $\Box \equiv \eta^{\mu\nu}\partial_\mu\partial_\nu$ is the flat spacetime wave operator.

Linearised general relativity is invariant under two kinds of coordinate transformations; global Lorentz transformations and infinitesimal general coordinate transformations (Maggiore, 2007). The latter, which we are going to use to recast the linearised Einstein's equations in a simpler form, is defined by the coordinate change of $x^\mu \rightarrow x^\mu + \xi^\mu$ (noting $\partial_\rho\xi^\mu \ll 1$). Under this coordinate transformation law, the metric perturbation components will change as (e.g. Carroll, 2004; Maggiore, 2007):

$$\bar{h}_{\rho\sigma} \rightarrow \bar{h}'_{\rho\sigma} = \bar{h}_{\rho\sigma} - (\partial_\rho\xi_\sigma + \partial_\sigma\xi_\rho \ - \eta_{\rho\sigma}\partial_\mu\xi^\mu). \tag{2.21}$$

One can choose a coordinate system, in which:

$$\partial^\rho\bar{h}_{\rho\sigma} = 0. \tag{2.22}$$

Such a gauge transformation is possible, if ξ^μ is chosen, such that $\Box\eta_\mu = \partial^\nu\bar{h}_{\nu\mu}$ is satisfied. This can be understood from the transformation law shown in Eq. 2.21, which implies $\partial^\rho\bar{h}'_{\rho\sigma} = \partial^\rho\bar{h}_{\rho\sigma} - \Box\eta_\sigma$. This transformation is called the "Lorenz gauge", and in these coordinates, the Einstein's field equations (Eq. 2.1) take the form of wave equations:

$$\Box\bar{h}_{\mu\nu} = -\frac{16\pi G}{c^4}T_{\mu\nu} \ . \tag{2.23}$$

That is, in the Lorentz gauge, all components of the metric perturbation exhibit wave-like behaviour. This, however, does not mean that all components indeed describe physical oscillations of distortions in the spacetime. Many of these are spurious modes, exhibiting non-physical, non-radiative gauge-dependent wave behaviour only due to the specific choice of the coordinate system (defined by the Lorentz gauge).

If we consider globally vacuum spacetimes (i.e. in which $T_{\mu\nu} = 0$), there is an additional gauge condition that can be applied on top of the Lorentz gauge, which fixes all the local gauge freedom (and does not ruin the condition $\partial^\rho \bar{h}_{\rho\sigma} = 0$). In this case, only the gauge-independent, wave-like solution components of the metric perturbations remain, which express the radiative degrees of freedom in spacetime. Only these metric perturbation components describe the physical gravitational waves [4]. This particular gauge condition is called the traceless transverse gauge (TT-gauge) and this transformation can be achieved by choosing η^μ, such that $\Box\eta_\mu = 0$. This has three important implications for the metric perturbations, which can be expressed as:

$$\delta_{ij} h_{ij}^{\mathrm{TT}} = 0 \qquad \partial_i h_{ij}^{\mathrm{TT}} = 0 \qquad h^{0\mu} = 0 \tag{2.24}$$

This tells us that GWs are transverse and the metric perturbation describing GWs are traceless. The TT gauge reduces the degrees of freedom of the metric perturbation to two.

If we have a plane wave solution for h_{ij}, propagating in the direction of $\mathbf{n}$, given in the Lorentz gauge, the TT gauge form can easily be found with the help of the so-called projection tensor:

$$P_{ij} = \delta_{ij} - n_i n_j. \tag{2.25}$$

From this, the transverse and traceless metric perturbation can be obtained as (Maggiore, 2007):

$$h_{ij}^{\mathrm{TT}} = h_{kl} \left(P_{ki} P_{lj} - \frac{1}{2} P_{kl} P_{ij} \right). \tag{2.26}$$

If the coordinate system is fixed such that z-axis points in the direction of the propagation of GWs (i.e. in the direction of $\mathbf{n}$), then the metric perturbations describing the GWs can be

[4] Note, however, that in the non-vacuum solution, some components of the metric perturbation could also describe non-radiative degrees of freedom due to the non-zero stress-energy tensor. However, these generally will not exhibit wave-like behaviour.

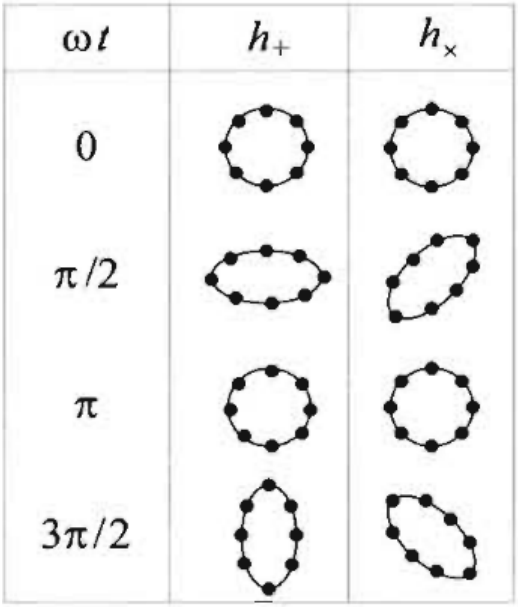

Figure 2.1: The effect of two polarizations of GWs on a ring of test masses. Figure from Maggiore (2007).

written in a matrix form as (Maggiore, 2007):

$$h_{ij}^{TT} = \begin{bmatrix} h_+ & h_\times & 0 \\ h_\times & -h_+ & 0 \\ 0 & 0 & 0 \end{bmatrix} cos\left[\omega(t - z/c)\right], \tag{2.27}$$

where the independent amplitude tensor components have been denoted as h_+ and $h_\times$ referring to plus and cross polarizations, furthermore, ω is the angular frequency of the GW. In Fig. 2.1, we show how a ring of test masses are deformed under the effect of a passing GW with only the $+$ or only the $\times$ polarisation as a function of time.

In the following paragraphs, we describe how to calculate the GWs generated by a source characterised by a given stress energy tensor $T_{\mu\nu}$. If we consider a source point $\mathbf{x}'$ and a field point $\mathbf{x}$ for which $\bar{h}_{\mu\nu}$ is calculated, then the Eq. 2.23 can be solved with Green's function (M. P. Hobson, 2006):

$$\bar{h}_{\mu\nu}(\mathbf{x}, t) = \frac{4G}{c^4} \int \frac{T_{\mu\nu}(\mathbf{x}', t - |\mathbf{x} - \mathbf{x}'|/c)}{|\mathbf{x} - \mathbf{x}'|} d^3x' \,, \tag{2.28}$$

where we integrate the coordinates over the spatial extent of the source. The solution at t de-

pends on what happens to the source at the so-called retarded time ($t_{\rm ret} \equiv t - |\mathbf{x} - \mathbf{x}'|/c$) and causal propagation of information is considered from $\mathbf{x}'$ to $\mathbf{x}$. Considering only the the spatial component of Eq. 2.28, and assuming the source to be far away (i.e. $|\mathbf{x} - \mathbf{x}'| \simeq R$) we get:

$$\bar{h}_{ij} \simeq \frac{4}{R}\frac{G}{c^4}\int T_{ij}(t_{\rm ret}, \mathbf{x}')d^3x' \ . \tag{2.29}$$

The local conservation of energy and momentum $\nabla^\mu T_{\mu\nu} = 0$ becomes $\partial^\mu T_{\mu\nu} = 0$ in the linearised theory. Therefore, in the chosen coordinates, we can write:

$$\partial^t T_{tt} + \partial^j T_{jt} = 0 \ , \qquad \partial^t T_{tj} + \partial^i T_{ij} = 0 \ . \tag{2.30}$$

Combining the above and noting $\partial^t = -\partial_t$; and using integration by parts we can express

$$\int T_{ij}(t, \mathbf{x}')\, d^3x' = \frac{1}{2}\frac{d^2}{dt^2}\int x^{i'} x^{j'} T_{tt}(t, \mathbf{x}')\, d^3x' \equiv \frac{1}{2}\frac{d^2}{dt^2} I_{ij}(t) \ . \tag{2.31}$$

where we introduced the *quadrupole moment* I_{ij}. The transverse-traceless waveform then becomes:

$$h_{ij}^{\rm TT} = \frac{2}{R}\frac{G}{c^4}\frac{d^2 I_{kl}}{dt^2}\left(P_{ik}P_{jl} - \frac{1}{2}P_{kl}P_{ij}\right) \ . \tag{2.32}$$

It can be shown (M. P. Hobson, 2006) that the trace $I \equiv I_{ii}$ does not contribute to Eq. 2.32. We hence typically use the reduced quadrupole moment as:

$$M_{ij} = I_{ij} - \frac{1}{3}\delta_{ij} I \ , \tag{2.33}$$

therefore, Eq. 2.32 can be re-expressed in terms of the reduced quadrupole, as:

$$h_{ij}^{\rm TT} = \frac{2}{R}\frac{G}{c^4}\frac{d^2 M_{kl}}{dt^2}\left(P_{ik}P_{jl} - \frac{1}{2}P_{kl}P_{ij}\right) \ . \tag{2.34}$$

This is known as the *quadrupole formula* for GW emission.

Using equation 2.34, the plus and the cross polarization components of the GW in a coordinate system for which the z-axis is pointing in the direction of propagation of the GW (i.e. in a coordinate system, in which the propagation vector has the form of $\mathbf{n} = [0, 0, 1]$) can be given

as:

$$h_+ = \frac{G}{c^4 r}(\ddot{M}_{11} - \ddot{M}_{22})$$
$$h_\times = \frac{2G}{c^4 r}\ddot{M}_{12}. \tag{2.35}$$

where we have introduced the notation $d^2 M_{\rm ij}/dt^2 = \ddot{M}_{\rm ij}$. The equation above can be expressed in an arbitrary coordinate system:

$$h_+(t;\theta,\phi) = \frac{G}{c^4 r}\Big(\ddot{M}_{11}(\cos^2\phi - \sin^2\phi\cos^2\theta) + \ddot{\rm M}_{22}(\sin^2\phi - \cos^2\phi\cos^2\theta) - \ddot{M}_{33}\sin^2\theta - \ddot{\rm M}_{12}\sin 2\phi(1+\cos^2\theta) + \ddot{\rm M}_{13}\sin\phi\sin 2\theta + \ddot{\rm M}_{23}\cos\phi\sin 2\theta\Big) \tag{2.36}$$

$$h_+(t;\theta,\phi) = \frac{G}{c^4 r}\Big((\ddot{M}_{11} - \ddot{M}_{22})\sin 2\phi\cos\theta + \ddot{\rm M}_{12}\cos 2\phi\cos\theta - 2\ddot{M}_{13}\cos\phi\sin\theta - \ddot{\rm M}_{23}\sin\phi\sin\theta\Big), \tag{2.37}$$

,

where the two angles (ϕ and θ) describe the orientation of the arbitrarily chose coordinate system with respect to the the coordinate system aligned with the propagation of the GW. The relationship between the two coordinate systems can be expressed in terms of two subsequent rotations. If we assume that the axes of the coordinate system aligned with the propagation of GW are (x, y, z), then the arbitrary coordinate system is obtained by first rotating the z-axis by ϕ, and then rotating the new x-axis by θ. In this respect ϕ can be considered as the azimuthal and θ the latitude angle, as often defined in the context of spherical coordinate systems. If the arbitrary coordinate system is aligned with a GW detector, then (θ, ϕ) essentially expresses the sky location of the incoming GW signal.

2.4 GWs from binary systems

In this section, we use the formalism derived in Section 2.3 to derive the GWs arising from a merging compact binary. In this section, we will closely follow the formalism of Hughes (2009)

and Maggiore (2007). We consider a binary composed of two compact objects (MBHs, in our case) with masses of m_1 and m_2, in a circular orbit, with an orbital separation of R. We assume that binary components can be modelled as point masses. As the members of the binary are moving in a circular orbit, the GWs emitted carry away energy from the binary and thus its orbit will shrink until the system merges. In the early phase of this process, the change in the orbit is small, such that the orbit can be regarded quasi-Keplerian. When such an assumption is valid, we say that the binary is *inspiralling*. From the point of view of this thesis, this is perhaps the most important phase for merging compact objects, as the majority of the signal-to-noise ratio is typically contributed from the inspiral phase, and the emitted inspiral GW signal allows for the most important parameters of the binary system to be inferred.

In the weak-field, low velocity approximation, it is possible to derive the strain characterising the GWs emitted by the binary using the mass quadrupole formula introduced in Eq. 2.34. For a binary with point masses the stress energy tensor is (see e.g. Maggiore, 2007):

$$T^{\mu\nu} = \sum_A \frac{p_A^\mu p_A^\nu}{\gamma_A m_A} \delta^{(3)}(\mathbf{x}(t) - \mathbf{x}_A(t)), \tag{2.38}$$

where the sum is over the components of the binary, γ_A is the Lorentz factor, m_A is the mass of the binary component and $\delta^{(3)}$ is a three-dimensional delta function. From Eq. 2.38, it follows that the second mass moment of the binary is $M^{ij} = \mu x_0^i(t) x_0^j(t)$. Given that the coordinates of the binary can be given as $\mathbf{x}(t) = [R\cos(\omega_s t + \pi/2), \sin(\omega_s + \pi/2), 0]$, where ω_s is the angular frequency of the binary, the only non-vanishing terms of the second derivatives of the reduced quadrupole moments are:

$$\begin{aligned} \ddot{M}_{11} = -\ddot{M}_{22} &= 2\mu R^2 \omega_s^2 \cos(2\omega_s t) \\ \ddot{M}_{12} &= 2\mu R^2 \omega_s^2 \sin(2\omega_s t), \end{aligned} \tag{2.39}$$

Substituting these expressions into Eq. 2.37, we get the plus and cross polarizations quadrupole

terms for an inspiralling binary:

$$h_+ = -\frac{2G\mathcal{M}_c}{c^2 r}\left(\frac{\pi G\mathcal{M} f_{\rm GW}}{c^3}\right)^{2/3}(1+\cos^2\iota)\cos(2\pi f_{\rm GW} t_{\rm ret}+2\phi)\ ,$$
$$h_\times = -\frac{4G\mathcal{M}_c}{c^2 r}\left(\frac{\pi G\mathcal{M} f_{\rm GW}}{c^3}\right)^{2/3}\cos\iota\sin(2\pi f_{\rm GW} t_{\rm ret}+2\phi))\ , \quad (2.40)$$

where r is the distance between the observer and the source emitting GWs, $t_{\rm ret}$ is the retarded time, $f_{\rm GW}$ is the frequency of the GW signal and it is twice of the orbital frequency, i.e. $f_{\rm GW} = 2f_{\rm s}$, where $f_{\rm s} = \omega_{\rm s}/2\pi$ and since we assume quasi-Keplerian orbits, $\omega_{\rm s} = (GM_t/R^3)^{1/2}$, where $M_t = m_1 + m_2$ is the total mass of the binary. We have also introduced ι, which is the inclination angle defined as the angle between the normal to the orbit and line-of-sight of the observer. Furthermore, $\mathcal{M}_c$ is the *chirp mass* of the binary and it is defined as:

$$\mathcal{M}_c = \mu^{3/5} M_t^{2/5} = \eta^{3/5} M_t, \quad (2.41)$$

where $\mu = m_1\, m_2/M_t$ is the reduced mass and $\eta = m_1\, m_2/M_t^2$ is the symmetrical mass ratio.

However, if one takes into account the long-term evolution of the inspiralling binary, then one has to account for the significant change in the orbit over long timescales. In this case, the the coordinates of the binary can be given as $\mathbf{x} = [R(t)\cos(\Phi_{\rm N}(t)/2), {\rm R(t)sin}(\Phi_{\rm N}(t)/2), 0]$, where $\Phi_N(t)$:

$$\Phi_N(t) = 2\int \omega_{\rm s}\, dt = \Phi_c - \left[\frac{c^3(t_c - t)}{5G\mathcal{M}_c}\right]^{5/8}\ , \quad (2.42)$$

where Φ_c is the phase of the binary at the moment of coalescence. In this case, Eq. 2.40 can be rewritten as:

$$h_+ = -\frac{2G\mathcal{M}_c}{c^2 d_L}\left(\frac{\pi G\mathcal{M} f_{\rm GW}(t)}{c^3}\right)^{2/3}(1+\cos^2\iota)\cos(2\Phi_N(t))\ ,$$
$$h_\times = -\frac{4G\mathcal{M}_c}{c^2 d_L}\left(\frac{\pi G\mathcal{M} f_{\rm GW}(t)}{c^3}\right)^{2/3}\cos\iota\sin(\Phi_N(t))\ , \quad (2.43)$$

We note that we replaced the distance from the source r to the luminosity distance d_L (see section 4.1.4 of Maggiore, 2007, why this is a proper treatment for GWs travelling at cosmological distances).

Eq. 2.43 shows us that the amplitude of the GW singal and its frequency $f_{\rm GW}$ will increase as the binary is inspiralling. Below, we will show the qualitative behaviour of these features. The orbital energy associated with the binary at its rest (source) frame can be expressed as

$$E^{\rm r} = \frac{1}{2}m_1 v_1^2 + \frac{1}{2}m_2 v_2^2 - \frac{G m_1 m_2}{R} = -\frac{G\mu M_t}{2R} \ , \tag{2.44}$$

where v_1, v_2 are the velocities of the binary components. Far from the source, the energy radiated by the GWs from the binary in a circular orbit can be expressed in terms of R and $\omega_{\rm s}$ (Peters & Mathews, 1963):

$$\frac{dE}{dt}^{\rm GW} = -\frac{32}{5}\frac{G}{c^5}\mu^2 R^4 \omega_{\rm s}^6 \ . \tag{2.45}$$

If we assume that the binary orbit evolves only due to the emission of GW (which is a valid assumption in the GW regime of MBHB lifecycle, see section 1.6), then

$$\frac{dE^{\rm r}}{dt} + \frac{dE}{dt}^{\rm GW} = 0 \ . \tag{2.46}$$

The evolution of the binary orbit, $dE^{\rm r}/dt$ can be considered to be occurring in small intervals dt in increments dR and can be written using the chain rule as:

$$\frac{dE^{\rm r}}{dt} = \frac{dE^{\rm r}}{dR}\frac{dR}{dt} \ . \tag{2.47}$$

From Eqs. (2.45), (2.46), and (2.47), we can express the distance of separation of the two MBHs as a function of time:

$$R(t) = \left[\frac{256 G^3 \mu M_t^2 (t_c - t)}{5c^5}\right]^{1/4} \ , \tag{2.48}$$

and the evolution of the orbital evolution during the inspiral phase:

$$\omega_{\rm r}({\rm s}) = \left[\frac{5{\rm c}^5}{256({\rm G}\mathcal{M}_{\rm c})^{5/3}({\rm t_c} - {\rm t})}\right]^{3/8} \ . \tag{2.49}$$

The chirp mass determines the rate at which a binary "chirps" or evolves in frequency. If we assume the binary to merge at a separation $R = 0$, the time at merging can be written as t_c. In

this case, the time required by a circular binary to coalesce due to the emission of GW waves is:

$$t_{\rm coal} = \frac{5}{256}\frac{c^5 R^4}{G^3 M_t^2 \mu}. \tag{2.50}$$

In most cases, it is more realistic to assume that the binary merges at $R = 6GM_t/c^2$, which is a good approximation for the innermost stable circular orbit for a binary black hole (see e.g. Maggiore, 2007). Taking this into account when determining the coalescence time modifies the relation shown in Eq. 2.50 only by a negligible amount, however.

The expressions we have discussed so far are only valid for circular orbits. There are theoretical arguments that a sizeable fraction of MBHBs have non-neglible eccentricities when they enter the GW regime (Armitage & Natarajan, 2005; Bonetti et al., 2016; Tiede & D'Orazio, 2023). However, GWs tend to circularise the orbit very efficiently, which means that by the time inspiralling compact binaries enter the frequency band of a detector, most systems might have only a negligible eccentricities (Peters & Mathews, 1963). Therefore, the treatment we provided in this section is valid for a wide range of astrophysical scenarios.

An eccentric binary with a given semi-major axis has a shorter coalescence time than its circular counterpart. The equations governing the orbital evolution of eccentric inspiralling binaries can be given as (see e.g. Peters & Mathews, 1963):

$$\dot{a} = -\frac{64}{5}\frac{G^3 m_1 m_2 (m_1+m_2)}{c^5 a^3 (1-e^2)^{7/2}}\left(1 + \frac{73}{24}e^2 + \frac{37}{96}e^4\right), \tag{2.51}$$

$$\dot{e} = -\frac{304}{15}e\frac{G^3 m_1 m_2 (m_1+m_2)}{c^5 a^4 (1-e^2)^{5/2}}\left(1 + \frac{121}{304}e^2\right), \tag{2.52}$$

where a and e is the semi-major axis and eccentricity of the binary. A more degtailed treatment of GWs emitted by eccentric binaries can be found in e.g. Hughes (2009).

2.5 GW detectors

Gravitational wave detectors typically fall into two categories: resonant mass detectors and beam detectors (Sathyaprakash & Schutz, 2009).

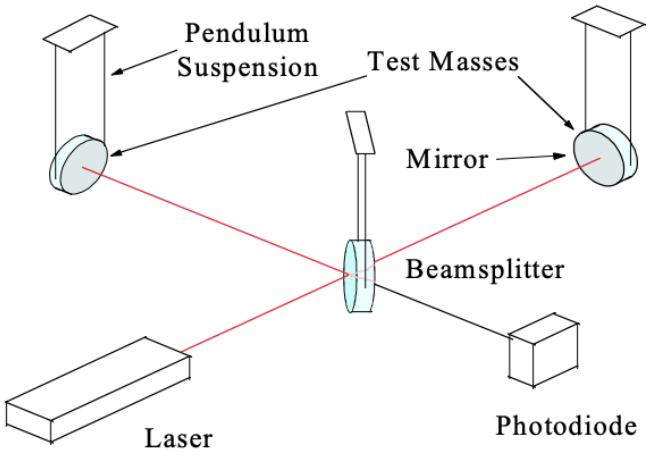

Figure 2.2: Schematic diagram of GW detection with laser interferometry. Figure taken from Pitkin et al. (2011)

Resonant mass detectors observe the oscillations resulting from the transfer of energy to a massive body by GWs (Weber, 1967). These detectors include a cylindrical body of a given length l made from aluminum vibrates when a GW burst with a strain characterized by h passes through it with an amplitude which is proportional to $\sim hl$. Resonant detectors include the Allegro detector (Mauceli et al., 1996), AURIGA (Conti & Auriga Collaboration, 2004) and International Gravitational Event Collaboration (IGEC) (PRODI et al., 2000) to form joint-data analysis with beam detectors like LIGO. However, the sensitivity of resonant detectors is very low which provides motivation to lean into the science of beam GW detectors.

Beam detectors involve the interaction of GWs with a beam of electromagnetic radiation, monitored to detect the wave's passage. Beam detectors include interferometers such as the ground based LIGO (Abbott et al., 2017b), Virgo (Bersanetti et al., 2021) and the space-based LISA (Amaro-Seoane et al., 2023) which was formally adopted by the European Space Agency (ESA) on 25th January 2024. Apart from interferometers, signatures in the radio beams from distant pulsar can also carry the imprint of GW passing through the beams.

In interferometers, laser light is used to detect the changes in the difference of lengths of the detector arms. Using the principle of Michelson interferometer, perpendicular propagation of GWs to the plane of the detector will cause one interferometer to elongate while the other perpendicular arm to shorten and vice versa. These changes in the arm lengths will result in tiny changes in the observed light intensity at the output of the interferometer (Freise & Strain, 2010). A schematic representation of the above is shown in Fig. 2.2.

We now briefly describe how passing of gravitational wave can affect the beam of light which forms the basis of detection through interferometers.

Let us assume a beam of light starting from a point where a clock measures the proper time t and reaches another point at a distance L, where another clock measures the reception time of the beam as t_f. If the clock at the starting point puts timestamps onto the light beam, then the receiving clock can measure the arrival rate of the timestamps. If the plane GW passes through the beam of light at an angle θ and recalling Eq. 2.40 to assume $h_+(t)$ as the GW polarization component, the arrival rate of the timestamps of the light beam with the interference of passing GW can be expressed as:

$$\frac{dt_{\rm f}}{dt} = 1 + \frac{1}{2}(1+\cos\theta)\left\{h_+[t+(1-\cos\theta)L] - h_+(t)\right\}. \tag{2.53}$$

So, the basic idea is a GW of phase t passes when the light beam is emitted and the emitter GW of phase $t + (1 - \cos\theta)L$ passes when the light beam reaches the receiver. So the time delay is affected only by the amplitude of the GW in the plane wave case. In such an arrangement, stability of the clocks is crucial and presently, we can reach the stability of a few parts in 10^{16} (Armstrong, 2006). This means a minimum GW amplitude of $h \sim 10^{-15}$ can be detected by such a two-clock arrangement. Eq. 2.53 is also the principle behind pulsar timing arrays (see Sec. 5.5 for a brief overview) where each pulsar can be treated as a clock at the origin and correlation of signals from many pulsars can help in measuring the amplitude of GW. For the space-based interferometer, LISA with the orbital planes of three spacecrafts arranged in a triangular array (see Fig. 2.3), the measured signal is a bit complex but still retains the same principle.

Let us now look at the geometry of the planes of the detector and the source of GWs. Let us assume the GW propagates along the direction $\hat{N}$ plane which is transverse to the direction contains the radiation basis vectors: $\hat{e}_x^R$ and $\hat{e}_y^R$ (see fig. 2.4).

Recalling Eq. 2.40, the GW wave amplitude can then be written as:

$$\mathbf{h}(t) = h_+(t)\mathbf{e}_+ + h_\times(t)\mathbf{e}_\times, \tag{2.54}$$

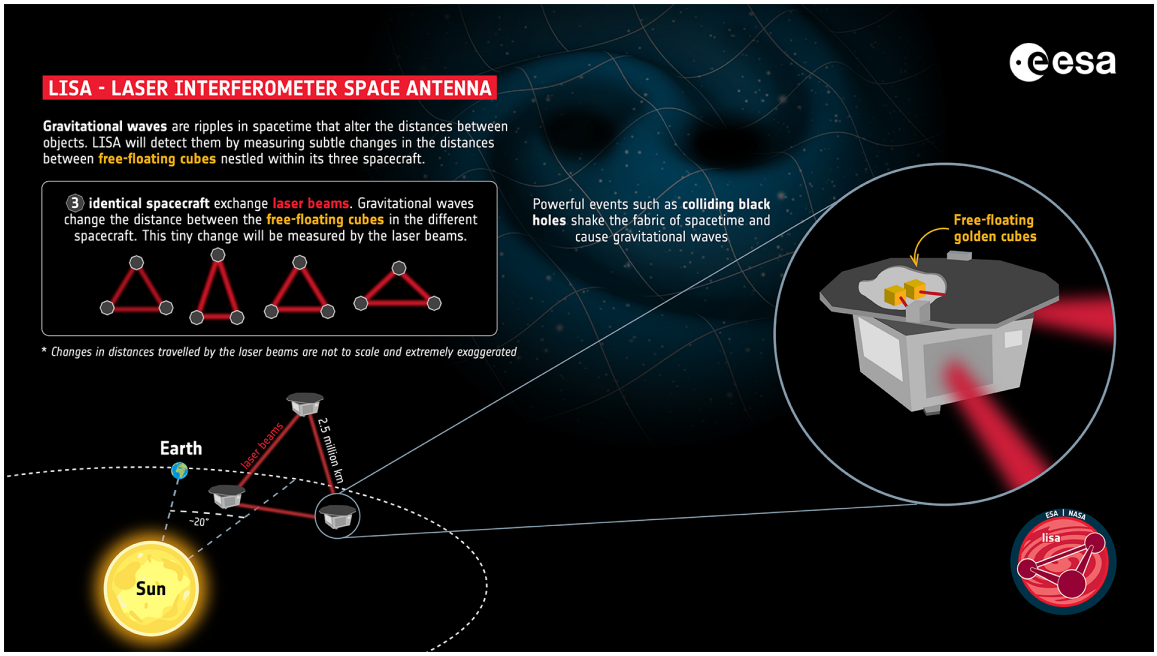

Figure 2.3: Configuration of LISA. Three spacecrafts, connected by laser beams are at the vertices of an equilateral triangle. Each spacecraft contains free-floating cubes made of gold which acts as test masses. Passing GW will change the distance between the test masses in different spacecrafts which can then be measured by the laser beams. Picture credit: European Space Agency

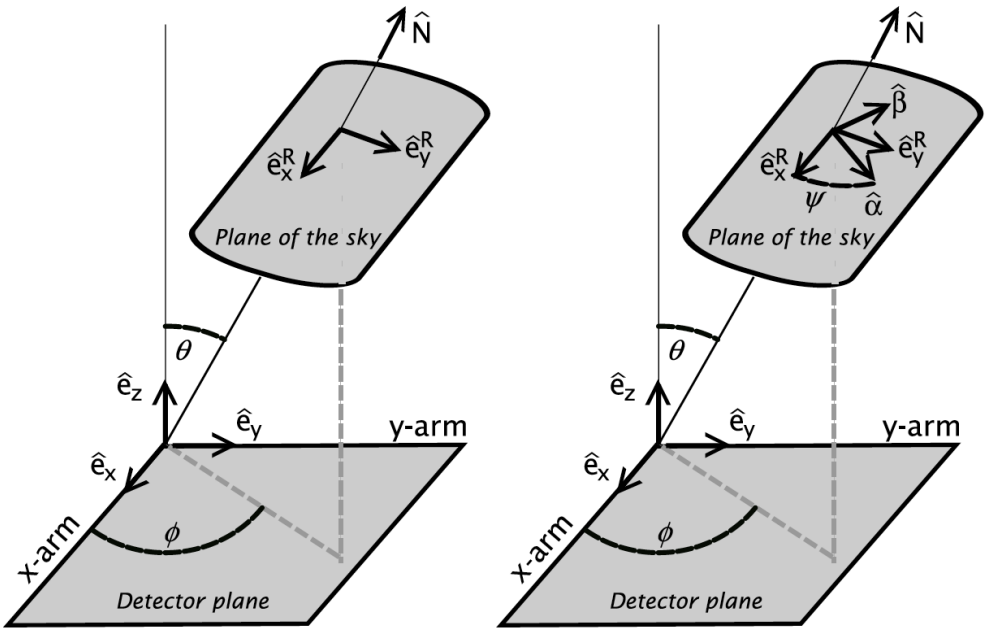

Figure 2.4: Schematic diagram of the geometry of the source and detector planes. The relative orientation of the sky and detector frames (left panel) and the effect of a rotation by the angle ψ in the sky frame (right panel). Figure taken from Sathyaprakash & Schutz (2009)

where

$$\mathbf{e}_+ = (\hat{e}_x^R \otimes \hat{e}_x^R - \hat{e}_y^R \otimes \hat{e}_y^R), \quad \mathbf{e}_\times = (\hat{e}_x^R \otimes \hat{e}_y^R + \hat{e}_y^R \otimes \hat{e}_x^R). \tag{2.55}$$

Similarly, we define the detector tensor as (Dhurandhar & Tinto, 1988) :

$$\mathbf{d} = L(\hat{e}_x \otimes \hat{e}_x - \hat{e}_y \otimes \hat{e}_y), \tag{2.56}$$

with L being the proper distance in the absence of any waves as mentioned above. We can then derive the instantaneous time delay measure by the observer as (Sathyaprakash & Schutz, 2009):

$$\delta t_{\rm ins}(t) = \mathbf{d} : \mathbf{h}. \tag{2.57}$$

where $\mathbf{d} : \mathbf{h} \equiv d_{lm} h^{lm}$ is the Euclidean scalar product of the tensors $\mathbf{d}$ and $\mathbf{h}$. This expression can be used to describe the response of any interferometer and it is dependant on the direction of the wave. An important assumption that was made to derive the above expression is that the arm lengths of the interferometer are shorter than the wavelength which can then lead to defining a local inertial coordinate system that covers the entire interferometer. In terms of change in the arm-length of the detector due to passing of the GW, we can write

$$\delta L(t) = \frac{1}{2}\, \mathbf{d} : \mathbf{h}, \tag{2.58}$$

where we note that the differential change in arm length is half the differential time delay.

It is more useful to have a more general convention for the orientation of basis vectors to account for detectors in different orientations. In a more general situation,if we assume basis vectors $\hat{\alpha}$ and $\hat{\beta}$ (as shown in the right panel of Fig. 2.4)to be rotated at an ψ from the basis vectors shown in the left panel, we can rewrite the polarization tensors as:

$$\epsilon_+ = (\hat{\alpha} \otimes \hat{\alpha} - \hat{\beta} \otimes \hat{\beta}), \quad \epsilon_\times = (\hat{\alpha} \otimes \hat{\beta} + \hat{\beta} \otimes \hat{\alpha}), \tag{2.59}$$

are found by the following transformation from the previous ones:

$$\begin{aligned} \epsilon_+ &= \mathbf{e}_+ \cos 2\psi + \mathbf{e}_\times \sin 2\psi, \\ \epsilon_\times &= -\mathbf{e}_+ \sin 2\psi + \mathbf{e}_\times \cos 2\psi. \end{aligned} \tag{2.60}$$

Then Eq. 2.58 can be rewitten as:

$$\frac{\delta L(t)}{L} = F_+(\theta,\, \phi,\, \psi)h_+(t) + F_\times(\theta,\, \phi,\, \psi)h_\times(t), \tag{2.61}$$

where F_+ and $F_\times$ are called the *antenna pattern* functions for the two polarizations defined on the sky-plane basis by

$$F_+ \equiv \mathbf{d} : \mathbf{e}_+, \quad F_\times \equiv \mathbf{d} : \mathbf{e}_\times. \tag{2.62}$$

From fig. 2.4, we can derive the antennae pattern functions as (Hawking & Israel, 1989):

$$\begin{aligned} F_+ &= \frac{1}{2}\left(1 + \cos^2\theta\right)\cos 2\phi \cos 2\psi - \cos\theta \sin 2\phi \sin 2\psi, \\ F_\times &= \frac{1}{2}\left(1 + \cos^2\theta\right)\cos 2\phi \sin 2\psi + \cos\theta \sin 2\phi \cos 2\psi. \end{aligned} \tag{2.63}$$

In the coordinates of the detector, $\psi = 0$ and the maximum values of F_+ or $F_\times$ is 1. A single detector cannot simultaneously measure the two polarizations of GW and instead detects a linear combination of the two polarizations depending on the direction of GW source and geomtry of the detector.

For short-lived wave, three independent detectors can be sufficient for a proper estimation of the source location and the polarization of the GW.

Now, we can rewrite Eq. 2.40 as

$$h_+ = \frac{h_0}{2}\left(1 + \cos^2\iota\right)\cos\Phi(t), \quad h_\times = h_0 \cos\iota \sin\Phi(t),$$

where $h_0 = -\frac{4G\mathcal{M}_c}{c^2 d_L}\left(\frac{\pi G \mathcal{M}_c f}{c^3}\right)^{2/3}$ and $\Phi(t) = 2\Phi_N(t)$ with ι being the angle made by the LOS with the direction of the source. Therefore, the response can be simplistically described as:

$$h(t) = F_+ h_+ + F_\times h_\times = A h_0 \cos(\Phi(t) - \Phi_0), \tag{2.64}$$

where

$$A = \left(A_+^2 + A_\times^2\right)^{1/2}, \quad \tan\Phi_0 = \frac{A_\times}{A_+}, \quad A_+ = \frac{1}{2}F_+(1+\cos\iota^2), \quad A_\times = F_\times \cos\iota.$$

Just like F, A ranges between 0 to 1.

As we mentioned in the beginning, beam based detectors include ground-based and space-based interferometers (and PTAs, separately). A schematic representation of the GW spectrum across various frequencies and compatible detectors is shown in Fig. 2.5.

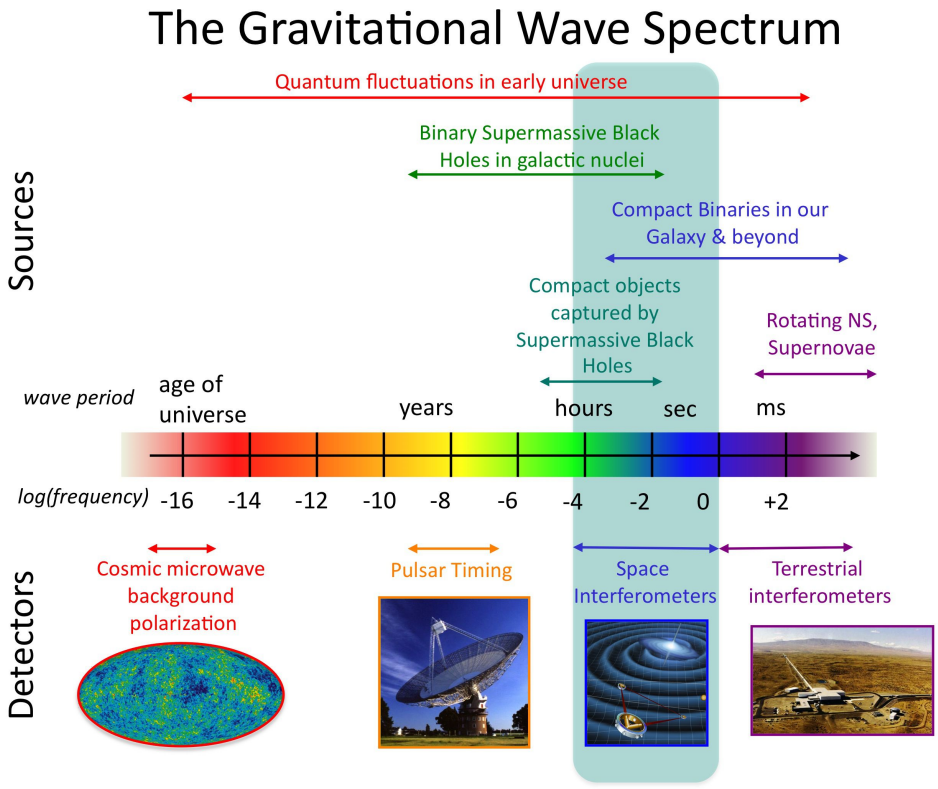

Figure 2.5: The GW spectrum across different frequencies. The green patch highlights in particular the range of space interferometers such as LISA. Credit: NASA

Ground based interferometers can detect the GW emission from various sources such as stellar mass black hole binary merger, neutron star-BH merger, explosions of supernovae ans isolated pulsars (see for example Abbott et al., 2016c, 2017a, 2020). PTAs, on the other hand

can detect low-frequency GW from SMBH binaries (see for example Sesana et al., 2008; Xu et al., 2023). However both these systems are useful to probe low redshift ($z \sim 2$) Universe (Dominik et al., 2015; Belczynski et al., 2014, 2016). The GW signal is extracted from the noise due to various factors relevant to each detection technique. For example, for ground based detectors, seismic vibrations, thermal noise due to the vibration of mirrors and pendulums as well as absorption of light, shot noise produced by the fluctuations of the interferometry photons and quantum effects can all lead to the contamination of the GW signal. Some of these noises can be screened out, but the seismic noise arising from the surface of Earth cannot be completely filtered out. As the frequency of GW increases, the spectrum steeply falls as a result of which for any GW detection above 1 Hz, it is necessary to go to space (Harms et al., 2013). So, to probe GWs at higher redshifts (z >2) and frequencies, space-based observatory such as LISA is the perfect candidate.

The power spectral density (PSD) of a GW detector helps quantify the background noise and determines the sensitivity of the detector and its ability to discern signals at different frequencies. In practice, the PSD is obtained by analyzing the detector's output signal in the frequency domain. The data is typically Fourier transformed to obtain the signal's frequency components, and the square root of the power in each frequency bin gives the amplitude of the gravitational wave signal. Analyzing the PSD allows researchers to identify the detector's optimal frequency range and improve its performance by minimizing noise.

If we assume the output from a GW detector to be composed of a time-series $x(t)$ as a result of the GW signal and the noise background $n(t)$, then the output of the interferometer can be written as (Maggiore, 2007):

$$x(t) = \begin{cases} n(t) + h(t), & \text{if signal is present} \\ n(t), & \text{no signal present} \end{cases} \tag{2.65}$$

Titi:write a bit more here about noiseassumptions, also write why we move from time domain to frequency domain.

We assume that the noise is stationary and their components are uncorrelated in frequency. The noise auto-correlation function is defined as

$$\kappa \equiv \overline{n(t_1)n(t_2)}, \tag{2.66}$$

where an overline indicates the average over an ensemble of noise realizations.

For a given PSD, $P_n(f)$ of detector noise, the spectral sensitivity of the strain can be defined as (Larson et al., 2000):

$$S_n(f) = \frac{P_n(f)}{\mathcal{R}(f)}. \tag{2.67}$$

$S_n(f)$ is known as the single-sided spectral density. It describes how the power of the noise is distributed over the frequency.

$\mathcal{R}(f)$ is known as the response function of the sky and polarization averaged signal which relates the PSD that is detected by the detector to the PSD of the incident GW signals.

$\mathcal{R}(f)$ is computed in the frequency domain, so we convert Eq. 2.40 in the frequency space through Fourirer transformation and rewrite it as:

$$\tilde{h}(f) = F^{+}(f)\tilde{h}_{+}(f) + F^{\times}(f)\tilde{h}_{\times}(f)\,, \tag{2.68}$$

For the case of LISA, the response function has to be computed numerically to obtain the form:

$$\mathcal{R}(f) = \frac{3}{10}\frac{1}{(1+0.6(f/f_*)^2)}\,. \tag{2.69}$$

The LISA rms noise $h_{\rm rms}$ as a function of frequency f is given by (Klein et al., 2016; Robson et al., 2019) :

$$h_{\rm rms}(f) \equiv \sqrt{\Delta f S_n(f)}, \tag{2.70}$$

where S_n is the LISA power spectral density (PSD):

$$\begin{aligned} S_n(f) = \frac{20}{3}\frac{4S_{\rm n,acc}(f) + S_{\rm n,sn}(f) + S_{\rm n,omn}(f)}{L^2} \\ \times \left[1 + \left(\frac{f}{\frac{0.41c}{2L}}\right)^2\right], \end{aligned} \tag{2.71}$$

L corresponds to the detector arm length, and $S_{\rm n,acc}$, $S_{\rm n,sn}$ and $S_{\rm n,omn}$ are the noise components

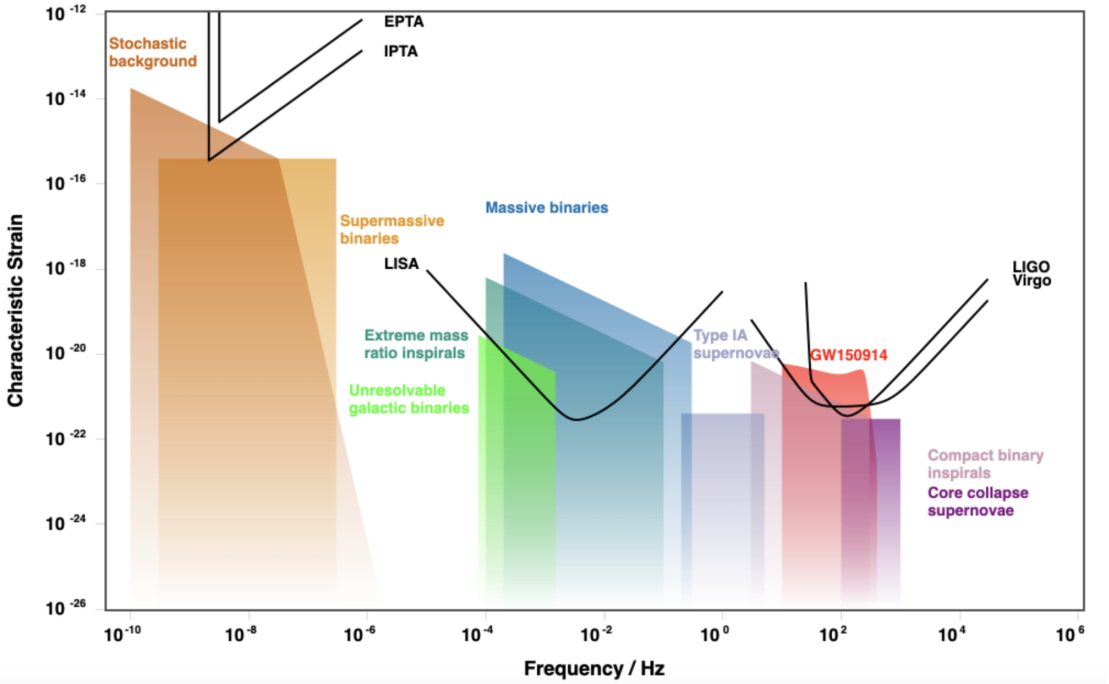

Figure 2.6: GW detectors sensitivity and sources. Figure made from `http://gwplotter.com/` (Moore et al., 2014).

due to low-frequency acceleration, shot noise and other measurement noise, respectively (Smith & Caldwell 2019; Klein et al. 2016), parametrised as follows[5]:

$$
\begin{aligned}
S_{\mathrm{n,acc}} &= \frac{9\times10^{-30}}{(2\pi f)^4}\left(1+\frac{10^{-4}}{f}\right)\ [\mathrm{m^2Hz^{-1}}],\\
S_{\mathrm{n,sn}} &= 2.22\times10^{-23}\ [\mathrm{m^2Hz^{-1}}],\\
S_{\mathrm{n,omn}} &= 2.65\times10^{-23}\ [\mathrm{m^2Hz^{-1}}].
\end{aligned}
\tag{2.72}
$$

The sensitivity curve of different GW instruments can be seen in Fig.2.6. For low frequency sources, we have shown GW signals from the stochastoc background and SMBHB mergers detectable by PTA facilities such as EPTA and IPTA. For mid-frequency range, which will be covered by LISA, we show the sensitivity of LISA to detect MBHB mergers (including the inspiral phase), EMRIs and unresolvable galactic binaries (which contributes to the sensitivity curve of LISA). And finally for the high frequency range, we show the GW source GW150914 and the sensitivities of LIGO and Virgo accordingly.

[5]These values hold for the current LISA design, that presents three spacecrafts connected by 6 links. Given the large uncertainties on the very-low frequency LISA sensitivity, we adopt a pessimistic cut at 10^{-4} Hz (Sesana et al., 2004).

For LISA, Eq. 2.5 can be written in the frequency space as:

$$\tilde{h}_+(f) = \frac{1}{2}h_0\frac{1+\cos^2\iota}{2}e^{i\phi_0}\delta_T(f-f_0), \tilde{h}_\times(f) = \frac{-i}{2}h_0\cos\iota e^{i\phi_0}\delta_T(f-f_0), \tag{2.73}$$

where we assumed $\Phi(t) = \omega_0(t) + \phi_0$

It is valid to assume LISA as static for transient signal such as those arising from MBHB coalescence for which the duration of the detectable part of the signal ($\sim$ months) is shorter than the characteristic time of LISA's motion ($\sim$ year). Under this assumption, the signal-to-noise ratio (SNR) of LISA can be described by

$$\mathrm{SNR}^2 = 4\mathrm{Re}\left(\int_0^{\mathrm{f_{max}}}\frac{\tilde{\mathrm{h}}(\mathrm{f})\tilde{\mathrm{h}}^*(\mathrm{f})}{\mathrm{S_n(f)}}\mathrm{df}\right), \tag{2.74}$$

2.6 Electromagnetic signals from merging MBHs

As discussed before, it has been found that MBHs are often nested in the nuclei of their host galaxies (Lynden-Bell, 1969; Wise et al., 2019) and MBHB mergers could often result from the mergers of their host galaxies (Yu & Tremaine, 2002; Volonteri et al., 2021). After a galactic merger, dynamical friction by gas/stars exerted on the MBHs will be a key mechanism to reduce the separations of MBHBs and bind them gravitationally (see Sec. 1.6). GW emission will be effective from MBHB separations of about 0.01 parsec (Sesana & Khan, 2015; Dotti et al., 2015; Volonteri et al., 2020). At such separations, the EM signatures are most likely to be associated with gas accretion flows surrounding the MBHBs.

At present, even though no such multi-wavelength detections have been made for MBH mergers, we can still predict some possible scenario for which we would expect EM signals of a GW event:

i) *Pre-merger phase*: During the inspiral phase we can expect EM signals (Armitage & Natarajan, 2002; Franchini et al., 2024) arising from the CBDs (which we discussed in Sec. 1.6) of the MBHBs; The binary motion hollows-out a pocket in the CBD while gas flows from the inner edge of the CBDs and form minidisks surrounding each MBH, contributing to spectral

features and variable EM emission at various wavelengths before the merger (Roedig et al., 2014). Milosavljević & Phinney (2005) showed EM emissions arising from the CBDs can be within the reach of next generation X-ray surveys. EM emission can also arise from the mini-disks that surrounds the individual MBHs (Noble et al., 2012; Bowen et al., 2017). Gutié rrez et al. (2022) showed that just before coalescence, mini-disks of spinning BHs can be 3 to 5 times brighter than non-spinning BHs and can be probed in the far-UV and soft X-ray bands. Along with these, accretion streams channeling into the mini-disks can also emit EM signals (Combi et al., 2022), particularly in the hard X-ray band (Roedig et al., 2014). Depending on the efficiency of the accretion rates, periodic variations in the radio and X-ray bands as well as emission lines from $\mathrm{Fe_{II}}$ and $\mathrm{O_{III}}$ can be expected from merging SMBHs (Wang et al., 2022).

ii) *Merger phase*: During the merger phase, the presence of magnetic field and matter close to the binary can cause dynamic interaction with the MBHB and can result in EM emission through different channels (for a comprehensive review, see Gold (2019)). Depending on whether the mergers are occuring in radiatively efficient or inefficient gas flows, EM signatures during the merger can also be expected in the UV band (Krolik, 2010). Jets in magnetized accretion flows could also emit EM signatures in the sub-mm bands(Kelly et al., 2017).

iii) *Post-merger phase*: After the merger, EM signatures could appear on longer timescales after merger as EM afterglows. MBHB mergers can release a significant amount of energy and momentum which will perturb the surrounding accretion disk. Such perturbations can produce density waves or shocks in the disk, which in turn would produce EM signatures that is different from standard accretion emission. EM afterglows could arise from the circumbinary gap refilling resulting in emissions peaking in the hard UV and X-ray bands (see for eg. Dotti et al., 2006; Schnittman & Krolik, 2008; Tanaka & Menou, 2010). GW recoil kicks (Lippai et al., 2008), on the other hand, would result in emissions peaking in the UV or soft X-ray bands (Anderson et al., 2010; Rossi et al., 2010; Ponce et al., 2011; Meliani et al., 2017). Apart from these, we could also expect long-lived EM signatures from GW recoiling. Blecha et al. (2015) predict that large surveys with the Vera Rubin Observatory, the Nancy Grace Roman Space Telescope, and Euclid could potentially detect hundreds of spatially offset AGNs,if pre-merger MBH spins are not always highly aligned. Also, stellar tidal disruption events following a GW recoil kick could

also produce EM signals (Stone & Loeb, 2011).

However, detection of most of these EM signatures would require extremely precise sky-localizatiom of a GW event as well as high resolution tracking of MBHB by EM instruments.

In the foreseeable future, with the advancement of EM facilities with ground and space-based telescopes it will be possible to probe deeper in the EM searches of the fraction of SMBH population at high redshift universe. GW astronomy can be jointly exploited by electromagnetic signals to provide new information on the earliest accreting black holes, the dimmest AGN of the low-mass tail of SMBH population, binary or/and multiple AGN in interacting systems, and ultimately will let us identify the EM signals of the loudest GW signals from merging MBHs. LISA detections of MBHBs could be complemented with different EM observations: At X-ray frequencies, LISA detections of MBHBs could be complemented by observatories such as Chandra, Athena, LynX and AXIS. In the infrared band, the recently launched James Webb Space telescope (JWST) in Near Infrared, ORIGINS for Mid Infrared, and ALMA, AtLAST for Far Infrared frequencies can support the LISA detections. Also Vera C. Rubin Observatory for optical and SKA in radio wavelengths can probe any potential EM signatures to complement LDEs.

At lower redshifts ($z \leq 4$) morphological signatures (tidal tails,disturbed stellar components, shells of stellar light) of host galaxies of major black hole mergers post coalescence have been investigated (DeGraf et al., 2021). Signatures of binaries can also be detected form the water maser emission in their environment (Padmanabhan & Loeb, 2022). Further investigation is required on how such signatures would propagate at higher redshifts.

At higher redshifts, previous studies have shown a promising premise for possible EM signals from LISA events. Valiante et al. 2018 showed that heavy seeds shows to be promising candidates with detections through future electromagnetic facilities such as JWST and Athena (Valiante et al., 2018). Mangiagli et al. (2022) explores the detectability of EM emissions of LDEs and shows that depending on the astrophysical model, while there could be possibility of EM detections in the soft X-ray, optical and radio bands, in reality, the signals will be too faint to be detected by future EM observations.

Part II

Numerical background

Cosmological simulations 3

3.1 Introduction

In recent decades, cosmological simulations have become crucial tools for understanding galaxy formation and structure, modelling complex physical processes across vast scales and tracking galaxy evolution. These simulations benefit from improved knowledge, refined numerical techniques, and increased computing power, allowing them to reproduce observed galaxy properties and explore alternative cosmological models.

Modern astrophysics has a lot of data to study galaxies and validate theoretical models of galaxy formation. The complexity of data collection and validation requires the use of numerical simulations. Simulations can numerically decode various astrophysical models while simultaneously considering various physical factors such as gas dynamics, star formation, chemical evolution, feedback from stars and AGNs, and the growth of massive black holes. Over the past two decades, numerical simulations have successfully replicated a wide range of observations, advancing our understanding of the Universe.

3.2 Key components of cosmological simulations

Galaxy formation is a complex process that operates on multiple scales. It involves physical processes occurring at scales as small as parsecs (pc) where star formation occurs, and at much larger cosmic scales that regulate galaxy abundance and clustering ($\sim$100 Mpc). Cosmological simulations, therefore offer valuable insights into this multi-scale and multi-physics approach

for studying our Universe. To create a comprehensive and realistic representation to be comparable with observations, various physical factors must be considered. Modern cosmological simulations typically include:

- A cosmological framework: To provide the backbone of cosmological principles to be applied in our models.
- Dark Matter (DM) and gravitational interactions: To outline structure formation from DM overdensities.
- Baryonic physics: To incorporate more complex processes such as star formation, stellar feedback, magnetic fields and so on.

Based on these key ingredients, simulations incorporate a wide range of physics, as illustrated in Fig. 3.1, which we will explore in greater detail in the following sections.

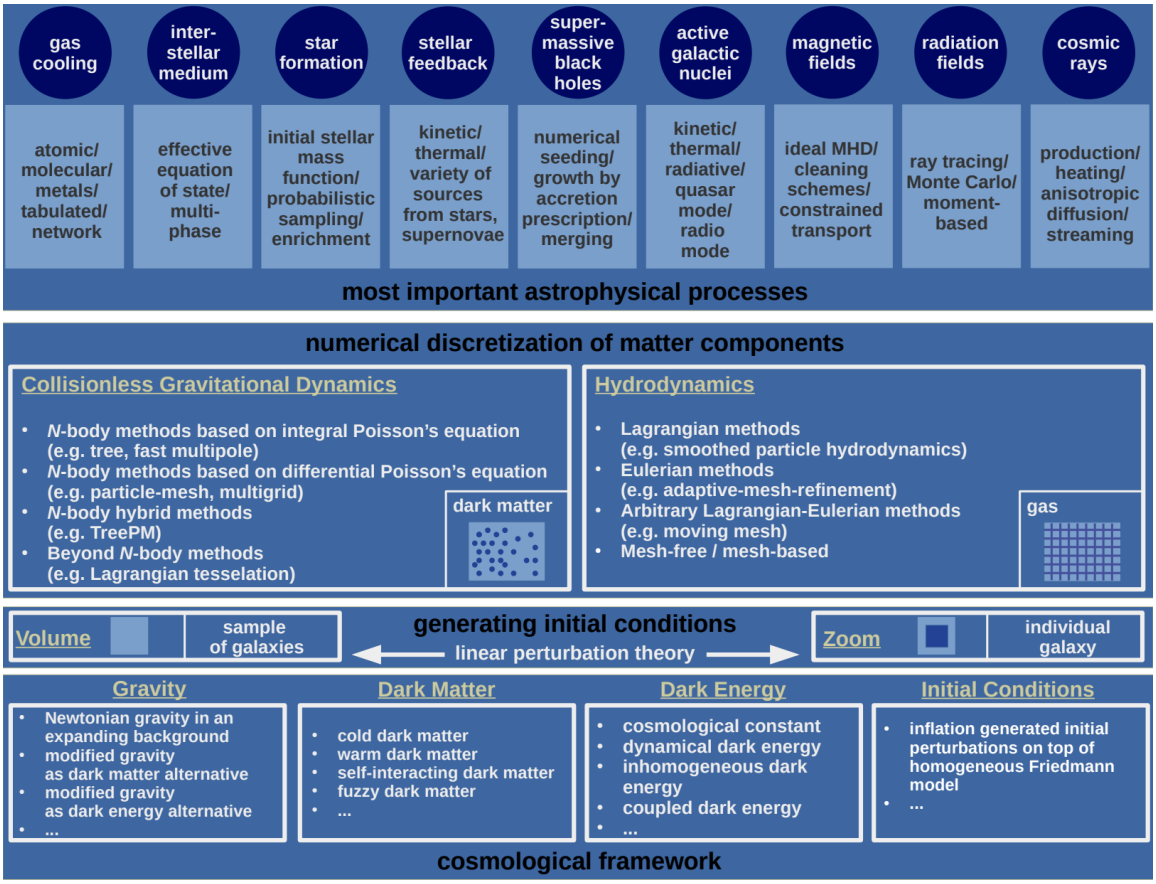

Figure 3.1: Overview of basic components of cosmological simulations. Figure taken from Vogelsberger et al. (2019).

3.2.1 Cosmological framework

For a comprehensive model of our Universe, it is important to assume a cosmological framework. Typically, cosmological simulations rely on a specific cosmological model with defined initial conditions to accurately represent a variety of physical processes within the Universe.

As we mentioned in the introduction, a variety of observations support the ΛCDM model, which serves as the basis for understanding how galaxies form. These observations include, for example, studying the cosmic microwave background (Smoot et al., 1992; Page et al., 2003; Komatsu et al., 2009; Planck Collaboration et al., 2016) and examining data from Type Ia supernovae to determine distance and redshift (Riess et al., 1998; Perlmutter et al., 1999). Additionally, the abundance of galaxy clusters and the way galaxies cluster together help us to narrow down the essential parameters of the ΛCDM model. Essentially, in this model we assume our Universe to be composed of dark matter and dark energy, constituting 95% of its energy density, with baryons accounting for the remaining 5% in a flat FLRW geometry. Once we have this framework, we then need to set up the initial conditions that support the structure formation process as mentioned in the Introduction.

After the geometry and the composition of the Universe are specified, we set up the initial conditions that drive the structure formation process, as mentioned in the Introduction. Specific initial conditions are needed to replicate the perturbations on top of the homogeneous expanding background. These perturbations are determined by the power spectrum $P(|k|)$, which results from convolving the primordial fluctuations generated during inflation with the linear growth regime in the post-recombination era (Eisenstein & Loeb, 1995). After defining the linear density fluctuation field at an initial time, typically around redshift $z \sim 100$, we proceed to assign dark matter particle positions and velocities, as well as baryon density, velocity, and temperature fields.

Cosmological simulations can be categorized into two main types: large volume simulations and zoom-in simulations. In large volume simulations, an extensive region is simulated (several hundreds of Mpc^3), with periodic sampling of initial conditions. Conversely, zoom-in simulations involve selecting a region of interest($\sim Mpc$) from a lower-resolution simulation and enhancing the resolution within that specific area. The computational expense of these zoom-in

simulations increases with the mass of the object that is studied for a fixed mass resolution. Some simulations employ initial conditions that mimic specific regions of the Universe, like those with matter overdensities (e.g., Hoffman & Ribak (1991)), termed constrained initial conditions. Additionally, it is necessary to define a set of boundary conditions.

3.2.2 DM simulations

As previously discussed in the Introduction, there is substantial evidence supporting the theory that galaxies exist within extended halos of dark matter. These dark matter halos come into existence through gravitational instability. Initially, density perturbations undergo linear growth until they reach a critical density, at which point they reverse their expansion due to the cosmic expansion and proceed to collapse, forming virialized dark matter halos. These halos then continue to increase in mass and size, either by gathering material from their vicinity or by merging with other halos. Following mergers into larger halos, some of these structures may persist as bound entities, thus contributing to the population of subhalos.

In the scenario of non-interacting dark matter particles, we arrive at the continuum limit by considering the collisionless Boltzmann equation, which shows the conservation of the local phase-space density along with Poisson's equation which describes the gravitational potential :

$$\frac{\mathrm{d}f}{\mathrm{d}t} = \frac{\partial f}{\partial t} + \mathbf{v}\frac{\partial f}{\partial \mathbf{r}} - \frac{\partial \Phi}{\partial \mathbf{r}}\frac{\partial f}{\partial \mathbf{v}} = 0 \tag{3.1}$$

$$\nabla^2 \Phi = 4\pi G \int f \mathrm{d}\mathbf{v} \tag{3.2}$$

where $f = f(\mathbf{r}, \mathbf{v}, t)$ represents the probability density function in the phase space, and Φ is the gravitational potential.

The solution to this pair of equations is required within the context of an expanding background Universe, as determined by the Friedmann equations which, in turn, stem from the field equations of general relativity.

The high dimensionality of the Boltzmann equation requires special numerical techniques which have been well developed in the past few decades. A widely used approach is the N-body method, which tracks the collisionless behavior of dark matter. In this method, the phase-space

density is represented by an ensemble of N phase-space points, each associated with a mass m_i. As the number of particles increases, the Poisson noise diminishes, thus making the N-body method more efficient. However, it is still challenging for this method to tackle the Poisson equation and thereby quantifying the gravitational forces of interaction between the particles (Heggie, 2005). There are broadly two ways this challenge can be overcome:

1) The Poisson equation is solved using its integral form, and forces are calculated through direct summation. To make the computation more efficient, a tree structure is employed to approximate the contributions from distant particles. A caveat of this method is that two-body scatterings between nearby DM particles are prevented by 'softening' the gravitational force of small scales , thus forming a smoothed density field.

2) The Poisson equation is solved in its differential form. Typically, this involves solving the equation in Fourier space after creating a grid structure known as the particle-mesh (PM) method.

Along with these, there are also hybrid methods which combine direct summation techniques for short-range forces with Fourier transform-based methods for long-range forces. For example, the tree-particle-mesh method, in which direct summation for short-range interactions is approximated using a tree-like method. Additionally, combinations of the multigrid method with the fast Fourier transform are applied, employing the Fourier transform as a force solver on the coarsest grid (Bode & Ostriker, 2003). The majority of modern simulations adopt these hybrid solvers to attain optimal computational efficiency.

N-body simulations offer a deeper understanding of the process of hierarchical structure formation (Navarro et al., 1996; Sheth et al., 2001; Springel et al., 2017) and provide further insights into the composition and distribution of DM halos which is the framework of our Universe.

3.2.3 Baryonic simulations

Even though dark matter and dark energy are the fundamental component of structure formation, baryons are crucial to describe the actual physical universe that is visible to us. Initially the baryons are mainly comprised of primordial gases: hydrogen and helium some of which eventually contribute to stellar structures. These cosmic gases can be modelled using Euler's

equations:

$$\frac{\partial \rho}{\partial t} + \nabla \cdot (\rho \mathbf{v}) = 0 \tag{3.3}$$

$$\frac{\partial \rho \mathbf{v}}{\partial t} + \nabla \cdot (\rho \mathbf{v} \otimes \mathbf{v} + P) = 0 \tag{3.4}$$

$$\frac{\partial \rho e}{\partial t} + \nabla \cdot (\rho e + P)\mathbf{v} = 0 \tag{3.5}$$

where ρ is the gas density, $\mathbf{v}$, the gas velocity, P the pressure and $e = u + \mathbf{v}^2/2$ the energy per unit mass, with u being the internal energy.

Hydrodynamical equations can be differentiated in various ways. One such way typically separates into three categories: Lagrangian, Eulerian, or arbitrary Lagrange-Eulerian methods. In the Lagrangian approach, we imagine following individual fluid parcels, each with its unique properties like density, mass, mometum etc. as they move through space and time. In contrast, the Eulerian approach focuses on specific spatial locations where the fluid flows over time. Additionally, there are two numerical approaches: mesh-free and mesh-based algorithms. Mesh-free methods, unlike the mesh-based approach, don't need node connections; instead, they rely on interactions between nodes and their neighbors.

In Eulerian method, the hydrodynamic equations are commonly solved on a grid by using approaches of finite volume, finite difference, finite element, spectral or wavelet methods to calculate the derivatives.Over the years, several Godunov schemes (Godunov & Bohachevsky, 1959) have been developed. These schemes aim to solve the Riemann problem at cell interfaces to accurately handle shocks and reduce numerical diffusion. (For example, see Colella & Woodward (1984)) Since the ranges of the cosmological simulations are huge, an adaptive mesh refinement (AMR) strategy is used (Berger & Oliger, 1984; Bryan & Norman, 1995; Klein et al., 2016). This helps in adapting the local physical conditions for the grid as a result of the increased spatial accuracy derived from AMR.

A mesh-free technique is instead used in the Lagrangian formulation. In this case, for each particle the equations of motion derived from the hydrodynamical equations are implemented to sample the fluid dynamics. This is commonly known as the Smoothed Particle Hydrodynamics

(SPH) method and in this case conservation of energy, linear momentum, angular momentum, mass, and entropy are simultaneously implemented in case there is no artificial viscosity.

In order to present a realistic picture of the universe that agrees with the observations, various astrophysical processes must be modelled along with the hydrodynamical equations as mentioned before. The spatial scales for many of these processes are below the range of the simulations. Hence, sub-resolution models are needed to operate on such small spatial ranges. The various astrophysical processes that require the sub-resolution prescription can be summarised as follows:

- **Gas cooling:** The internal energy in gas are released through various cooling methods such as ionization, excitation, inverse Compton scattering, recombination and so on (see introduction for a more detailed overview). Typically, in cosmological simulations, cooling functions are calculated explicitly (Schaye et al., 2015a) or directly implemented through chemical networks (Pallottini et al., 2022). But we should keep in mind that it is challenging to track all gas cooling processes simultaneously as each gas phase needs different numerical resolution.

- **Star formation:** Stars are formed when cold, dense gas collapses due to gravitational forces. In simulations, this process is tackled by converting a portion of gas particles into stellar particles by assuming an initial stellar mass function (Salpeter, 1955; Kroupa, 2001; Chabrier, 2003). The local star formation rate is usually calculated by the Schmidt-Kennicutt type relation (Schmidt, 1959; Kennicutt, 1998):

$$\frac{dM_\star}{dt} = \epsilon \frac{M_\mathrm{g}}{t_\mathrm{ff}} \tag{3.6}$$

  , where M_g denotes the gas cell/particle mass, t_ff represents the gravitational free fall time and ϵ is a conversion efficiency which ranges between $0.01 - 1$ (Springel & Hernquist, 2003; Hopkins et al., 2018). The selection criteria for gas particles to be transformed into stellar particles can be based on a density threshold (for e.g. Schaye et al. (2015a)) or Jeans-length-criterion (for e.g. Hopkins et al. (2014)).

- **Stellar feedback:** At the end of the stellar lifecycle, supernovae blast diffuses energy and

momentum from the stars to the surrounding gas, essentially forming a feedback cycle that regulates further star formation (see introduction for more details). Typically, energy is injected either thermally or kinetically. Thermal diffusion of energy requires prevention of excessive radiative cooling of gas since the resolution of cosmological simulations are not sensitive to these cooling models (e.g. Stinson et al., 2006). In the latter case, kinetic energy is radiated away through hydrodynamically-decoupled particles of wind which essentially makes non-local injection of momentum in the star-forming environmental gas possible. This is turn provides with a proper reproduction of the galactic outflows in the simulations (e.g. Springel & Hernquist, 2003). Along with these methods, in recent times stellar winds, photo-ionization and radiation pressure are also modelled in various simulations (see also Agertz et al., 2013). All these processes when considered simultaneously, reproduces a clear picture of stellar feedback in the simulations (Springel & Hernquist, 2003; Hopkins et al., 2014).

- **Black hole seeding:** The origin of SMBHs is still an active topic of debate. Different theoretical scenarios have been proposed to explain the origin of SMBH seed (see Sec. BLA SMBH in the Introduction). Therefore, in simulations BH particles are generally seeded directly into halos once the mass of the halo crosses a certain threshold mass (typically between 10^9 to $10^{11}\mathrm{M}_\odot$). The BH seed mass varies according to the theoretical prescription considered. Once the BHs are seeded, they then grow by merging with other BHs and by accreting gas from the surroundings. Gas accretion is followed by the Bondi-Hoyle-Littleton prescription (Bondi & Hoyle, 1944; Bondi, 1952) with certain tweaks implemented depending on the numerical resolution such as using a numerical boost factor (Booth & Schaye, 2009) or using special techniques to model the angular momentum of gas (for e.g. Anglès-Alcàzar et al., 2017).

- **AGN feedback:** A fraction of the rest mass energy accreted by the BH is radiated away, and a part of it is further coupled to the surrounding gas (AGN feedback), possibly triggering multi-scale, multi-phase outflows (Harrison et al., 2018; Clavijo-Bohórquez et al., 2023). There are different ways AGN feedback is implemented in various simulations. Two prevalent methods of feedback implementation are the quasar mode and the radio

mode. In quasar mode, AGN feedback, which is considered to be a fraction of the AGN luminosity, is coupled to the surrounding gas in the form of either energy or momentum. Quasar mode feedback provides a strong framework for radiatively efficient mode of black hole growth (Springel et al., 2005a; Matteo et al., 2005). Radio mode, on the other hand, uses the concept of AGN jets for the feedback. This mode provides a good model to regulate star formation in massive galaxies (Sijacki et al., 2007).

- **Additional components:** There are numerous other processes that go into the physics of galaxy formation and evolution. Different simulations take into account different physical processes, such as magnetic fields (Ferriè re, 2001), cosmic rays from supernovae explosions and AGN jets (Ferrière, 2005; Field et al., 1969; Uhlig et al., 2012), radiative transfer effects (Gnedin & Kaurov, 2014; Rosdahl et al., 2018; Ocvirk et al., 2020), thermal conduction (Barnes et al., 2018; Kannan et al., 2016) and gas viscosity (Parrish et al., 2012; ZuHone et al., 2014).

The overall impact of the aforementioned physical processes is included into simulations by means of sub-grid models that typically involve only a few adjustable parameters, which are fine-tuned to match observations. Simulations often vary in how they precisely apply these sub-grid methods, leading to differences in results that can vary significantly. More research is necessary to improve these models, as they presently represent the primary source of uncertainty in the predictions made by cosmological simulations.

3.3 Overview of modern simulations

In Fig. 3.2, we show a brief overview of some simulations from the last few decades. On the left column, we show the N-body simulations whereas in the right we show the simulations which also include baryons. Each of these categories are further subdivided into zoom-in (top panel) and large volume (bottom panel) simulations.

From top left, we show zoom-in, N-body simulations: Aquarius (Springel et al., 2008), Via Lactea (Kuhlen et al., 2008), GHALO (Stadel et al., 2009), Phoenix (Gao et al., 2012) and ELVIS (Garrison-Kimmel et al., 2014). Apart from these, a few more notable zoom-in, N-body include

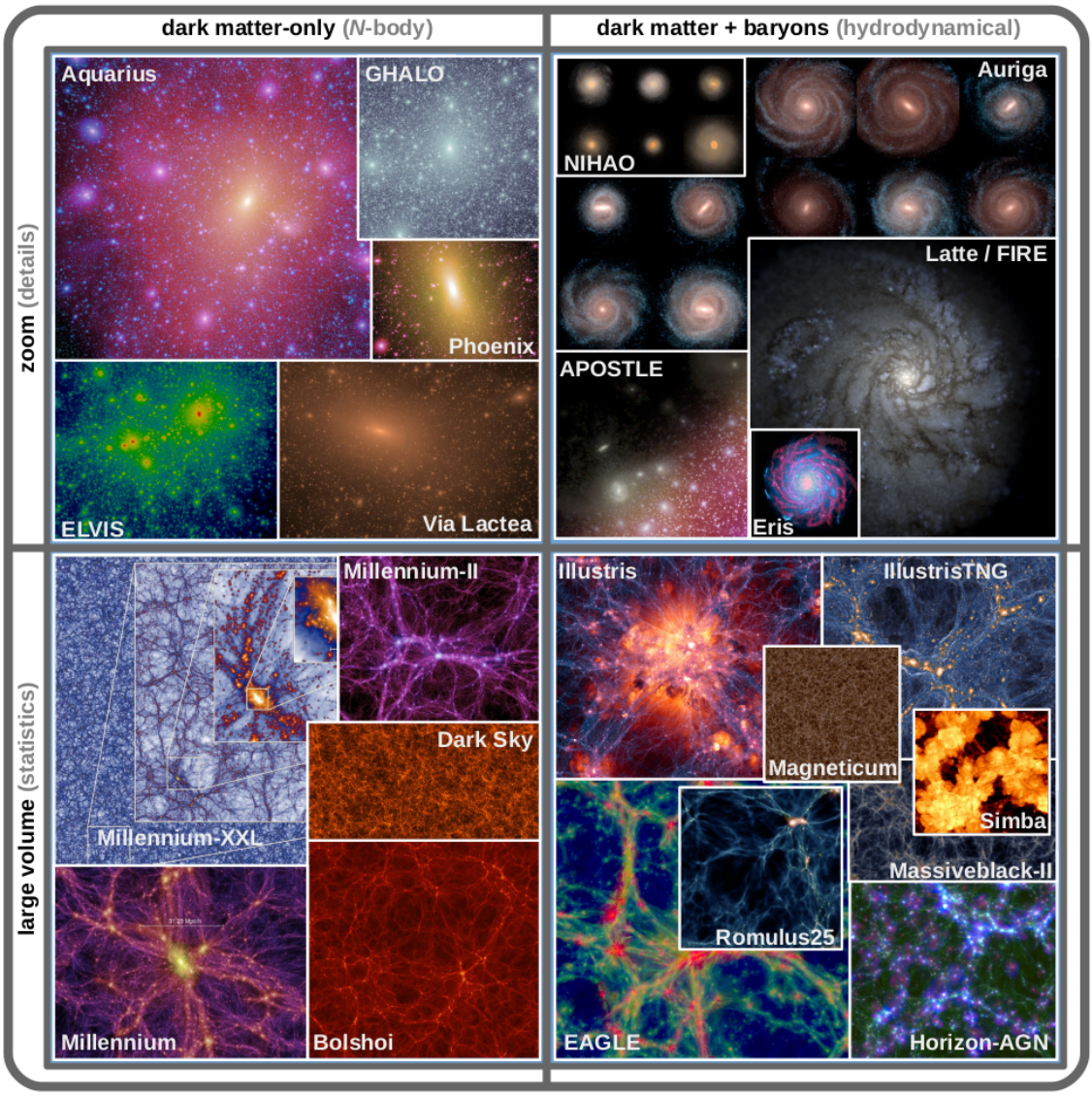

Figure 3.2: Overview of various simulations as described in Sec. 3.3.Figure taken from Vogelsberger et al. (2019):

CLUES (Libeskind et al., 2010) and COCO (Hellwing et al., 2016). The spatial resolution can range from 0.02 kpc (Aquarius) to 0.33 kpc (COCO).

On top right, we show zoom-in, hydrodynamical simulations: Eris (Guedes et al., 2011), NIHAO (Wang et al., 2015), APOSTLE (Sawala et al., 2016), Auriga (Grand et al., 2017) and Latte/FIRE (Wetzel et al., 2016). Along with these, there are some other notable works such as VELA (Ceverino et al., 2014), MACSIS (Barnes et al., 2016), Cluster-EAGLE (Barnes et al., 2017), The Three Hundred Project (Cui et al., 2018), FABLE (Henden et al., 2018), and RomulusC (Tremmel et al., 2018). These simlations can range in spatial resolution from 0.03 kpc (VELA) to 9.59 kpc (The Three Hundred Project).

On bottom left, we show large volume DM only simulations: Millennium (Springel et al.,

2005b), Millennium-II (Boylan-Kolchin et al., 2009), Bolshoi (Klypin et al., 2011), Millennium-XXL (Angulo et al., 2012) and Dark Sky (Skillman et al., 2014). We can also refer to Horizon 4π (Teyssier et al., 2009), Full Universe Run (Alimi et al., 2012), Multidark (Prada et al., 2012), ν^2Gc (Ishiyama et al., 2015), Q-Continuum (Heitmann et al., 2015), OuterRim (Habib et al., 2016) and EuclidFlagship (Potter et al., 2016) for further reference. The cosmological volume (spatial resolution) can range from (137 Mpc)^3 (1.37 kpc) (Millennium-II) to $(29167\mathrm{Mpc})^3$ (55.6 kpc) (Full Universe Run).

Finally, we show large volume baryonic simulations on the bottom right: Illustris (Vogelsberger et al., 2014), Horizon-AGN (Dubois et al., 2014), EAGLE (Schaye et al., 2015b), MassiveBlack-2 (Khandai et al., 2015), Magneticum (Bocquet et al., 2015), Romulus25 (Tremmel et al., 2017), IllustrisTNG (Springel et al., 2017) and Simba (Davé et al., 2019). Apart from these it is worthwhile to mention Bluetides (Feng et al., 2015), MUFASA (Davé et al., 2016) and BAHAMAS (McCarthy et al., 2016). In this case, the cosmological volume ranges fromc$(25^3\mathrm{Mpc})^3$ (Romulus25) to $(574^3\mathrm{Mpc})^3$ (Bluetides) whereas the DM (gas) spatial resolution can range from 0.24 (0.19) in Bluetides (IllustrisTNG) to 2.64 (2.64) in MassiveBlack-2.

After this brief overview, we finally proceed to discuss the hydrodynamical simulations adopted in this work.

3.4 Hydrodynamical simulations used in this work

In this section, we describe the cosmological hydrodynamical simulations adopted in this work. We select simulations from the suites introduced by Valentini et al. (2021) – hereafter V21 – and Barai et al. (2017) – hereafter B18.

The simulations are performed with the TreePM (particle mesh) + SPH (Smoothed Particles Hydrodynamics) code GADGET-3, an evolution of the public GADGET-2 code (Springel, 2005), and follow the evolution of a $\sim 10^{12}$ $\mathrm{M}_\odot$ halo at $z = 6$. In particular, we consider the following runs from V21:

- *AGN_fid*: our fiducial model, featuring thermal AGN feedback;
- *BHs_noFB*: a control run, analogous to AGN_fid, in which BHs and their accretion are

included, but AGN feedback is turned off;

and the following runs from B18:

- *AGNcone*: in which the kinetic feedback is distributed in a bi-cone with and half-opening angle of 45 °.
- *AGNsphere*: featuring isotropic, kinetic AGN feedback;

We selected these specific simulations to investigate the impact of different AGN feedback mechanisms on the GW predictions. The objective was to compare two simulations that are identical in resolution and other parameters, but differing only in the AGN feedback prescriptions used. As a result of this comparison, we can quantify the importance of AGN feedback on the merger rates and consequently the GW observables detected by LISA. This allows us to obtain order-of-magnitude estimates of how variations in AGN feedback models can affect GW predictions, and hence to give a broader perspective between AGN feedback and the evolution of massive black hole binaries.

We summarise in the following sections the other main features of the simulations that are relevant for the present study, while we refer to the aforementioned papers for details.

3.5 V21 simulations: *AGN_fid* and *BHs_noFB* runs

3.5.1 Initial conditions and resolution

The initial conditions are generated with the code MUSIC[1] (Hahn & Abel, 2011), assuming a ΛCDM cosmology[2]. First, a dark matter (DM)-only simulation is run from $z = 100$ to $z = 6$, with DM particles having a mass of 9.4×10^8 $\mathrm{M}_\odot$ in a comoving volume of $(148\ \mathrm{Mpc})^3$. Then, a halo as massive as $M_{\mathrm{halo}} = 1.12 \times 10^{12}$ $\mathrm{M}_\odot$ at $z = 6$ is selected for a zoom-in procedure, to run the full hydrodynamical simulation. In the zoom-in region, the highest resolution particles

[1] MUSIC–Multiscale Initial Conditions for Cosmological Simulations: `https://bitbucket.org/ohahn/music`.

[2] We adopt the following parameters by the Planck Collaboration et al. (2016): $\Omega_{\mathrm{M},0} = 0.3089$, $\Omega_{\Lambda,0} = 0.6911$, $\Omega_{\mathrm{B},0} = 0.0486$, $H_0 = 67.74\ \mathrm{km\ s^{-1}\ Mpc^{-1}}$.

Table 3.1: Summary of the main features of the suites of the cosmological hydrodynamical simulations adopted in this work (Valentini et al. 2021, Barai et al. 2017)

	AGN_fid	***BHs_noFB***	***AGNcone***	***AGNsphere***
z=6	Mass resolution[$M_\odot$]: $m_{\rm DM} = 1.5 \times 10^6$ $m_{\rm gas} = 2.9 \times 10^5$ Gas particle smoothing length[pc]=59 Size of the zoomed region=5.25cMpc DM halo host: $M_{\rm halo} = 1.1 \times 10^{12} M_\odot$ ϵ_r = 0.03 V21		Mass resolution[$M_\odot$]: $m_{\rm DM} = 7.54 \times 10^6$ $m_{\rm gas} = 1.41 \times 10^6$ Gas particle smoothing length[pc]=211 Size of the zoomed region=5.21cMpc DM halo host: $M_{\rm halo} = 4.4 \times 10^{12} M_\odot$ ϵ_r = 0.1 B18	
$M_\star[M_\odot]$	4×10^{10}	3.5×10^{10}	7×10^{10}	6×10^{10}
SFR [$M_\odot yr^{-1}$]	200	190	200	300
$M_{\rm BH}[M_\odot]$	10^9	5×10^{11}	2×10^9	5×10^8
BHAR[$M_\odot yr^{-1}$]	35	3×10^4	89	3
Feedback	Stellar, AGN(thermal)	Stellar	Stellar, AGN(kinetic, bi-conical geometry)	Stellar, AGN(kinetic, spherical geometry)

have a mass of $m_{\rm DM} = 1.55 \times 10^6$ $M_\odot$ and $m_{\rm gas} = 2.89 \times 10^5$ $M_\odot$. The gravitational softening lengths are[3] $\epsilon_{\rm DM} = 0.72$ ckpc and $\epsilon_{\rm bar} = 0.41$ ckpc for DM and baryon particles, respectively.

3.5.2 Sub-resolution physics

- **Cooling, star formation and stellar feedback**: the multiphase interstellar medium (ISM) is described by means of the MUlti Phase Particle Integrator (MUPPI) sub-resolution model (Murante et al., 2010, 2015; Valentini et al., 2017, 2019). It features metal lines cooling, an H_2-based star formation, thermal and kinetic stellar feedback, the presence of an UV background, and the Tornatore et al. (2007) model for chemical evolution.

- **Black holes seeding and merging**: BHs are treated as collisionless sink particles. Seeds of mass $M_{\rm BH,seed} = 1.48 \times 10^5$ $M_\odot$ are implanted in DM halos with mass exceeding $M_{\rm DM,seed} = 1.48 \times 10^9$ $M_\odot$. This seeding prescription is meant to mimic in a simplistic way the DCBH scenario described in Sec. 1.5. Two BHs are allowed to merge when their

[3] We use the following convention when indicating distances: a letter *c* before the corresponding unit refers to *comoving* distances (e.g. ckpc), while the letter *p* refers to *physical* units (e.g. pkpc). When not explicitly stated, we are referring to physical distances.

relative distance becomes smaller than twice the BH gravitational softening length, and their relative velocity is lower than the sound speed of the local ISM. The final BH is set on the position of the most massive BH which underwent the merger. BH repositioning (or *pinning*) is implemented, in order to prevent BHs from wandering from the centre of the halo in which they reside: at each time-step BHs are shifted towards the position of minimum gravitational potential within their softening length (as also done in e.g. Booth & Schaye, 2009; Schaye et al., 2015a; Weinberger et al., 2017; Pillepich et al., 2018).

- **Gas accretion on BHs**: besides BH-BH mergers, black holes are also allowed to grow via gas accretion, as described by the classical Bondi-Hoyle-Lyttleton (BHL) model (Hoyle & Lyttleton, 1939; Bondi & Hoyle, 1944; Bondi, 1952; Edgar, 2004):

$$\dot{M}_{\rm Bondi} = \frac{4\pi G^2 M_{\rm BH}^2 \rho}{(c_{\rm s}^2 + v^2)^{3/2}}, \tag{3.7}$$

where G is the gravitational constant, $M_{\rm BH}$ is the BH mass, ρ is the gas density, $c_{\rm s}$ is the sound speed, and v is the velocity of the BH relative to the gas. These quantities are evaluated by averaging over the SPH gas particles within the BH smoothing length, with kernel-weighted contributions. Eq. 3.7 is used to estimate the contribution to the accretion rate from the cold and hot phase of the ISM, separately (Steinborn et al., 2015; Valentini et al., 2020). Accretion from the cold gas is reduced by taking into account its angular momentum (see Valentini et al., 2020, for details). The BH accretion rate is capped to the Eddington accretion rate.

- **Quasar feedback**: a fraction of the accreted rest-mass energy is radiated away with a radiative efficiency $\epsilon_{\rm r}$, thereby providing a bolometric luminosity for an accreting BH equals to:

$$L_{\rm bol} = \epsilon_{\rm r} \dot{M}_{\rm BH} c^2, \tag{3.8}$$

where c is the speed of light and $\epsilon_{\rm r} = 0.03$ (Sądowski & Gaspari 2017). Then, a fraction $\epsilon_{\rm f} = 10^{-4}$ (V21) of the radiated luminosity $L_{\rm bol}$ is coupled thermally and isotropically to the gas surrounding the BH. The AGN feedback energy is distributed to the hot and cold phases of the multiphase gas particles within the BH smoothing volume (Valentini et al.,

2020).

3.6 B18 simulations: *AGNcone* and *AGNsphere* runs

3.6.1 Initial conditions and resolution

Initial conditions are generated as in V21 with the code MUSIC and adopting the same cosmology. The parent, DM-only simulation follows a comoving volume of $(500\ \mathrm{Mpc})^3$, with DM particles having $m_{\rm DM} = 2\times10^{10}\ \mathrm{M}_\odot$. The zoom-in run focuses on a DM halo as massive as $M_{\rm halo} = 4.4\times 10^{12}\ \mathrm{M}_\odot$; the highest resolution particles have $m_{\rm DM} = 7.54\times10^6\ \mathrm{M}_\odot$ and $m_{\rm gas} = 1.41\times10^6\ \mathrm{M}_\odot$, with a gravitational softening length $\epsilon_{\rm bar} = \epsilon_{\rm DM} = 1.48$ ckpc.

3.6.2 Sub-resolution physics

- **Cooling, star formation and stellar feedback**: radiative heating and cooling is accounted for by employing the CLOUDY cooling tables computed by Wiersma et al. (2009). Star formation is implemented following the ISM multiphase model by Springel & Hernquist (2003), in which an hot and a cold phase co-exist in pressure equilibrium, and assuming a density threshold for the star formation of $n_{\rm SF} = 0.13\ \mathrm{cm}^{-3}$. A Chabrier (2003) initial mass function (IMF) in the mass range $(0.1-100)\ \mathrm{M}_\odot$ is adopted. Stellar evolution and chemical enrichment are computed following Tornatore et al. (2007).

- **Black hole seeding and merging**: As in B18, the theoretical mass of seed BHs is $10^5 M_\odot$. However, their dynamical mass is much smaller in the V21 simulations ($\sim 10^5\ \mathrm{M}_\odot$ in V21 versus $\sim 10^7 \mathrm{M}_\odot$ in B18). The prescription is, in fact, more refined in V21, where seeded BHs are linked to stellar particles instead of DM particles. We further discuss this point in Sec. 5.2.

- **Gas accretion on BHs**: as in V21, the BHL model is adopted. However, the lower resolution of the B18 simulations does not allow to properly describe the accretion process: thus Eq. 3.7 is multiplied by a numerical boost factor $\alpha = 100$ (Springel et al., 2005a;

Sijacki et al., 2009; Vogelsberger et al., 2014). No angular momentum effects are included in the B18 formalism, and no distinction between the hot and cold gas phases is considered.

- **Quasar feedback**: black holes are assumed to radiate energy away with an efficiency of $\epsilon_{\rm r} = 0.1$, and a fraction $\epsilon_{\rm f} = 0.05$ of this energy is coupled to the surrounding gas via kinetic feedback as an energy-driven wind (see Barai et al. (2017) for details). The geometry of the feedback is bi-conical (i.e. energy is injected onto a bi-cone with a half-opening angle of 45 °) in *AGNcone* and spherical (i.e. energy distributed isotropically) in *AGNsphere*. BHs grow ~ 10 times more massive at $z = 6$ in the *AGNcone* case than in the *AGNsphere* run as shown in top panels of fig: 2 in B18. This is because in the *AGNcone* run more gas can inflow along the perpendicular direction to the bi-cone, and accrete onto the black hole.

A summary of the two different simulation models are provided in Table 3.1 for a comprehensive view.

3.7 Summary

In this chapter we presented an overall description of cosmological simulations. In Sec. 3.1, we briefly introduce the concept behind numerical simulations. Then in Sec. 3.2, we described the three main ingredients of every cosmological simulations: the cosmological framework (described in Sec. 3.2.1), the dark matter (Sec. 3.2.2) and the baryonic components (Sec. 3.2.3). Next, we show a synopsis of modern simulations of the last two decades in Sec. 3.3; this includes N-body and hydrodynamical simulations of small (zoom-in) and large volumes of the Universe. Finally, in Sec. 3.4 we provided a thorough walk-through of the two simulations (V21 and B18) that we use in this work, underlying the common features and the main differences among them.

Radiative Transfer

4

4.1 Introduction

Radiative transfer describes how the propagation of EM radiation through medium is modified by various processes, such as absorption, scattering and re-emission (e.g. Rybicki & Lightman, 1979). Solving the RT problem is indispensable in interpreting spectra and the accompanying emission/absorption lines of numerous astrophysical objects such as galaxies, AGNs, stars, stellar atmospheres, planetary nebulae, supernovae remnants, etc.

In the context of cosmology and galaxy evolution, dust is one of the most important medium that modifies the radiation field originating from AGNs and the (young and hot) stars embedded in galaxies (see e.g. Steinacker et al., 2013). Dust grains, found in the interstellar medium, are known to absorb and scatter optical and UV radiation and re-emit in infrared and submilimeter wavelengths. Therefore, in order to correctly interpret EM observations of spectra of entire galaxies, one needs to understand how the surrounding dust modifies the radiation field.

In this work, to solve the RT problem through a dusty medium we use the code `SKIRT`. In what follows, we first discuss the RT problem in a general context (Sec. 4.2, 4.3, and 4.4) and then we introduce the main features of the `SKIRT` code (Sec. 4.5).

4.2 Equation of radiative transfer

The radiative field is characterised by the specific intensity $I(\mathbf{x}, \mathbf{n}, \lambda)$. By definition, it is the energy carried away by EM radiation of wavelength λ per unit time, at a location $\mathbf{x}$, in a unit

solid angle $d\Omega$, in the direction of $\mathbf{n}$. The RT equations describe how the specific intensity changes due to the various interactions between the radiation and the medium and in a general form can be given as (Chandrasekhar, 1960; Rybicki & Lightman, 1979):

$$\mathbf{n} \cdot \nabla I(\mathbf{x}, \mathbf{n}, \lambda) = \kappa(\mathbf{x}, \lambda)\rho(\mathbf{x})I(\mathbf{x}, \mathbf{n}, \lambda) + j(\mathbf{x}, \mathbf{n}, \lambda), \tag{4.1}$$

where the left-hand term describes the change in specific intensity of the radiation along the path defined by $\mathbf{n}$. The first term on the right-hand side describes extinction, which encompasses all the processes that dissipate the energy from the radiative field (e.g. due to absorption and scattering). In the extinction term, κ is the mass extinction coefficient and ρ is the density of the medium. The second term on the right-hand side is the source term, which describes the radiant energy added to the field at $\mathbf{x}$ along $\mathbf{n}$. This could originate from AGNs or stars, or from the intervening medium, e.g. from its free electrons via Bremsstrahlung emission or via thermal emission from dust particles.

In the context of RT in dusty media, equation 4.1 can be recast in a more specific form that also highlights the challenges of solving the RT equation:

$$\frac{dI}{ds}(\mathbf{x}, \mathbf{n}, \lambda) = \kappa_{\rm abs}(\mathbf{x}, \lambda)\rho(\mathbf{x})I(\mathbf{x}, \mathbf{n}, \lambda) + \kappa_{\rm sca}(\mathbf{x}, \lambda)\rho(\mathbf{x})I(\mathbf{x}, \mathbf{n}, \lambda) + j_*(\mathbf{x}, \mathbf{n}, \lambda) + j_{\rm d,th}(\mathbf{x}, \lambda) + \kappa_{\rm sc}(\mathbf{x}, \lambda)\rho(\mathbf{x}) \int_{4\pi} \Phi(\mathbf{n}, \mathbf{n}', \mathbf{x}, \lambda) I(\mathbf{x}, \mathbf{n}', \lambda) d\Omega'. \tag{4.2}$$

In this equation, four different processes are distinguished:

- *Absorption:* it occurs when a photon is absorbed by a dust grain and its energy is transformed into the internal energy of the dust grain. It is characterised by the first term on the right-hand side of equation 4.2.

- *Scattering:* this occurs when a photon is scattered in a random direction by a dust particle. It is described by the second (sink term) and the last term (source term) in equation 4.2. In the source term, the phase function $\Phi(\mathbf{n}, \mathbf{n}', \mathbf{x}, \lambda)$ determines the probability that an incoming photon propragating along $\mathbf{n}'$ is scattered at $\mathbf{x}$ in a direction of $\mathbf{n}$.

- *Primary emission:* this is characterised by j_* in equation 4.2. It includes all sources of

radiation that is not due to the dust, for example radiation from AGN, stars and ionized gas.

- *Thermal emission from dust:* characterised by $j_{\mathrm{d,th}}$. This typically occurs on wavelengths of $\lambda_{\mathrm{d,th}} \gtrsim 1\,\mu\mathrm{m}$ and it is mostly driven by the increased internal energy caused by absorption.

There are several complicating factors that make equation 4.2 particularly hard to solve. Firstly, scattering acts as a sink, as well as a source term, since the interacting photons are not absorbed but instead scattered in random directions. The radiation field becomes coupled at different positions and different directions (see the integral term in equation 4.2) and this introduces a significant layer of complexity in solving the RT problem for dusty media. Mathematically, this means that the RT equation becomes an integro-differential equation, which is computationally expensive to solve. Furthermore, dust scattering is anisotropic, especially for the UV-NIR range (Mattila, 1970; Calzetti et al., 1995; Burgh et al., 2002; Gordon, 2004). Therefore, simple approximations for the phase functions (e.g. assuming isotropy or two-stream approximations, see e.g. Code & Whitney, 1995; Natta & Panagia, 1984; Calzetti et al., 1994) are known to introduce significant errors (e.g Bruzual A. et al., 1988; Witt et al., 1992; Baes & Dejonghe, 2001) and therefore are not sufficient for an accurate description of the radiative field in dusty environments. The most commonly used phase functions in this context are based on the parameterization of Henyey & Greenstein (1941), see e.g. Kattawar (1975); Hong (1985); Draine (2003b).

Secondly, in dusty media, there is a diverse range of dust grain species present, with different characteristic sizes, shapes, chemical compositions and consequently with different mass absorption coefficients. Consequently, absorption and scattering coefficients in equation 4.2 need to be determined as a number-density-weighted sum of coefficients of each dust grain type, i.e.:

$$\kappa_{\mathrm{abs}}(\mathbf{x}, \lambda) = \sum_i w_i(\mathbf{x}) \kappa_{\mathrm{abs,i}}(\lambda), \tag{4.3}$$

$$\kappa_{\mathrm{sc}}(\mathbf{x}, \lambda) = \sum_i w_i(\mathbf{x}) \kappa_{\mathrm{sc,i}}(\lambda), \tag{4.4}$$

where $w_i(\mathbf{x})$ is the number density of the ith dust species.

Thirdly, the thermal emission from dust grains can be challenging to compute, especially for grains with relatively small sizes. It is commonly assumed that the dust grains are in thermal equilibrium with the local radiation field. In this case, the emissitivty $j_{\rm dt,th}$ can be determined as (see e.g. Steinacker et al., 2013):

$$j_{\rm dt,th} = \sum_i w_i(\mathbf{x}) \kappa_{\rm abs,i}(\lambda) \rho(\mathbf{x}) B[T_i(\mathbf{x}), \lambda], \tag{4.5}$$

where the sum is over different types of dust grains and $B[T_i(\mathbf{x}), \lambda]$ is the Planck function. Note that, generally, the equilibrium temperature is different for different types of dust grains. The equilibrium temperature then can be determined by the principle of energy balance, assuming that the total amount of absorbed energy by a dust grain species i equals to the total amount of energy emitted via thermal radiation:

$$\int_0^\infty \kappa_{\rm abs,i}(\lambda) J(\mathbf{x}, \lambda) d\lambda = \int_0^\infty \kappa_{\rm abs,i}(\lambda) B[T_i(\mathbf{x}), \lambda] d\lambda, \tag{4.6}$$

where $J(\mathbf{x}, \lambda) = 1/4\pi \int_{4\pi} I(\mathbf{x}, \mathbf{n}, \lambda) d\Omega$, that is the mean intensity of the local radiation field.

4.3 Methods to solve the radiative transfer problem

Previous sections highlighted the complexity of solving 3D dust RT problems. Over recent years, various strategies have been developed to address this challenge (see also Steinacker et al., 2013). In this section, we summarise the most popular methods that can be used to solve the RT problem.

- **Finite difference:** This method involves discretising the RT problem and numerically solving the RT equations (see e.g. Stenholm et al., 1991). Since a large number of quantities are involved (3D spatial and directional coordinates, wavelength and dust properties), even a sparse grid requires immense computational power and memory. Due to this high dimensionality, the choice of an optimised grid is crucial. These include adaptively refined (hierarchical) Cartesian grids (see e.g. Kurosawa & Hillier, 2001; Lunttila & Juvela, 2012; Niccolini & Alcolea, 2006) and multiwavelength adaptive mesh refinement grids

(see e.g. Steinacker et al., 2002). Numerically solving the 3D RT equation can be computationally extremely expensive, even on optimised grids. Therefore, this method is often only used for 1D or 2D problems (for example, problems where the dust distribution have symmetry).

- **Moment-based methods:** In this method, the zeroth and the first moments of the RT equations are solved. This approach reduces the angular dimensions of the RT equations. In this approximation, the bulk motion of the photons are described and the simplified RT equations become similar to the Euler equations of hydrodynamics and thus can be solved with methods designed for hydrodynamics (see e.g. Rosdahl et al., 2013). Mathematically, the zeroth and the first moment of the RT equations can be expressed with three unknowns: the zeroth, the first and the second moment of the specific intensity, which are the radiation energy density, the radiation flux and the tensor of the radiation pressure, respectively (see e.g Mihalas & Mihalas, 1984). In order to solve for the radiative field through the moment-based method, an additional relation is needed, namely the so-called "closure relation", which parametrizes the relationship between the moments of the specific intensity. A commonly used (see e.g. González et al., 2007; Rosdahl & Teyssier, 2015) approach is the M1 closure relation (Levermore, 1984).

- **Ray-tracing:** The basis of the ray-tracing approach is to solve the RT equation along a given direction, i.e. along a *ray* (see e.g. Abel & Wandelt, 2002; Steinacker et al., 2013). This approach also requires discretisation. It is typically assumed that in a grid cell, the mass density (ρ_0), the mass extinction coefficient (κ_0) and the source function (j_0) are constant for a given wavelength. The grid cells crossed by the ray have to be identified and the change in intensity along the ray in each cell has to be determined as:

$$I(s + \Delta s, \lambda) = I(s, \lambda)e^{\tau_0(\lambda)} + \frac{j_0(\lambda)\Delta s}{\tau_0(\lambda)} \left(1 - e^{-\tau_0(\lambda)}\right), \tag{4.7}$$

where the intensity changes from from $I(s, \lambda)$ to $I(s + \Delta s, \lambda)$ in a grid cell and $\tau_0 = \kappa_0(\lambda)\rho_0\Delta s$, where Δs is the spatial interval used to discretize the line of sight. One of the most challenging part of the Ray-tracing method is to find the optimal strategy of casting

rays across the computational domain that delivers the global solution to the RT problem with a sufficient accuracy. This optimal strategy is sensitively dependent on the types and spatial distribution of radiative sources (see e.g. Fig. 3 of Steinacker et al., 2013).

- **Monte Carlo method:** This method is perhaps the most widely adopted approach to solve complex 3D dust RT problems. This can be considered as a more sophisticated variation of the Ray-tracing method, in which a large number of photon packets are generated and followed. A defining characteristic of this method is its probabilistic nature. We discuss this approach in more details in the next section since this method is used by the `SKIRT` code.

4.4 Monte Carlo approach

The term Monte Carlo (MC) is used to describe a broad class of techniques that is often applied to find an approximate solution for a wide range of physical and mathematical problems. The basis of this approach is to generate a large number of random samples from a specific probability distribution, which characterises the given problem (see e.g. Metropolis & Ulam, 1949; Mackay, 2003). This approach has also been successful in solving complicated 3D dust RT problems (e.g. Mattila, 1970; Roark et al., 1974; Witt, 1977; Baes et al., 2003; Stamatellos & Whitworth, 2003; Niccolini et al., 2003; Gonçalves et al., 2004; Juvela & Padoan, 2003; Whitney et al., 2003; Pascucci et al., 2004; Kurosawa et al., 2004).

An MC simulation is initiated with launching a large number of photon packets (usually called simply photons) from the radiative sources. The paths and interactions of these photons are tracked, until they are absorbed by the medium or leave the computational domain. The properties of the sampled photons, such as their initial location and propagation direction, wavelength and the location and type of their interactions are determined in a probabilistic fashion, i.e. by drawing samples from pre-specified probability density functions that characterise all the relevant physics involved in the process. Consequently, the MC method provides an approximate, numerical solution to the RT problem, which is subject to Poisson noise. The accuracy can simply be increased by generating more photons.

Below, we summarise the most important ingredients of this method in the context of 3D dust radiative problem by following the discussion of Steinacker et al. (2013). For simplicity, we assume a steady-state, monochromatic emission only. This means that all the emitted photons have a frequencty of ν and both the source emissitivity $j_*(\mathbf{x}, \mathbf{n}, \nu)$ and its total luminosity $L_{\rm tot}(\nu)$ are independent of time. If the emission from all the radiative sources is represented with N number of generated photons, then each is assumed to carry a luminosity of $L(\nu) = L_{\rm tot}/N$. The initial position and propagation is sampled from the following PDF:

$$p(\mathbf{x}, \mathbf{n}) d\mathbf{x} d\mathbf{n} = \frac{j_*(\mathbf{x}, \mathbf{n}, \nu)}{L_{\rm tot}(\nu)}, \tag{4.8}$$

which, in case of a point source and isotropic emission, reduces to a uniform distribution on the solid angle:

$$p(\mathbf{n}) d\mathbf{n} = \frac{d\mathbf{n}}{4\pi} = \frac{\sin\theta \mathrm{d}\theta \mathrm{d}\phi}{4\pi}, \tag{4.9}$$

where θ and ϕ are the polar and azimuthal angles, known from the standard spherical coordinate system.

Once the photons are launched from the radiative source, the photon path and the interactions with the medium is determined. The PDF describing the free path length before an interaction can be expressed in terms of the optical depth as $p(\tau) = e^{-\tau} d\tau$. This means that the optical depth that a particular photon travels through before interactions is sampled from an exponential distribution. In practice, this sampling is carried out via transformation method; a random number (ξ) is generated from a uniform distribution and then τ is determined via the following equation:

$$\xi = \int_0^{\tau} e^{-\tau'} d\tau. \tag{4.10}$$

If the sampled τ is larger than the physical optical depth evaluated up to the surface of the computational domain in the direction of propagation ($\tau_{\rm path}$), then the photon is assumed to have escaped the system. Otherwise (i.e. $\tau < \tau_{\rm path}$), the sampled optical depth is converted into a physical location of the interaction. This is equivalent to solving following equation for s:

$$\int_0^{s} \kappa_{\rm ext}(s', \lambda) \rho(s') ds' = \tau. \tag{4.11}$$

Once the location of the interaction is known, the type of the interaction is determined. The particle can either be scattered or absorbed, where the probability of the latter is given by the dust albedo, i.e. $a = \kappa_{\rm ext}/\kappa_{\rm ext}$. The type of the interaction is again determined by sampling a number (ξ) from a uniform distribution. The photon is scattered, if $\xi \leq a$, and absorbed, if $\xi > a$.

In case of absorption, the photon is removed from the simulation and the absorbed luminosity is stored in the interaction cell, which is then later used to calculate the dust thermal emission. In case of scattering, the propagation direction is calculated from the PDF constructed from the scattering phase function:

$$p(\mathbf{n})d\mathbf{n} = \frac{\Phi(\mathbf{n}, \mathbf{n}^{'}, \mathbf{x}, \lambda)d\mathbf{n}}{4\pi}, \tag{4.12}$$

where $\mathbf{n}$ and $\mathbf{n}^{'}$ are the new and the original direction of the photon, respectively. The steps described by equation 4.10-4.12 are repeated for each photon until it either leaves the computational domain or it gets absorbed by an interaction cell. The large number of scatterings in regions with large optical depth can lead to significant computational demands. To overcome this issue, simulations frequently set a cap on the maximum number of scatterings that can occur, however this can introduce systematic errors in the calculation (see Steinacker et al., 2013).

4.5 SKIRT

SKIRT[1] is a publicly available, multi-purpose 3D Monte Carlo dust radiative transfer code (Baes et al., 2003; Baes & Camps, 2015; Camps & Baes, 2015; Camps et al., 2018). By taking into account absorption, multiple anisotropic scattering and stochastic heating of small dust grains, SKIRT self-consistently determines the temperature distribution of the dust, its thermal re-emission and consequently the radiative field in a dusty medium. An important feature of SKIRT is that it offers flexibility in several aspects of the simulation setup. It can deal with 3-D snapshots from SPH, AMR, and Voronoi-grid-based hydrodynamical simulations as inputs for the density distribution of dust, gas and for the positions of radiative sources. SKIRT can be applied to a wide range of different astrophysical systems, such as dusty galaxies (e.g. Baes &

[1] http://www.skirt.ugent.be

Dejonghe, 2002; Baes et al., 2010, 2011; De Looze et al., 2012; De Geyter et al., 2014; Saftly et al., 2015; Behrens et al., 2018), AGNs (e.g. Stalevski et al., 2012), and stellar systems (e.g. Deschamps et al., 2015). Multiple dust mixtures, different types of radiative sources and various physical mechanisms (e.g. self-absorption) can also be easily implemented in `SKIRT`.

4.5.1 Dust properties and implementation

The properties of dust that significantly influence the observed SEDs are the total dust mass, its chemical composition, and the grain size distribution (e.g. Mathis et al., 1977; Bohren et al., 1983; Weingartner & Draine, 2001; Draine et al., 2007; Nozawa & Fukugita, 2013; Asano et al., 2014).

The total dust mass is typically parameterised in terms of the total metal mass (e.g. Draine et al., 2007):

$$f_d = \frac{M_d}{M_z}, \tag{4.13}$$

where f_d is the dust-to-metal ratio, M_d is the dust mass and M_z is the gas-phase metal mass. Observations suggest that low redshfit spiral galaxies, including the Milky way, have a dust-to-metal ratio of $f_d \approx 0.3$ (e.g. Spitzer, 1978; Issa et al., 1990; Hirashita, 1999; Edmunds, 2001). On the other hand, f_d remains poorly constrained for high redshift galaxies (see e.g. Wiseman et al., 2017). Semi-analytical models exist that describe the evolution of f_d as a function of initial (gas-phase) metallicity and time (see e.g. Inoue, 2003; Asano et al., 2013a,b; Nozawa et al., 2015; Aoyama et al., 2017). Yet, reliable quantitative predictions for f_d are not yet available, as the predictions of these models are sensitively dependent on several poorly constrained processes. These include dust accretion and and growth (e.g. Dwek, 1998; Liffman & Clayton, 1989; Jones & Nuth, 2011), dust destruction due to supernova blast waves (Jones et al., 1994, 1996; Nozawa et al., 2015), yields from different dust forming channels, e.g. from type II supernova, (Liang & Li, 2009) or from AGB stars (Valiante et al., 2009).

Recently (Behrens et al., 2018) showed that the SED of the A2744YD dusty galaxy at $z \approx 8.4$ (Laporte et al., 2017) can be reproduced with a Milky-Way-like extinction curve and a dust-to-metal ratio of $f_d \approx 0.1$, broadly consistent with the findings of Asano et al. (2013a) and Aoyama et al. (2017). Motivated by these results, we adopt $f_d = 0.1$ in the following chapters.

In order to characterise the chemical composition and grain size distribution of dust, we follow the model of Weingartner & Draine (2001) developed to reproduce the extinction curve of the SMC. This assumes that the dust is composed of carbonaceous and silicate grains, but does not contain any polycyclic aromatic hydrocarbons (PAH) molecules. Due to the lack of PAHs, the smallest dust grains have a characteristic size of $a_{\rm dust} \approx 10^{-3}\mu{\rm m}$ (as opposed to $a_{\rm dust} \approx 4\times10^{-4}\mu{\rm m}$ for dust mixtures with PAH molecules). We also assume that all dust grains are in thermal equilibrium with the local radiation field. The grain temperature and emissivity is then determined via Eq. 4.6 for all dust species. Self-absorption by dust is taken into account, however, heating from CMB is neglected. Furthermore, it is assumed that gas particles hotter than 10^6 K are dust-free, since at such high temperatures thermal sputtering efficiently destroys the dust (see e.g. Draine & Salpeter, 1979; Tielens et al., 1994; Hirashita, 2015).

4.5.2 Radiation: sources and implementation

The primary sources of the UV radiation that is responsible for dust heating are (young, massive) stars and accreting BHs. Below, we briefly describe these sources and the motivation behind the implementation.

- **Stars**

  Each particle in the simulation that is associated with star formation is transformed into a Single Stellar Population (SSP), which is characterised by a time-dependent SED that is equivalent to a large cluster of stars formed at the same time and the same metallicity and following a given initial mass function. The intrinsic SED from an SSP is modelled following by Bruzual & Charlot (2003), which assumes an IMF of Chabrier (2003).

- **AGN**

  Accreting BHs are treated as point sources, as the typical size of an accretion disk ($\lesssim 10\,{\rm pc}$) is much smaller than the size of grid cell.

  The shape of the SED of an AGN is dominantly determined by physical processes associated with the gas accretion on the SMBH (e.g. Shakura & Sunyaev, 1973). Several, AGN

SED templates exist which are mostly motivated from observations (see e.g. Vanden Berk et al., 2001; Richards et al., 2006; Hopkins et al., 2007; Sazonov et al., 2004; Krawczyk et al., 2013; Lusso et al., 2015; Manti et al., 2016; Shen et al., 2020).

In our models, we adopt the following piece-wise continuous, composite power-law to model the intrinsic emission from AGNs:

$$L_\lambda = c_i \left(\frac{\lambda}{\mu\mathrm{m}}\right)^{\alpha_i} \left(\frac{L_{\mathrm{bol}}}{L_\odot}\right) L_\odot \mu\mathrm{m}^{-1}, \tag{4.14}$$

where i is the index denoting the wavelength band, α_i is the power-law index for each band, c_i is the coefficient that determines the normalisation of the SED and also ensures continuity across different band, and L_{bol} is the bolometric luminosity.

In Table 4.1, we summarise the chosen values for α_i and c_i for each wavelength band. For the hard X-ray band (2-10 keV, corresponding to 1.2-6.2 Å), we follow Piconcelli et al. (2005) and adopt $\alpha_{\mathrm{X,hard}} = -1.1$. Fiore et al. (1994) finds $-0.7 < \alpha_{\mathrm{X,soft}} < 0.3$ for the soft X-ray band (0.5-2 keV, corresponding to 6.2-24.8 Å). We adopt the lower end of this range (i.e. $\alpha_{\mathrm{X,soft}} = -0.7$) and extrapolate this relation up to $\lambda = 50$ Å. For the wavelength band between X-ray and Extreme UV (50Å $< \lambda <$ 912Å), we follow Shen et al. (2020) and assume $\alpha = 0.4$. For the Extreme UV (EUV), we apply $\alpha_{\mathrm{EUV}} = -0.3$, following Lusso et al. (2015). For the wavelength range 912Å $< \lambda <$ 5000Å, we adopt $\alpha = -1.5$, which is in broad agreement with the observations of low redshift ($z \lesssim 2.4$) quasars (see Richards et al., 2003; Lusso et al., 2015). For the infrared band of the spectrum we assume it follows the Rayleigh-Jeans tail of a blackbody spectrum (i.e. $\alpha = -4$).

If a dusty torus is present around the SMBH, it provides a signficant contribution to the IR band of the SED (see e.g. Schartmann et al., 2005; Nenkova et al., 2008; Stalevski et al., 2012, 2016). Since the torus cannot be resolved in our simulations (as they have characteristic sizes of $\sim$ 1-10 pc), we neglect its contribution.

- **Implementation**

  The photon rest-freame wavelength grid ranges from 0.1 μm to 10^3 μm. The lower limit approximately coincides with the Lyman-limit ($\lambda = 91.2$ nm). This choice is determined

by the fact that hydrogen photoionization is not treated in our simulations (similarly to several other studies, such as Schneider et al., 2015; Behrens et al., 2018). The choice of the upper limit is motivated by the fact that above this wavelength the dust thermal emission in typically negligible.

In a simulation run, 10^6 photons are initialised per each wavelength bin and per each grid cell that contains a radiative source. We track the radiation escaping from our computational domain along six lines of sight, each perpendicular to the faces of the cube-shaped computational domain.

Table 4.1: The parameters for the composite power-law AGN SED shown in Eq. 4.14.

	hard X-ray	**soft X-ray**	**X-ray to EUV**	**EUV**	**UV to NIR**	**NIR to FIR**
λ_i [Å]	[1.2-6.2]	[6.2-50]	[50-600]	[600-912]	[912-5000]	[500-10^6]
c_i	2	0.042	14.13	1,972	0.111	6.225
α_i	-1.1	-0.7	0.4	-0.3	-1.5	-4.0

Part III

Analysis and results

Coalescence rate of MBHBs

5

5.1 Introduction

In this chapter we present our first results on the coalescence rates of MBHBs in our simulations. In Sec. 5.2, we calculate the merger rate of MBHBs in the overdense regions considered in our simulations. We compare the results from B18 and V21 for different AGN feedback models and discuss the possibility of differentiating the different runs from the merger rates of the MBHBs. In Sec. 5.3, we examine the bias that arises from considering overdense regions in our simulations and estimate the correction factor for this bias semi-analytically. Finally, we conclude this chapter in Sec. 5.4 by comparing our results with contemporary works involving SAMs and HDS.

5.2 Merger rate from overdense regions

For the models summarised in Tab. 3.1, we compute the redshift evolution of the MBH merger rate (per unit redshift, per unit time) for different chirp mass ranges, where Eq. 2.41 can be simplified as (e.g. Cutler & Flanagan 1994; Blanchet et al. 1995):

$$\mathcal{M}_c = \frac{(m_1 m_2)^{3/5}}{(m_1 + m_2)^{1/5}}, \tag{5.1}$$

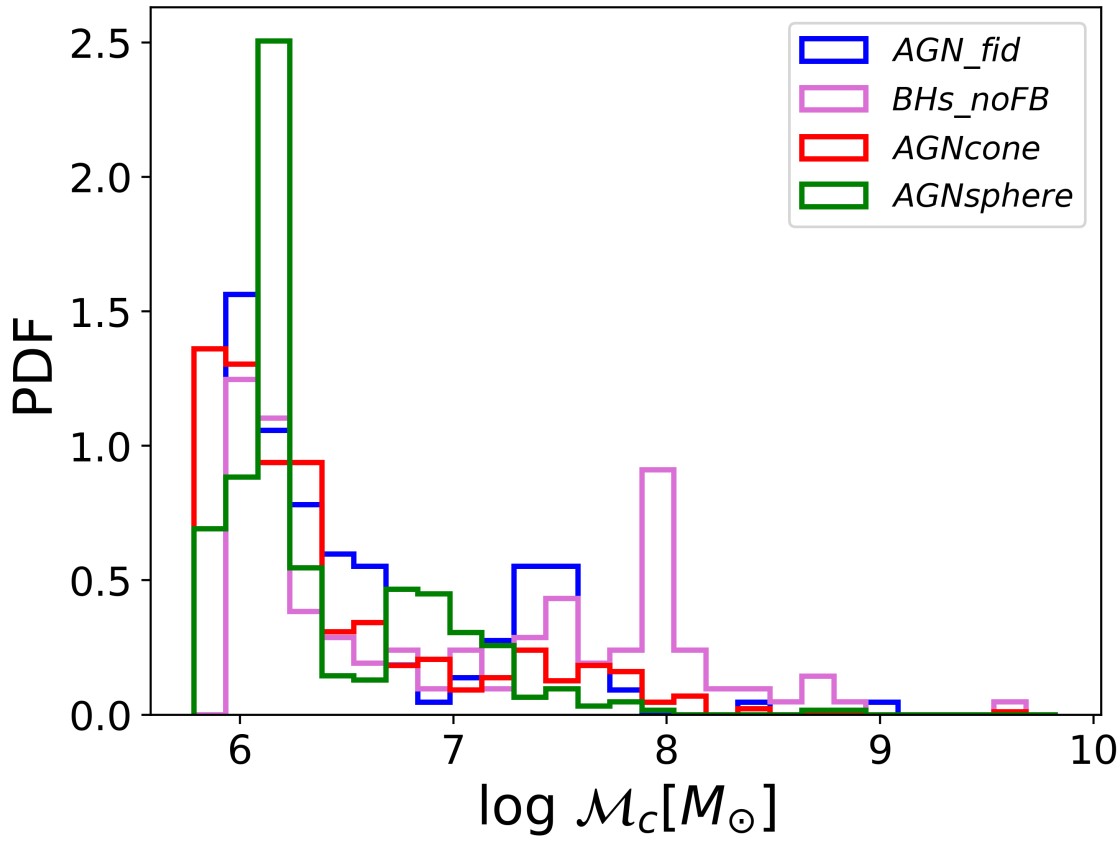

Figure 5.1: PDF of chirp mass as resulting from the *AGN_fid* (blue), *BHs_noFB* (magenta), *AGNcone* (red) and *AGNsphere* (green).

and m_1 and m_2 are the masses of the merging black holes[1]. We show in Fig. 5.1 the normalized probability distribution function (PDF) of the chirp masses resulting from different simulations. Although no evident differences among different models can be seen from this plot, we note that the B18 simulations predict a larger number of small chirp masses ($\mathcal{M}_c < 10^6 \mathrm{M}_\odot$) with respect to to V21, and only the *BHs_noFB* and *AGNcone* simulations predict MBHBs with $\mathcal{M}_c > 10^9 \mathrm{M}_\odot$.

We then calculate the merger rate from the number density of mergers, dN/dz per comoving volume, dV as (e.g. Haehnelt 1994; Ciardi & Loeb 2000):

$$\frac{dN}{dz dt_{\rm obs}} = \frac{4\pi c d_L^2}{(1+z)^2} \frac{dN}{dz dV}, \tag{5.2}$$

where d_L is the luminosity distance of the event. The results are shown in Fig. 5.2.

[1] In these calculations, we do not include those MBHBs that cannot be associated with any galaxy in the simulations. We discuss these spurious events in Sec. 6.2

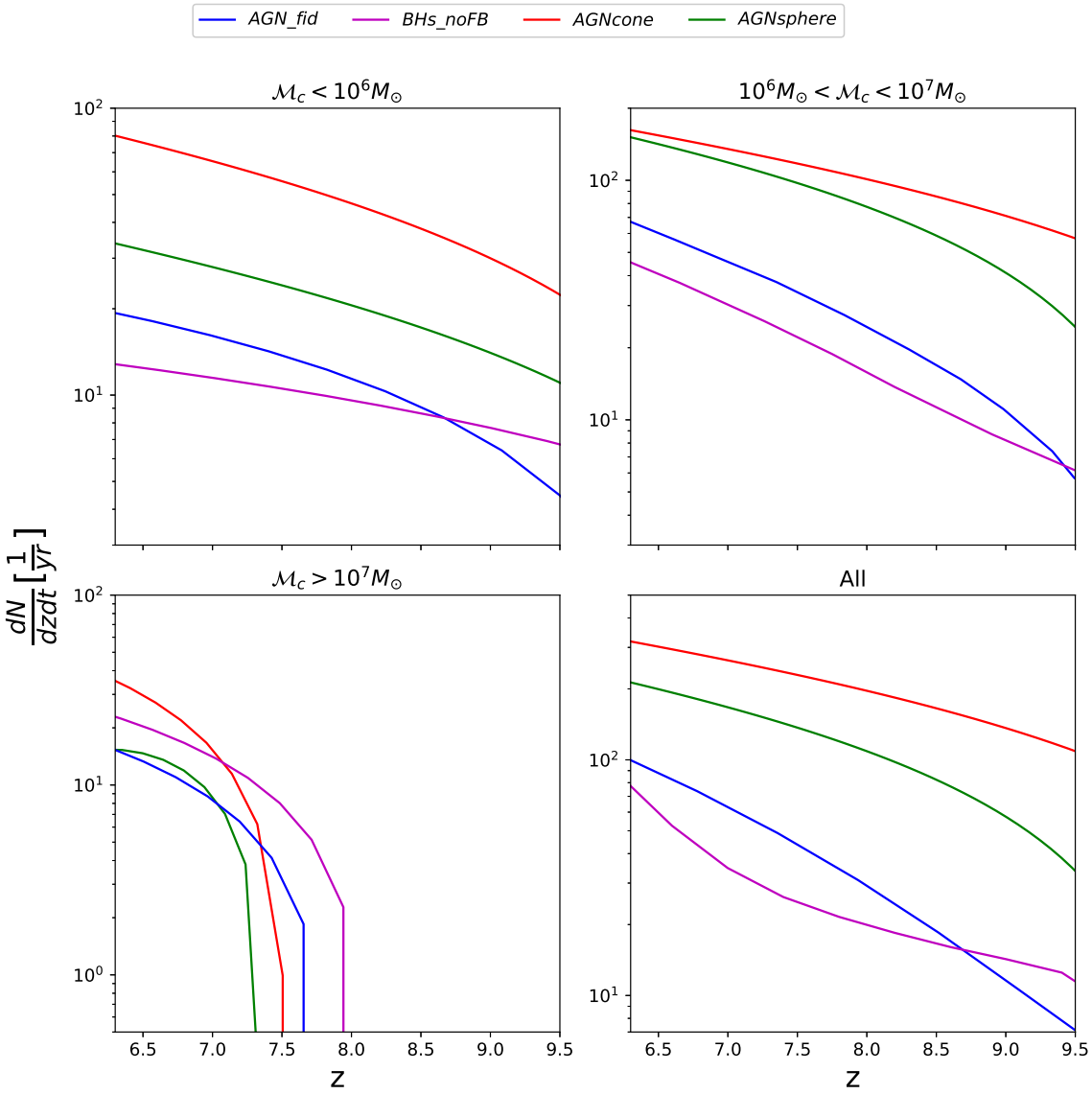

Figure 5.2: Number of mergers per unit redshift per unit time for *AGN_fid* (blue), *BHs_noFB* (purple), *AGNcone* feedback (red), and *AGNsphere* feedback (green). The upper left (right) panel shows the merger rates for MBHB systems with chirp mass $< 10^6 M_\odot$ ($10^6 < \mathcal{M}_c < 10^7 M_\odot$); the lower left panel shows the merger rates for chirp mass $>10^7 M_\odot$, while the lower right panel refers to the the cumulative merger rates for all chirp mass ranges.

The number of MBH mergers predicted by our zoom-in cosmological simulations increases with decreasing redshift, as a consequence of the hierarchical structure formation process. Fig. 5.2 shows that the two sets of simulations have different merging histories that depend both on the numerical resolution adopted and on the feedback implemented.

In particular, Fig. 5.2 shows that the number of mergers predicted by the V21 simulations (~ 100 at $z = 6.5$ for both *AGN_fid* and *BHs_noFB*) is smaller by a factor of at least 2 than the one by the B18 simulations (>200 for both *AGNcone* and *AGNsphere* case at $z \sim 6.5$). This major difference is likely linked to the better numerical resolution of the V21 simulations with

respect to the B18 ones (see table 3.1). The condition for seeding ($M_h > 10^9 \mathrm{M}_\odot$) is more easily satisfied in B18 with respect to V21, because of the larger mass of its resolution elements. This thus implies a larger number of seeds and consequently a larger number of mergers. Even more importantly, the excess of mergers in B18 is driven by the high dynamical mass which enters in the BH-BH merger algorithm within the code.

For a fixed numerical resolution, it is possible to study the dependence of the number of mergers on the feedback implemented. In the V21 simulations, we find that for low chirp masses ($< 10^7 \mathrm{M}_\odot$) the merger rate predicted by the *AGN_fid* model is higher than the *BHs_noFB* case. We further note that for $\mathcal{M}_c > 10^7 \mathrm{M}_\odot$ this trend is reversed, the merger rate in the *BHs_noFB* run is higher than in the *AGN_fid* case. The lack of AGN feedback allows a more efficient gas accretion which makes the black holes to grow more massive and numerous in the *BHs_noFB* case in this particular chirp mass range.

Furthermore, we study the trend of the local sound speed in the ISM. In the left panels of Fig. 5.3 we show the results for the V21 simulation runs. We note that the sound speed is larger in the *BHs_noFB* run because of the following. In the *BHs_noFB* run, the accretion rate is higher than in *AGN_fid* (see Tab. 3.1); furthermore, on scales over which c_s is computed (i.e. the smoothing length of the black holes), the heating due to accretion (gravitational compression) dominates the heating due to feedback. Thus, the gas temperature (and consequently c_s) in the *BHs_noFB* run is higher than *AGN_fid*. We thus conclude that for $\mathcal{M}_c < 10^7 \mathrm{M}_\odot$, the merger rate is driven mainly by the gravity, dynamics and substructure mergers.

For the B18 runs, we observe from Fig. 5.2 that in *AGNcone* the number of mergers is larger by a factor of $\sim$2 with respect to the *AGNsphere* case. To investigate this point, in the right panels of Fig. 5.3 we show the PDF of the relative sound speed of the merging BHs resulting from these simulations. This figure shows that in the *AGNcone* case, the PDF is shifted towards larger values. As discussed in Sec. 3.4 two BHs are allowed to merge when their relative velocity is lower than the sound speed of the local ISM. The higher is the sound speed the larger is the probability for two BHs to merge. The sound speed is larger in the *AGNcone* run because in this case the accretion is by far higher than in *AGNsphere* (see Tab. 3.1), resulting in a higher number of mergers.

We further note that Zana et al. (2022) already found that different feedback prescriptions result into different merger rates: in *AGNcone*, galaxies merge faster and more easily than in *AGNsphere*, possibly because of the stronger feedback due to the larger black hole accretion rate (see Tab. 3.1). This determines a more diffuse gas and stellar component around the host galaxies which can boost the effect of dynamical friction when two galaxies approach, thus lowering the dynamical timescale for their merging to occur.

We finally note that different resolutions and feedback prescriptions also affect the epoch at which the furthest merger event is occurring. For example, for $\mathcal{M}_c > 10^7 \mathrm{M}_\odot$, the furthest GW signal occurs in the redshift interval $7.7 < z < 8$ and $7.3 < z < 7.5$ in the case of V21 and B18 simulations, respectively.

5.3 Bias in zoom-in simulations

Our results are based on small box simulations, zoomed-in on a massive, biased ($> 3\sigma$, e.g. Barkana & Loeb, 2001) dark matter halo. As a result, the number density of MBHB mergers within the simulated box overestimates the value in an average region of the Universe. In what follows, we estimate the bias of our predictions considering our fiducial run (*AGN_fid*).

Following the halo mass history suggested by Correa et al. (2015a), we first calculate the accreted mass ($M_{h,0}$) at $z = 0$ of a 10^{12} $\mathrm{M}_\odot$ halo at $z = 6$:

$$M_h(z) = M_{h,0}\,(1+z)^{\alpha} e^{\beta z}, \tag{5.3}$$

where $\alpha = 0.24$ and $\beta = -0.75$, respectively (Correa et al., 2015b). We find $M_{h,0} = 10^{13.75}\,\mathrm{M}_\odot$.

In practice, when computing the merger rate with Eq. 5.2, we are considering a Universe where all DM halos have $M_h = 10^{13.75}$ $\mathrm{M}_\odot$ and comoving volume $(5.25\ \mathrm{cMpc})^3$. The result of this procedure will be clearly biased compared to a proper calculation in which DM halos span a wider mass range ($M_h = 10^{10} \sim 10^{16}$ $\mathrm{M}_\odot$) and have different abundances. This bias cannot be directly computed from our simulations, but we need to rely on a semi-analytical model (SAM). In SAMs, in fact, a wide range of halos are simulated and the merger rate is computed from their collective output, by weighting each halo mass according to the Press and Schechter halo

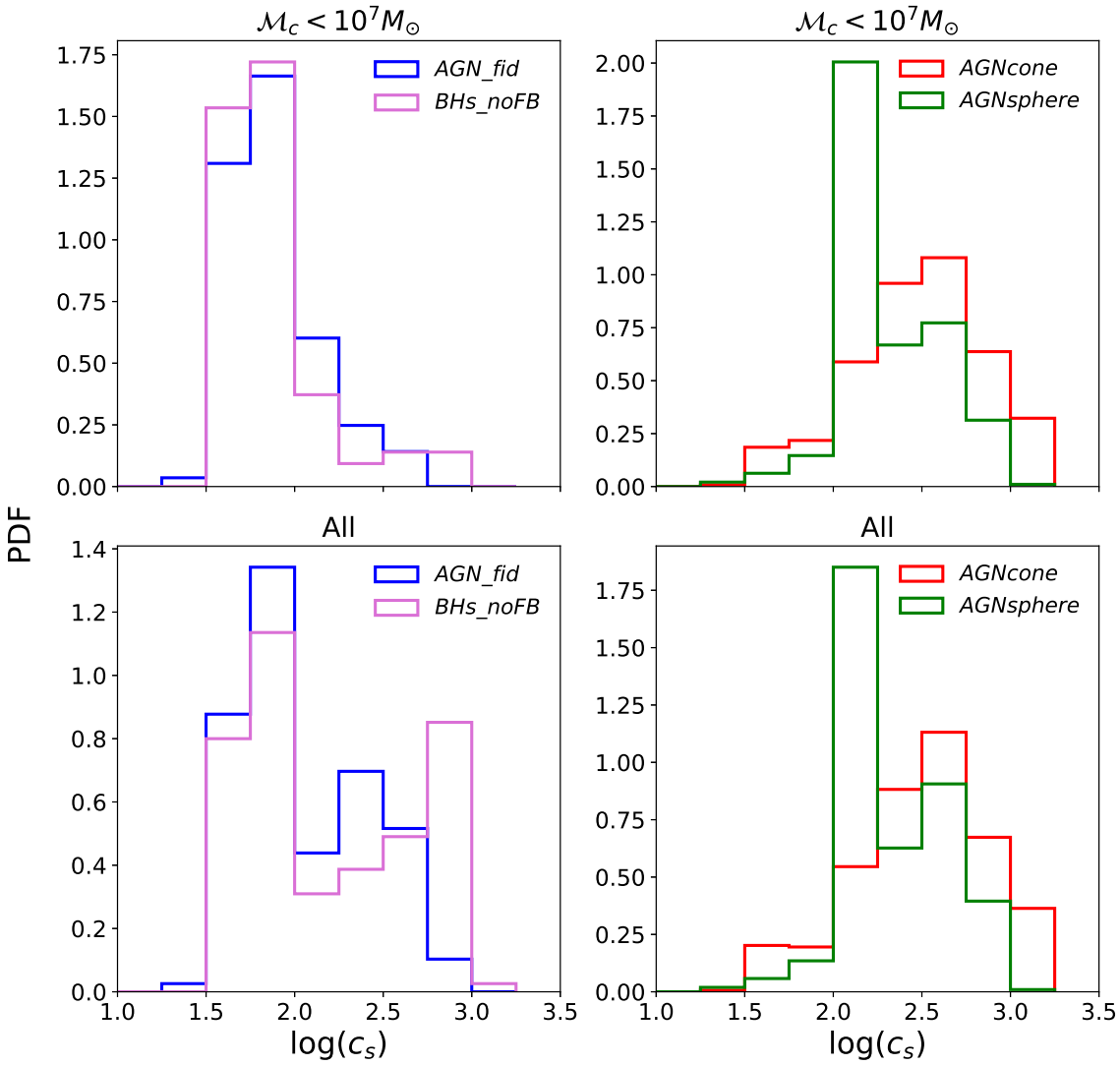

Figure 5.3: PDF of relative sound speed of merging black holes for *AGN_fid* feedback and *BHs_noFB* from V21 (left panel) and *AGNcone* and *AGNsphere* feedback from B18 (right panel).The top panels show the distribution of the sound speeds of MBHBs with $\mathcal{M}_c < 10^7 \mathrm{M}_\odot$ while the bottom panels show the same for all MBHBs.

mass function (Press & Schechter, 1974). This latter step is simply obtained by dividing the the merger rate by the effective comoving volume occupied by that halo. It is therefore also possible to use the SAM output to create biased universes, simply by taking halos of a desired mass and weighting them with a desired effective comoving volume. By comparing the rates obtained from this biased universe to the total one, we can infer the bias. This is the procedure we follow here.

We then use the semi-analytical model by Klein et al. (2016); Barausse (2012, see also), and we consider the output of all the trees, weighted on the Press and Schechter halo mass function (Press & Schechter, 1974). For these calculations, we consider the "Q3nod" run, since

it is based on a model that more closely resembles our prescriptions (heavy seeds and no time delays). Furthermore, for a fair comparison with our results, we only consider $z > 6$ merger events occurring in dark matter haloes $> 10^9$ M$_\odot$ (the threshold mass used in our simulations to seed MBHs) and involving binaries with both BH masses $> 10^5$ M$_\odot$ (the mass of our seeds). The merger rate obtained in this case is ~ 3 yr^{-1}.

We next consider two specific merger trees, whose halos at $z = 0$ are the closest to the $M_{h,0}$ value computed above, namely $M_{h1,0} = 10^{13.7}$ M$_\odot$ and $M_{h2,0} = 10^{13.8}$ M$_\odot$. We weight the merger rates in these two merger trees with the inverse of the comoving volume of our refined simulation, namely (5.25 cMpc)^3. The average of the two merger rates obtained in this way can be used as a proxy for the merger rate in a Universe made only of halos of $M_{h,0} = 10^{13.75}$ M$_\odot$ at $z = 0$. The merger rate obtained in this case is $\sim$60 yr^{-1}.

We thus estimate that the merger rates computed from our zoom-in simulations is biased by a factor ~ 20. We repeat the above calculations for the model "popIII" (which assumes light seeds and delays between MBH and galaxy mergers) and the model "Q3-d" (heavy MBH seeds and delays). In both cases the bias does not change significantly, being $\sim$ 20 to 30.

To summarize, our zoom-in simulations predicts a total number of merger events per year, at $z \sim 6$, that varies between 80 and 300, depending on the resolution and the star formation/AGN feedback prescriptions adopted. By accounting for the halo bias, the number of merger events lower to $\sim$ 3-15 yr^{-1}.

5.4 Comparison with contemporary works

In this section, we compare our results with contemporary works that make similar calculations, both using SAMs and hydrodynamical simulations (HDS). For this comparison, we focus our attention at $z \gtrsim 6$. This is because our simulations stop at this redshift[2]. Furthermore, we only consider those models that do not include any time delay in MBHB coalescence,

[2]We are aware that extending the calculations reported in this Thesis to lower redshifts (e.g., $z = 0$) would be very interesting and important for correctly driving future LISA experiments. Nevertheless, producing a zoom-in simulation of a 10^{12} M$_\odot$ DM halo at $z = 0$ is not trivial, because of the huge dynamic range required to properly follow SMBH growth. To be more quantitative, if the virial radius $r_{\rm vir}$ of a 10^{12} M$_\odot$ DM halo at $z = 0$ is 263 kpc, while $r_{\rm vir}(z = 6, M_{\rm DM} = 10^{12}$ M$_\odot) \sim 48$ kpc, we should have zoomed-in on a box that is $\sim 263/48 \sim 6$ times larger.

which is consistent with our work[3]. We summarize results from different models in Table 5.1.

We first compare our results with the predictions by Sesana et al. (2007) based on the models by Begelman et al. (2006). In these works, DCBH formation is efficient when the halos overcome a given threshold of virial temperature ($T_{\rm vir} \geq 10^4$K): the "high-feedback" (BVRhf) and "low-feedback" (BVRlf) models differ for the efficiency in the distribution of metals produced during the star formation process. In the BVRhf (BVRlf) model, the merger rate is 1.5 (25) yr^{-1}. This difference is due to the following: in BVRhF, as a consequence of the high stellar feedback efficiency that ensures a swift metal enrichment, the DCBH formation stops as early as $z \sim 18$; in the BVRlf, the DCBH formation only stops at $z \sim 15$, since the low stellar feedback efficiency allows halos to remain pristine longer.

Klein et al. (2016) also investigated the effect of different seeding models and time delays between galactic and MBHB mergers on the merger rate. For this, they adopted the SAM by Barausse (2012) and varied the seeding mass (light seed vs heavy seed) and hence their halo occupation fraction. They also consider delays in MBHB caused by MBH environment as well as by triple interactions. Considering the model with heavy seeds and instantaneous mergers (model "Q3-nod") at redshift 6, they predict a merger rate of 10 per year.

We further consider the results by Hartwig et al. (2018) for instantaneously merging binaries with $10^4 < M_{\rm seed} < 10^6$ M$_\odot$, as derived by assuming a critical LW flux[4] of $J_c = 30 J_{21}$. In the Hartwig et al. (2018) calculations, the merger rate the DCBH formation rate peaks at approximately $z \sim 7$ after which the DCBH formation stops, as a result of the metal enrichment and cosmic reionization processes. The resulting merger rate at $z = 6$ is 10 yr^{-1}.

For what concerns Dayal et al. (2019), they use the SAM of galaxy formation *Delphi* to track the effect of different BH parameters on the BH merger rates. The merger rate at $z = 6$ is found to be < 10 per year. We only consider the case of instantaneous mergers which doesn't assume any delays between galactic and MBH mergers, referred to as *ins1* model in the Dayal et al. (2019). We also note that they only report the intrinsic merger rate for all BH mergers (stellar BBH mergers, 'mixed' merger with stellar seed and DCBH as well as DCBH-DCBH mergers).

[3] We further discuss this point in Chap. 6.
[4] J_{21} is the LW flux in units of 10^{-21}ergs cm^{-2}s^{-1}Hz^{-1}sr^{-1}.

For this reason[5], we consider this estimate as an upper limit to the merger rate when only DCBH are seeded.

For what concerns HDS, Katz et al. (2019) used `Illustris` to study different populations of MBHs. They predict the effect on LISA detection rate for different MBH evolutionary scenario such as the effect of delay on the BH particle mergers in the simulations combined with different BH masses. At $z \sim 6$ they predict the intrinsic merger rate ~ 0.01 per year for heavy seeds and instantaneous mergers (model *ND*).

To summarise, our results are consistent with previous predictions from semi-analytical works (after being corrected for the halo-bias), while they are above the predictions by Katz et al. (2019). This inconsistency can be ascribed to the different seeding mechanisms adopted in their work $M_{\rm seed} = 1.42 \times 10^5 {\rm M}_\odot$ BHs seeded in $M_{\rm DM} = 7.1 \times 10^{10} {\rm M}_\odot$ DM halos): since the DM haloes in which BHs are seeded are more massive (i.e. less numerous) than ours, we expect fewer BHs to be seeded in the simulations, resulting into a lower merger rate. **We underline here that we are comparing our results with the ones reported in Katz et al. (2019) that do not include any time delay. Therefore, we are comparing our findings with the red line reported in the right panel of Fig. 7 shown in their paper. We do not compare with predictions that include time delay corrections, since the model we are adopting for including these effects is different from the ones used in Katz et al. (2019), reported as DA17 and K17 in the right panel of their Fig. 7 (blue and orange lines, respectively). We discuss in further details time delay effects in Sec. 6.3.**

5.5 Constraints from PTA

We compare our predictions with upper limits placed by several Pulsar Timing Array (PTA) observations. PTAs are sensitive to GWs with frequencies between 10^{-9} to 10^{-7} Hz. In this nano-Hz regime, the signal mostly arises from stochastic gravitational wave background (GWB) produced by the incoherent superposition of GWs from the population of inspiralling MBHBs overlapping in frequencies. The characteristic strain arising from this stochastic GWB can be

[5]They also show that DCBH mergers, noted as "type 3" mergers, are the rarest in their BH population.

Table 5.1: Comparison with contemporary literature for merger rates at $z = 6$. The results of our work are reported after being corrected for the halo bias computed in Sec. 5.3.

Reference	**Model**	$\frac{dN}{dz\ dt}\ [\mathrm{yr}^{-1}]$
Sesana et al. 2007	SAM	1.5-25
Klein et al. 2016	SAM	10
Hartwig et al. 2018	SAM	5
Dayal et al. 2019	SAM	<10
Katz et al. 2019	HDS	0.01
This work (bias corrected)	HDS	3-15

written as (Sesana et al., 2008):

$$h_c^2(f) = \frac{4G^{5/3}}{f^2 c^2 \pi} \int\int \frac{dz d\mathcal{M}}{(1+z)} \frac{d^2N}{dz d\mathcal{M}} \frac{d\mathrm{E}_{\mathrm{GW}}(\mathcal{M})}{d\ln f_r}, \tag{5.4}$$

where $d^2N/dzd\mathcal{M}$ is the comoving number density of MBHB merger per unit redshift, and rest-frame chirp mass, f is the frequency of the GWs in the observer frame, and $d\mathrm{E}_{\mathrm{GW}}/d\ln f_r$ is the energy emitted per logarithmic rest-frame frequency, f_r.

Assuming the inspiralling population of MBHBs in the PTA band are in perfect circular orbits, Eq. 5.4 can be re-written as:

$$h_c^2(f) = \frac{4G^{5/3} f^{-4/3}}{3c^2 \pi^{1/3}} \int\int dz d\mathcal{M} \frac{d^2N}{dz d\mathcal{M}} \frac{\mathcal{M}^{5/3}}{(1+z)^{1/3}}. \tag{5.5}$$

This type of relation is typically written as:

$$h_c(f) = A \left(\frac{f}{f_0}\right)^{-2/3}, \tag{5.6}$$

where A is the amplitude of the signal at the reference frequency f_0 which is usually normalized at $f_0 = 1\mathrm{yr}^{-1}$, and $\mathrm{A}(f_0 = 1\mathrm{yr}^{-1})$ is typically denoted as $A_{\mathrm{yr}^{-1}}$.

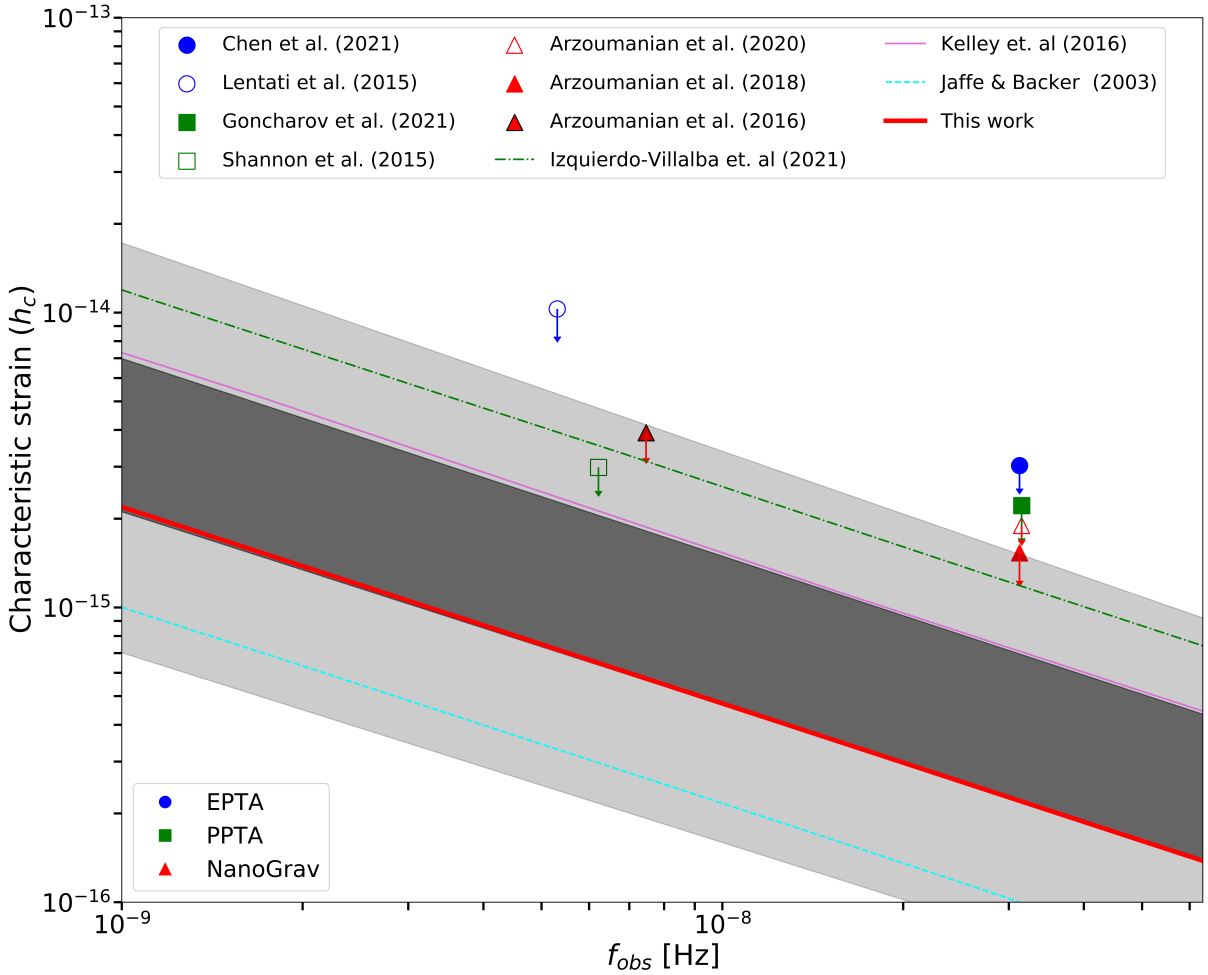

Figure 5.4: Stochastic Gravitational Wave Background spectrum calculated from our fiducial model (red solid line). The circles, squares, and triangles represent EPTA, PPTA and NanoGrav data respectively. Dark (light) gray shaded region depicts the 1σ (2σ) confidence level of the predictions by Sesana et al. (2016). The green dot-dashed line shows the results by Izquierdo-Villalba et al. (2021): $A_{\rm yr^{-1}} \sim 1.2\times10^{-15}$. The solid pink line refers to the `Illustris` predictions of $A_{\rm yr^{-1}} \sim 7.1\times10^{-16}$ (Kelley et al., 2016). The cyan dashed line shows the results by Jaffe & Backer (2003): $A_{\rm yr^{-1}} \sim 1\times10^{-16}$.

We present our predictions in Fig. 5.4, where we apply a bias correction factor of 20 (see Sec. 5.3). We find $A_{\rm yr^{-1}} \sim 2\times10^{-16}$, which is below the upper limits placed by the NANOGrav (Arzoumanian et al., 2018), EPTA (Lentati et al., 2015) observations and the PPTA observations (Shannon et al., 2015). We emphasize that our predictions do not include any contribution from sources at $z < 6$, which are instead expected to dominate the background (e.g. Izquierdo-Villalba et al., 2021). We make this exercise for only a sanity check to make sure that our predictions are not overshooting current observational constraints.

Delays in MBHB mergers 6

6.1 Introduction

In our simulations, given the limited spatial and temporal resolution, we are not able to properly follow the dynamics of MBHBs up to coalescence. This explains the simplified prescription typically adopted in zoom-in cosmological simulations for BH merging described in Sec. 3.4. However, the actual timescale over which MBHBs merge depends on several factors, e.g. the mass ratio of the MBHs, their initial separation, and the physical properties of the galaxy hosting the MBHB. In what follows, for our fiducial model, we first describe how we associate a MBHB to its host galaxy, and then we correct in post-processing the coalescing time of MBHB mergers including a time delay due to dynamical friction from the surrounding stars[1]. This allows us to get a first order estimate of how our merger rates change due to these effects. The final results may anyway vary to some degree from what we report below, if the dynamical friction were actually implemented in the code, instead of applying its effect in post-processing.

6.2 Galaxy-MBHB association

In this section, we describe the method we adopt to associate a MBHB to its host galaxy. Galaxy identification follows a similar approach to what has been done in Zana et al. (2022). We identify[2] dark matter halos through the AMIGA halo finder code (Knollmann & Knebe, 2009). The

[1] In Sec. 6.4, we describe the stellar hardening physical process that could further delay the coalescence of MBHBs. We find that the resolution of our simulations prevents us to make realistic predictions about this effect.

[2] To define a halo we require a minimum of 20 bound particles.

merger tree for each halo at $z \simeq 6$ is built by tracing back in time the constituent dark matter particles: their ID is matched in the progenitor structures in the previous snaphots. Baryon particles are assigned to their related galaxy when: (i) they are located within $\beta r_{\rm vir}$ of a given halo, where $r_{\rm vir}$ is the virial radius of the halo and $\beta = 0.3$; and (ii) their velocity is lower than the escape velocity, as evaluated through an analytical integration of the Navarro-Frank-White profile (Navarro et al., 1996) to speed up calculations. We restrict our analysis only to those galaxies with $M_{\rm vir} > 10^9$ M$_\odot$ and $M_* > 10^7$ M$_\odot$.

We associate a host galaxy to each merger event, by using the following procedure: (i) we first assign to each merger event that galaxy for which its centre of mass is the closest to the position of the primary BH (BH$_p$); (ii) we consider only those mergers which are within $\beta r_{\rm vir}$ of any galaxy. When we associate the galactic properties (derived from a snapshot) to a merger event, we consider the closest[3] snapshot in time to the event itself (see Chap. 9 for further discussion).

In some cases, our algorithm fails to associate a host galaxy to a merger event. This may occur because during the time passing between the redshift of the event and the closest snapshot, the BH$_p$ may have moved out of the $r_{\rm vir}$ of the host galaxy. Another possibility is related to the fact that during the simulation a MBH may be spuriously seeded into a transient matter overdensity (incorrectly identified as a galaxy by the on-the-fly halo finder); such a MBH would then rapidly merge with the MBH of the closest halo (due to the repositioning algorithm) in less than 1 timestep (e.g., Blecha et al. 2015; Kelley et al. 2016; Katz et al. 2019).

We find, in our fiducial model, over the 145 total events, 72 per cent occur within $\beta r_{\rm vir}$, 22 per cent outside $\beta r_{\rm vir}$ but inside $r_{\rm vir}$, and 6 per cent outside the $r_{\rm vir}$. We remove these spurious events from our calculations.[4]

[3] We have also considered the case in which galactic properties are linearly interpolated from the two snapshots immediately before and after the merger event, finding no appreciable differences in the main results of our work.

[4] We also calculate the spurious events in *AGNcone* for comparison of different resolutions and we find that the fraction of spurious events increase with the decrease of resolution of the numerical simulation. Over the 1812 total events in *AGNcone*, only 10 per cent occur within $\beta r_{\rm vir}$, 20 per cent outside $\beta r_{\rm vir}$ but inside $r_{\rm vir}$, and 70 per cent outside the $r_{\rm vir}$. This further strengthens our selection of *AGN_fid* as our fiducial model.

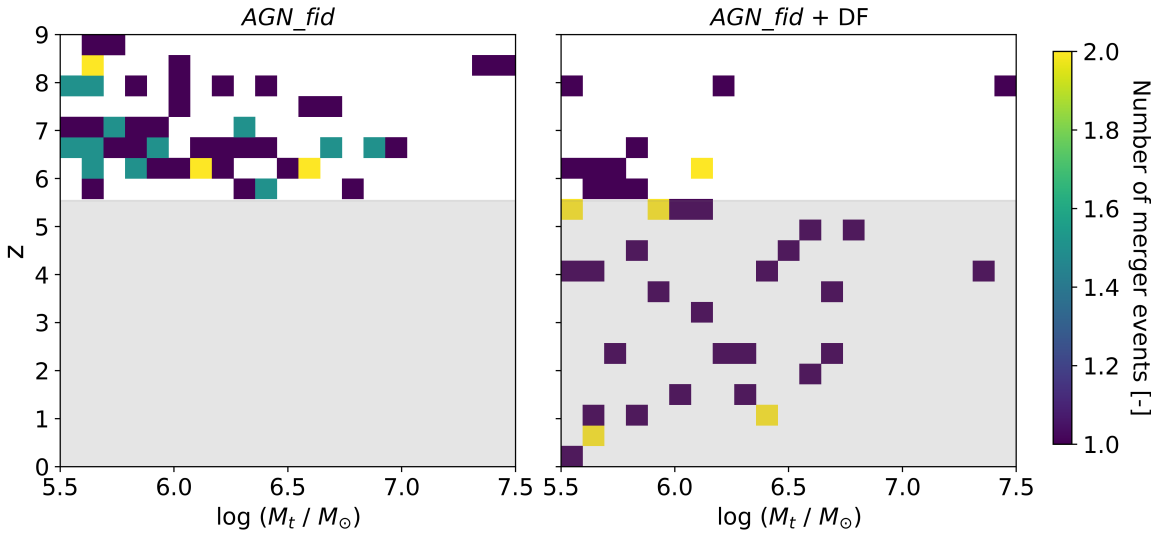

Figure 6.1: Number of merger events as a function of the total mass of the system M_t and the redshift z of the binary, as resulting from our fiducial run. The left panel shows the merger distribution resulting from the simulations while the right panel shows the same distribution after adding the delay time due to dynamical friction. The white region in each plot shows the redshift range accessible to the simulations (z>6) and the grey region denotes the redshift range inaccessible to our simulations.

6.3 Time delay due to dynamical friction

The interaction of the MBHBs with stars in their surroundings results in the MBHs to lose energy, to slow down, and to spiral inwards gradually. (Chandrasekhar, 1943; Ostriker, 1999). This process effectively increases the timescale of the MBHB merger with respect to the adopted simulations, potentially delaying it by millions or even billions of years. The amount of dynamical friction experienced by MBHBs depends on the density and distribution of the surrounding stars, as well as the mass and velocity of the binary. In general, the effect of dynamical friction is strongest in regions of high density, such as the centers of galaxies, where the density of dark matter and stars is the highest. We make a simple calculation following the prescription of Krolik et al. (2019), but see also Volonteri et al. (2020) for more details.

The frictional timescale for a massive object in an isothermal sphere can be written as (Binney & Tremaine, 2008):

$$t_{\rm df} = 0.67\,{\rm Gyr}\left(\frac{a}{4\,{\rm kpc}}\right)^2\left(\frac{\sigma}{100\,{\rm km\,s^{-1}}}\right)\left(\frac{M_{\rm BH_s}}{10^8\,M_\odot}\right)^{-1}\frac{1}{\Lambda}, \tag{6.1}$$

where a is the distance of the MBH from the galaxy centre[5], σ is the central stellar velocity

[5]We calculate a at the snapshot closest in time to the numerical merger.

dispersion:

$$\sigma = (0.25GM_*/R_{\rm eff})^{1/2}, \tag{6.2}$$

M_* is the total stellar mass of the galaxy hosting the MBHs, computed as described in Sec. 6.2,

$$\Lambda = \ln(1 + M_*/M_{\rm BH_s}), \tag{6.3}$$

$R_{\rm eff}$ = 0.1 $r_{\rm vir}$[6], and $M_{\rm BH_s}$ denotes the mass of the secondary (less massive) MBH.

The total time taken by the MBHBs to merge including the dynamical friction correction is then given by:

$$t_{\rm tot,df} = t_{\rm in} + t_{\rm df}, \tag{6.4}$$

where $t_{\rm in}$ is the time at which the merger occurs in the simulation.

The results of our calculations are reported in Fig. 6.1 where we show the number of merger events (for which we can associate a host galaxy) across different mass and redshift ranges without including any post-processing delay (left panel), and including dynamical friction (right panel). The grey region in each panel denotes the redshift range outside the reach of our simulations (z < 6). Fig. 6.2 helps to better visualise the difference in the merger rate predictions if we assume instantaneous merger (blue line), or we include delay due to dynamical friction (yellow line) in post-processing. By adding the delay due to dynamical friction, we find that 17 per cent of the MBHBs of our fiducial calculations are not merging within the Hubble time, 21 per cent of the MBHBs merge at $z > 6$ and the rest will be delayed to a redshift range $z < 6$.

Apart from time delays caused by dynamical friction between the merging MBHs with its surrounding stars, further interaction with the neighbouring stars can cause additional delays in the merging time of MBHBs. However, for our simulated MBHBs, this effect can be neglected as we discuss in the next section.

[6]**For the effective radius, we have considered the value $R_{\rm eff}$ = 0.1 $r_{\rm vir}$, following Volonteri et al. (2020). If the value of $R_{\rm eff}$ is increased, say to 0.3 $r_{\rm vir}$ (as in Sec. 6.2), then from Eq. 6.1, we can see that $t_{\rm df}$ decreases by a factor of ~ 0.6, resulting in shorter coalescence time of mergers.**

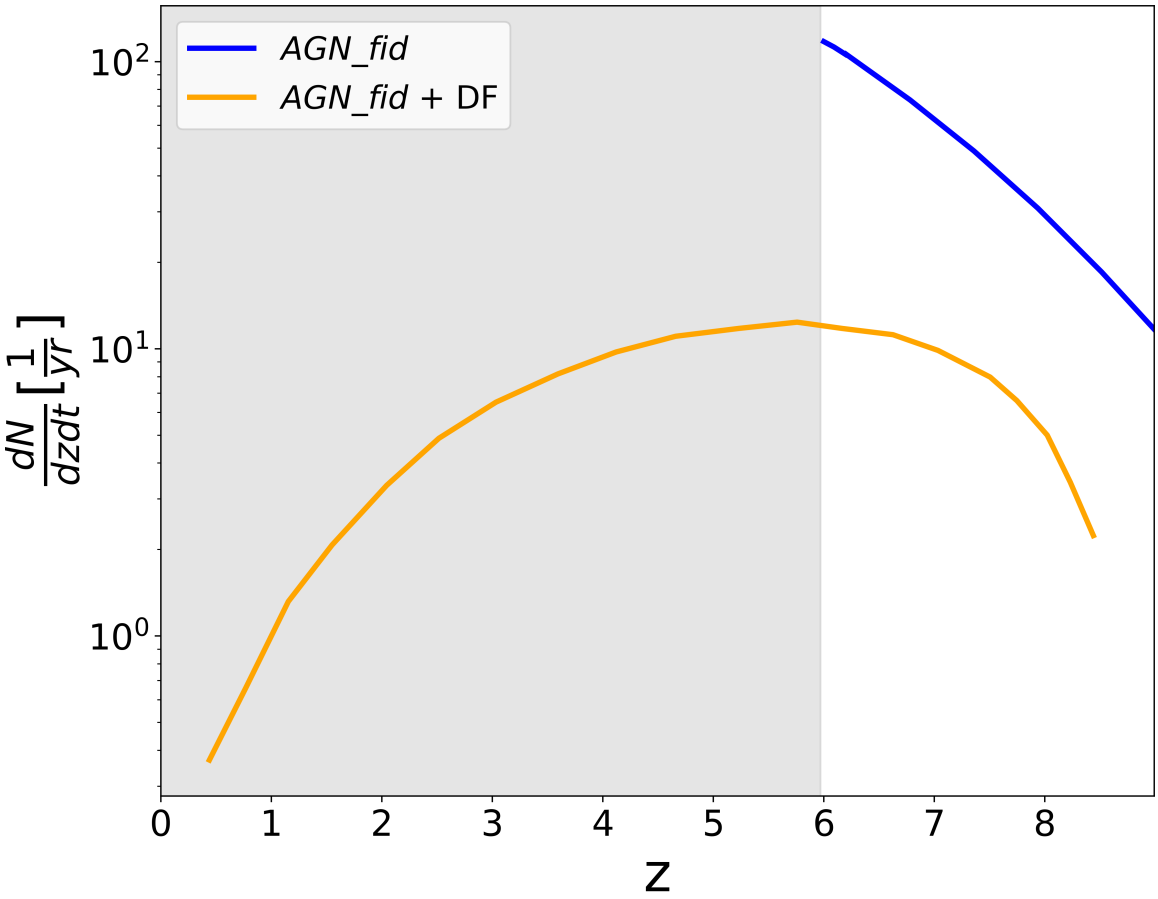

Figure 6.2: Merger rate per unit redshift z of MBHBs, considering delay times in post-processing. In blue, mergers from *AGN_fid* are shown and the same events which can be associated with a host galaxy are shown in orange after adding the delay time due to dynamical friction. The gray shaded region depicts the redshift range which is inaccessible in our simulations.

6.4 Time delay due to stellar hardening

Stellar hardening is the process by which stars interact with the MBHB and gradually become more tightly bound to it over time. For already bound MBHBs, the gravitational field can be strong enough to disrupt the orbits of nearby stars. As a result, some of these stars can be captured by the MBHB and start to orbit around it (Mikkola & Valtonen, 1992). As these stars continue to interact with the binary, they can extract energy and angular momentum from the MBHB, causing it to become more tightly bound (Quinlan, 1996).

We compute the stellar hardening timescale following Sesana & Khan (2015):

$$t_{\rm stellar} = 15.18\,{\rm Gyr}\left(\frac{\sigma_{\rm inf}}{{\rm km\,s^{-1}}}\right)\left(\frac{\rho_{\rm inf}}{{\rm M_\odot pc^{-3}}}\right)^{-1}\left(\frac{a_{\rm gw}}{10^{-3}{\rm pc}}\right)^{-1}, \tag{6.5}$$

where $\sigma_{\rm inf}$ and $\rho_{\rm inf}$ are the velocity dispersion and the stellar density at the sphere of influence[7], and $a_{\rm gw}$ is the transition separation of stellar hardening and GW hardening at which the binary spends most of its time:

$$\sigma_{\rm inf} = (GM_{\rm t}/r_{\rm inf})^{1/2}, \tag{6.6}$$

$$\rho_{\rm inf} = \frac{(3-\gamma)M_* r_{\rm inf}^{-\gamma}}{8\pi R_{\rm eff}^{3-\gamma}}, \tag{6.7}$$

$$\begin{aligned} a_{\rm gw} =& 2.64\times10^{-2}{\rm pc}\times \\ & \left[\frac{\sigma_{\rm inf}}{\rm km\,s^{-1}}\frac{\rm M_\odot pc^{-3}}{\rho_{\rm inf}}\frac{15}{H}\left(\frac{M_{\rm BH_p}M_{\rm BH_s}M_t}{2\times10^{24}{\rm M_\odot^3}}\right)\right]^{1/5}, \end{aligned} \tag{6.8}$$

where $r_{\rm inf}$ is the radius containing twice the binary mass in stars:

$$r_{\rm inf} = R_{\rm eff}\left(\frac{4M_t}{M_*}\right)^{1/(3-\gamma)}, \tag{6.9}$$

and we assume the index γ = 2 (Volonteri et al., 2020) and $H = 15$ Sesana & Khan (2015).

Finally, the total time of the MBHB merger including dynamical friction and stellar hardening is given by:

$$t_{\rm tot,stellar} = t_{\rm tot,df} + t_{\rm stellar} \tag{6.10}$$

According to the formalism reported above, we find that $t_{\rm stellar}$ varies in the range 1-10 Gyr, since central stellar densities are in the range 40-600 $\rm M_\odot pc^{-3}$. These $\rho_{\rm inf}$ values are not a fair representation, likely because the resolution of our simulations do not allow us to properly determine the matter distribution on such small scales. For comparison, in Sgr A* $\rho_{\rm inf} \sim 7\times10^4 \rm M_\odot pc^{-3}$. In addition, galaxies at high redshift are likely more centrally concentrated than local galaxies. Thus, we would expect $\rho_{\rm inf}$ values even larger than what is found in Sgr A*. For all these reasons, we do not include the delay due to stellar hardening in our post-processing calculations.

[7]The sphere of influence is approximated as the sphere containing twice the binary mass in stars.

GWs from high redshift MBHBs

7

7.1 Introduction

In this chapter, we estimate the detectability of the merger events predicted by the V21 *AGN_fid* simulations[1], by computing the signal-to-noise ratio (SNR) and the angular resolution Ω of their GW signals. We also show how these properties vary if time delay due to dynamical friction is considered. We assume that a GW signal is detectable if SNR>5. Hereafter, for the sake of brevity, we refer to these "LISA detectable events" as LDEs. Furthermore, we also depict the fraction of LDEs in the "mass ratio"-"total mass" plane with and without considering delay effects. Finally, we discuss the different scales of interest in time, frequency and spatial ranges of the LDEs.

7.2 Signal-to-noise ratio and angular resolution

The SNR accumulated over the observational time τ is computed following the Flanagan & Hughes (1998) formalism:

$$\left(\frac{S}{N}\right)^2_{\Delta f} = \int_f^{f+\Delta f} d\ln f' \left[\frac{h_c(f'_r)}{h_{\rm rms}(f')}\right]^2, \tag{7.1}$$

[1] In Appendix A, we compare the GW properties reported in this chapter for the *AGN_fid* with the other simulation runs presented in Sec. 3.4.

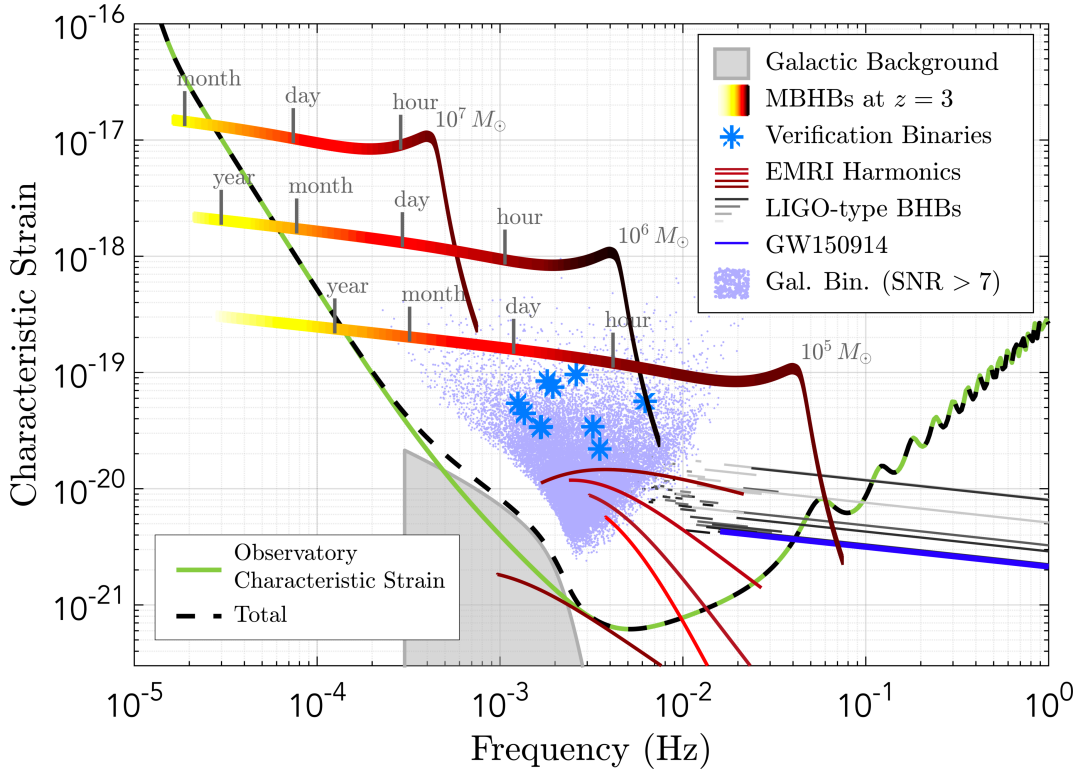

Figure 7.1: The yellow-red lines shows the varying characteristic strains through the inspiral, merger and ringdown phases for MBHB systems of total masses $10^5, 10^6, 10^7 \mathrm{M}_\odot$ from bottom to top. Expected sensitivity (green) with various possible sources in units of dimensionless characteristic strain amplitude for a three arm configuration of LISA. Plot taken from the LISA L3 mission proposal.[3]

where f_r is the GW rest-frame frequency, $f = f_r/(1+z)$ is the observed frequency, Δf is the frequency shift in the duration of τ, h_c is the *characteristic strain*, and $h_{\rm rms}$ is the effective[2] rms noise of the instrument.

We start defining the strain amplitude (sky and polarization averaged) of GWs emitted by two black holes of chirp mass $\mathcal{M}_c$ that are merging at redshift z, following Hawking & Israel (1989):

$$h = \frac{8\pi^{2/3}}{10^{1/2}} \frac{G^{5/3} {\mathcal{M}_c}^{5/3}}{c^4 r(z)} f_r^{2/3}, \tag{7.2}$$

where $r(z)$ is the luminosity distance of the merging events. MBHBs spend a mass-dependent amount of time in each frequency band, as shown in Fig. 7.1.

It is thus common to compute the characteristic strain amplitude that also depends on the

[2]The total LISA $h_{\rm rms}$ noise is the sum in quadrature of the instrumental rms noise and the confusion noise from unresolved galactic (Nelemans et al., 2001), extragalactic (Farmer & Phinney, 2003), and white dwarf-white dwarf binaries. The number of these sources is expected to decrease as the LISA mission progresses and a larger number of foreground sources are detected and removed.

[3]https://www.elisascience.org/files/publications/LISA_L3_20170120.pdf

number of cycles spent in the LISA bandwidth by the binaries:

$$h_c = h\sqrt{n} \simeq \frac{1}{3^{1/2}\pi^{2/3}} \frac{G^{5/6}{\mathcal{M}_c}^{5/6}}{c^{3/2}d_L} f_r^{-1/6}, \tag{7.3}$$

where n is the number of cycles spent in a frequency interval Δf:

$$n \simeq f_r^2/\dot{f}_r = \frac{5}{96\pi^{8/3}} \frac{c^5}{G^{5/3}{\mathcal{M}_c}^{5/3}} f_r^{-5/3}, \tag{7.4}$$

and the rest-frame frequency shift rate is expressed as:

$$\dot{f}_r = \frac{df_r}{dt_r} = \frac{96\pi^{8/3}G^{5/3}}{5c^5}{\mathcal{M}_c}^{5/3} f_r^{11/3}, \tag{7.5}$$

assuming that the backreaction from GW emission dominates the orbital decay of a binary.

The LISA rms noise $h_{\rm rms}$ is instead given by:

$$h_{\rm rms}(f) \equiv \sqrt{\Delta f S_n(f)}, \tag{7.6}$$

where S_n is the LISA PSD which we recall from Eq. 2.71.L corresponds to the detector arm length, and $S_{\rm n,acc}$, $S_{\rm n,sn}$ and $S_{\rm n,omn}$ are the noise components due to low-frequency acceleration, shot noise and other measurement noise, respectively (Smith & Caldwell 2019; Klein et al. 2016), parametrised as follows[4]:

$$\begin{aligned} S_{\rm n,acc} &= \frac{9\times10^{-30}}{(2\pi f)^4}\left(1+\frac{10^{-4}}{f}\right)\ [{\rm m^2 Hz^{-1}}], \\ S_{\rm n,sn} &= 2.22\times10^{-23}\ [{\rm m^2 Hz^{-1}}], \\ S_{\rm n,omn} &= 2.65\times10^{-23}\ [{\rm m^2 Hz^{-1}}]. \end{aligned} \tag{7.7}$$

In an ideal experiment, to maximize the SNR, one should integrate eq. 7.1 over the entire duration of the GW event. Most of the lifetime of a GW emitted by a MBHB is encompassed within the time interval between when the distance between the two MBHs becomes close to

[4]These values hold for the current LISA design, that presents three spacecrafts connected by 6 links. Given the large uncertainties on the very-low frequency LISA sensitivity, we adopt a pessimistic cut at 10^{-4} Hz (Sesana et al., 2004).

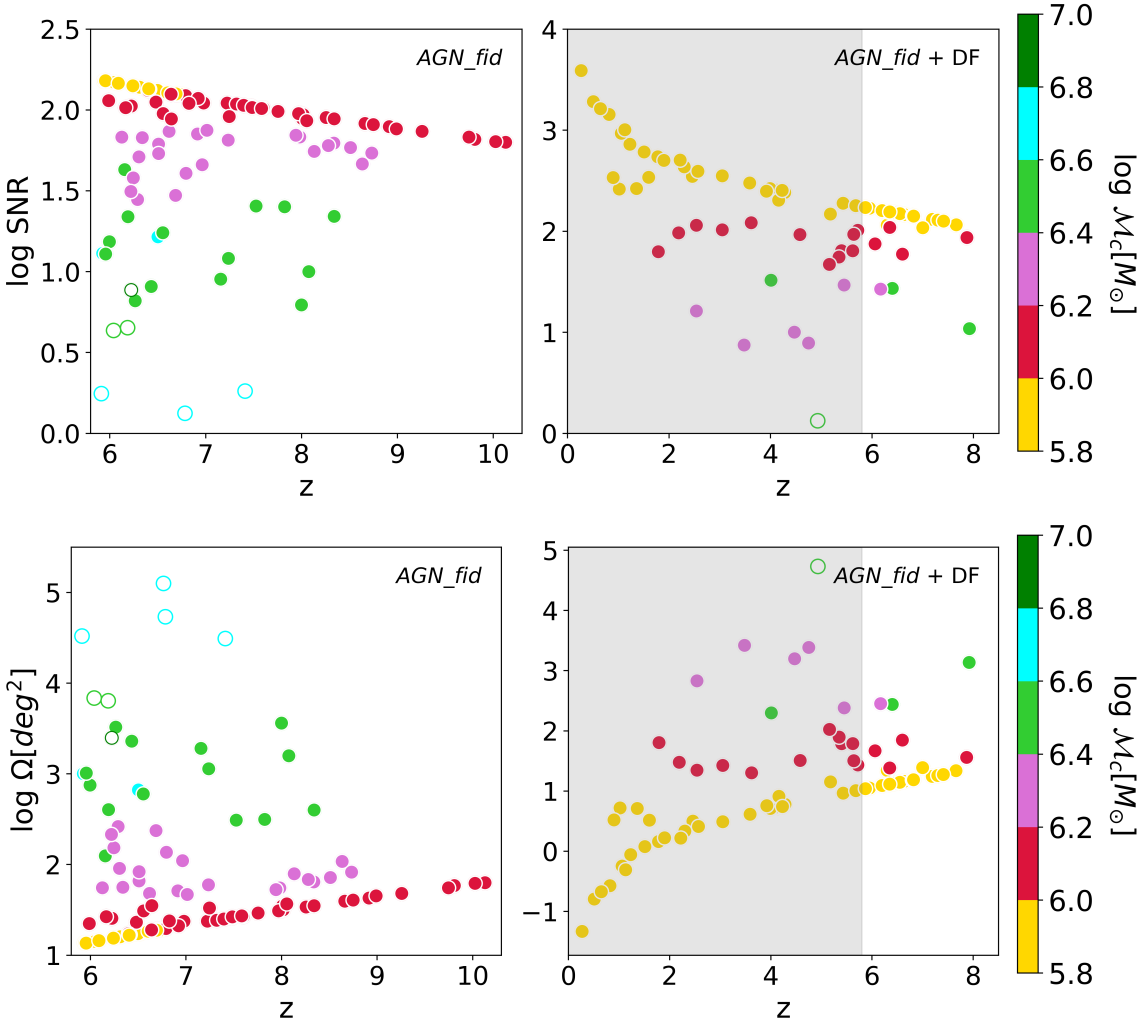

Figure 7.2: Signal-to-noise ratio (upper panel) and angular resolution (lower panel) of MBHB mergers resulting from our simulations, with (without) delay times considered in right (left) panel color-coded according to their chirp mass. The shaded gray area represents the redshift range inaccessible to our simulations. Filled and empty circles represents detectable and undetectable events, respectively. The detectability threshold has been set to $\mathrm{SNR}_{\mathrm{thres}} = 5$.

the *hardening* radius r_h (the inspiral phase begins) and when it reaches the *innermost-stable circular orbit* radius r_{isco} (the merging phase begins). In this case, the integration limits should range between a minimum frequency $f_{\mathrm{min}} = f_h$ at the r_h and the frequency $f_{\mathrm{max}} = f_{\mathrm{isco}}$ at the r_{isco}. However, in a real experiment, a GW event can be detected by LISA only if its frequency is included in the range $[10^{-4}$–1.0] Hz and the SNR overcomes a certain threshold (here taken as $\mathrm{SNR}_{\mathrm{thresh}} = 5$). We thus consider as f_{min} the frequency at which $\mathrm{SNR} > \mathrm{SNR}_{\mathrm{thresh}}$. We hence calculate the SNR for each merger event in *AGN_fid*, and we find the results shown in the upper panels of Fig. 7.2.

The upper left panel of fig. 7.2 shows the trend of the SNR with redshift, without assuming

Table 7.1: Detectability of MBHBs with LISA for the simulation runs adopted in this work (first column). The second column reports the total number of mergers in each run ($N_{\rm total}$) while the third shows the LDEs fraction ($f_{\rm det}$) in each run. The fourth (fifth, sixth, seventh) column the chirp mass (observational time, observed frequency and observed initial distace of separation) ranges for the LDEs. The eighth (ninth)column shows the fraction $f_{\rm out}$ ($f_{\rm und}$) of MBHBs whose frequency is outside the LISA band (inside the LISA band but do not reach the required SNR threshold). In the last column the minimum and maximum SNR accumulated by MBHBs which merge within the LISA band but fail to reach the SNR threshold for detectability ($\rm SNR_{und}$) are also shown.

Run	$N_{\rm total}$	$f_{\rm det}$	$\mathcal{M}_c[10^6 \rm M_\odot]$	$t_{\rm obs}$[days]	$\nu_{\rm obs}$[mHz]	$R_{\rm obs}[10^{-6}\rm pc]$	$f_{\rm out}$[mHz]	$f_{\rm und}$[mHz]	$SNR_{\rm und}$
AGN_fid	145	0.69	0.9-7.0	0.5-30	0.10-0.38	1.9-9.3	0.31	0.04	0.8-4.0
***AGN_fid*+DF**	116	0.66	0.2-3.2	0.0-18	0.10-0.9	0.1-9.6	0.31	0.01	1.33
BHs_noFB	140	0.46	0.9-6.0	0.7-39	0.09-0.38	1.9-9.5	0.50	0.03	0.7-3.9
AGNcone	583	0.76	0.6-10	1.1-75	0.09-0.42	1.8-10.5	0.22	0.02	0.4-4.7
AGNsphere	415	0.78	0.6-7.5	0.6-54	0.09-0.40	1.6-8.4	0.22	0.005	1.6-3.7

any time delay. For a given chirp mass, the further the source is located, the lower is the SNR of the GW event. Furthermore, although h_c increases with the mass of the MBHB system, for a fixed redshift, the SNR is higher for sources with lower chirp mass. This trend occurs because low-mass binaries merge slower and enter in the LISA band sooner: hence, they stay in the LISA band for longer time and accumulate more SNR over their inspiraling lifetime. The maximum SNR that is resulting in this case is ~ 100.

The upper right panel of fig. 7.2 shows instead the same trend of the SNR with redshift, when time delay due to dynamical friction is taken into account. We find that in this case events delayed at epochs $z < 6$ are characterized by SNRs that can be as high as $10^3 - 10^4$, while at $z > 6$ the highest SNR limit remains the same as *AGN_fid* without any delays (SNR ~ 150).

Finally, for the prospect of follow-up observations with electromagnetic telescopes, we calculate the LISA angular resolutions of LDEs to quantify how large is the region in the sky that must be covered by a telescope to detect the electromagnetic signals from merging MBHBs. We adopt the results found by McGee et al. (2020), which are derived from a range of population models: the median angular resolution Ω can be associated to the median SNR at which a merger is observed by the following relation:

$$\Omega \approx 0.5 \left(\frac{\rm SNR}{10^3}\right)^{-7/4} \rm deg^2 \,. \tag{7.8}$$

The lower panel of Fig. 7.2 tracks the redshift evolution of the angular resolution for LDEs. Following the SNR trend, the optimal angular resolution is found for lower redshift (higher

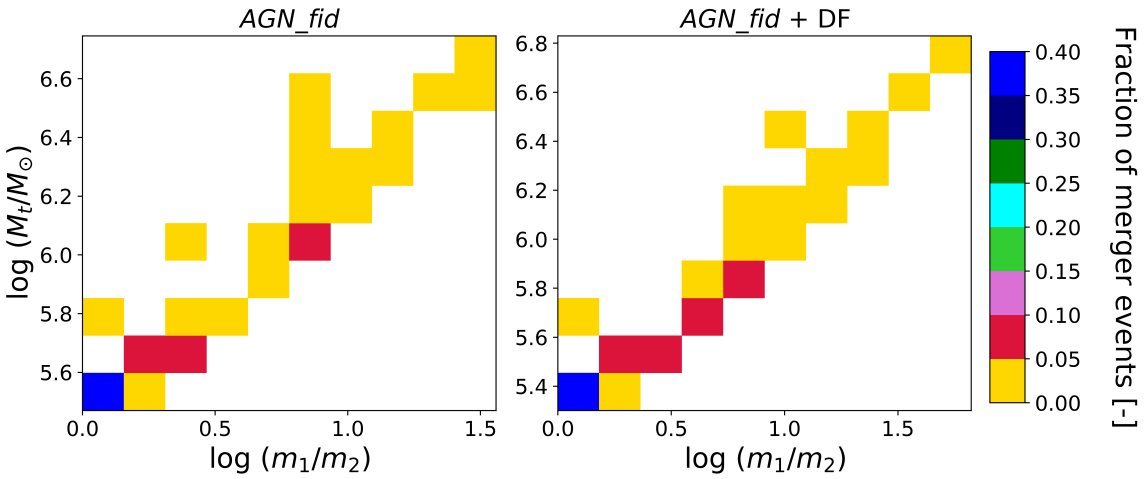

Figure 7.3: Fraction of detectable merger events as a function of the total mass of the system $M_t = m_1 + m_2$ and the mass ratio m_1/m_2 of the binary.

h_c) and smaller chirp mass (higher SNR) systems. This figure clearly shows that, although GW events from MBHB coalescence can be detected at high-z, their sky localization is poor (10 deg^2 in the most optimistic case; see also McWilliams et al., 2011), making follow-up observations in different EM bands challenging.

7.3 Mass ratio

Fig. 7.3 shows how the number of LDEs is distributed in terms of the "mass ratio" (defined as m_1/m_2, and shown in the x axis) and the "total mass" ($M_t = m_1 + m_2$, and shown in the y axis), for *AGN_fid* with (right) and without (left) considering additional delay in the mergers due to dynamical friction.

The highest fraction of LDEs occurs for equi-mass binaries, in the low mass range ($M_t \lesssim 3 \times 10^6 \mathrm{M}_\odot$), irrespective of consideration of delay time and is about 35 per cent to 40 per cent of the total LDE population in each run. In other words, "just-seeded" black holes in binaries have a higher probability to coalesce as compared to black holes with higher mass, assembled by accretion and/or merging.

Furthermore, we note that for a fixed M_t, the larger is the mass ratio the higher is the fraction of mergers. This is simply due to the fact that the number of black holes decreases with increasing masses, thus for a fixed M_t most of the mergers occurs for the BHs with lowest mass.

7.4 Time, frequency, and spatial scales of interest

As seen in Sec. 2.4, two MBHs[5] at a distance R require a certain time to merge through the emission of GWs. Such a time scale is called *coalescing* time ($t_{\rm coal}$) and it can be expressed in terms of the total mass M_t and the reduced mass μ as shown in Eqn. 2.50.

However, as already mentioned in Sec. 7.2, we can detect the GW signal only after SNR>SNR$_{\rm thresh}$. We thus compute the *observational* time as the time interval between the moment when SNR>SNR$_{\rm thresh}$ and when the two MBHs start merging:

$$t_{\rm obs} = t_{\rm coal}|_{\rm SNR>SNR_{thresh}}, \tag{7.9}$$

which provides the period of time during which the GW event is actually observable. This timescale provides the interval of time required to eventually trigger electromagnetic telescopes for follow-up observations to find the EM counterpart of the MBHB merging (see for example Loeb, 2016), or to simply probe the host galaxies of the system.

To the observational time $t_{\rm obs}$ of a merger event we can associate the frequency $\nu_{\rm obs}$ and the separation of the MBHs such that SNR>SNR$_{thresh}$, which are related by the following expression:

$$\nu_{obs} = \pi^{-1}\left(\frac{GM_t}{R^3_{obs}}\right)^{1/2}. \tag{7.10}$$

We summarise the resulting scales of interest in Table 7.1.

[5] We only consider binary coalescences in our analysis, neglecting systems composed by three (or more) MBHs.

RT calculations of LDEs

8

8.1 Introduction

The advancement of electromagnetic observatories such as the JWST has opened a new window in observational astronomy. This chapter mainly focuses on the observational aspects of LDEs in EM regime. We begin Sec. 8.2, by selecting the LDEs on the basis of their intrinsic properties ($\dot{M}$, SFR, metallicity, stellar mass, gas mass and dust mass) which are expected to be bright in one or more EM bands (e.g. rest-frame X-ray, UV and FIR). Furthermore, we restrict our selection to those LDEs that, after considering the effect of delay in the MBH coalescence due to dynamical friction are still occurring at $z \gtrsim 6$. This leads us to Sec. 8.3, in which we post-process these events with dust radiative transfer calculations to make proper predictions (synthetic spectra and maps) about their EM observational properties. We search for possible signatures of galaxy merging (e.g. variations in $\dot{M}$ and SFR, and/or morphological distorsion) in the simulated observations finding that it would be hard to distinguish an LDE from a galaxy hosting a single accreting MBH. Finally, in Sec. 8.4, we investigate the possibility to distinguish accreting and merging MBHs by analyzing their H_α profiles.

8.2 Selection of LDEs for RT calculations

In this section, among the GW events previously identified in chapter 7 we want to select those that are both detectable with LISA as well as with EM follow-up observations.

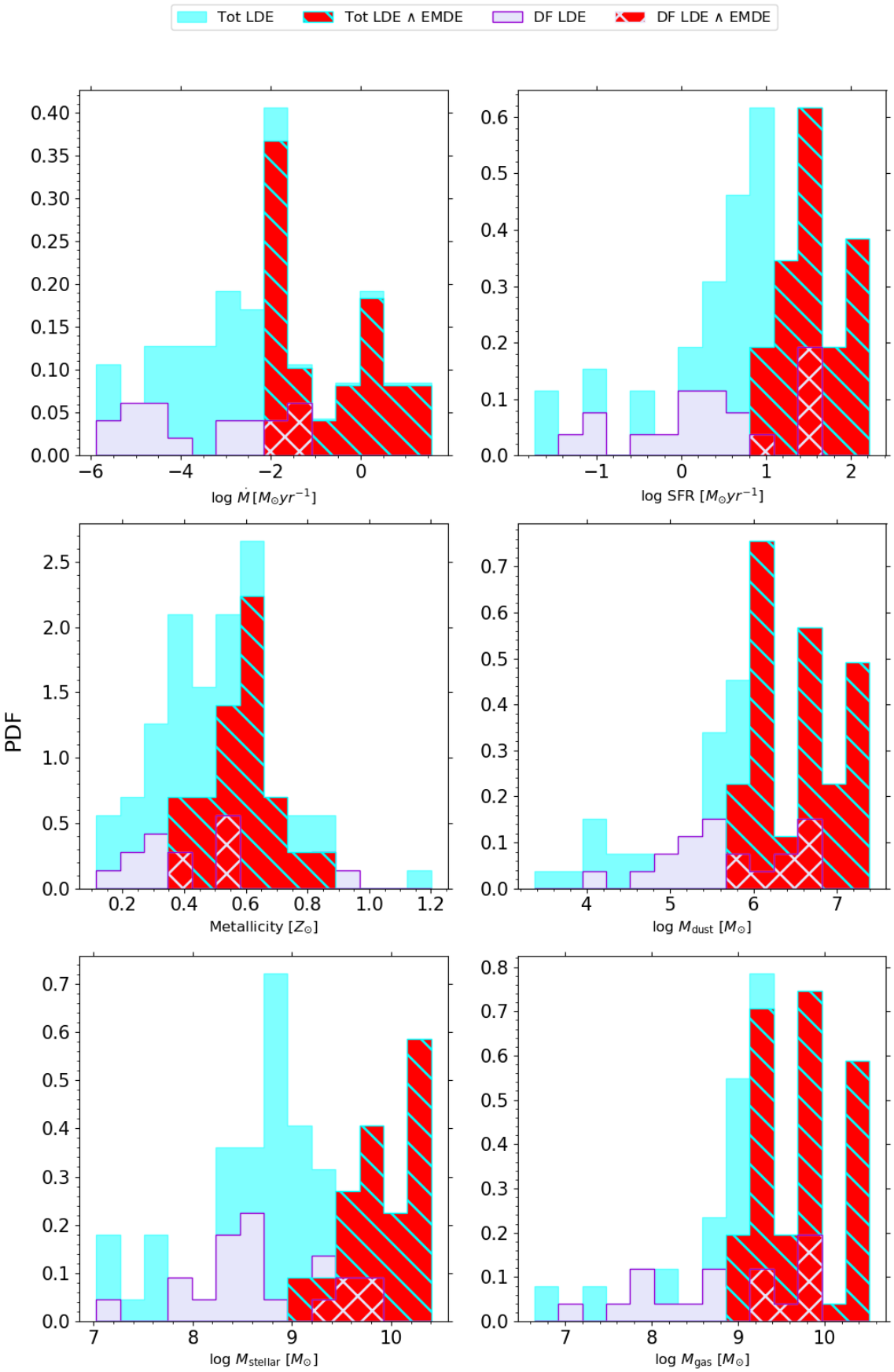

Figure 8.1: Probability Distribution Functions (PDFs) of different intrinsic properties of LDEs associated with a host galaxy before (cyan) and after (lilac) adding time delay due to DF at $z > 6$. In each panel, the red region with cyan hatches represents the LDEs which are also EMDEs (see Sec. 8.2.2) for all events while the white cross-hatched region represents the same for the events which occur after considering time delays due to DF. *Top left*: total accretion rates of the LISA events. *Top right*: star formation rate of the host galaxies. *Middle left*: distribution of the metallicities of the host galaxies. *Middle right*: dust mass distribution in the host galaxies. *Bottom left*: stellar mass of the host galaxies. *Bottom right*: gas mass of the host galaxies. Mass and metallicities are represented in solar units.

8.2.1 Intrinsic properties of systems hosting merging MBHs

Following the procedure described in Sec. 6.2, we first associate to each GW event previously identified by chapter 7 the intrinsic properties of the galaxies hosting merging MBHs: the total (primary plus secondary) BH accretion rate (BHAR), the star formation rate (SFR), the metallicity (Z), the dust mass ($M_{\rm dust}$), the stellar mass ($M_{\rm stellar}$) and the gas mass ($M_{\rm gas}$). In table C.1, we report the intrinsic properties of the merger events to which a galaxy is associated without including dynamical friction (DF) effects. In what follows, we report the results with and without including DF effects.

In Fig. 8.1, we show the Probability Distribution Function (PDF) of the intrinsic properties of all the LDEs assuming instantaneous merger (cyan shaded region, Tot LDE). This PDF is normalized to one. For these events, we compute the time delay due to stellar DF (as described in Sec. 6.3). We then select only those MBHs whose merging occurs at $z \gtrsim 6$ after taking into account the time delay effects. The lilac-shaded region denotes the LDEs among these events, called DF LDEs in the figure. In this case, for visual purposes, we normalize the PDFs to Tot LDE.

From the left top panel of Fig. 8.1, we can see that the total BHAR of LDEs in the *AGN_fid* run peaks at $\dot{M} \sim 0.01\ {\rm M}_\odot\ {\rm yr}^{-1}$, and varies in the range $[\sim 10^{-6} - 10\ {\rm M}_\odot\ {\rm yr}^{-1}]$. If considering the DF time delay effect, the highest BHAR of LDEs shifts to a lower value of around $\dot{M} \sim 0.1\ {\rm M}_\odot\ {\rm yr}^{-1}$. In the right top panel of Fig. 8.1, we show the distribution of the SFRs in the host galaxies of LDEs. We find that the average SFR of LDEs in the *AGN_fid* is SFR$\sim 63\ {\rm M}_\odot\ {\rm yr}^{-1}$, while it is $\sim 33\ {\rm M}_\odot\ {\rm yr}^{-1}$ if DF effects are taken into account. For what concerns the metallicities (Z) and the dust masses ($M_{\rm dust}$), shown in the middle left and middle right panel respectively, we find average values of $Z_{\rm mean} \sim 0.6\ Z_\odot$ ($\sim 0.5\ Z_\odot$) and $M_{\rm dust} \sim 6.5 \times 10^6\ {\rm M}_\odot$ ($\sim 3 \times 10^6\ {\rm M}_\odot$) without (with) including DF effects. Finally, in the bottom left and bottom right panels, stellar mass ($M_{\rm stellar}$) and gas mass ($M_{\rm gas}$) on the host galaxies are shown. We find an average of $M_{\rm stellar} \sim 4.8 \times 10^9\ {\rm M}_\odot$ ($\sim 1.3 \times 10^9\ {\rm M}_\odot$) and $M_{\rm gas} \sim 6.7 \times 10^9\ {\rm M}_\odot$ ($\sim 2.5 \times 10^9\ {\rm M}_\odot$) without (with) including the delays due to DF.

Overall, we find that when including DF effects the PDFs of the intrinsic properties shift towards lower values. This occurs since, when applying DF effects, we lose all the events oc-

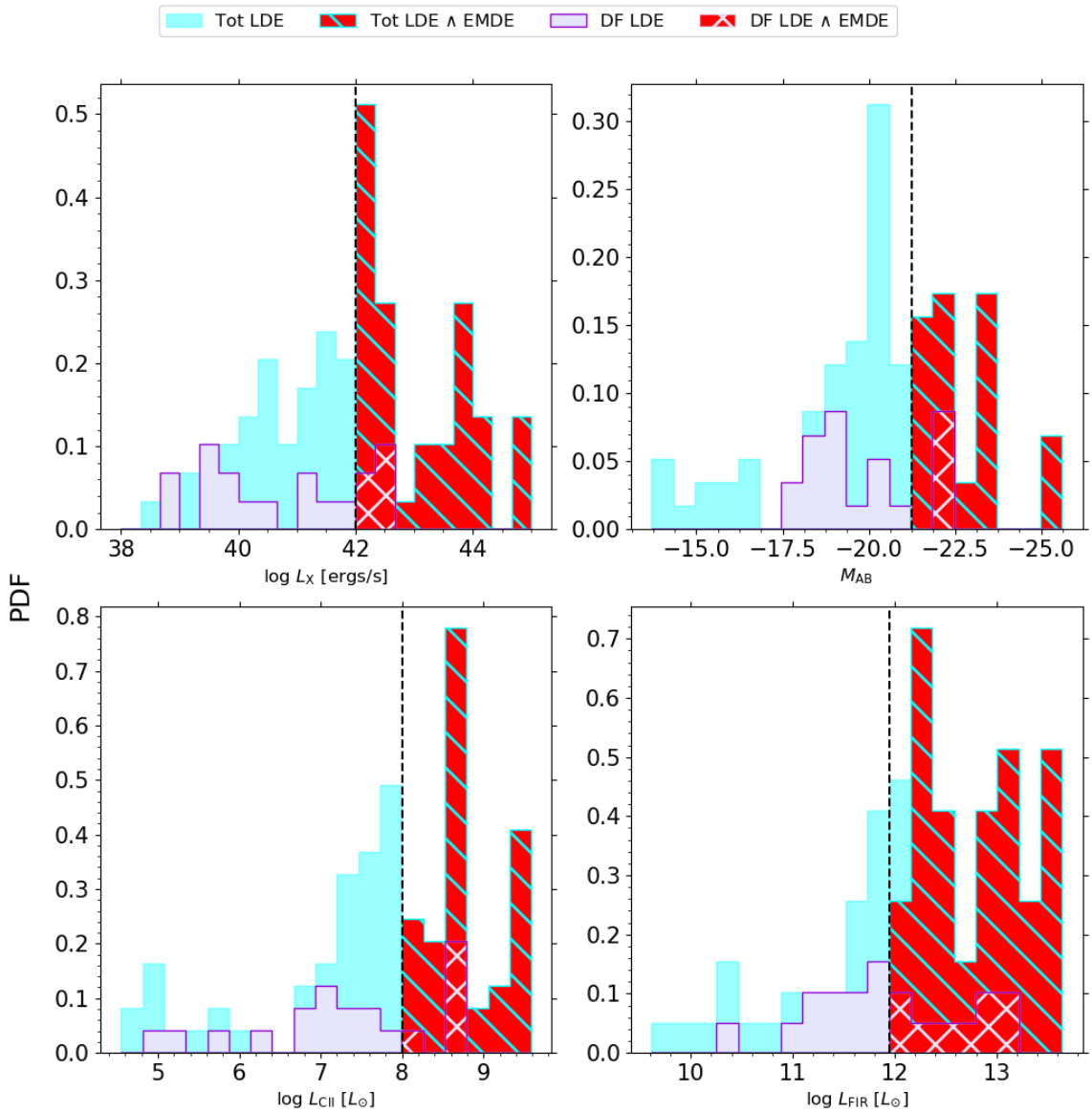

Figure 8.2: PDF comparison of different observable properties of LDEs (cyan), after adding time delay due to DF at $z > 6$ (lilac) for follow-up observations in different wavelength bands: X-ray (upper left panel), UV (upper right), [CII] (bottom left), FIR (bottom right). The colours are the same as explained in Fig.8.1.

curring at $z \sim 6$ (in the instantaneous merging approximations), namely the most evolved ones, thus being characterized by larger BHAR, SFR, $M_{\rm dust}$, Z, $M_{\rm stellar}$ and $M_{\rm gas}$.

8.2.2 Observable properties of systems hosting merging MBHs

Starting from the intrinsic properties described above and following the formalism described in the Appendix B, we compute the following observable properties: the X-ray luminosity ($L_{\rm X}$), the total (from stars and accreting BHs) UV luminosity ($L_{\rm UV}$) and the corresponding UV magnitude ($M_{\rm AB}$), the [CII] luminosity ($L_{\rm CII}$), and the far-infrared luminosity ($L_{\rm FIR}$). We report in table

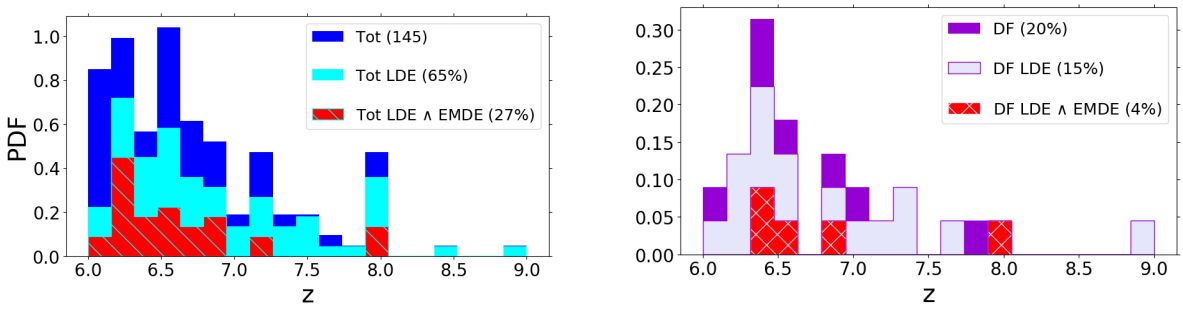

Figure 8.3: PDFs of all merging events and all LDEs (left panel) and DF events and DF LDEs (right panel). In the left panel, the blue area represents the total number of merging events in our *AGN_fid* run. The cyan area represents the LDEs in *AGN_fid* and the red hatched area further denotes the LDEs which are also detectable in UV, X-ray, CII, and/or FIR bands by JWST, LynX, and ALMA. In the right panel, the dark violet area represents the mergers that take place at $z > 6$ after we consider time delay due to dynamical friction. The lilac area shows the LDEs of these aforementioned mergers while the red cross-hatched area represents the LDEs and EMDEs from these mergers.

C.2, the observable properties of the galaxies to which a merger is associated (corresponding to the events reported in table C.1).

In Fig. 8.2, we show the PDFs of the aforementioned observational properties. The vertical lines represent the luminosity thresholds that we adopt to identify those sources that are more likely detectable with EM telescopes. In particular, for the UV, [CII], and FIR emissions, we consider the typical values found in the ALPINE survey (Le Fèvre et al., 2020) for $z \sim 5-6$ galaxies (Béthermin et al., 2020; Faisst et al., 2020; Sommovigo et al., 2022). For the X-ray, we consider a threshold of $L_X \sim 10^{42}$ erg s^{-1}, that is both close to the confusion limit of Athena (Aird et al., 2013) and expected to be reached through a Lynx-like[1] instrument in ~ 40 ks (see, e.g., Table 2 in Lops et al., 2023).

Hereafter, we call "Electro-Magnetic Detectable Events" (EMDEs) those events whose observable properties are above at least one of the sensitivities of the EM telescopes considered. The red cyan-hatched region denotes those events that are both detectable with LISA and through EM telescopes, assuming instantaneous merger (Tot LDE $\wedge$ EMDE). The red cross-hatched region reports the EM AND LISA detectable events that are at $z \gtrsim 6$ after having considered DF effects. These are labelled in the figure as DF LDE $\wedge$ EMDE (also in Fig. 8.1).

Considering DF effects, the fraction of LDE events that are EM detectable decreases from 31 % to 21% in the Xray, from 26 % to 18% in the rest frame UV, from 32% to 21% in [CII],

[1] https://wwwastro.msfc.nasa.gov/lynx/docs/LynxConceptStudy.pdf

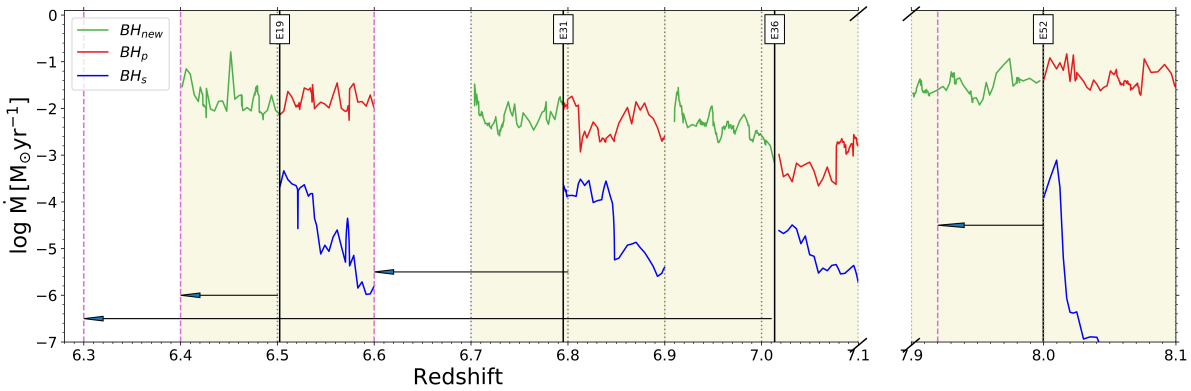

Figure 8.4: Redshift evolution of the MBH accretion rates ($\dot{M}$) for LDEs. We select 4 events for which the merger occurs at $z \gtrsim 6$ after adding time delays due to DF. For each event, the red (blue) line refers to the primary (secondary) MBH, labelled BH_p (BH_s) in the figure, while the green line shows $\dot{M}$ of the new MBH resulting from the mergere (BH_{new}). The black solid vertical lines show the times at which the merger occurs in the simulation, according to the instantaneous merging approximation. The vertical pink-dashed lines show the new redshifts at which the BHs merge after adding delays due to DF. The black arrows show the change in the merger redshifts upon considering time delays due to DF in post-processing. The yellow patches show the time span for which the selected BHs evolve without undergoing any other mergers between two snapshots (the redshifts of the snapshots are depicted by vertical gray-dotted lines.

from 45 % to 32% in the FIR. In conclusion, only 20-30% of the total LDEs in the *AGN_fid* run are also detectable with EM telescopes.

8.2.3 Final selection of LDEs

The redshift distribution of the events as selected based on their observability with LISA and EM telescopes is shown in Fig. 8.3. In the left panel, all events (Tot) are shown with a blue-shaded region, the LDEs (Tot LDEs) with a cyan-shaded region, and LDEs detectable with EM telescopes (Tot LDE $\wedge$ EMDE) with a red cyan-hatched region. In the right panel, the PDFs of those MBHs whose merging is occurring at $z \gtrsim 6$ after including time delay effects (DF) are shown with a dark-violet shaded region, the LDEs among the DF events (DF LDEs) with a lilac shaded region, the EM detectable events among the DF LDEs with a red cross-hatched region (DF LDE $\wedge$ EMDE).

We end up with a total of 4 events that are interesting from the point of view of their observational properties, being the brightest in different electromagnetic bands (L_X, $\mathrm{L_{UV}}$, $\mathrm{L_{CII}}$, and $\mathrm{L_{FIR}}$): E19 at $z = 6.5$, E31 at $z = 6.8$, E36 at $z = 7.0$ and E52 at $z = 8.0$. Fig. 8.4 shows the accretion rate evolution of the MBHs involved in these events. We remind that these events are characterised by the following properties: (i) they are detectable with LISA with a SNR>5;

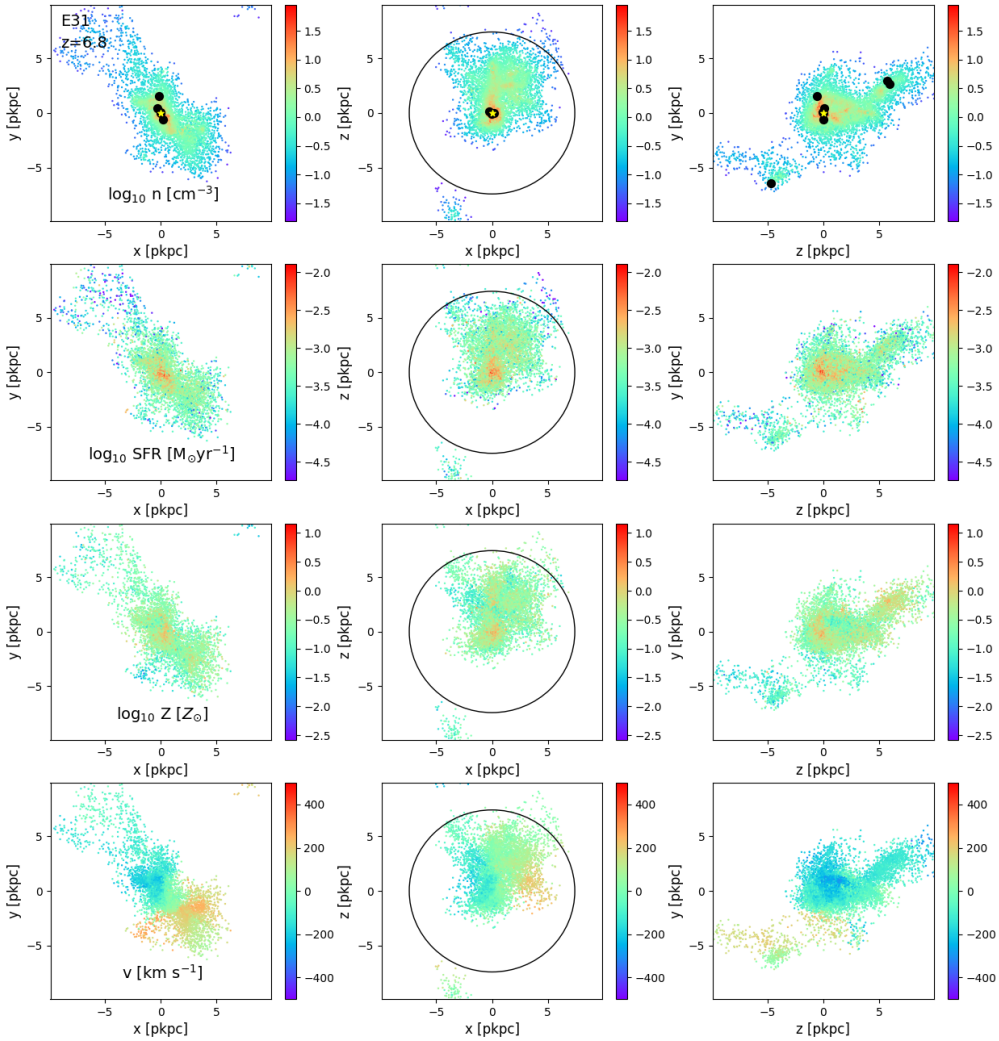

Figure 8.5: 3D representation of the intrinsic properties for the event 31 (E31) at $z = 6.8$. Each box has a side of 20 pkpc and 1.2 pkpc along the z/y/x directions (in the left/middle/right panel, respectively) for three different lines of sight (LOS). First row: gas density of the star-forming particles. The black circle identifies the region adopted to compute the intrinsic properties in Sec. 8.2.1, corresponding to 30% of the virial radius. The filled black circles represent the location of the BHs in the simulation; in particular, the location of the event is denoted by a yellow-filled star. Second row: star formation rate of the SF particles. Third row: gas metallicity of the SF particles. Fourth row: gas velocity of the SF particles along the different LOS considered.

(ii) they are detectable with EM telescopes in at least one band (see Fig. 8.2); (iii) the merging of the MBHs is expected to occur at $z \gtrsim 6$ after considering the time delay due to dynamical friction.

In Fig. 8.4 we show the accretion rate of the primary and secondary MBH before the merger,

and the accretion rate of the MBH after the merger, namely after that the primary MBH has swallowed the secondary one. The final MBH has thus inherited the location of the primary BH, while its total mass is given by the sum of the primary plus secondary. We see that the accretion rate after the merger event mostly follows the accretion rate of the primary MBH before the merger; its larger mass as compared to the secondary MBHs is thus always dominating the accretion rate of the system.

8.2.4 3D representation of intrinsic properties

We finally showcase the spatial distribution of the intrinsic properties of the selected events. Fig. 8.5 shows the gas density (top panels), the SFR (second row), gas metallicity (third row), and the gas velocity (bottom panels) of the star-forming particles relative to the event 31 along three different lines of sight (LOS). In Fig. D.1, D.2, and D.3 we report the same properties for the other three selected events. The filled black circles represent the location of the BHs in the simulation; in particular, the location of the merger is denoted by a yellow-filled star. The solid circle identifies the region adopted to compute the intrinsic properties in Sec. 8.2.1, namely 30% of the virial radius, hereafter called "SF region": $r_{\rm SF} = 8.2, 7.4, 5.0, 4.8$ kpc, for E19, E31, E36, E52, respectively).

These figures clearly show that the location of the star-forming particles coincides with regions of relatively high density ($\log_{10} n \gtrsim 10 - 100\ {\rm cm}^{-3}$), which thus become the most metal-enriched ones ($\log_{10} Z \sim 0.1 - 1\ {\rm Z}_{\rm M_\odot}$), reaching the solar metallicity in the densest regions. From the bottom row, we notice that along the z and y directions, the gas velocities of the star-forming particles resemble the dynamics of a rotating disk in the edge-on view. The dynamics of the star-forming particles will be further analysed in Sec. 8.4. Here, we underline that a disk-like velocity distribution is also visible in E52 along the x direction and that these findings are in agreement with recent ALMA results (Rowland et al., 2024).

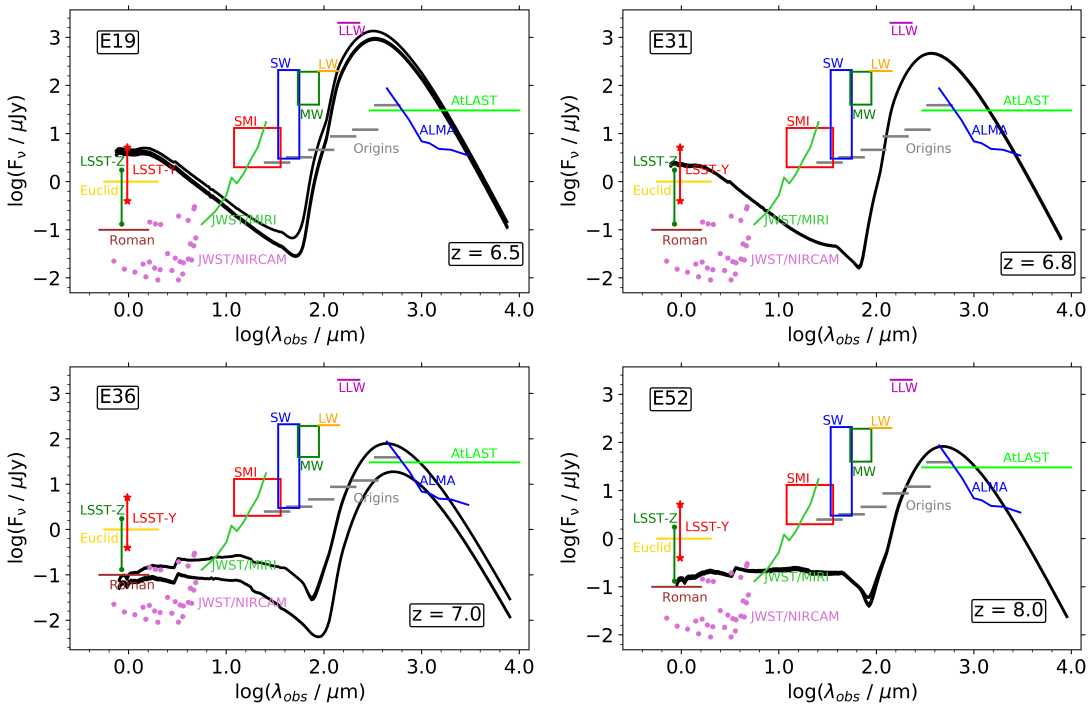

Figure 8.6: Spectral energy distributions (SEDs) of the selected events: E19 at $z = 6.5$ (top left), E31 at $z = 6.8$ (top right), E36 at $z = 7.0$ (bottom left), E52 (bottom right) at $z = 8.0$, extracted from different lines of sight (as in Fig. 8.5) from an aperture containing the SF region ($r_{\rm SF} = 8.2, 7.4, 5.0, 4.8$ kpc, respectively). The synthetic SEDs are compared with the sensitivities of the different EM telescopes: LSST filters Z (dark green vertical line) and Y (red vertical line), Roman (brown horizontal line), JWST/NIRCAM (orchid dots), JWST/MIRI (green curved line, for an exposure time of ~ 3 hours), Origins-like (gray horizontal lines, at 5σ in 1 hour), SPICA-like (red, blue, green boxes, yellow, magenta horizontal lines at 5σ in 1 hour represented by the top portions of the rectangles and at 3σ represented by the lower sides of the rectangle; if the confusion limit is achieved within an hour, then the sensitivies are depicted by the lines), ALMA (blue curved line, in 10 hours of observation time) and AtLAST (light green horizontal line) are shown.

8.3 EM signals from selected events

For the RT calculations (as described in Sec. 4.5), we select a cubic region with size 40 kpc, centered on the centre of mass of the most-massive halo, where the galaxies associated to the merging events reside and run SKIRT on the merger events.

8.3.1 Synthetic spectra

In Fig. 8.6, we show the SEDs resulting from our RT calculations for the selected events, and we compare them with the sensitivities of different EM telescopes. From this comparison, it results that E19 and E31 are detectable at short ($\lambda_{\rm obs} \lesssim 10$ μm) and long ($\lambda_{\rm obs} \gtrsim 100$ μm) wavelengths with any of the current/planned EM telescopes sensitive to these wavelengths (e.g. LSST, Euclid, Roman, JWST, and Origins, ALMA, AtLAST, respectively), whereas they are far

below the detection limit of a SPICA-like telescope (see also PRIMA[2]). However, we underline that our model does not include any dusty torus emission. The detectability of LDEs at these wavelengths thus depends on the possible presence of the torus and on its properties (i.e. dust mass and temperature, see e.g. Fig. 11 in Di Mascia et al., 2021). Similar considerations apply to E36 and E52, but these events will be detectable only by JWST (and barely by Roman).

8.3.2 Synthetic maps of E31

Once we have checked that the selected events are detectable in one or more EM bands, we investigate whether their emission properties differ from the ones of a typical AGN, powered by a single MBH. For this kind of study, we focus our attention on a specific event, e.g. E31. This event is predicted to occur at $z = 6.8$ ($z = 6.6$) assuming instantaneous merger (considering the time delay due to stellar dynamical friction), as can be deduced from Fig. 8.4 (see the solid black vertical line associated to E31, and the dashed magenta vertical line indicated by the arrow).

In the panels of Fig. 8.7, the second and third rows show maps of the continuum emission predicted by our RT calculations for E31 in the wavelength ranges covered by LSST, JWST, and ALMA (left-most, middle, and right-most panels, respectively). In the same panels, coloured (black) circles represent the position of MBHs accreting with $\dot{M}$ larger (smaller) than $10^{-4}\,\mathrm{M}_{\odot}\,\mathrm{yr}^{-1}$. MBHs involved in the merger event are highlighted with white circles.

We also show in the top and bottom panels the SEDs relative at z = 6.8 and z = 6.7, namely at redshifts before and after the merging. In particular, we show the emission from the entire simulated field of view (left panel), the emission associated with the merging BH and with other representative individual AGNs (two at $z = 6.8$ and three at $z = 6.7$) in the field of view (middle and right panels). By comparing the SEDs of the post-merger BH against the ones of isolated AGN we find only marginal differences in the synthetic spectra, mostly in the mid infra-red band. However, in this region, the flux is below the detection limit of current/planned telescopes sensitive to this wavelength range.

We conclude that it will be impossible to identify a LDE from the continuum SEDs because of the absence of specific signatures from the merging MBHs. **Although in this work we have**

[2]https://prima.ipac.caltech.edu/

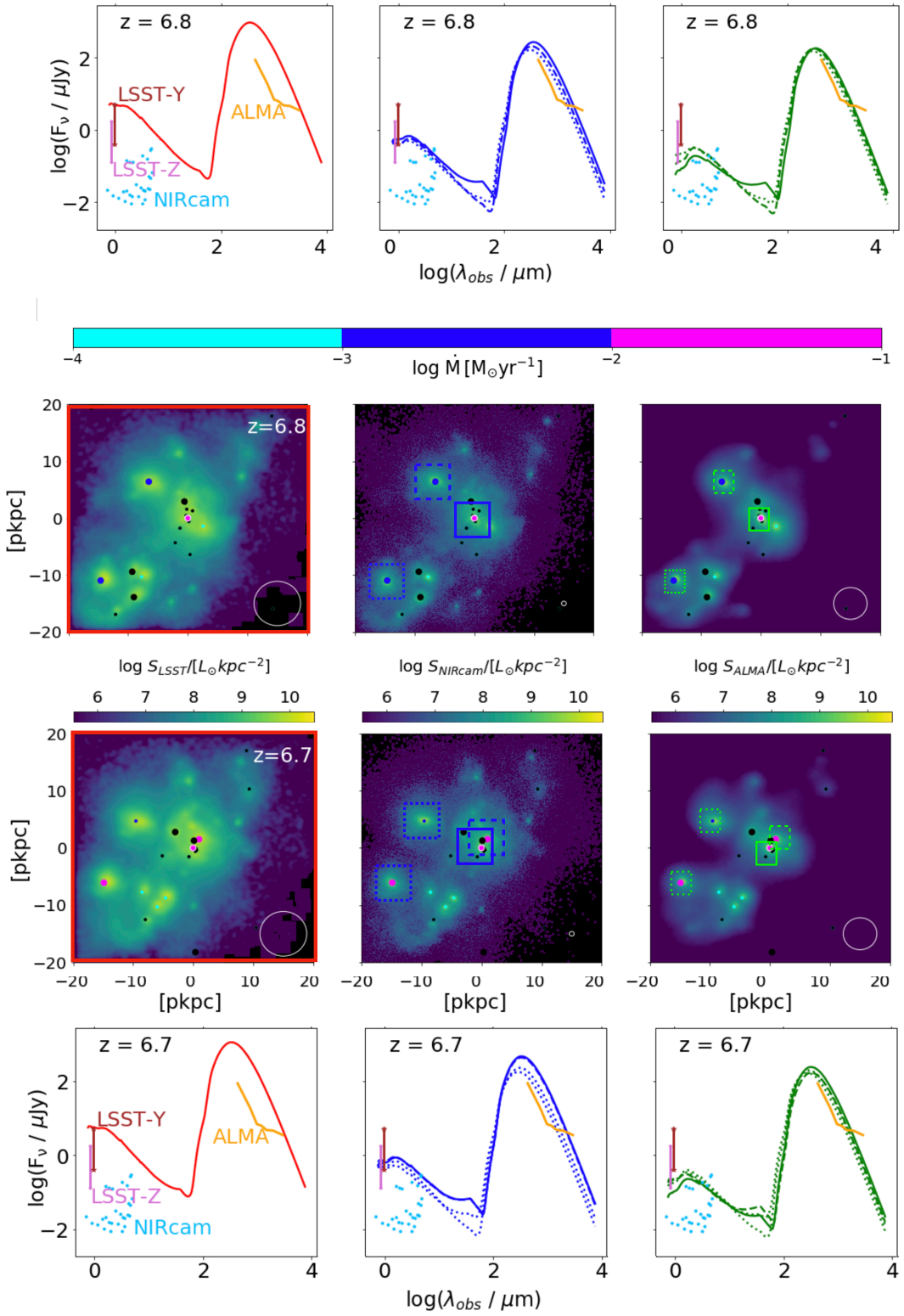

Figure 8.7: Simulated maps (second and third row) in different observable bands and SEDs (first and bottom row) relative to event 31. From left to right we show the maps in the wavelength range of LSST (0.9-1.1 μm), NIRcam (3.8-5.1 μm), and ALMA (0.8-1.1 mm). Each map is convolved to match the angular resolution of the corresponding instruments considered: LSST (0.7"), NIRCAM (0.07"), and ALMA (0.5"). These values correspond to beam sizes of approximately 4 kpc, 0.4 kpc, and 3 kpc, respectively, at $z \sim 6.8$, and are shown as white circles at the bottom of each panel in the second and third rows. The circles with white edgecolor represent the coalescing MBHs while the others represent the non-coalescing MBHs in the same halo. MBHs are coloured based on their mass accretion rates: MBHs with $\dot{M} < 10^{-4}$ M$_\odot$ are represented in black, 10^{-4} M$_\odot$ $\leq \dot{M} < 10^{-3}$ M$_\odot$ in cyan, 10^{-3} M$_\odot$ $\leq \dot{M} < 10^{-2}$ M$_\odot$ in blue, and MBHs with $\dot{M} > 10^{-1}$M$_\odot$ in magenta. Small, medium and large circles represent MBHs with masses M$_{\rm BH} \leq 10^5$ M$_\odot$, $10^{5.5}$ M$_\odot$ $\leq$ M$_{\rm BH} \leq 10^6$ M$_\odot$ and M$_{\rm BH} > 10^6$ M$_\odot$, respectively. The top and bottom rows show the SEDs at z = 6.8 and z = 6.7, respectively. The left panel indicates the emission relative to the entire field of view. In the middle and right panels, a square region with size 2 kpc and 800 pc respectively is selected around the merging BH (solid contour in the emission maps) to extract the SED (solid line in the SED). The same is done for other AGN in the field of view (dashed contour in the emission maps and dashed line in the SED).

not thoroughly explored the impact of all the assumptions done in our model, we do not expect that this main conclusion would change, e.g., varying the dust-to-metal mass ratio, the dust properties, the slopes of the AGN SED. Furthermore, although the inclusion of the dusty torus would ease the detectability of the EM emission in the mid infra-red band, it still would not help to distinguish an AGN powered by a single MBH from a LDEs.

8.4 H_α emission line from merging MBHs

High-z dual AGN recently suggested by JWST observations are discovered by the means of double-peaked, broad emission Balmer lines (e.g. Maiolino et al., 2023; Übler et al., 2023). To investigate whether it is possible to infer the presence of the accreting and merging MBHs in our selected events, we compute their H_α emission lines. The H_α line arises from recombinations occurring in the ISM of the host galaxy and in the broad line region (BLR) of the accreting BHs, producing a narrow and two broad components, respectively.

The luminosity of the narrow component (in units of erg s^{-1}) scales with the galaxy SFR (in units of $M_\odot$ yr^{-1}), following Kennicutt & Evans (2012):

$$L_{H_\alpha}^{SFR} = 1.86 \times 10^{41} SFR. \tag{8.1}$$

For what concerns its profile, it is shaped by the velocity distribution of the SF particles. To compute the profile of the line resulting from the star formation, we first calculate the PDF of the velocities of the SF particles, weighted by their SFR, and then we re-normalise it in such a way that its integrated flux corresponds to L_{H_α}, as per Eq. 8.1.

The luminosity of the broad components ($L_{H_\alpha}^{M_{BH}}$) is instead proportional to the luminosity of the accreting BHs at 5100 Å(L_{5100}), as in eq. 2 by Reines et al. (2013):

$$L_{H_\alpha}^{M_{BH}} = 5.25 \times 10^{42} \left(\frac{L_{5100}}{10^{44} \text{ erg s}^{-1}} \right)^{1.157} \text{erg s}^{-1}, \tag{8.2}$$

where $L_{5100} = f_{bol} L_{bol} \sim f_{bol} \epsilon \lambda_{EDD} \dot{M}_{EDD} c^2$, $f_{bol} = 0.1$ (Lusso et al., 2012), and λ_{EDD} is the Eddington ratio, namely the ratio between $\dot{M}$ and the Eddington accretion rate $\dot{M}_{EDD}$ of each

BH. The full width at half maximum of the broad components ($FWHM_{BH}$) is finally related to the above quantities through eq. 5 by Reines et al. (2013):

$$\log \frac{M_{\rm BH}}{\rm M_\odot} = 6.6 + 0.47 \log \left(\frac{L_{H_\alpha}^{\rm M_{BH}}}{10^{42}\ {\rm erg\ s^{-1}}} \right) + 2.06\ \log \left(\frac{FWHM_{\rm BH}}{10^3\ {\rm km\ s^{-1}}} \right). \tag{8.3}$$

The line centroids associated with the BLR of the MBHs are shifted with respect to each other based on their relative velocity. In particular, their relative position in the velocity space depends on the following relative velocities: we call $v_{\rm gal} - v_p$ the relative velocity between the galaxy and the primary BH, and $v_p - v_s$ the relative velocity between the merging BHs.

To summarise, the profile of the Hα line is determined by the following quantities: SFR, velocity distribution of the SF particles, $\lambda_{\rm EDD,p}$, M_p, $\lambda_{\rm EDD,s}$, M_s, $v_{\rm gal} - v_p$, and $v_p - v_s$. All these properties are predicted by our simulation[3] that allows us to properly compute the H_α emission line arising from our selected events.

8.4.1 Synthetic H_α emission line from the selected events

We report in Fig. 8.8 the H_α line predicted by our simulations for the 4 selected events (E19, E31, E36, E52, from the top to the bottom), along different LOSs (along the z, y, and x direction in the left, middle, and right panel, respectively). The shaded region represents the result of our calculations, the solid black line denotes the total flux from the three components (the SF, and the two accreting BHs) plus noise[4], the red dotted line shows the contribution from the SF.

We notice that, for what concerns E19, along the three directions, the line profile is characterized by a complex, multi-peaked structure. This resembles the "Disturbed Disk" (DD) stage analysed in Kohandel et al. (2020), where the presence of multiple star-forming clumps of gas perturbs the main galaxy disk (see Fig. D.1). Furthermore, we remark that for many of the LOSs shown in Fig. 8.8 the H_α line shows a single peak shape, apart from E31, along the z and y directions, and E52 along the x direction. Along these last three LOSs, the H_α profile is char-

[3]The relative velocities between the primary and secondary MBHs were computed at those timesteps when the first condition for the merging is satisfied but not the second one (see condition (i) and (ii) in Sec. 3.5.2, respectively).

[4]We add to our simulated spectra, on velocity bins of $\Delta v = 5$ km s^{-1}, a random number extracted by a Gaussian distribution having mean equal to zero and standard deviation equal to 5×10^{-21}erg s^{-1} cm^{-2} A^{-1}.

acterised by a double peak shape. This is consistent with what has been noted at the end of Sec. 8.2.4, namely that the gas velocity distribution along these directions resembles the dynamics of a rotating disk in the edge-on view[5].

Independently on the shape of the H_α line, it can be seen that the total flux (black solid line) always coincides with the flux arising from the star-forming regions (red dotted line), along any of the LOS analysed, and for all the events considered. This means that the merging MBHs in our simulation are not accreting efficiently enough to leave any signature in the synthetic H_α line.

8.4.2 Boosting the accretion rate of the merging BHs

In the previous subsection, we concluded that the properties of our simulated systems are such that no signature of merging MBHs can be seen from the H_α profile. To make this result more generic, we now ask ourselves the following question: *How efficiently two merging MBHs should accrete in order to be detectable?*

To answer this question, we re-simulate the H_α line, keeping constant the contribution from the SFR, and artificially boosting the accretion rates and masses of the merging MBHs (both in the primary and in the secondary). For simplicity's sake, we restrict the analysis to a single event and to a single LOS. We choose E36 and the LOS along the x direction since, in this case, the H_α line neither resembles a DD stage nor the dynamics of a rotating disk in the edge-on view.

The results of this experiment are shown in Fig. 8.9: in the left column, we keep the masses of the MBHs involved in the merging of E36, and we vary their accretion rates from Eddington ($\lambda_{\rm EDD,p} = \lambda_{\rm EDD,s} = 1$), up to $10\times$ Eddington; in the right column, we repeat the same exercise in terms of the accretion rate, but we consider a primary MBH that is $10\times$ more massive than the original one. While doing these calculations, we assume $L_{\rm bol} \propto \lambda_{\rm EDD}$, though we are aware of the sub-linear increasing of the luminosity with the accretion in super-Eddington regimes (e.g. Madau et al., 2014b). We verify *a posteriori* that our assumption is conservative.

From Fig. 8.9, it is clear (and obvious) that the more the MBHs are accreting and the more they are massive, the larger is the deviation from the original H_α line. The point here is whether

[5]The spectral profile of a disk in the edge-on (face-on) view is characterised by a double (single) peak shape (e.g. Elitzur et al., 2012).

or not, even in these extreme cases, we would be able to infer the presence of the two accreting MBHs. To understand this point, we adopt a procedure similar to the one described in Gallerani et al. (2018, see also Carniani et al. 2023), developed to infer the presence of outflowing gas from the shape of the [CII] (H_α) emission line. This method is based on the analysis of the residuals, as obtained by subtracting from the emission line data its best-fitting model. We thus fit our simulated H_α lines both with a single Gaussian (SG) and a double Gaussian (DG) profile. The green and orange lines in Fig. 8.9 report the best fitting results, assuming an SG and a DG profile, respectively. In the bottom panel of each figure, we further report the residual of the best-fitting procedure, along with the random noise added to the synthetic spectrum.

To measure the goodness of the fit, we apply the two-sample Kolmogorov–Smirnov (K-S) test (Kolmogorov, 1933; Smirnov, 1948) to our simulated data and we compute the K-S probability (p_{KS}). In particular, we apply the two-sample KS test to the cumulative distribution function (CDF) of the SG residual versus the CDF of the noise and to the CDF of the DG residual versus the CDF of the noise to test whether the residuals come from the same random distribution used to simulate the noise. We remind that, according to the K-S test, two samples are not drawn from the same underlying distribution if $p_{KS} < 0.05$. We report the results of the K-S test in the bottom panels of each figure, along with the best-fit parameters, where the amplitudes of the Gaussians are in units of 10^{-19}erg s^{-1} cm^{-2} A^{-1}.

We find that, even in the case $\lambda_{\rm EDD,p} = \lambda_{\rm EDD,s} = 1$ (top, left panel), the H_α line can be well fitted with an SG profile. In all the other cases, the extreme accretion rates considered lead the profile to deviate in a statistically significant way from an SG profile ($p_{KS,SG} < 0.05$). However, we also find that, in most of the cases, a DG profile is enough to provide a good fit to the synthetic spectra ($p_{KS,DG} > 0.05$). The only exception occurs for the following (very extreme) combination of parameters: $M_{\rm BH,p} = 10^6$ M$_\odot$; $M_{\rm BH,s} = 10^5$ M$_\odot$; $\lambda_{\rm EDD,p} = 5$; $\lambda_{\rm EDD,s} = 10$, shown in the second column and third row. In this case $p_{KS,SG} < 0.05 \wedge p_{KS,DG} < 0.05$, meaning that a third component is required to provide a good fit to the data.

To summarise, the presence of two accreting MBHs could be possibly inferred only in very extreme (i.e. rare) circumstances ($\lambda_{\rm EDD} \sim 5-10$). We underline that this is true even if, with the assumption $L_{\rm bol} \propto \lambda_{\rm EDD}$, we are maximising the effects of the multiple accreting MBHs on the

shape of the H_α line. We thus conclude that the combined detection of GW and EM signals from $z \gtrsim 6$ MBHs is challenging (if not impossible) not only because of the poor sky-localization ($\sim$10 deg^2) provided by LISA but also because the loudest GW emitters ($M_{\rm BH} \sim 10^{5-6}\,\mathrm{M}_\odot$) are not massive enough to leave significant signatures (e.g. extended wings) in the emission lines arising from the broad line region.

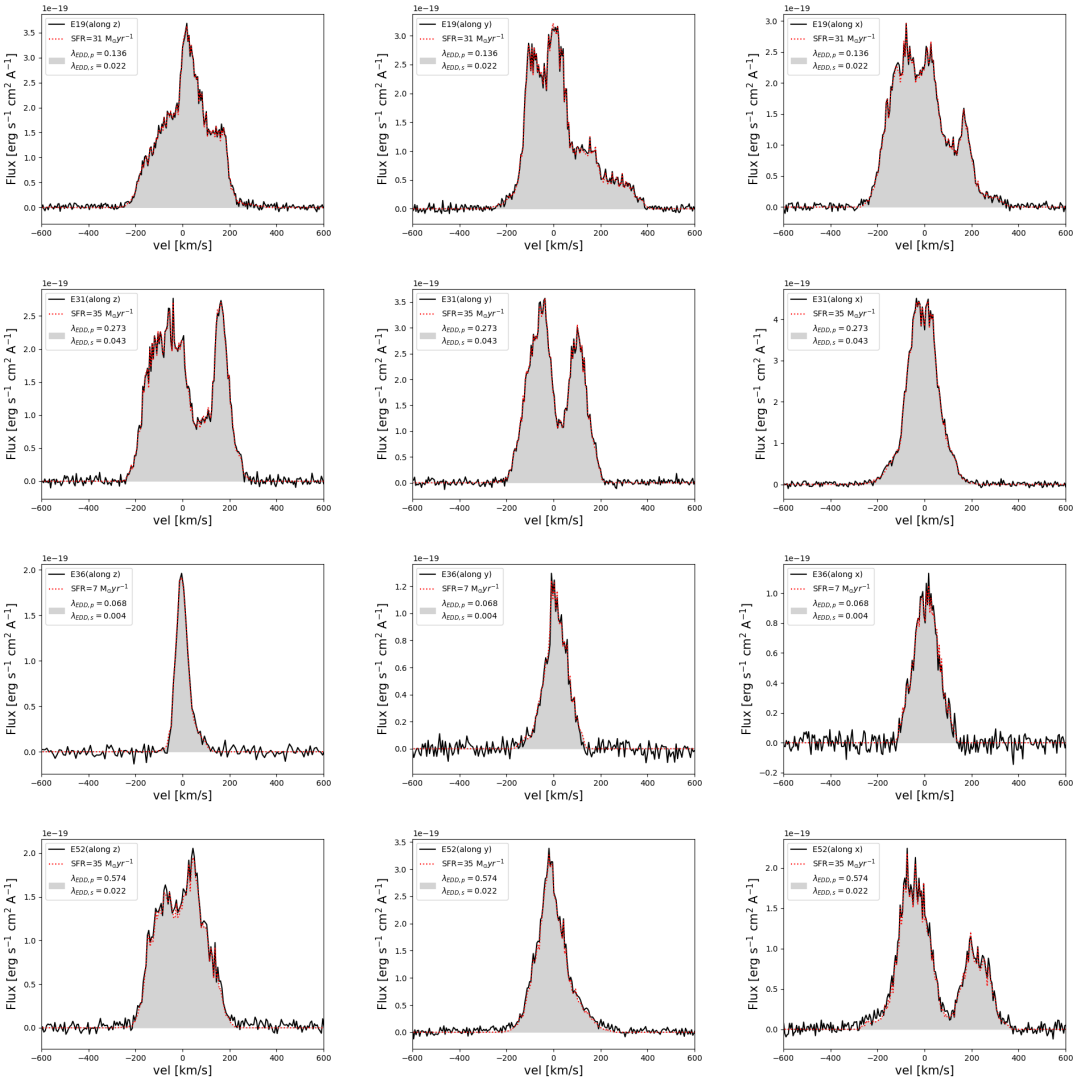

Figure 8.8: Predicted H_α line profiles from simulations for E19, E31, E36 and E52 (first, second, third, and last rows, respectively) shown along LOS in the z, y, and x (first, second and last columns, respectively) directions. The grey-shaded regions represent the calculated results. The solid black lines indicate the total flux (from SF, the accreting primary and secondary MBHs) along with the noise component and the red-dotted lines show the contribution only from SF.

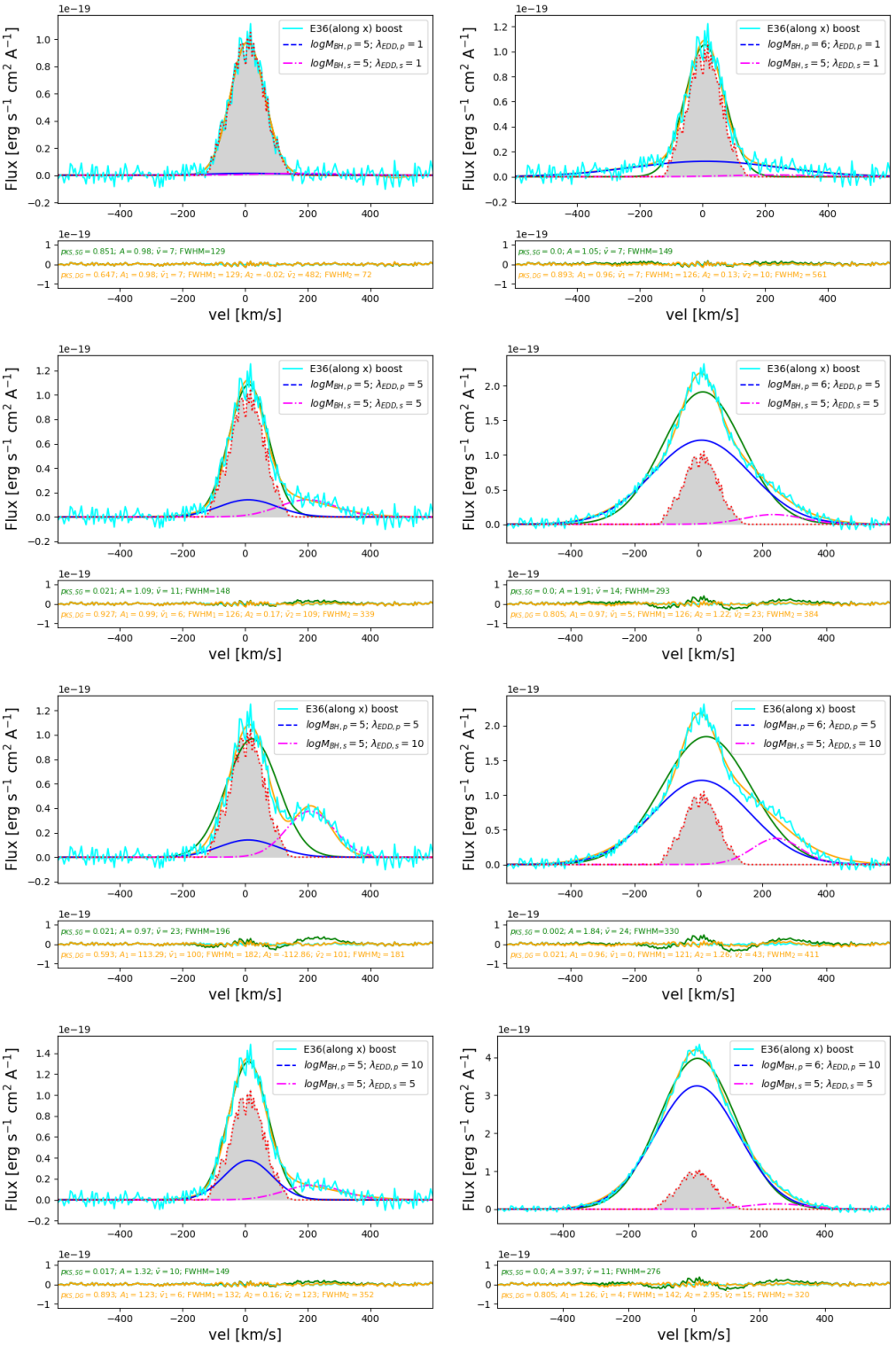

Figure 8.9: Re-simulated H_α profile for E36 in the LOS along the x direction. The left column shows results for constant masses of MBHs but varying accretion rates. For the same values of the accretion rates as shown in the left column, we show the results when the primary MBH is ten times more massive than the secondary MBH. The blue (pink) dashed line represents the contribution from primary (secondary) MBH. The bottom panel in each figure refers to the added random noise in the synthetic spectrum along with the residual of the best-fitting model as explained in Sec. 8.4.2.

Part IV

Summary and conclusions

Summary and conclusions

9

The existence of supermassive black holes (SMBHs) in the early Universe (less than one Gyr after the Big Bang) challenges our understanding of black hole (BH) formation and growth mechanisms. The purpose of this Ph.D. research was to dig deeper on the evolution of SMBH seeds using GW and multi-wavelength EM observations.

In this work, we adopted a suite of cosmological hydrodynamical simulations of galaxy formation and BH co-evolution, developed with the GADGET-3 code, and zoomed-in on biased ($> 3\sigma$) overdense regions ($M_h \sim 10^{12}$ M$_\odot$ dark matter halos at $z = 6$) of the Universe. These simulations are characterised by different numerical resolutions and star formation/AGN feedback prescriptions, and are based on a seeding prescription such that $M_{\rm seed} \sim 10^5$M$_\odot$ BHs are planted in $M_{\rm DM} \sim 10^9$M$_\odot$ DM halos. We use these simulations to investigate the coalescence of massive black holes ($M_{\rm BH} \gtrsim 10^6$ M$_\odot$) at $6 < z < 10$, and, in particular, to compute their GW and EM properties. We summarise below the main results found in this work, starting from the GW properties.

- **Merger rate:** We calculated the merger rates of MBHBs with different AGN feedback scenarios and numerical resolution: thermal (*AGN_fid* and *BHs_noFB* by V21, $m_{\rm DM} = 1.5 \times 10^6$ M$_\odot$) and kinetic (*AGNcone* and *AGNsphere* by B18, $m_{\rm DM} = 7.5 \times 10^6$ M$_\odot$) feedback. We found that the merger rate strongly depends on the numerical resolution adopted, ranging within 80 to 300 events per year in the V21 and B18, respectively at $z \sim 6$. Furthermore, the merger rates of MBHBs, at fixed resolution, depend on the feedback recipe implemented: the *AGN_fid* model predicts a merger rate that is a factor $\times$ 2 higher than *BHs_noFB* at $z \sim 6$ for chirp masses in the range $10^6 < \mathcal{M}_c < 10^7$ M$_\odot$;

analogously, the *AGNcone* model predicts a merger rate that is a factor $\times$ 3 higher than *AGNsphere* at $z \sim 6$ both for low ($\mathcal{M}_c < 10^6$ M$_\odot$) and high ($\mathcal{M}_c > 10^7$ M$_\odot$) chirp masses. Different feedback prescriptions and numerical resolutions also affect the epoch of the furthest GW signal detectable with LISA: in the V21 simulations, for $\mathcal{M}_c > 10^7 \mathrm{M}_\odot$, the furthest GW signal occurs at $z \sim 7.7 - 8.0$ while in the B18 at $z \sim 7.3 - 7.5$. We discussed in details all the physical and numerical explanations for these trends and we underlined the several motivations that make our predictions stringent upper limits to the actual merger rates that are expected to be observed. We find that considerable different merger rates result from the simulations in our suite. To get a more reliable constraint on this important issue, the shortage of currently adopted models should be addressed, as detailed at the end of this section.

- **Halo bias:** Our merger rate predictions are biased since they are based on zoom-in simulations targeting massive DM halos, namely overdense regions in the Universe ($> 3\sigma$). To quantify this bias, we adopted the semi-analytical model by Barausse (2012) and showed that a MBH model like ours (with heavy BH seeds and instantaneous mergers) overpredicts the actual merger rate by a factor of ~ 20 at comparable redshifts (z > 6).

- **Delays in MBHB mergers:** We corrected in post-processing the coalescing time of MBHB mergers including a time delay due to dynamical friction from the surrounding stars. We found that, if this delay is considered, 83 per cent of MBHBs will merge within the Hubble time, but only 21 per cent of them, will merge within 1 Gyr, namely the age of the Universe at $z > 6$.

- **Signal-to-noise ratio and angular resolution:** Taking into account the LISA frequency bands, we calculated the signal-to-noise ratio and the angular resolution of the GW events predicted by our fiducial run, *AGN_fid*. The fraction of LISA detectable events (LDEs), namely GW events with high signal-to-noise ratio (SNR>5), ranges between 66-69 per cent depending on the inclusion of time delays in post-processing. The largest SNR is reached in the case of low chirp masses ($< 10^6 \mathrm{M}_\odot$) which, although being characterized by a smaller characteristic strain, remain in the LISA band for a longer time, thus decreasing

the noise and increasing the SNR. These systems are however, characterized by very low angular resolutions (10 $\deg^2$).

- **Mass ratio of LDEs:** We computed the distribution of the mass ratio of the LDEs in the *AGN_fid* run and we found that the maximum number of mergers occurs for equi-massed binaries which are 'just-seeded' (i.e. with $M_{\rm BH} \sim 10^5 {\rm M}_\odot$). For a fixed total mass of a MBHB, the number of mergers increases with increasing mass ratio which can be attributed to hierarchical structure formation: several low-mass MBHs merge (and accrete) to form more massive MBHs. This remained true even when further time delays in merging are considered.

For what concerns the EM signals arising from LDEs, the main challenge remains the poor LISA sky localization that in the most optimistic case ($\mathcal{M}_c \sim 10^6$ M$_\odot$ at $z = 6$) is around 10 $\deg^2$. We further investigate the EM properties of LDEs to search for eventual, unique signatures from MBH coalescences to maximize the chances of their detections. We find the following results.

- **Intrinsic properties:** According to our simulations, LDEs are characterized by the following intrinsic properties: BH accretion rate $\dot{M} \sim 0.01$ M$_\odot$ yr^{-1}, star formation rate SFR$\sim 10-40$ M$_\odot$ yr^{-1}, metallicity $Z \sim 0.4-0.6\ Z_\odot$, dust mass $M_{\rm dust} \sim 10^5-10^6$ M$_\odot$, stellar mass $M_{\rm stellar} \sim 10^9 - 10^{10}$ M$_\odot$, and gas mass $M_{\rm gas} \sim 10^9 - 10^{10}$ M$_\odot$.

- **Observational properties:** Starting from the intrinsic propertied of LDEs, we compute their observational properties, searching for LDEs that are expected to be bright in one or more electromagnetic (EM) bands (e.g. rest-frame X-ray, UV, and FIR). We find that $\sim$20-30% of the LDEs are also detectable with EM telescopes.

- **Radiative transfer calculations:** We have post-processed the brightest LDEs with dust radiative transfer calculations to make accurate predictions about their spectral energy distributions (SEDs) and continuum maps in the JWST to ALMA wavelength range. By comparing the spectra arising from galaxies hosting the merging MBHs with those arising from AGN powered by single accreting BHs, we have found that it will be impossible to

identify an LDE from the continuum SEDs because of the absence of specific imprints from the merging MBHs.

- **H_α line profile:** We have computed the profile of the H_α line arising from LDEs, taking into account both the contribution from their star-forming regions and the accreting MBHs. We find that even in the extreme case of both MBHs accreting at super-Eddington rates the shape of the H_α line does not deviate significantly from the one arising from star formation only.

We conclude that the combined detection of GW and EM signals from $z \gtrsim 6$ MBHs is challenging (if not impossible) not only because of the poor sky-localization ($\sim$10 deg^2) provided by LISA, but also because of the following two reasons: (i) it is not possible to identify an LDE from the continuum SEDs because of the absence of specific imprints from the merging MBHs; (ii) the loudest GW emitters ($M_{\rm BH} \sim 10^{5-6}$ $\mathrm{M}_\odot$) are not massive enough to leave significant signatures (e.g. extended wings) in the emission lines arising from the broad line region.

The results presented in this work are affected by several caveat and limitations. We conclude by reporting the ones that we consider to be the most important, to indicate the direction to be taken to improve the main results of our research.

- **Spatial resolution:** the dynamical range required to study galaxy formation and BH co-evolution through numerical simulations is extremely large, ranging from hundreds of Mpc scales (to search for massive DM halos in N-body simulations) to sub-kpc scales (required to properly model gas accretion onto BHs and the subsequent feedback processes). This implies that the spatial resolution that is possible to achieve within a reasonable amount of computational time is typical limited to tens of pc scale[1], namely more than 7 orders of magnitude larger than the typical scales of interest for GW studies (see Table 7.1).

- **Temporal resolution:** a discussion similar to the spatial resolution can be done for what concerns the temporal resolution. Black hole properties in our simulations are evolved with time-steps of $\sim 0.01 - 1$ Myr, which are several orders of magnitude larger than the

[1]The largest spatial resolution achieved so far by zoom-in cosmological simulations is $\sim$15 pc of a z = 7 quasar (Lupi et al., 2019).

typical scales of interest for GW studies (see Table 7.1). The situation gets worse if we consider the time interval between two snapshots ($\sim$ tens Myr). This implies that we are not associating an LDE to the galaxy properties at the time of the coalescence (see Sec. 6.2).

- **Seeding prescription:** our simulations are based on a seeding prescription that mimicks the DCBH, given the mass of the seeds that we choose. However, the formation of a DCBH is governed by a complex network of physical processes (i.e. H_2 formation, metal enrichment, radiative transfer) that is impossible to take into account self-consistently in cosmological zoom-in hydrodynamical simulations. Our seeding prescription (namely a BH of mass $10^5 M_\odot$ in each $10^9 M_\odot$ DM halo) is thus certainly overestimating the number of MBHs in our simulations (see e.g. Vito et al., 2022) and consequently the expected number of merger events reported. **The seeding condition can be varied by (i) either changing the mass of the seed which is implanted in the halo or (ii) by changing the threshold mass of the halo, keeping the seed mass constant. In the case (i), an increase (decrease) in seed mass would result in higher (lower) chirp masses, thereby decreasing (increasing) the time spent in LISA band as mentioned in Chapter. 7, resulting in a lower (higher) SNR and poorer (better) angular resolution as compared to the seed mass used in our simulations. In the case (ii), an increase (decrease) in halo mass for MBH seed implantation would result in a lower (higher) abundance of MBHs thus decreasing (increasing) the number of mergers in our models.**

Part V

Supplementary material

GW detectables for different simulation runs

A

Here we show the comparison of different GW detectables for the simulation runs *AGNcone*, *AGNsphere* and *BHs_noFB* compared with *AGN_fid*. In all cases we report the results for a biased halo with no delays in post-processing.

Fig. A.1 shows the redshift distribution of SNR (upper panel) and angular resolution (lower panel) of the GW events for different chirp masses in our four different simulation suits. The overall trend in the SNR and resolution distribution is explained in Sec. 7.2. Since only in the B18 simulations the chirp mass PDF is populated for $\mathcal{M}_c < 10^6 \mathrm{M}_\odot$, this explains why for these simulations the SNR predicted reaches the highest value (SNR>160). Apart from this aspect (and the different number of events predicted, already discussed in Sec. 5.2), we do not find in the SNR predictions huge differences among different models. Consequently, the corresponding angular resolutions of event the loudest GW events remain quite poor ($\sim 10 deg^2$) for all models.

In Fig. A.2, we also show the fraction of mergers are distributed in the "mass ratio" and "total mass" plane, in the four simulation runs analysed in this work. The different coverage of the "mass ratio"-"total mass" plane simply reflects the different numbers of LDEs in the simulations runs: as shown in table 7.1 a higher number of LDEs occurs in the *AGNcone* run, which shows the most densely populated "mass ratio"-"total mass" plane, while the smaller number of LDEs is predicted in the *BHs_noFB* run.

As seen in Sec.7.3, highest fraction of LDEs occurs for equi-mass binaries, in the low mass range ($M_t \lesssim 3 \times 10^6 \mathrm{M}_\odot$), independent of the feedback implemented and the simulation resolution and it ranges between 20 per cent and 40 per cent of the total LDE population in each run.

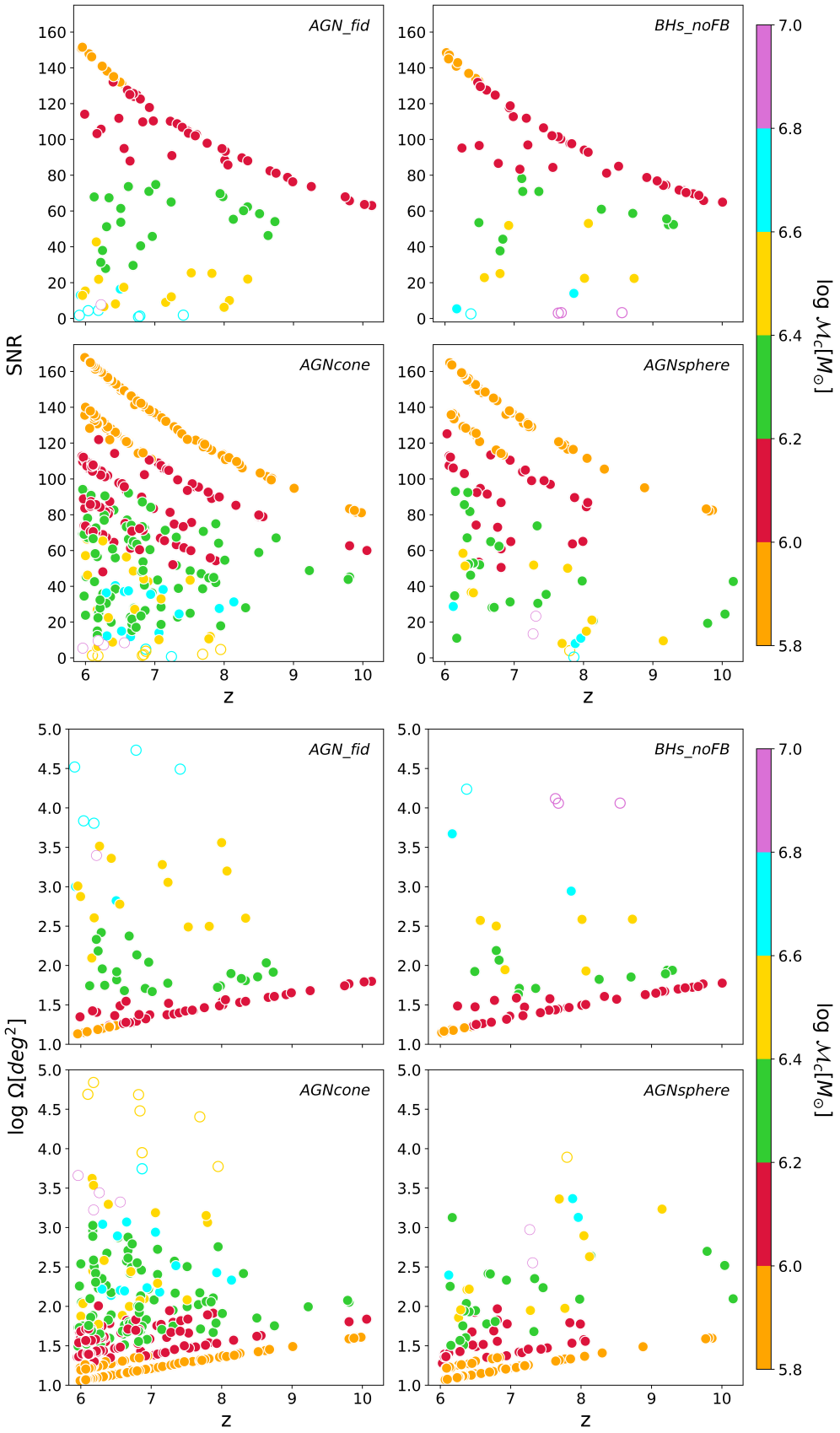

Figure A.1: Signal-to-noise ratio (upper panel) and angular resolution (lower panel) of MBHB mergers resulting from different runs of our simulations, color-coded according to their chirp mass. Filled and empty circles represents detectable and undetectable events, respectively. The detectability threshold has been set to $\mathrm{SNR}_{\mathrm{thres}} = 5$.

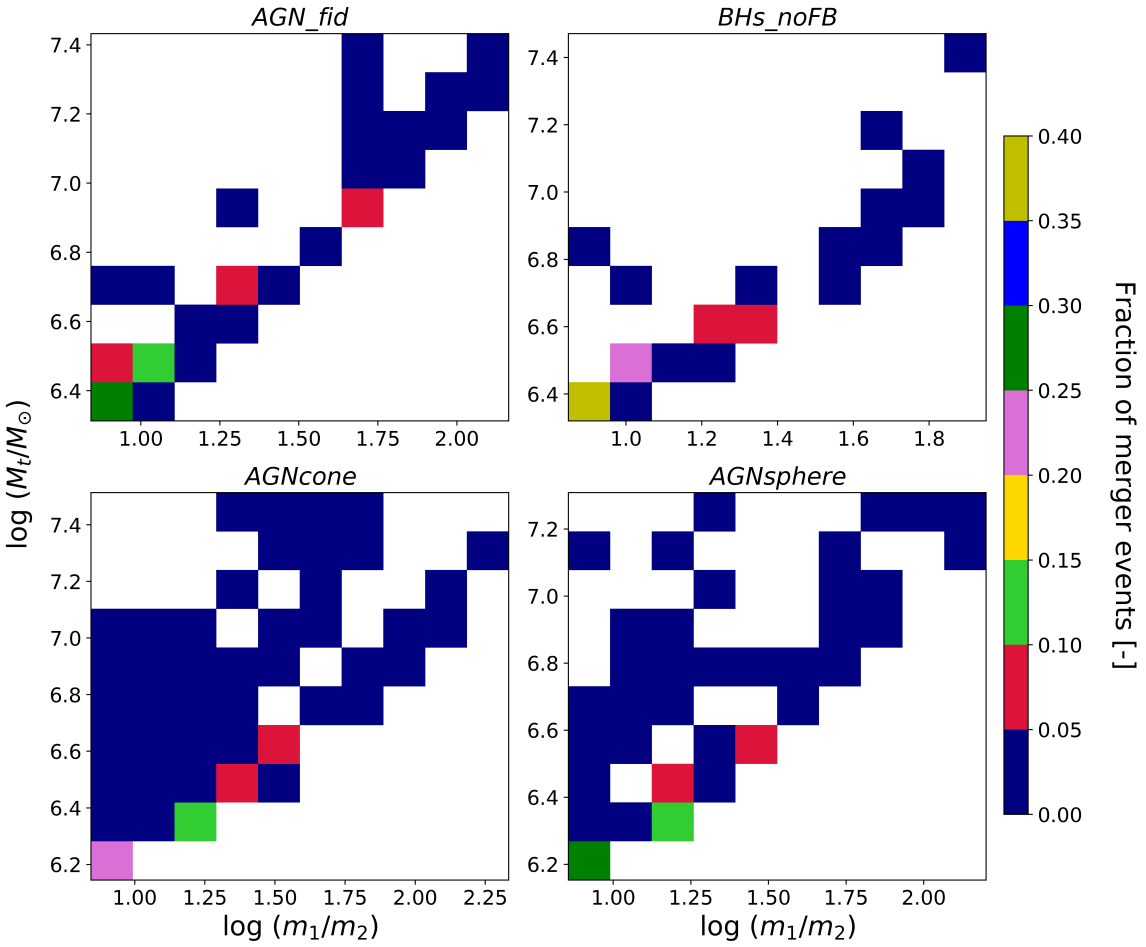

Figure A.2: Fraction of detectable merger events as a function of the total mass of the system $M_t = m_1 + m_2$ and the mass ratio m_1/m_2 of the binary.

Observable properties

B

B.0.1 UV and X-ray Luminosity

We compute the UV luminosity considering the contributions from both stars and accreting MBHs:

$$L_{\rm UV} = L_{\rm UV,*} + L_{\rm UV,AGN}. \tag{B.1}$$

For what concerns stars, we adopt the SFR-$L_{\rm UV,*}$ relation derived by Murphy et al. (2011):

$$\left(\frac{\rm SFR_{UV}}{M_\odot\ \rm yr^{-1}}\right) = 4.42 \times 10^{-44} \left(\frac{L_{\rm UV,*}}{\rm erg\ s^{-1}}\right). \tag{B.2}$$

The AGN UV luminosity is instead computed as follows:

$$L_{\rm UV,AGN} = f_{\rm UV} L_{\rm bol}, \tag{B.3}$$

where the bolometric luminosity $L_{\rm bol}$ is related to the accretion rate of the MBH, $L_{\rm bol} = \epsilon_r \dot{M} c^2$, ϵ_r is the radiative efficiency, and $f_{\rm UV}$ represents the UV bolometric correction parametrized as in Hopkins et al. (2007):

$$\frac{L_{\rm bol}}{L_{\rm band}} = c_1 \left(\frac{L_{\rm bol}}{10^{10} L_\odot}\right)^{k_1} + c_2 \left(\frac{L_{\rm bol}}{10^{10} L_\odot}\right)^{k_2}, \tag{B.4}$$

where, $c_1 = 1.862$, $k_1 = -0.361$, $c_2 = 4.870$, $k_2 = -0.0063$ (Shen et al., 2020).

Similarly, we compute the X-ray luminosity as $L_{\rm X} = f_{\rm X} L_{\rm bol}$, with the following parameters for the bolometric correction: $c_1 = 4.073$, $k_1 = -0.026$, $c_2 = 12.6$, $k_2 = 0.278$ (Hopkins et al.,

2007). These bolometric corrections well reproduce the X-ray SED template proposed by Shen et al. (2020).

B.0.2 Far-infrared luminosity

The far-infrared luminosity associated with dust emission in the optically-thin regime can be computed as follows (Carniani et al., 2019):

$$L_{\rm FIR} = 4\pi M_{\rm dust} \int k_\nu B_\nu(T_{\rm dust}) d\nu, \tag{B.5}$$

where $B_\nu(T_{\rm dust})$ is the Planck function associated to the dust component at temperature $T_{\rm dust}$:

$$B_\nu(T_{\rm dust}) = \frac{2h\nu^3}{c^2} \frac{1}{e^{\frac{h\nu}{k_B T_{\rm dust}}} - 1}, \tag{B.6}$$

and

$$k_\nu = k_0 \left(\frac{\nu}{\nu_0}\right)^\beta, \tag{B.7}$$

where we assume the dust emissivity index $\beta = 2.2$, and the mass absorption coefficient $k_0 = 34.7$ at a frequency ν_0 that corresponds to $\lambda = 100$ μm (Draine 2003a; Draine 2004). These parameters fit the dust emissivity in the far-infrared band k_ν of the Small Magenallic Cloud. The dust mass is given by $M_{\rm dust} = f_{\rm d} \times M_{\rm metals}$, with $f_{\rm d}$ = 0.1 and $M_{\rm metals} = Z \times M_{\rm gas}$.

B.0.3 [CII] Luminosity

To compute the [CII] luminosity $L_{\rm CII}$ we adopt the following fitting formula proposed by Yue et al. (2013) and based on the ISM sub-grid models by Vallini et al. (2013, 2015):

$$\begin{aligned} \log(L_{\rm CII}) = 7.0 + 1.2 \times \log({\rm SFR}) + 0.021 \times \log({\rm Z}) \\ + 0.012 \times \log({\rm SFR})\log({\rm Z}) - 0.74 \times \log^2({\rm Z}), \end{aligned} \tag{B.8}$$

where $L_{\rm CII}$, SFR, and Z are given in units of $\rm L_\odot$, $\rm M_\odot yr^{-1}$ and $Z_\odot$, respectively.

List of events bright in LISA and EM bands

C

In this appendix, we report the values of various intrinsic and observable properties of LDEs and their host galaxies. We present the events for which either the SNR or the brightness in various EM bands are significant.

Table C.1: Intrinsic properties of GW host galaxies. In this table, for each merging event (first column) associated with a host galaxy in the *AGN_fid* case, we report the redshift of the merger (second column), the distance between the primary BH and the associated galaxy (third column), the masses of the merging BHs (fourth and fifth column), the accretion rate (in $\mathrm{M_\odot yr^{-1}}$) of the merged MBH (sixth column), the star formation rate (in $\mathrm{M_\odot yr^{-1}}$, seventh column), the stellar mass (eighth column), the dust mass (ninth column) and the metallicity (tenth column) in solar units.

Event Number	***Redshift***	***Distance between galaxy and BH (physical kpc)***	M_1 ($\mathrm{M_\odot}$)	M_2 ($\mathrm{M_\odot}$)	$\dot{M}$ ($\mathrm{M_\odot yr^{-1}}$)	***SFR*** ($\mathrm{M_\odot yr^{-1}}$)	$M_{\rm stellar}$ ($\mathrm{M_\odot}$)	$M_{\rm dust}$ ($\mathrm{M_\odot}$)	$Metallicity$ ($Z_\odot$)
1	6	0.48	1.31×10^6	1.02×10^5	0.012	13.1	2.02×10^9	1.7×10^6	0.88
2	6	0.08	6.67×10^8	1×10^5	37	166	2.53×10^{10}	2.5×10^7	0.62
3	6.09	0.51	1.01×10^5	1×10^5	1.58×10^{-5}	0.03	1.06×10^7	9.43×10^3	0.13
4	6.12	0.59	3.71×10^8	1.03×10^5	11.3	142	2.41×10^{10}	2.1×10^7	0.61
5	6.13	3.57	3.82×10^5	1×10^5	2.9×10^{-2}	21.9	5.55×10^9	6.76×10^6	0.72
6	6.17	4.36	2.17×10^5	1.01×10^5	2.9	116	2.1×10^{10}	1.88×10^7	0.59
7	6.19	0.89	9.86×10^5	1×10^5	5.3×10^{-3}	11.3	2.02×10^9	2.16×10^6	0.57
8	6.22	1.55	7.58×10^5	1.04×10^5	1.37×10^{-3}	9.84	1.18×10^9	1.31×10^6	0.75
9	6.22	1.84	2.03×10^5	1.01×10^5	2.83×10^{-2}	21.2	5.33×10^9	6.65×10^6	0.73
10	6.29	0.82	8.07×10^5	1.01×10^5	5.18×10^{-3}	10.9	1.95×10^9	2.14×10^6	0.53
11	6.29	0.22	2.37×10^8	1.0×10^5	3.42	83.7	1.71×10^{10}	1.46×10^7	0.56
12	6.3	0.34	4.82×10^5	1.02×10^5	1.07×10^{-2}	8.19	1.15×10^9	1.34×10^6	0.61
13	6.31	1.08	1.01×10^5	1×10^5	1.95×10^{-5}	0.11	1.49×10^7	1.71×10^4	0.11
14	6.36	0.75	2.2×10^8	1.0×10^5	1.25	59.6	1.2×10^{10}	1.1×10^7	0.52
15	6.4	0.13	1.09×10^5	1.01×10^5	1.82×10^{-4}	1.12	1.71×10^8	2.06×10^5	0.29
16	6.41	1.16	1.47×10^8	1.01×10^5	0.78	27.1	9.96×10^9	6.46×10^6	0.61
17	6.42	2.23	1.03×10^5	1×10^5	2.27×10^{-3}	7.72	7.55×10^8	1.02×10^6	0.45
18	6.5	0.04	1.39×10^8	7.84×10^5	0.72	29.6	9.63×10^9	6.46×10^6	0.60
19*	6.5	0.17	1.25×10^6	2.01×10^5	9.84×10^{-3}	31.08	4.8×10^9	5.82×10^6	0.53
20	6.51	0.67	3.78×10^5	1.03×10^5	4.55×10^{-3}	6.96	1.27×10^9	1.26×10^6	0.63
21	6.51	0.79	4.33×10^5	1×10^5	5.89×10^{-3}	2.06	5.98×10^8	5.17×10^5	0.58
22	6.51	0.88	6.66×10^6	1.0×10^5	8.32×10^{-2}	8.5	1.11×10^9	7.49×10^5	0.72
23	6.55	1.23	1.65×10^8	1.01×10^5	0.77	50.46	1.06×10^{10}	9.29×10^6	0.52
24	6.6	0.31	1.04×10^5	1.01×10^5	9.49×10^{-4}	7.31	6.83×10^8	1.02×10^6	0.35
25	6.61	0.28	1.45×10^8	1.0×10^5	1.72	39.33	7.88×10^9	7.05×10^6	0.46
26	6.68	0.71	1.02×10^8	9.05×10^6	3.93	33.28	6.95×10^9	5.46×10^6	0.46
27	6.69	0.45	1.02×10^5	1.0×10^5	4.72×10^{-5}	1.14	1.83×10^8	2.65×10^5	0.51
28	6.7	0.07	1.05×10^5	1.01×10^5	3.02×10^{-5}	1.02	1.71×10^8	2.17×10^5	0.36
29	6.76	1.4	6.41×10^7	1.0×10^5	9.84×10^{-1}	33.21	6.38×10^9	4.99×10^6	0.47
30	6.79	0.40	1.02×10^5	1.0×10^5	2.9×10^{-6}	0.31	8.77×10^7	9.02×10^4	0.84
31*	6.8	0.27	5.24×10^5	1.01×10^5	1.9×10^{-2}	34.7	2.88×10^9	3.87×10^6	0.41
32*	6.91	0.68	2.4×10^5	2.1×10^5	0.0031	27.48	2.4×10^9	3.4×10^6	0.38
33	6.92	0.88	1×10^5	1×10^5	3×10^{-5}	1.86	2.4×10^8	3.2×10^5	0.41
34	6.96	2.71	4.5×10^5	1×10^5	0.0045	5.55	7.5×10^8	7.1×10^5	0.48
35	6.98	1.80	1.2×10^5	1×10^5	0.0005	2.98	4.2×10^8	4.7×10^5	0.38
36*	7.01	0.65	2.51×10^5	1.02×10^5	0.0026	6.77	8.4×10^8	1.2×10^6	0.44
37	7.04	2.49	9.9×10^7	1×10^5	0.38	21.97	7.9×10^9	5.2×10^6	0.65
38	7.2	0.15	8.67×10^7	1.0×10^5	0.89	26.35	6.6×10^9	4.9×10^6	0.59
39	7.24	1.32	2.8×10^5	1×10^5	0.021	5.68	5.8×10^8	6.7×10^5	0.38
40	7.24	2.19	1.2×10^6	1×10^5	0.013	16.13	1.5×10^9	1.4×10^6	0.46
41	7.32	1.33	1×10^5	1×10^5	1.9×10^{-6}	5.56	3.2×10^8	5.1×10^5	0.33
42	7.36	1.28	3.6×10^6	1×10^5	0.024	21.32	3.2×10^9	2.3×10^6	0.44
43	7.4	0.09	1.02×10^5	1.01×10^5	0.00019	5.17	3.5×10^8	5×10^5	0.25
44*	7.48	0.61	1.03×10^5	1.02×10^5	1.8×10^{-5}	6.76	5.3×10^8	8.2×10^5	0.28
45	7.48	0.72	1.01×10^5	1.01×10^5	1.2×10^{-5}	0.25	3.7×10^7	4.6×10^4	0.18
46	7.53	1.41	6.5×10^5	1×10^5	0.0079	12.99	1.1×10^9	1.2×10^6	0.39
47	7.58	0.52	1.04×10^5	1.01×10^5	1.3×10^{-4}	1.98	1.7×10^8	2.5×10^5	0.28
48	7.62	1.05	5.3×10^7	1×10^5	0.44	31.52	6.4×10^9	4.6×10^6	0.63
49	7.75	1.18	1×10^5	1×10^5	1.7×10^{-4}	4.46	3.3×10^8	5×10^5	0.28
50	7.9	0.19	2.87×10^7	9.57×10^5	1	31.32	4.7×10^9	4×10^6	0.6
51	7.98	0.79	2.06×10^5	1.0×10^5	4.6×10^{-4}	1.13	1.3×10^8	1.8×10^5	0.30
52*	8	0.01	1.49×10^6	1.02×10^5	0.13	34.7	2.1×10^9	2.3×10^6	0.36
53	8.01	0.39	1.22×10^5	1.01×10^5	7.4×10^{-5}	2.22	3.2×10^8	3.4×10^5	0.37
54	8.02	0.52	1.02×10^5	1.01×10^5	8.3×10^{-5}	3.13	2.6×10^8	3.5×10^5	0.25
55	8.51	0.29	2.18×10^5	1.01×10^5	8.60×10^{-4}	4.12	2.35×10^8	3.80×10^5	0.25
56	8.99	0.07	1.06×10^5	1.01×10^5	2.02×10^{-4}	5.43	2.8×10^8	3.6×10^5	0.25

Table C.2: Observable properties of GW host galaxies. In this table, for each GW event (first column) associated with a host galaxy in the *AGN_fid* case, we report the redshift of the merger (second column), the distance between the primary BH and the associated galaxy (third column), the chirp mass (fourth column), the X-ray (fifth column), [CII] (sixth column) and FIR (seventh column) luminosities in solar units, the apparent and absolute UV magnitudes (eighth and ninth column), the SNR (tenth column) and the angular resolution (eleventh column). We show the cases with either significant SNR or significant brightness in different EM bands.

Event Number	***Redshift***	***Distance between galaxy and BH (physical kpc)***	$\mathcal{M}_c$ ***(M/$M_\odot$)***	L_x ***(ergs/s)***	$L_{\rm CII}$ ***(L/$L_\odot$)***	$L_{\rm FIR}$ ***(L/$L_\odot$)***	***Apparent Magnitude***	$M_{\rm ab}$	***SNR***	***Angular Resolution*** Ω (Deg^2)
1	6	0.48	1.9×10^6	1.4×10^{42}	2.1×10^8	3×10^{12}	28.01	-20.85	24.12	859.33
2	6	0.08	2.4×10^7	6.2×10^{44}	3.9×10^9	4.4×10^{13}	23.26	-25.60	Not Detectable	Not Applicable
3	6.09	0.51	6.2×10^5	4.1×10^{39}	3.5×10^4	1.7×10^{10}	34.46	-14.44	164.27	18.53
4	6.12	0.59	1.9×10^7	2.6×10^{44}	3.2×10^9	3.8×10^{13}	24.34	-24.57	Not Detectable	Not Applicable
5	6.13	3.57	1.2×10^6	2.8×10^{42}	3.7×10^8	1.2×10^{13}	27.48	-21.42	89.62	62.25
6	6.17	4.36	9.1×10^5	9.5×10^{43}	2.5×10^9	3.3×10^{13}	25.25	-23.69	129.01	30.04
7	6.19	0.89	1.8×10^6	7.1×10^{41}	1.5×10^8	3.8×10^{12}	28.27	-20.68	32.90	461.85
8	6.22	1.55	1.6×10^6	1.5×10^{42}	1.4×10^8	2.3×10^{12}	28.4	-20.55	45.29	243.81
9	6.22	1.84	8.9×10^5	2.8×10^{42}	3.6×10^8	1.2×10^{13}	27.56	-21.38	131.39	28.96
10	6.29	0.82	1.7×10^6	7×10^{41}	1.4×10^8	3.8×10^{12}	28.35	-20.64	40.86	299.42
11	6.29	0.22	1.6×10^7	1.1×10^{44}	1.6×10^9	2.6×10^{13}	25.42	-23.56	Not Detectable	Not Applicable
12	6.3	0.34	1.3×10^6	1.3×10^{42}	1×10^8	2.4×10^{12}	28.64	-20.35	69.82	102.57
13	6.31	1.08	6.4×10^5	5×10^{39}	1.2×10^5	3×10^{10}	33.31	-15.67	156.91	20.31
14	6.36	0.75	1.6×10^7	5×10^{43}	1×10^9	1.9×10^{13}	26.13	-22.89	Not Detectable	Not Applicable
15	6.4	0.13	6.8×10^5	3.9×10^{40}	5.7×10^6	3.6×10^{11}	30.86	-18.16	152.63	21.46
16	6.41	1.16	1.4×10^7	3.6×10^{43}	4.4×10^8	1.1×10^{13}	26.87	-22.15	Not Detectable	Not Applicable
17	6.42	2.23	6.6×10^5	3.5×10^{41}	8.2×10^7	1.8×10^{12}	28.76	-20.26	153.28	21.28
18	6.5	0.04	4.7×10^7	3.3×10^{43}	4.8×10^8	1.1×10^{13}	26.88	-22.18	Not Detectable	Not Applicable
19*	6.5	0.17	3×10^6	1.2×10^{42}	4.8×10^8	1×10^{13}	27.29	-21.78	26.34	720.46
20	6.51	0.67	1.2×10^6	6.3×10^{41}	8.8×10^7	2.2×10^{12}	28.91	-20.16	81.70	74.91
21	6.51	0.79	1.3×10^6	7.8×10^{41}	2×10^7	9.1×10^{11}	30.2	-18.87	72.44	95.28
22	6.51	0.88	4×10^6	6.4×10^{42}	1.2×10^8	1.3×10^{12}	28.51	-20.55	Not Detectable	Not Applicable
23	6.55	1.23	1.5×10^7	3.5×10^{43}	8.5×10^8	1.6×10^{13}	26.45	-22.61	Not Detectable	Not Applicable
24	6.6	0.31	6.8×10^5	1.7×10^{41}	6.3×10^7	1.8×10^{12}	28.9	-20.20	147.28	23.05
25	6.61	0.28	1.4×10^7	6.4×10^{43}	5.8×10^8	1.2×10^{13}	26.33	-22.77	Not Detectable	Not Applicable
26	6.68	0.71	1.8×10^8	1.2×10^{44}	4.8×10^8	9.7×10^{12}	25.87	-23.27	Not Detectable	Not Applicable
27	6.69	0.45	6.8×10^5	1.1×10^{40}	9×10^6	4.7×10^{11}	30.96	-18.18	145.09	23.75
28	6.7	0.07	6.9×10^5	7.5×10^{39}	6.1×10^6	3.9×10^{11}	31.08	-18.06	144.11	24.08
29	6.76	1.4	1×10^7	4.2×10^{43}	4.8×10^8	8.8×10^{12}	26.79	-22.39	Not Detectable	Not Applicable
30	6.79	0.40	6.9×10^5	8×10^{38}	2.3×10^6	1.6×10^{11}	32.42	-16.76	142.15	24.74
31*	6.8	0.27	1.5×10^6	2×10^{42}	4.6×10^8	6.8×10^{12}	27.28	-21.90	56.30	157.75
32*	6.91	0.68	1.5×10^6	4.5×10^{41}	3.3×10^8	6.1×10^{12}	27.57	-21.64	94.08	56.49
33	6.92	0.88	7.1×10^5	7.3×10^{39}	1.4×10^7	5.7×10^{11}	30.5	-18.72	137.90	26.29
34	6.96	2.71	1.4×10^6	6.3×10^{41}	5.7×10^7	1.3×10^{12}	29.34	-19.91	62.59	127.61
35	6.98	1.80	7.8×10^5	9.6×10^{40}	2.3×10^7	8.4×10^{11}	30.02	-19.23	132.05	28.67
36*	7.01	0.65	1.1×10^6	4×10^{41}	6.9×10^7	2.1×10^{12}	29.13	-20.12	96.34	53.87
37	7.04	2.49	1.3×10^7	2×10^{43}	3.5×10^8	9.1×10^{12}	27.52	-21.73	Not Detectable	Not Applicable
38	7.2	0.15	1.2×10^7	3.9×10^{43}	4.2×10^8	8.7×10^{12}	27.13	-22.19	Not Detectable	Not Applicable
39	7.24	1.32	1.2×10^6	2.2×10^{42}	5×10^7	1.2×10^{12}	29.33	-19.99	84.97	69.25
40	7.24	2.19	2.2×10^6	1.5×10^{42}	2×10^8	2.5×10^{12}	28.25	-21.07	19.22	1352.89
41	7.32	1.33	7.3×10^5	5.4×10^{38}	4.4×10^7	9×10^{11}	29.45	-19.90	128.22	30.41
42	7.36	1.28	3.5×10^6	2.4×10^{42}	2.7×10^8	4.1×10^{12}	28.01	-21.38	Not Detectable	Not Applicable
43	7.4	0.09	7.4×10^5	4×10^{40}	3×10^7	8.8×10^{11}	29.57	-19.82	126.26	31.36
44*	7.48	0.61	7.5×10^5	4.6×10^{39}	4.7×10^7	1.4×10^{12}	29.31	-20.12	123.98	32.53
45	7.48	0.72	7.5×10^5	3×10^{39}	5.7×10^5	8.1×10^{10}	32.88	-16.54	124.48	32.27
46	7.53	1.41	1.8×10^6	9.8×10^{41}	1.4×10^8	2.1×10^{12}	28.59	-20.83	37.11	363.07
47	7.58	0.52	7.6×10^5	2.9×10^{40}	1.1×10^7	4.4×10^{11}	30.68	-18.78	121.53	33.86
48	7.62	1.05	1.1×10^7	2.3×10^{43}	5.3×10^8	8.2×10^{12}	27.39	-22.07	Not Detectable	Not Applicable
49	7.75	1.18	7.9×10^5	3.7×10^{40}	2.9×10^7	8.8×10^{11}	29.86	-19.66	117.33	36.32
50	7.9	0.19	3.3×10^7	4.3×10^{43}	5.2×10^8	7.2×10^{12}	27.2	-22.36	Not Detectable	Not Applicable
51	7.98	0.79	1.1×10^6	8.9×10^{40}	6×10^6	3.2×10^{11}	31.41	-18.18	87.25	65.69
52*	8	0.01	2.7×10^6	8.8×10^{42}	4.1×10^8	4.1×10^{12}	27.62	-21.96	10.65	4408.89
53	8.01	0.39	8.7×10^5	1.7×10^{40}	1.6×10^7	6.1×10^{11}	30.68	-18.90	108.16	42.74
54	8.02	0.52	8×10^5	1.9×10^{40}	1.6×10^7	6.1×10^{11}	30.3	-19.28	112.29	39.66
55	8.51	0.29	1.2×10^6	1.5×10^{41}	2.3×10^7	7.1×10^{11}	30.16	-19.58	75.95	86.69
56	8.99	0.07	9×10^5	4.3×10^{40}	3.2×10^7	6.3×10^{11}	30.0	-19.88	93.90	56.71

3D representation of intrinsic properties for the other events

D

In Fig. 8.5 we showed the intrinsic properties (gas density, SFR, gas metallicity and gas velocity) relative to E31. In this Section, we show the same properties for events E19, E36, E52.

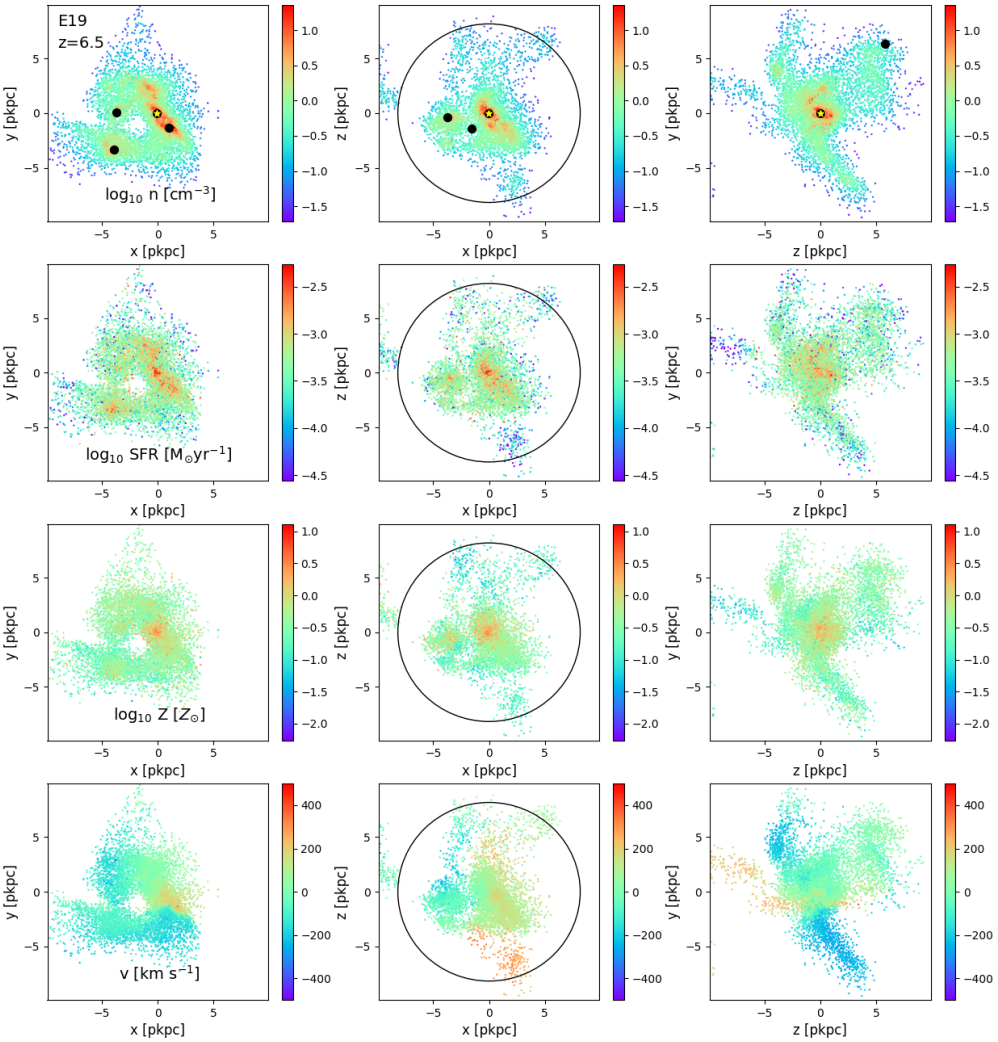

Figure D.1: Same as in Fig. 8.5, but for E19.

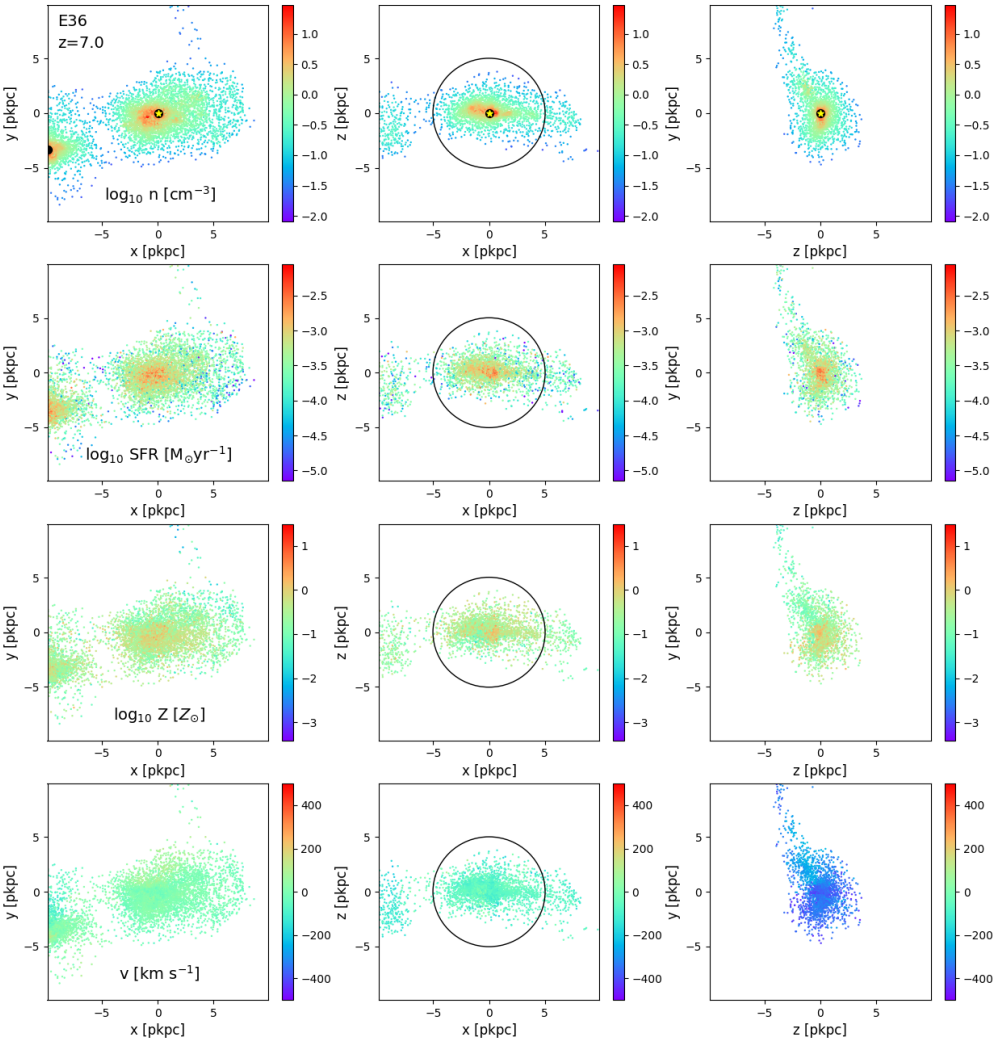

Figure D.2: Same as in Fig. 8.5, but for E36.

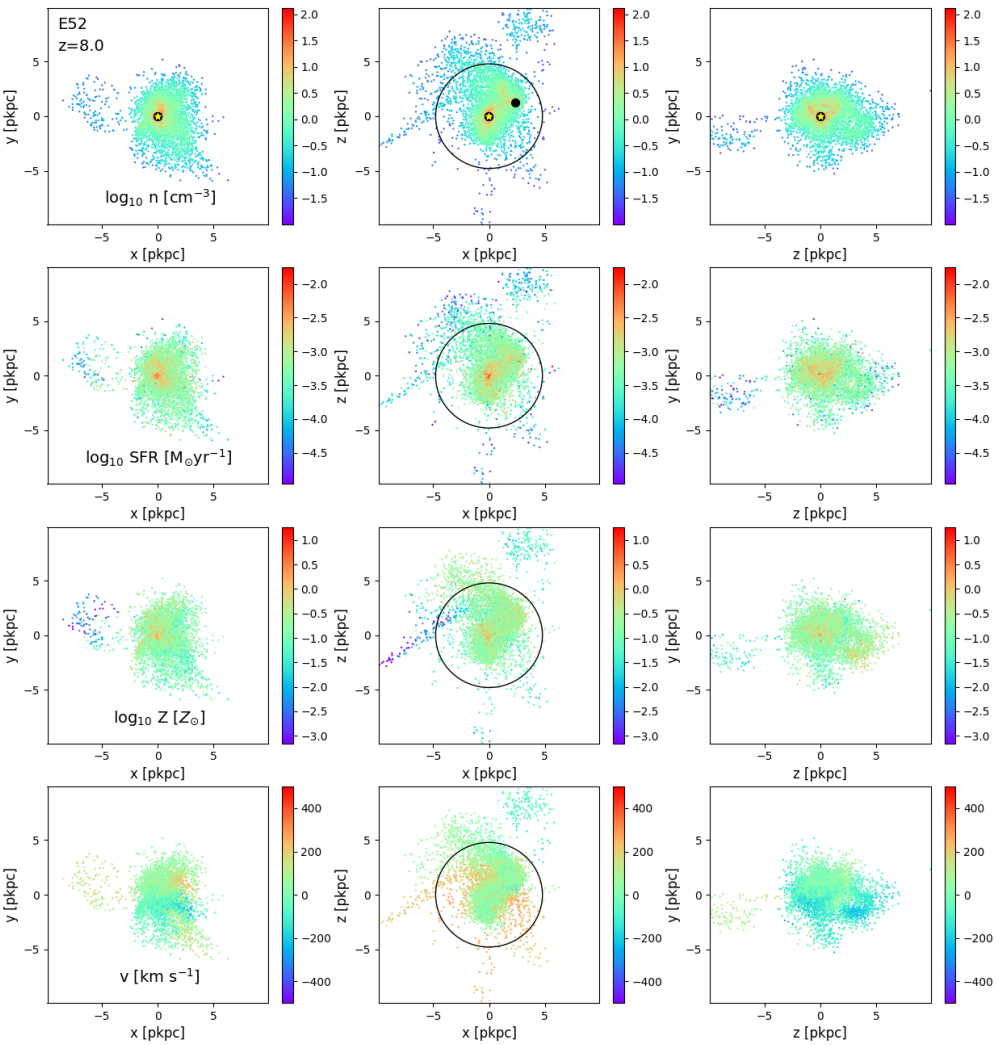

Figure D.3: Same as in Fig. 8.5, but for E52.

Bibliography

Abbott B., et al., 2016a, Physical Review Letters, 116

Abbott B., et al., 2016c, Physical Review Letters, 116

Abbott B., et al., 2016b, Physical Review Letters, 116

Abbott B., et al., 2017a, Physical Review Letters, 118

Abbott B. P., et al., 2017b, The Astrophysical Journal, 848, L12

Abbott R., et al., 2020, Physical Review Letters, 125

Abel T., Wandelt B. D., 2002, Monthly Notices of RAS, 330, L53

Abramowicz M. A., Fragile P. C., 2013, Living Reviews in Relativity, 16

Agarwal B., Smith B., Glover S., Natarajan P., Khochfar S., 2016, Monthly Notices of the Royal Astronomical Society, 459, 4209–4217

Agarwal B., Cullen F., Khochfar S., Ceverino D., Klessen R. S., 2019, Monthly Notices of the Royal Astronomical Society, 488, 3268–3273

Agertz O., Kravtsov A. V., Leitner S. N., Gnedin N. Y., 2013, The Astrophysical Journal, 770, 25

Aird J., et al., 2013, arXiv e-prints, p. arXiv:1306.2325

Alimi J.-M., et al., 2012, DEUS Full Observable LambdaCDM Universe Simulation: the numerical challenge (arXiv:1206.2838)

Alpher R. A., Bethe H., Gamow G., 1948, Physical Review, 73, 803

Amaro-Seoane P., et al., 2023, Living Reviews in Relativity, 26

Anderson M., Lehner L., Megevand M., Neilsen D., 2010, Physical Review D, 81

Anglès-Alcàzar D., Faucher-Giguère C.-A., Keres D., Hopkins P. F., Quataert E., Murray N., 2017, MNRAS, 470, 4698

Angulo R. E., Springel V., White S. D. M., Jenkins A., Baugh C. M., Frenk C. S., 2012, Monthly Notices of the Royal Astronomical Society, 426, 2046

Antonucci R., 1993, ARA&A, 31, 473

Aoyama S., Hou K.-C., Shimizu I., Hirashita H., Todoroki K., Choi J.-H., Nagamine K., 2017, Monthly Notices of RAS, 466, 105

Armitage P. J., Natarajan P., 2002, The Astrophysical Journal, 567, L9

Armitage P. J., Natarajan P., 2005, The Astrophysical Journal, 634, 921–927

Armstrong J. W., 2006, Living Reviews in Relativity, 9, 1

Arzoumanian Z., et al., 2018, The Astrophysical Journal, 859, 47

Asano R. S., Takeuchi T. T., Hirashita H., Inoue A. K., 2013a, Earth, Planets and Space, 65, 213

Asano R. S., Takeuchi T. T., Hirashita H., Nozawa T., 2013b, Monthly Notices of RAS, 432, 637

Asano R. S., Takeuchi T. T., Hirashita H., Nozawa T., 2014, Monthly Notices of RAS, 440, 134

Bañados E., et al., 2018, Nature, 553, 473

Baes M., Camps P., 2015, Astronomy and Computing, 12, 33

Baes M., Dejonghe H., 2001, Monthly notices of RAS, 326, 733

Baes M., Dejonghe H., 2002, Monthly Notices of RAS, 335, 441

Baes M., et al., 2003, MNRAS, 343, 1081

Baes M., et al., 2010, Astronomy and Astrophysics, 518, L39

Baes M., Verstappen J., De Looze I., Fritz J., Saftly W., Vidal Pérez E., Stalevski M., Valcke S., 2011, Astrophysical Journal, Supplement, 196, 22

Bahr-Kalus B., Parkinson D., Mueller E.-M., 2023, Monthly Notices of the Royal Astronomical Society, 524, 2463–2476

Barai P., Gallerani S., Pallottini A., Ferrara A., Marconi A., Cicone C., Maiolino R., Carniani S., 2017, Monthly Notices of the Royal Astronomical Society, 473, 4003–4020

Barausse E., 2012, Monthly Notices of the Royal Astronomical Society, 423, 2533

Barkana R., Loeb A., 2001, Physics Reports, 349, 125–238

Barnes D. J., Kay S. T., Henson M. A., McCarthy I. G., Schaye J., Jenkins A., 2016, Monthly Notices of the Royal Astronomical Society, 465, 213

Barnes D. J., et al., 2017, Monthly Notices of the Royal Astronomical Society, 471, 1088

Barnes D. J., Kannan R., Vogelsberger M., Marinacci F., 2018, Radiative AGN feedback on a moving mesh: the impact of the galactic disc and dust physics on outflow properties (arXiv:1812.01611)

Barrows R. S., Mezcua M., Comerford J. M., 2019, The Astrophysical Journal, 882, 181

Bartelmann M., 2010, Reviews of Modern Physics, 82, 331–382

Baumgarte T., Shapiro S., 2011, Physics Today, 64, 32

Begelman M. C., Volonteri M., Rees M. J., 2006, Monthly Notices of the Royal Astronomical Society, 370, 289–298

Behrens C., Pallottini A., Ferrara A., Gallerani S., Vallini L., 2018, Monthly Notices of RAS, 477, 552

Belczynski K., Buonanno A., Cantiello M., Fryer C. L., Holz D. E., Mandel I., Miller M. C., Walczak M., 2014, The Astrophysical Journal, 789, 120

Belczynski K., Repetto S., Holz D. E., O'Shaughnessy R., Bulik T., Berti E., Fryer C., Dominik M., 2016, The Astrophysical Journal, 819, 108

Bennett C. L., et al., 2003, ApJS, 148, 1

Berczik P., Merritt D., Spurzem R., Bischof H.-P., 2006, The Astrophysical Journal, 642, L21–L24

Berger M. J., Oliger J., 1984, Journal of Computational Physics, 53, 484

Bersanetti D., Patricelli B., Piccinni O. J., Piergiovanni F., Salemi F., Sequino V., 2021, Universe, 7, 322

Béthermin M., et al., 2020, A&A, 643, A2

Binney J., Tremaine S., 2008, Galactic Dynamics: Second Edition. Princeton University Press

Blanchet L., Damour T., Iyer B. R., Will C. M., Wiseman A. G., 1995, Physical Review Letters, 74, 3515

Blecha L., et al., 2015, Monthly Notices of the Royal Astronomical Society, 456, 961

Blumenthal G. R., Faber S., Primack J. R., Rees M. J., 1984, Nature, 311, 517

Bocquet S., Saro A., Dolag K., Mohr J. J., 2015, Monthly Notices of the Royal Astronomical Society, 456, 2361

Bode P., Ostriker J. P., 2003, The Astrophysical Journal Supplement Series, 145, 1

Bogdanović T., 2014, Supermassive Black Hole Binaries: The Search Continues. Springer International Publishing, p. 103–119, doi:10.1007/978-3-319-10488-1_9, http://dx.doi.org/10.1007/978-3-319-10488-1_9

Bogdanović T., Miller M. C., Blecha L., 2022, Living Reviews in Relativity, 25

Bohren C. F., Huffman D. R., Kam Z., 1983, Nature, 306, 625

Bondi H., 1952, MNRAS, 112, 195

Bondi H., Hoyle F., 1944, MNRAS, 104, 273

Bonetti M., Haardt F., Sesana A., Barausse E., 2016, Monthly Notices of the Royal Astronomical Society, 461, 4419–4434

Booth C. M., Schaye J., 2009, Monthly Notices of the Royal Astronomical Society, 398, 53–74

Bowen D. B., Campanelli M., Krolik J. H., Mewes V., Noble S. C., 2017, The Astrophysical Journal, 838, 42

Boylan-Kolchin M., Springel V., White S. D. M., Jenkins A., Lemson G., 2009, Monthly Notices of the Royal Astronomical Society, 398, 1150

Bruzual G., Charlot S., 2003, MNRAS, 344, 1000

Bruzual A. G., Magris G., Calvet N., 1988, Astrophysical Journal, 333, 673

Bryan G. L., Norman M. L., 1995, in American Astronomical Society Meeting Abstracts. p. 95.04

Burgh E. B., McCandliss S. R., Feldman P. D., 2002, Astrophysical Journal, 575, 240

Calzetti D., Kinney A. L., Storchi-Bergmann T., 1994, ApJ, 429, 582

Calzetti D., Bohlin R. C., Gordon K. D., Witt A. N., Bianchi L., 1995, Astrophysical Journal, Letters, 446, L97

Camps P., Baes M., 2015, Astronomy and Computing, 9, 20

Camps P., et al., 2018, Astrophysical Journal, Supplement, 234, 20

Carniani S., et al., 2019, Monthly Notices of the Royal Astronomical Society

Carniani S., et al., 2023, arXiv e-prints, p. arXiv:2306.11801

Carroll S. M., 2004, Spacetime and Geometry. Addison-Wesley

Ceverino D., Klypin A., Klimek E. S., Trujillo-Gomez S., Churchill C. W., Primack J., Dekel A., 2014, Monthly Notices of the Royal Astronomical Society, 442, 1545

Chabrier G., 2003, Publications of the Astronomical Society of the Pacific, 115, 763–795

Chandrasekhar S., 1943, ApJ, 97, 255

Chandrasekhar S., 1960, Radiative transfer. Dover publication

Chon S., Omukai K., 2020, Monthly Notices of the Royal Astronomical Society, 494, 2851–2860

Ciardi B., Loeb A., 2000, The Astrophysical Journal, 540, 687–696

Clavijo-Bohórquez W. E., de Gouveia Dal Pino E. M., Melioli C., 2023, AGN and Star Formation feedback in the evolution of galaxy outflows (arXiv:2306.11494)

Coc A., Vangioni E., 2017, International Journal of Modern Physics E, 26, 1741002

Code A. D., Whitney B. A., 1995, Astrophysical Journal, 441, 400

Colella P., Woodward P. R., 1984, Journal of Computational Physics, 54, 174

Colless M., et al., 2001, Monthly Notices of the Royal Astronomical Society, 328, 1039–1063

Combi L., Armengol F. G. L., Campanelli M., Noble S. C., Avara M., Krolik J. H., Bowen D., 2022, The Astrophysical Journal, 928, 187

Conti L., Auriga Collaboration 2004, Nuclear Instruments and Methods in Physics Research A, 518, 236

Cooray A., et al., 2019, Cosmic Dawn and Reionization: Astrophysics in the Final Frontier (arXiv:1903.03629)

Correa C. A., Wyithe J. S. B., Schaye J., Duffy A. R., 2015a, Monthly Notices of the Royal Astronomical Society, 450, 1514

Correa C. A., Wyithe J. S. B., Schaye J., Duffy A. R., 2015b, Monthly Notices of the Royal Astronomical Society, 450, 1521

Cuadra J., Armitage P. J., Alexander R. D., Begelman M. C., 2009, Monthly Notices of the Royal Astronomical Society, 393, 1423–1432

Cui W., et al., 2018, Monthly Notices of the Royal Astronomical Society, 480, 2898

Cutler C., Flanagan É . E., 1994, Physical Review D, 49, 2658

Czerny B., Hryniewicz K., 2010, Astronomy & Astrophysics, 525, L8

Dasyra K. M., Ho L. C., Netzer H., Combes F., Trakhtenbrot B., Sturm E., Armus L., Elbaz D., 2011, The Astrophysical Journal, 740, 94

Davé R., Thompson R., Hopkins P. F., 2016, Monthly Notices of the Royal Astronomical Society, 462, 3265

Davé R., Anglés-Alcázar D., Narayanan D., Li Q., Rafieferantsoa M. H., Appleby S., 2019, MNRAS, 486, 2827

Davies M. B., Miller M. C., Bellovary J. M., 2011, ApJL, 740, L42

Dayal P., Rossi E. M., Shiralilou B., Piana O., Choudhury T. R., Volonteri M., 2019, Monthly Notices of the Royal Astronomical Society, 486, 2336–2350

De Geyter G., Baes M., Camps P., Fritz J., De Looze I., Hughes T. M., Viaene S., Gentile G., 2014, Monthly Notices of RAS, 441, 869

De Looze I., Baes M., Fritz J., Verstappen J., 2012, Monthly Notices of RAS, 419, 895

DeGraf C., Sijacki D., Di Matteo T., Holley-Bockelmann K., Snyder G., Springel V., 2021, MNRAS, 503, 3629

Deschamps R., Braun K., Jorissen A., Siess L., Baes M., Camps P., 2015, Astronomy and Astrophysics, 577, A55

Devecchi B., Volonteri M., 2009, The Astrophysical Journal, 694, 302–313

Devecchi B., Volonteri M., Rossi E. M., Colpi M., Portegies Zwart S., 2012, MNRAS, 421, 1465

Dhurandhar S. V., Tinto M., 1988, MNRAS, 234, 663

Di Mascia F., et al., 2021, MNRAS

Dominik M., et al., 2015, The Astrophysical Journal, 806, 263

Doppler C., 1846, Beitrage zur fixsternenkunde.. Prag, Druck von G. Haase sohne

Doroshkevich A., Tucker D. L., Allam S., Way M. J., 2004, Astronomy & Astrophysics, 418, 7–23

Dotti M., Colpi M., Haardt F., 2006, Monthly Notices of the Royal Astronomical Society, 367, 103

Dotti M., Merloni A., Montuori C., 2015, Monthly Notices of the Royal Astronomical Society, 448, 3603

Draine B., 2003a, Annual Review of Astronomy and Astrophysics, 41, 241

Draine B. T., 2003b, Astrophysical Journal, 598, 1017

Draine B. T., 2004, in , Vol. 32, The Cold Universe. Springer Berlin Heidelberg, p. 213, doi:10.1007/3-540-31636-1_3

Draine B. T., Salpeter E. E., 1979, ApJ, 231, 77

Draine B. T., et al., 2007, Astrophysical Journal, 663, 866

Dubois Y., et al., 2014, Monthly Notices of the Royal Astronomical Society, 444, 1453

Dwek E., 1998, Astrophysical Journal, 501, 643

D'Orazio D. J., Haiman Z., Duffell P., MacFadyen A., Farris B., 2016, Monthly Notices of the Royal Astronomical Society, 459, 2379–2393

Ebisuzaki T., et al., 2001, The Astrophysical Journal, 562, L19

Edgar R., 2004, New Astronomy Reviews, 48, 843–859

Edmunds M. G., 2001, Monthly Notices of RAS, 328, 223

Einstein A., 1916, Annalen der Physik, 354, 769

Eisenstein D. J., Loeb A., 1995, The Astrophysical Journal, 443, 11

Elitzur M., Asensio Ramos A., Ceccarelli C., 2012, MNRAS, 422, 1394

Escala A., Larson R. B., Coppi P. S., Mardones D., 2004, The Astrophysical Journal, 607, 765–777

Escala A., Larson R. B., Coppi P. S., Mardones D., 2005, The Astrophysical Journal, 630, 152–166

Faisst A. L., et al., 2020, ApJS, 247, 61

Fan X., et al., 2006, The Astronomical Journal, 132, 117–136

Farmer A. J., Phinney E. S., 2003, Monthly Notices of the Royal Astronomical Society, 346, 1197–1214

Feng Y., Di-Matteo T., Croft R. A., Bird S., Battaglia N., Wilkins S., 2015, Monthly Notices of the Royal Astronomical Society, 455, 2778

Fernandez R., Bryan G. L., Haiman Z., Li M., 2014, Monthly Notices of the Royal Astronomical Society, 439, 3798–3807

Ferrara A., Salvadori S., Yue B., Schleicher D., 2014, Monthly Notices of the Royal Astronomical Society, 443, 2410–2425

Ferrarese L., Merritt D., 2000, The Astrophysical Journal, 539, L9–L12

Ferriè re K. M., 2001, Reviews of Modern Physics, 73, 1031

Ferrière K., 2005, in Chyzy K. T., Otmianowska-Mazur K., Soida M., Dettmar R.-J., eds, The Magnetized Plasma in Galaxy Evolution. pp 147–155

Field G. B., Goldsmith D. W., Habing H. J., 1969, ApJL, 155, L149

Fiore F., Elvis M., McDowell J. C., Siemiginowska A., Wilkes B. J., 1994, Astrophysical Journal, 431, 515

Fixsen D. J., 2009, The Astrophysical Journal, 707, 916–920

Flanagan É. É., Hughes S. A., 1998, Phys. Rev. D, 57, 4535

Flanagan É. É., Hughes S. A., 2005, New Journal of Physics, 7, 204

Franchini A., Bonetti M., Lupi A., Sesana A., 2024, Emission signatures from sub-pc Post-Newtonian binaries embedded in circumbinary discs (arXiv:2401.10331)

Freise A., Strain K., 2010, Living Reviews in Relativity, 13

Friedmann A., 1922, Zeitschrift fur Physik, 10, 377

Galeev A. A., Rosner R., Vaiana G. S., 1979, ApJ, 229, 318

Gallerani S., Pallottini A., Feruglio C., Ferrara A., Maiolino R., Vallini L., Riechers D. A., Pavesi R., 2018, MNRAS, 473, 1909

Gao L., Navarro J. F., Frenk C. S., Jenkins A., Springel V., White S. D. M., 2012, Monthly Notices of the Royal Astronomical Society, 425, 2169

Garrison-Kimmel S., Boylan-Kolchin M., Bullock J. S., Lee K., 2014, Monthly Notices of the Royal Astronomical Society, 438, 2578

Gebhardt K., et al., 2000, The Astrophysical Journal, 539, L13–L16

Gnedin N. Y., Kaurov A. A., 2014, The Astrophysical Journal, 793, 30

Godunov S. K., Bohachevsky I., 1959, Matematiceskij sbornik, 47(89), 271

Gold R., 2019, Galaxies, 7

Goldhaber G., Cline D. B., 2009, in AIP Conference Proceedings. AIP, doi:10.1063/1.3232196, http://dx.doi.org/10.1063/1.3232196

Gonçalves J., Galli D., Walmsley M., 2004, Astronomy and Astrophysics, 415, 617

González M., Audit E., Huynh P., 2007, Astronomy and Astrophysics, 464, 429

Gordon K. D., 2004, in Witt A. N., Clayton G. C., Draine B. T., eds, Astronomical Society of the Pacific Conference Series Vol. 309, Astrophysics of Dust. p. 77 (arXiv:astro-ph/0309709), doi:10.48550/arXiv.astro-ph/0309709

Grand R. J. J., et al., 2017, MNRAS, 467, 179

Greene J. E., et al., 2010, The Astrophysical Journal, 721, 26–45

Guedes J., Callegari S., Madau P., Mayer L., 2011, The Astrophysical Journal, 742, 76

Guth A. H., 2007, Journal of Physics A: Mathematical and Theoretical, 40, 6811–6826

Gutié rrez E. M., Combi L., Noble S. C., Campanelli M., Krolik J. H., Armengol F. L., García F., 2022, The Astrophysical Journal, 928, 137

Habib S., et al., 2016, New Astronomy, 42, 49

Habouzit M., Volonteri M., Latif M., Dubois Y., Peirani S., 2016, Monthly Notices of the Royal Astronomical Society, 463, 529–540

Haehnelt M. G., 1994, Monthly Notices of the Royal Astronomical Society, 269, 199–208

Hahn O., Abel T., 2011, Monthly Notices of the Royal Astronomical Society, 415, 2101–2121

Harms J., Slagmolen B. J. J., Adhikari R. X., Miller M. C., Evans M., Chen Y., Müller H., Ando M., 2013, Physical Review D, 88

Harrison C. M., Costa T., Tadhunter C. N., Flütsch A., Kakkad D., Perna M., Vietri G., 2018, Nature Astronomy, 2, 198–205

Hartwig T., Agarwal B., Regan J. A., 2018, Monthly Notices of the Royal Astronomical Society: Letters, 479, L23–L27

Hawking S. W., Israel W., 1989, Three Hundred Years of Gravitation. Cambridge University Press

Hayasaki K., Mineshige S., Sudou H., 2007, Publications of the Astronomical Society of Japan, 59, 427–441

Heckman T. M., Best P. N., 2014, Annual Review of Astronomy and Astrophysics, 52, 589–660

Heger A., Fryer C. L., Woosley S. E., Langer N., Hartmann D. H., 2003, The Astrophysical Journal, 591, 288–300

Heggie D. C., 2005, The Classical Gravitational N-Body Problem (arXiv:astro-ph/0503600)

Heitmann K., et al., 2015, The Astrophysical Journal Supplement Series, 219, 34

Hellwing W. A., Frenk C. S., Cautun M., Bose S., Helly J., Jenkins A., Sawala T., Cytowski M., 2016, Monthly Notices of the Royal Astronomical Society, 457, 3492

Henden N. A., Puchwein E., Shen S., Sijacki D., 2018, Monthly Notices of the Royal Astronomical Society, 479, 5385

Henyey L. G., Greenstein J. L., 1941, Astrophysical Journal, 93, 70

Hirashita H., 1999, Astronomy and Astrophysics, 344, L87

Hirashita H., 2015, Monthly Notices of RAS, 447, 2937

Ho L. C., 2008, Annual Review of Astronomy and Astrophysics, 46, 475–539

Hoffman Y., Ribak E., 1991, ApJL, 380, L5

Hogg D. W., Eisenstein D. J., Blanton M. R., Bahcall N. A., Brinkmann J., Gunn J. E., Schneider D. P., 2005, ApJ, 624, 54

Hong S. S., 1985, Astronomy and Astrophysics, 146, 67

Hopkins P. F., Richards G. T., Hernquist L., 2007, The Astrophysical Journal, 654, 731

Hopkins P. F., Keres D., Oñorbe J., Faucher-Giguère C.-A., Quataert E., Murray N., Bullock J. S., 2014, Monthly Notices of the Royal Astronomical Society, 445, 581

Hopkins P. F., et al., 2018, Monthly Notices of the Royal Astronomical Society, 480, 800

Hosokawa T., Omukai K., Yorke H. W., 2012, The Astrophysical Journal, 756, 93

Hoyle F., Lyttleton R. A., 1939, Proceedings of the Cambridge Philosophical Society, 35, 405

Hubble E., Humason M. L., 1931, ApJ, 74, 43

Hughes S. A., 2009, Annual Review of Astronomy and Astrophysics, 47, 107–157

Inayoshi K., Omukai K., 2012, MNRAS, 422, 2539

Inoue A. K., 2003, Publications of the ASJ, 55, 901

Ishiyama T., Enoki M., Kobayashi M. A. R., Makiya R., Nagashima M., Oogi T., 2015, Publications of the Astronomical Society of Japan, 67, 61

Issa M. R., MacLaren I., Wolfendale A. W., 1990, Astronomy and Astrophysics, 236, 237

Izquierdo-Villalba D., Sesana A., Bonoli S., Colpi M., 2021, Monthly Notices of the Royal Astronomical Society, 509, 3488

Jaffe A. H., Backer D. C., 2003, The Astrophysical Journal, 583, 616–631

Jiang C. Y., Jing Y. P., Lin W. P., 2010, Astronomy and Astrophysics, 510, A60

Johnson J. L., Whalen D. J., Fryer C. L., Li H., 2012, The Astrophysical Journal, 750, 66

Jones A. P., Nuth J. A., 2011, Astronomy and Astrophysics, 530, A44

Jones A. P., Tielens A. G. G. M., Hollenbach D. J., McKee C. F., 1994, Astrophysical Journal, 433, 797

Jones A. P., Tielens A. G. G. M., Hollenbach D. J., 1996, Astrophysical Journal, 469, 740

Juvela M., Padoan P., 2003, Astronomy and Astrophysics, 397, 201

Kannan R., Springel V., Pakmor R., Marinacci F., Vogelsberger M., 2016, Monthly Notices of the Royal Astronomical Society, 458, 410

Kattawar G. W., 1975, Journal of Quantitiative Spectroscopy and Radiative Transfer, 15, 839

Katz M. L., Kelley L. Z., Dosopoulou F., Berry S., Blecha L., Larson S. L., 2019, Monthly Notices of the Royal Astronomical Society

Kelley L. Z., Blecha L., Hernquist L., 2016, Monthly Notices of the Royal Astronomical Society, 464, 3131

Kelly B. J., Baker J. G., Etienne Z. B., Giacomazzo B., Schnittman J., 2017, Physical Review D, 96

Kennicutt R. C., 1998, Annual Review of Astronomy and Astrophysics, 36, 189–231

Kennicutt R. C., Evans N. J., 2012, ARA&A, 50, 531

Khandai N., Matteo T. D., Croft R., Wilkins S., Feng Y., Tucker E., DeGraf C., Liu M.-S., 2015, Monthly Notices of the Royal Astronomical Society, 450, 1349

Klein A., et al., 2016, Physical Review D, 93, 024003

Klypin A. A., Trujillo-Gomez S., Primack J., 2011, The Astrophysical Journal, 740, 102

Knobel C., 2013, An Introduction into the Theory of Cosmological Structure Formation (arXiv:1208.5931)

Knollmann S. R., Knebe A., 2009, The Astrophysical Journal Supplement Series, 182, 608–624

Kohandel M., Pallottini A., Ferrara A., Carniani S., Gallerani S., Vallini L., Zanella A., Behrens C., 2020, MNRAS, 499, 1250

Kolmogorov A., 1933, Inst. Ital. Attuari, Giorn., 4, 83

Komatsu E., et al., 2009, The Astrophysical Journal Supplement Series, 180, 330

Kormendy J., 2001, AIP Conference Proceedings

Koushiappas S. M., Bullock J. S., Dekel A., 2004, Monthly Notices of the Royal Astronomical Society, 354, 292–304

Krawczyk C. M., Richards G. T., Mehta S. S., Vogeley M. S., Gallagher S. C., Leighly K. M., Ross N. P., Schneider D. P., 2013, Astrophysical Journal, Supplement, 206, 4

Krolik J. H., 1999, Active galactic nuclei : from the central black hole to the galactic environment. Princeton University Press

Krolik J. H., 2010, The Astrophysical Journal, 709, 774

Krolik J. H., Volonteri M., Dubois Y., Devriendt J., 2019, The Astrophysical Journal, 879, 110

Kroupa P., 2001, Monthly Notices of the Royal Astronomical Society, 322, 231

Kuhlen M., Diemand J., Madau P., Zemp M., 2008, Journal of Physics: Conference Series, 125, 012008

Kurosawa R., Hillier D. J., 2001, Astronomy and Astrophysics, 379, 336

Kurosawa R., Harries T. J., Bate M. R., Symington N. H., 2004, Monthly Notices of RAS, 351, 1134

Lahav O., Liddle A. R., 2019, The Cosmological Parameters (2019) (arXiv:1912.03687)

Laporte N., et al., 2017, Astrophysical Journal Letters, 837, L21

Larson S. L., Hiscock W. A., Hellings R. W., 2000, Physical Review D, 62

Latif M. A., Volonteri M., Wise J. H., 2018, Monthly Notices of the Royal Astronomical Society, 476, 5016–5025

Le Fèvre O., et al., 2020, A&A, 643, A1

Lentati L., et al., 2015, Monthly Notices of the Royal Astronomical Society, 453, 2577

Levermore C. D., 1984, Journal of Quantitiative Spectroscopy and Radiative Transfer, 31, 149

Liang S. L., Li A., 2009, Astrophysical Journal Letters, 690, L56

Libeskind N. I., Yepes G., Knebe A., Gottlöber S., Hoffman Y., Knollmann S. R., 2010, Monthly Notices of the Royal Astronomical Society, 401, 1889

Liffman K., Clayton D. D., 1989, Astrophysical Journal, 340, 853

Linde A., 2007, Inflationary Cosmology. Springer Berlin Heidelberg, p. 1–54, doi:10.1007/978-3-540-74353-8_1, http://dx.doi.org/10.1007/978-3-540-74353-8_1

Lippai Z., Frei Z., Haiman Z., 2008, The Astrophysical Journal, 676, L5

Lodato G., Natarajan P., 2006, Monthly Notices of the Royal Astronomical Society, 371, 1813–1823

Loeb A., 2016, The Astrophysical Journal, 819, L21

Loeb A., Rasio F. A., 1994, The Astrophysical Journal, 432, 52

Lops G., Izquierdo-Villalba D., Colpi M., Bonoli S., Sesana A., Mangiagli A., 2023, MNRAS, 519, 5962

Ludwig R. R., Greene J. E., Barth A. J., Ho L. C., 2012, The Astrophysical Journal, 756, 51

Lunttila T., Juvela M., 2012, Astronomy and Astrophysics, 544, A52

Lupi A., Colpi M., Devecchi B., Galanti G., Volonteri M., 2014, Monthly Notices of the Royal Astronomical Society, 442, 3616–3626

Lupi A., Volonteri M., Decarli R., Bovino S., Silk J., Bergeron J., 2019, MNRAS, 488, 4004

Lusso E., et al., 2012, MNRAS, 425, 623

Lusso E., Worseck G., Hennawi J. F., Prochaska J. X., Vignali C., Stern J., O'Meara J. M., 2015, Monthly Notices of RAS, 449, 4204

Lynden-Bell D., 1969, Nature, 223, 690

M. P. Hobson G. P. Efstathiou A. N. L., 2006, General relativity: An Introduction for Physicists. Cambridge University press

Maartens R., 2011, Philosophical Transactions of the Royal Society of London Series A, 369, 5115

Mackay D. J. C., 2003, Information Theory, Inference and Learning Algorithms. Cambridge University press

Madau P., Haardt F., Dotti M., 2014a, The Astrophysical Journal, 784, L38

Madau P., Haardt F., Dotti M., 2014b, ApJL, 784, L38

Maggiore M., 2007, Gravitational Waves. Oxford university press

Magorrian J., et al., 1998, The Astronomical Journal, 115, 2285–2305

Maiolino R., et al., 2023, arXiv e-prints, p. arXiv:2308.01230

Mandal A. K., Rakshit S., Stalin C. S., Petrov R. G., Mathew B., Sagar R., 2021, Monthly Notices of the Royal Astronomical Society, 502, 2140–2157

Mangiagli A., Caprini C., Volonteri M., Marsat S., Vergani S., Tamanini N., Inchauspé H., 2022, Massive black hole binaries in LISA: multimessenger prospects and electromagnetic counterparts, doi:10.48550/ARXIV.2207.10678, https://arxiv.org/abs/2207.10678

Manti S., Gallerani S., Ferrara A., Feruglio C., Graziani L., Bernardi G., 2016, Monthly Notices of RAS, 456, 98

Mapelli M., 2016, MNRAS, 459, 3432

Mathis J. S., Rumpl W., Nordsieck K. H., 1977, Astrophysical Journal, 217, 425

Matteo T. D., Springel V., Hernquist L., 2005, Nature, 433, 604

Mattila K., 1970, Astronomy and Astrophysics, 9, 53

Mauceli E., Geng Z. K., Hamilton W. O., Johnson W. W., Merkowitz S., Morse A., Price B., Solomonson N., 1996, Physical Review D, 54, 1264–1275

Mayer L., Fiacconi D., Bonoli S., Quinn T., Roskar R., Shen S., Wadsley J., 2015, ApJ, 810, 51

McCarthy I. G., Schaye J., Bird S., Brun A. M. C. L., 2016, Monthly Notices of the Royal Astronomical Society, 465, 2936

McGee S., Sesana A., Vecchio A., 2020, Linking gravitational waves and X-ray phenomena with joint LISA and Athena observations (arXiv:1811.00050)

McWilliams S. T., Lang R. N., Baker J. G., Thorpe J. I., 2011, Physical Review D, 84

Meliani Z., Mizuno Y., Olivares H., Porth O., Rezzolla L., Younsi Z., 2017, Astronomy & Astrophysics, 598, A38

Metropolis N., Ulam S., 1949, Journal of the American Statistical Association, 44, 335

Mezcua M., Civano F., Marchesi S., Suh H., Fabbiano G., Volonteri M., 2018, Monthly Notices of the Royal Astronomical Society, 478, 2576–2591

Mihalas D., Mihalas B. W., 1984, Foundations of radiation hydrodynamics. Oxford University Press

Mikkola S., Valtonen M. J., 1992, Monthly Notices of the Royal Astronomical Society, 259, 115

Milosavljević M., Phinney E. S., 2005, The Astrophysical Journal, 622, L93

Miralda-Escudé J., 2003, Science, 300, 1904

Moore C. J., Cole R. H., Berry C. P. L., 2014, Classical and Quantum Gravity, 32, 015014

Mortlock D. J., et al., 2011, Nature, 474, 616

Murante G., Monaco P., Giovalli M., Borgani S., Diaferio A., 2010, MNRAS, 405, 1491

Murante G., Monaco P., Borgani S., Tornatore L., Dolag K., Goz D., 2015, MNRAS, 447, 178

Murphy E. J., et al., 2011, The Astrophysical Journal, 737, 67

Natarajan A., Yoshida N., 2014, Progress of Theoretical and Experimental Physics, 2014, 6B112

Natta A., Panagia N., 1984, Astrophysical Journal, 287, 228

Navarro J. F., Frenk C. S., White S. D. M., 1996, The Astrophysical Journal, 462, 563

Nelemans G., Yungelson L. R., Portegies Zwart S. F., 2001, A&A, 375, 890

Nenkova M., Sirocky M. M., Ivezic Z., Elitzur M., 2008, Astrophysical Journal, 685, 147

Netzer H., 2013, The Physics and Evolution of Active Galactic Nuclei. Cambridge University Press

Netzer H., 2015, Annual Review of Astronomy and Astrophysics, 53, 365

Niccolini G., Alcolea J., 2006, Astronomy and Astrophysics, 456, 1

Niccolini G., Woitke P., Lopez B., 2003, Astronomy and Astrophysics, 399, 703

Noble S. C., Mundim B. C., Nakano H., Krolik J. H., Campanelli M., Zlochower Y., Yunes N., 2012, The Astrophysical Journal, 755, 51

Nozawa T., Fukugita M., 2013, Astrophysical Journal, 770, 27

Nozawa T., Asano R. S., Hirashita H., Takeuchi T. T., 2015, Monthly Notices of RAS, 447, L16

Ocvirk P., et al., 2020, Monthly Notices of the Royal Astronomical Society, 496, 4087

Oesch P. A., et al., 2016, The Astrophysical Journal, 819, 129

Omukai K., Palla F., 2003, The Astrophysical Journal, 589, 677

Orofino M. C., Ferrara A., Gallerani S., 2018, Monthly Notices of the Royal Astronomical Society, 480, 681–691

Osterbrock D. E., Ferland G. J., 2006, Astrophysics of gaseous nebulae and active galactic nuclei. University Science Books

Ostriker E. C., 1999, The Astrophysical Journal, 513, 252

PRODI G. A., et al., 2000, International Journal of Modern Physics D, 09, 237–245

Pacucci F., Ferrara A., 2015, Monthly Notices of the Royal Astronomical Society, 448, 104–118

Pacucci F., Ferrara A., Volonteri M., Dubus G., 2015, Monthly Notices of the Royal Astronomical Society, 454, 3771–3777

Padmanabhan H., Loeb A., 2022, Monthly Notices of the Royal Astronomical Society, 513, 976

Page L., et al., 2003, The Astrophysical Journal Supplement Series, 148, 233

Pallottini A., et al., 2022, MNRAS, 513, 5621

Parrish I. J., McCourt M., Quataert E., Sharma P., 2012, Monthly Notices of the Royal Astronomical Society, 422, 704

Pascucci I., Wolf S., Steinacker J., Dullemond C. P., Henning T., Niccolini G., Woitke P., Lopez B., 2004, Astronomy and Astrophysics, 417, 793

Peebles P. J. E., 1980, The large-scale structure of the universe. Princeton University Press

Peebles P. J. E., 1982, ApJL, 263, L1

Peebles P. J. E., Ratra B., 2003, Reviews of Modern Physics, 75, 559–606

Perlmutter S., et al., 1999, The Astrophysical Journal, 517, 565–586

Peters P. C., Mathews J., 1963, Phys. Rev., 131, 435

Peterson B. M., 1997, An Introduction to Active Galactic Nuclei. Cambridge, New York Cambridge University Press

Peterson B. M., et al., 2004, The Astrophysical Journal, 613, 682–699

Pezzulli E., Valiante R., Schneider R., 2016, Monthly Notices of the Royal Astronomical Society, 458, 3047–3059

Pezzulli E., Volonteri M., Schneider R., Valiante R., 2017, Monthly Notices of the Royal Astronomical Society, 471, 589

Pfister H., Lupi A., Capelo P. R., Volonteri M., Bellovary J. M., Dotti M., 2017, Monthly Notices of the Royal Astronomical Society, 471, 3646–3656

Piconcelli E., Jimenez-Bailón E., Guainazzi M., Schartel N., Rodríguez-Pascual P. M., Santos-Lleó M., 2005, Astronomy and Astrophysics, 432, 15

Pillepich A., et al., 2018, MNRAS, 473, 4077

Pitkin M., Reid S., Rowan S., Hough J., 2011, Living Reviews in Relativity, 14

Planck Collaboration Ade P. A. R., et al., 2016, Astronomy & Astrophysics, 594, A13

Ponce M., Faber J. A., Lombardi J. C., 2011, The Astrophysical Journal, 745, 71

Potter D., Stadel J., Teyssier R., 2016, PKDGRAV3: Beyond Trillion Particle Cosmological Simulations for the Next Era of Galaxy Surveys (arXiv:1609.08621)

Prada F., Klypin A. A., Cuesta A. J., Betancort-Rijo J. E., Primack J., 2012, Monthly Notices of the Royal Astronomical Society, 423, 3018

Press W. H., Schechter P., 1974, ApJ, 187, 425

Preto M., Berentzen I., Berczik P., Spurzem R., 2011, The Astrophysical Journal, 732, L26

Quinlan G. D., 1996, New Astronomy, 1, 35

Regan J. A., Wise J. H., Woods T. E., Downes T. P., O'Shea B. W., Norman M. L., 2020, The Formation of Very Massive Stars in Early Galaxies and Implications for Intermediate Mass Black Holes (arXiv:2008.08090)

Reines A. E., Volonteri M., 2015, The Astrophysical Journal, 813, 82

Reines A. E., Greene J. E., Geha M., 2013, The Astrophysical Journal, 775, 116

Reinoso B., Schleicher D. R. G., Fellhauer M., Klessen R. S., Boekholt T. C. N., 2018, A&A, 614, A14

Richards G. T., et al., 2003, Astronomical Journal, 126, 1131

Richards G. T., et al., 2006, Astrophysical Journal, Supplement, 166, 470

Richstone D., et al., 1998, Supermassive Black Holes and the Evolution of Galaxies (arXiv:astro-ph/9810378)

Riess A. G., et al., 1998, The Astronomical Journal, 116, 1009

Roark T., Roark B., Collins G. W. I., 1974, Astrophysical Journal, 190, 67

Robertson H. P., 1935, ApJ, 82, 284

Robson T., Cornish N. J., Liu C., 2019, Classical and Quantum Gravity, 36, 105011

Roedig C., Sesana A., Dotti M., Cuadra J., Amaro-Seoane P., Haardt F., 2012, Astronomy & Astrophysics, 545, A127

Roedig C., Krolik J. H., Miller M. C., 2014, The Astrophysical Journal, 785, 115

Rosdahl J., Teyssier R., 2015, Monthly Notices of RAS, 449, 4380

Rosdahl J., Blaizot J., Aubert D., Stranex T., Teyssier R., 2013, Monthly Notices of RAS, 436, 2188

Rosdahl J., et al., 2018, Monthly Notices of the Royal Astronomical Society

Rossi E. M., Lodato G., Armitage P. J., Pringle J. E., King A. R., 2010, Monthly Notices of the Royal Astronomical Society, 401, 2021

Rowland L. E., et al., 2024, MNRAS,

Rybicki G. B., Lightman A. P., 1979, Radiative processes in astrophysics. Wiley-VCH

Saadeh D., Feeney S. M., Pontzen A., Peiris H. V., McEwen J. D., 2016, Physical Review Letters, 117

Saftly W., Baes M., De Geyter G., Camps P., Renaud F., Guedes J., De Looze I., 2015, Astronomy and Astrophysics, 576, A31

Salpeter E. E., 1955, ApJ, 121, 161

Sanders D. B., Phinney E. S., Neugebauer G., Soifer B. T., Matthews K., 1989, ApJ, 347, 29

Sassano F., Schneider R., Valiante R., Inayoshi K., Chon S., Omukai K., Mayer L., Capelo P. R., 2021, Monthly Notices of the Royal Astronomical Society, 506, 613–632

Sathyaprakash B. S., Schutz B. F., 2009, Living Reviews in Relativity, 12

Sawala T., et al., 2016, Monthly Notices of the Royal Astronomical Society, 457, 1931

Sazonov S. Y., Ostriker J. P., Sunyaev R. A., 2004, Monthyl Notices of RAS, 347, 144

Schaerer D., 2002, A&A, 382, 28

Schartmann M., Meisenheimer K., Camenzind M., Wolf S., Henning T., 2005, Astrophysics and Astronomy, 437, 861

Schaye J., et al., 2015a, MNRAS, 446, 521

Schaye J., et al., 2015b, MNRAS, 446, 521

Schmidt M., 1959, ApJ, 129, 243

Schneider R., 2006, New Astronomy Reviews, 50, 64

Schneider R., Bianchi S., Valiante R., Risaliti G., Salvadori S., 2015, Astronomy and Astrophysics, 579, A60

Schnittman J. D., Krolik J. H., 2008, The Astrophysical Journal, 684, 835

Sesana A., Khan F. M., 2015, Monthly Notices of the Royal Astronomical Society: Letters, 454, L66

Sesana A., Haardt F., Madau P., Volonteri M., 2004, The Astrophysical Journal, 611, 623–632

Sesana A., Volonteri M., Haardt F., 2007, Monthly Notices of the Royal Astronomical Society, 377, 1711–1716

Sesana A., Vecchio A., Colacino C. N., 2008, Monthly Notices of the Royal Astronomical Society, 390, 192

Sesana A., Shankar F., Bernardi M., Sheth R. K., 2016, Monthly Notices of the Royal Astronomical Society: Letters, 463, L6

Shakura N. I., Sunyaev R. A., 1973, Astronomy and Astrophysics, 24, 337

Shang C., Bryan G. L., Haiman Z., 2010, MNRAS, 402, 1249

Shannon R. M., et al., 2015, Science, 349, 1522

Shen X., Hopkins P. F., Faucher-Giguère C.-A., Alexander D. M., Richards G. T., Ross N. P., Hickox R. C., 2020, Monthly Notices of the Royal Astronomical Society, 495, 3252

Sheth R. K., Mo H. J., Tormen G., 2001, Monthly Notices of the Royal Astronomical Society, 323, 1

Sijacki D., Springel V., Di Matteo T., Hernquist L., 2007, Monthly Notices of the Royal Astronomical Society, 380, 877–900

Sijacki D., Springel V., Haehnelt M. G., 2009, MNRAS, 400, 100

Silk J., Rees M. J., 1998, Astron. Astrophys., 331, L1

Sądowski A., Gaspari M., 2017, MNRAS, 468, 1398

Skibba R. A., Sheth R. K., 2009, Monthly Notices of the Royal Astronomical Society, 392, 1080–1091

Skillman S. W., Warren M. S., Turk M. J., Wechsler R. H., Holz D. E., Sutter P. M., 2014, Dark Sky Simulations: Early Data Release (arXiv:1407.2600)

Smirnov N., 1948, The annals of mathematical statistics, 19, 279

Smith T. L., Caldwell R. R., 2019, Physical Review D, 100

Smoot G. F., et al., 1992, ApJL, 396, L1

Sommovigo L., et al., 2022, MNRAS, 517, 5930

Spinoso D., Bonoli S., Valiante R., Schneider R., Izquierdo-Villalba D., 2022, Monthly Notices of the Royal Astronomical Society, 518, 4672–4692

Spitzer L., 1978, Physical processes in the interstellar medium. Wiley-Interscience Publication, doi:10.1002/9783527617722

Springel V., 2005, MNRAS, 364, 1105

Springel V., Hernquist L., 2003, Monthly Notices of the Royal Astronomical Society, 339, 289–311

Springel V., Di Matteo T., Hernquist L., 2005a, MNRAS, 361, 776

Springel V., et al., 2005b, Nature, 435, 629–636

Springel V., et al., 2008, Monthly Notices of the Royal Astronomical Society, 391, 1685

Springel V., et al., 2017, Monthly Notices of the Royal Astronomical Society, 475, 676

Stadel J., Potter D., Moore B., Diemand J., Madau P., Zemp M., Kuhlen M., Quilis V., 2009, Monthly Notices of the Royal Astronomical Society: Letters, 398, L21

Stalevski M., Fritz J., Baes M., Nakos T., Popovic L., 2012, Monthly Notices of RAS, 420, 2756

Stalevski M., Ricci C., Ueda Y., Lira P., Fritz J., Baes M., 2016, Monthly Notices of RAS, 458, 2288

Stamatellos D., Whitworth A. P., 2003, Astronomy and Astrophysics, 407, 941

Steinacker J., Bacmann A., Henning T., 2002, Journal of Quantitiative Spectroscopy and Radiative Transfer, 75, 765

Steinacker J., Baes M., Gordon K. D., 2013, Annual Review of Astron and Astrophysics, 51, 63

Steinborn L. K., Dolag K., Hirschmann M., Prieto M. A., Remus R.-S., 2015, MNRAS, 448, 1504

Stenholm L. G., Stoerzer H., Wehrse R., 1991, Journal of Quantitiative Spectroscopy and Radiative Transfer, 45, 47

Stinson G., Seth A., Katz N., Wadsley J., Governato F., Quinn T., 2006, MNRAS, 373, 1074

Stone N., Loeb A., 2011, Monthly Notices of the Royal Astronomical Society, 412, 75

Sugimura K., Omukai K., Inoue A. K., 2014, Monthly Notices of the Royal Astronomical Society, 445, 544–553

Sunyaev R. A., Chluba J., 2009, Astronomische Nachrichten, 330, 657–674

Taffoni G., Mayer L., Colpi M., Governato F., 2003, Monthly Notices of the Royal Astronomical Society, 341, 434–448

Tanaka T. L., Li M., 2014, Monthly Notices of the Royal Astronomical Society, 439, 1092–1100

Tanaka T., Menou K., 2010, The Astrophysical Journal, 714, 404

Tang Y., MacFadyen A., Haiman Z., 2017, Monthly Notices of the Royal Astronomical Society, 469, 4258–4267

Teyssier R., et al., 2009, A&A, 497, 335

Tiede C., D'Orazio D. J., 2023, Eccentric Binaries in Retrograde Disks (arXiv:2307.03775)

Tielens A. G. G. M., McKee C. F., Seab C. G., Hollenbach D. J., 1994, Astrophysical Journal, 431, 321

Tornatore L., Borgani S., Dolag K., Matteucci F., 2007, Monthly Notices of the Royal Astronomical Society, 382, 1050–1072

Tremmel M., Karcher M., Governato F., Volonteri M., Quinn T. R., Pontzen A., Anderson L., Bellovary J., 2017, Monthly Notices of the Royal Astronomical Society, 470, 1121

Tremmel M., et al., 2018, Monthly Notices of the Royal Astronomical Society, 483, 3336

Übler H., et al., 2023, arXiv e-prints, p. arXiv:2312.03589

Uhlig M., Pfrommer C., Sharma M., Nath B. B., Enßlin T. A., Springel V., 2012, Monthly Notices of the Royal Astronomical Society, 423, 2374

Urry M., 2003, The AGN Paradigm for Radio-Loud Objects (arXiv:astro-ph/0301309)

Urry C. M., Padovani P., 1995, Publications of the Astronomical Society of the Pacific, 107, 803

Valentini M., Murante G., Borgani S., Monaco P., Bressan A., Beck A. M., 2017, MNRAS, 470, 3167

Valentini M., Borgani S., Bressan A., Murante G., Tornatore L., Monaco P., 2019, MNRAS, 485, 1384

Valentini M., et al., 2020, MNRAS, 491, 2779

Valentini M., Gallerani S., Ferrara A., 2021, MNRAS,

Valiante R., Schneider R., Bianchi S., Andersen A. C., 2009, Monthly Notices of RAS, 397, 1661

Valiante R., Schneider R., Zappacosta L., Graziani L., Pezzulli E., Volonteri M., 2018, Monthly Notices of the Royal Astronomical Society, 476, 407

Vallini L., Gallerani S., Ferrara A., Baek S., 2013, Monthly Notices of the Royal Astronomical Society, 433, 1567–1572

Vallini L., Gallerani S., Ferrara A., Pallottini A., Yue B., 2015, The Astrophysical Journal, 813, 36

Van Wassenhove S., Capelo P. R., Volonteri M., Dotti M., Bellovary J. M., Mayer L., Governato F., 2014, Monthly Notices of the Royal Astronomical Society, 439, 474–487

Vanden Berk D. E., et al., 2001, Astronomical Journal, 122, 549

Vito F., Di Mascia F., Gallerani S., Zana T., Ferrara A., Carniani S., Gilli R., 2022, MNRAS, 514, 1672

Vogelsberger M., et al., 2014, Nature, 509, 177

Vogelsberger M., Marinacci F., Torrey P., Puchwein E., 2019, Cosmological Simulations of Galaxy Formation (arXiv:1909.07976)

Volonteri M., Haardt F., Madau P., 2003, The Astrophysical Journal, 582, 559–573

Volonteri M., et al., 2020, MNRAS, 498, 2219

Volonteri M., Habouzit M., Colpi M., 2021, Nature Reviews Physics, 3, 732

Wang L., Dutton A. A., Stinson G. S., Macciò A. V., Penzo C., Kang X., Keller B. W., Wadsley J., 2015, Monthly Notices of the Royal Astronomical Society, 454, 83

Wang J.-M., Songsheng Y.-Y., Li Y.-R., Du P., 2022, Final stage of merging binaries of supermassive black holes: observational signatures, doi:10.48550/ARXIV.2211.03947, https://arxiv.org/abs/2211.03947

Weber J., 1967, Phys. Rev. Lett., 18, 498

Weinberger R., et al., 2017, MNRAS, 465, 3291

Weingartner J. C., Draine B. T., 2001, Astrophysical Journal, 548, 296

Wetzel A. R., Hopkins P. F., Kim J.-h., Faucher-Giguère C.-A., Keres D., Quataert E., 2016, The Astrophysical Journal Letters, 827, L23

White S. D. M., Rees M. J., 1978, MNRAS, 183, 341

Whitney B. A., Wood K., Bjorkman J. E., Wolff M. J., 2003, Astrophysical Journal, 591, 1049

Wiersma R. P. C., Schaye J., Smith B. D., 2009, MNRAS, 393, 99

Wise J. H., Regan J. A., O'Shea B. W., Norman M. L., Downes T. P., Xu H., 2019, Nature, 566, 85

Wiseman P., Schady P., Bolmer J., Krühler T., Yates R. M., Greiner J., Fynbo J. P. U., 2017, Astronomy and Astrophysics, 599, A24

Witt A. N., 1977, Astrophysical Journal Supplement, 35, 1

Witt A. N., Thronson Harley A. J., Capuano John M. J., 1992, Astrophysical Journal, 393, 611

Wolcott-Green J., Haiman Z., Bryan G. L., 2011, Monthly Notices of the Royal Astronomical Society, 418, 838

Xu H., et al., 2023, Research in Astronomy and Astrophysics, 23, 075024

Yoshida N., Abel T., Hernquist L., Sugiyama N., 2003, The Astrophysical Journal, 592, 645–663

Yu Q., Tremaine S., 2002, Monthly Notices of the Royal Astronomical Society, 335, 965

Yue B., Ferrara A., Salvaterra R., Xu Y., Chen X., 2013, Monthly Notices of the Royal Astronomical Society, 433, 1556–1566

Zana T., Gallerani S., Carniani S., Vito F., Ferrara A., Lupi A., Di Mascia F., Barai P., 2022, MNRAS,

Zhao X., Marchesi S., Ajello M., Cole D., Hu Z., Silver R., Torres-Albà N., 2021, Astronomy & Astrophysics, 650, A57

ZuHone J. A., Kunz M. W., Markevitch M., Stone J. M., Biffi V., 2014, The Astrophysical Journal, 798, 90